University of Southampton

Faculty of Physical Sciences and Engineering

Optoelectronics Research Centre

Compact and Versatile Caesium Thermal Photonic-Cells Based on Microstructured Hollow Core Fibres for Frequency and Time References

by

Marcelo Botelho Alonso

Thesis for the degree of Doctor of Philosophy

February, 2019

University of Southampton

Abstract

Faculty of Physical Sciences and Engineering

Optoelectronics Research Centre

Thesis for the degree of Doctor of Philosophy

Compact and Versatile Caesium Thermal Photonics-Cells Based on Microstructured Hollow Core Fibres for Frequency and Time References

by

Marcelo Botelho Alonso

The recent developments in fabrication of hollow core Photonic crystal fibres (HC-PCFs), especially Anti-resonant fibres (ARFs), made this class of fibre very attractive for gas-phase applications, which ultimately led to the concept of photonic reference cell. This device is a fully-connectorised, stand-alone, HC-PCF filled with a gas specimen. Its application spans from instrument calibration, quantum optics to high-resolution spectroscopy and metrology.

For time and frequency applications, the use of alkali metals with narrow atomic features (in the kHz range) is a requirement for ultra-stable reference signals. However, the coherence time of atoms is strongly dependent on the vapour dynamics and photonic cell geometry. This dependency limits the use of alkali vapour in miniaturised reference cells, such as photonic cells, because of the short coherence time that leads to atomic features in the MHz range, for reference cells with cross-section of $100\ \mu m$, operating at room temperature. The diffusion of the vapour can be tailored by adding a mixture of inert gas (buffer gas), with resulting atomic features between kHz and sub-kHz range. This is a very well-known method widely used in standard reference cells.

This thesis reports on the advances in HC-PCFs technology for time and frequency reference applications. Firstly, I present a method to interconnect solid core fibres and HC-PCFs with dissimilar core sizes by employing a mode field adapter (MFA) to mediate the joint. I model and demonstrate the use of such MFAs for a photonic cell, fully-connectorised to SMFs. Secondly, I demonstrate for the first time spectroscopy of coherent population trapping (CPT) dark resonance in Kagome-lattice ARFs filled with Cs. CPT is a quantum effect very useful in frequency reference applications as it can provide an indirect measurement of the Cs clock transition ($\sim 9.2\ GHz$). I model and demonstrate world record line-width narrowing of CPT dark resonance in HC-PCFs and micro-metre scale capillaries filled with thermal Cs-vapour, with experimental observation of line-widths below $50\ kHz$ for a Kagome-lattice ARF with a hollow core diameter of $125\ \mu m$.

Table of Contents

List of Acronyms

ARF	Antiresonant fibre
BG	Buffer gas
BS	Beam splitter
CMOS	Complementary metal–oxide–semiconductor
CPT	Coherent Population Trapping
CSAC	Chip-scale atomic clock
ECDL	External cavity diode laser
EIT	Electromagnetically induced transparency
EMF	Electromagnetic field
EOM	Electro optical modulator
FEM	Finite element method
FM	Fundamental mode
FPS	Fibre polarisation controller
FUT	Fibre under test
FWHM	Full width at half maximum
GIF	Graded Index Fibre
HC-PBGF	Hollow core photonic bandgap fibre
HC-PCF	Hollow core photonic crystal fibre
HOM	Higher order mode
K-ARF	Kagome lattice antiresonant fibre
LHS	Left hand side
LIAD	Light induced atomic desorption
LMA	Large mode area fibre
LP	Linearly polarised

MFA	Mode field adapter
MFD	Mode field diameter
MMF	Multi-mode fibre
MMI	Multi-mode interference
NA	Numerical aperture
NANF	Nested anti resonant nodeless fibre
ND	Neutral Density filter
NIST	National Institute of Standards and Technology
NPL	National Physical Laboratory
OD	Optical Depth
ORC	Optoelectronic Research Centre
PD	Photo detector
RHS	Right hand side
RIN	Relative amplitude noise
SMF	Single mode fibre
SMMI	Spatial multi-mode interference
TE	Transverse electric
TLS	Tunable laser system
TM	Transverse magnetic
TT	Transit-time
UHV	Ultra-high vacuum
WKB	Wentzel-Kramers-Brillouin
WP	Wave plate

Table of Tables

Table of Tables

Table of Figures

Table of Figures

Table of Figures

Research Thesis: Declaration of Authorship

Print name:

Title of thesis:

Compact and Versatile Caesium Thermal Photonics-Cells Based on Microstructured Hollow Core Fibres for Frequency and Time References

I declare that this thesis and the work presented in it are my own and has been generated by me as the result of my own original research.

I confirm that:

1. This work was done wholly or mainly while in candidature for a research degree at this University;
2. Where any part of this thesis has previously been submitted for a degree or any other qualification at this University or any other institution, this has been clearly stated;
3. Where I have consulted the published work of others, this is always clearly attributed;
4. Where I have quoted from the work of others, the source is always given. With the exception of such quotations, this thesis is entirely my own work;
5. I have acknowledged all main sources of help;
6. Where the thesis is based on work done by myself jointly with others, I have made clear exactly what was done by others and what I have contributed myself;
7. Parts of this work have been published as:

M. A. Gouveia *et al.*, "Coherent Population Trapping in Cs-filled Kagome Hollow Core Fibers," in *Conference on Lasers and Electro-Optics*, 2018, p. JTh2A.42.

Signature: Date:

Acknowledgements

Normally, a regular PhD candidate – *like myself* – at this stage may ask: what is the real contribution for science that this thesis might give? Or rather, will this piece of writing have an impact over people's lives? - I did ask myself those questions and it took me months to figure out the answer. In fact, it took me the whole writing period.

Unfortunately, I do not have answer for the first question – *time is in charge of it!*

The answer for the second question, however, is simple: it already did, at least to one person…

It did change me from day-zero of this project, back in 2015. It brought into my life brilliant people who guided me through my years as a graduate student. The lessons taught throughout this period transformed me. I list here, without any particular order, the people who took part of this journey: Prof Marco Petrovich, Prof David Richardson, Prof Patrick Gill, Prof Francesco Poletti, Dr Peter Horak, Dr Radan Slavik, Dr Thomas Bradley, Dr Mohsin Haji, Dr Natalie Wheeler, Mr Pravin Patel, Dr Eric Nukam-Fukoa, Dr Seyed Reza Sandoghchi, Dr Yong Chen, Dr Gregory Jasion and Dr Dimitrios Zaouris. Yes! – it was big group. Without them and their patience, this thesis would only be a pile of blank paper sheets! And for this reason, I respect them deeply. Thank you.

All of them contributed somehow in the studies presented and discussed throughout this thesis. My special thanks go to Dr Thomas Bradley, Dr Natalie Wheeler and Dr Yong Chen for fabricating the superb hollow core fibres that I have used for CPT spectroscopy. I am also very thankful to Dr Mohsin Haji and Mr Pravin Patel for all the support when building the ultra-high vacuum setup and test equipment. – *Those very late evenings in the laboratory will never be forgotten!* Without Dr Reza Sandoghchi help building the precise cleaving setup, my work on mode field adapter for HC-PCFs would have been much harder – *Thank you, Reza!* I am grateful for the time that Dr Eric Nukam-Fukoa spent with me discussing the theoretical aspects of mode field adapters and physical properties of hollow core fibres. Finally, I am deeply thankful for having Prof Marco Petrovich, Prof David Richardson, Prof Patrick Gill, Dr Thomas Bradley and Dr Mohsin Haji as my supervisory team. – *Without your advice, patience and support I would not be able to perform a percentage of the studies reported in this thesis.*

Yours truly,

Marcelo Alonso

A note to my friends and family.

I am thankful for the friends I have. Their support, patience and love, albeit the distance, were fundamental to me throughout these four years - it has never been easy to say goodbye for the distant ones. I am the result of every second we spent together, and I carry you all with me.

I am also very fortunate to have found great and caring people in the UK. We stuck together and look after one another. We shared the joy and pain of our victories and failures, but still we kept going! To my family, I dedicate the last few sentences below…

> *Isso jamais fora planejado. Aconteceu, como quase tudo em nossas vidas. O apoio incondicional durante esse período foi fundamental. Ser fruto do amor, lutas e renúncias me deu a força necessária para seguir em frente, apesar da distância e a saudade. Esta tese marca o final deste período e dedico a vocês cada palavra nela contida.* ***– Essa conquista foi fruto de sua dedicação!***

Muito Obrigado,

Marcelo Alonso

Chapter 1 Introduction

1.1 Introduction

The objective of this thesis is to contribute to the development of hollow core photonic crystal fibres (HC-PCFs) for quantum-based technologies.

Thermal quantum and atom-based technologies for time and frequency reference rely strongly on the use of atomic reference cells. Such reference cells are generally millimetre to centimetre-size glass containers filled with a given atomic or molecular gas and they are called reference cells as they can provide a reliable and stable source of atomic (gas) absorption lines, which are fundamental to various application areas, for example sensing, instrument calibration, fundamental research and metrology. They can be implemented as free-space optical elements, often requiring complex optical configurations in order to obtain the optical signal carrying the atomic transition information. Their design and geometry can a play major role in certain applications by reducing the coherence time of the interacting atoms due to the highly interactive character of thermal atomic vapours. At room temperature, the coherence time is mainly dictated by collisional effects (atom-atom and atom-walls) [1]. Depending on the cell's dimensions and the number of atoms interacting, the coherence time of the atoms can be defined by the smallest dimension of the cell, since it depends on the time between two consecutive inelastic atom-wall collisions [1]. Therefore, the smaller the cell, the shorter the coherence time. This, in general, is a major drawback for reference cell miniaturisation. However, research groups worldwide have developed and methods to mitigate decoherence effects in thermal alkali vapours and, over the past two decades, there has been a vast improvement in reference cells technology and their miniaturisation [2]–[6]. The use of anti-relaxation coatings – i.e., polymer-based films that increase the number of elastic collisions between atoms and the cell walls [7], [8] – as well as the use of suitable buffer gases – i.e. inert gases that decrease the free-mean path of alkali atoms – have paved the way towards miniaturisation of free-space reference cells. Researchers from the US National Institute of Standards and technology (NIST) designed and demonstrated the first lithography-based, millimetre-size, reference cell [5]. Its demonstration was part of the development of a chip-scale atomic clock (CSAC) [2] – a device which is now commercially available.

A radical alternative is to use glass capillary and HC-PCFs as miniaturised reference cells. HC-PCFs are an especial class of optical fibres that, thanks to their complex cladding design, can guide light with very low loss in an air-filled core (hollow core). Figure 2.1 shows a selection of various recent types of HC-PCFs. ARFs, since their first demonstration [9], have been extensively used for gas phase applications, as they can be fabricated with a large hollow core ($> 100\ \mu m$, in diameter) [10] and

excellent optical guidance properties. Several research groups have demonstrated quantum related effects in ARFs and hollow-core photonic bandgap fibres (HC-PBGFs) filled with alkali vapours [11]–[20].

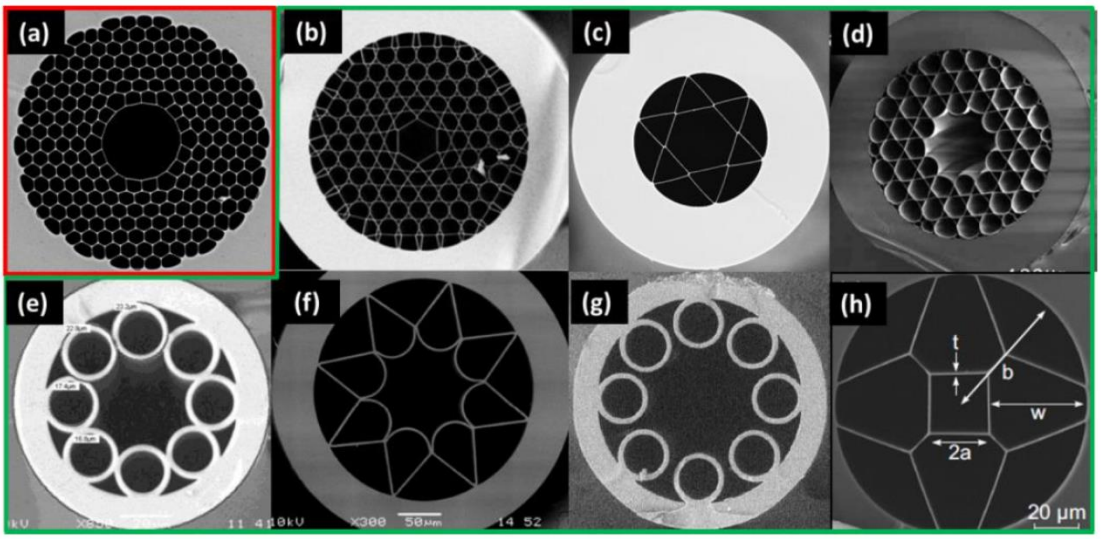

Figure 1.1: Scanning Electron Microscope images of various design of HC-PCFs. (a) HC-PBGF; (b) kagome-lattice-ARF (K-ARF); (c) Hexagram-ARF; (d) Hypocycloid core K-ARF; (e) Negative Curvature ARF; (f) Negative curvature ARF, also; (g) Nodeless Negative curvature ARF; (h) Double Clad ARF. Extracted from [21].

The use of HC-PCFs as reference cells, or generally referred to as photonic cells, has the potential to decrease the complexity and size of the optical apparatus greatly, eliminating the requirement for free-space components used in conventional reference cells. Also, its hollow core not only serves as a waveguide but also as an alkali vapour container. Crucially, the longer interaction paths can lead to stronger atomic lines, compared to millimetre size reference cells.

Photonic cells, however, still require further substantial development in order to compete on level field with the state-of-the-art miniature reference cells. For instance, a key requirement is the development of connectorisation techniques between HC-PCFs and conventional single mode fibres (SMFs), with low optical insertion loss, whilst providing a long-lasting seal to the hollow core. Also, due to the micrometre-size core, it is expected that the coherence time of atoms located inside the core will be much shorter than in millimetre-size cells. Therefore, research and development of suitable techniques to increase the coherence time of atoms inside the hollow core is paramount. Prof Benabid's group at the University of Limoges has studied coating the inner hollow core walls of ARFs with anti-relaxation films [19], [22], [23]. In their most recent publication, his group has demonstrated electromagnetically induced transparency peaks with sub-natural line-width as narrow as 200 kHz in Rb filled ARFs [23]. This result indicated that his group has successfully

developed a technique to internally coat the hollow core with anti-relaxation coatings and proved their functionality.

This thesis investigates for the first-time coherent population trapping in Cs filled ARFs. Coherent population trapping (CPT) is an electromagnetically induced transparency effect capable of generating resonances in the sub-kHz range [24], [25]. CPT is also a very elegant indirect way to obtain the clock transition frequency of alkali atoms ($9.192633770\ GHz$ for Cs atoms), making this quantum effect ideal for frequency and time reference applications.

In this thesis I study the use of Kagome Lattice anti resonant fibres (K-ARFs) as photonic cells for time and frequency reference applications. The study comprehends of demonstrating the filling of HC-PCFs with Cs vapour and performing high resolution spectroscopy of the CPT dark resonance observed from the atoms inside the hollow core. I summarise in the following the tasks performed during this study.

- Optical characterisation of the K-ARFs fabricated by the fabrication team at the Optoelectronics Research Centre, in term of propagation loss and bend loss at the CS D lines.
- Demonstrate a method to interconnect of HC-PCFs to standard SMFs. The connection should provide low insertion loss and minimised multi-mode interference.
- Study the experimental aspects of CPT in stand-alone, commercially available, millimetre size reference cells filled with Cs vapour and a mixture of buffer gas. This experiment is imperative to identify trends and pressure ranges that can be used in micrometre scale capillaries and HC-PCFs. To our knowledge, it has not been reported yet experimental data of line narrowing as a function of the buffer gas pressure in CPT dark resonance. The buffer mixture used was $71\ \%$ of N_2 and $29\ \%$ of Ar, with total pressure varying from $1\ torr$ to $120\ torr$.
- Design and build a HC-PCF filling rig with the capability of filling K-ARFs with Cs vapour and performing high resolution spectroscopy of CPT dark resonance in the Cs vapour found within the hollow core. The rig comprehends of a built-to-purpose vacuum system, with custom made parts designed to facilitate the filling and spectroscopy measurements. An optical system was also designed and built in order to maximise the optical coupling and collection of the signal to and from the HC-PCF samples.
- Estimate the filling status and atomic density in the HC-PCFs.
- Perform spectroscopy of CPT dark resonance in HC-PCFs filled with Cs vapour and identify trends of contrast and line-width as a function of laser input power, magnetic field strength and polarisation of the light. This is the first time a group reports CPT in HC-PCFs filled with pure alkali vapour.

- Perform spectroscopy of CPT dark resonance in HC-PCFs, filled with Cs vapour and with added buffer gas. This experiment demonstrates that by tuning the buffer gas pressure, it is possible to obtain ultra-narrow CPT dark resonances in photonic cells with micrometre scale cross-sections. I demonstrate here a line narrowing of more than two orders of magnitude, when $\sim 400\ torr$ of a buffer gas combination of N_2 and Ar is mixed with the Cs vapour found inside the hollow core.

1.2 Thesis Layout

This thesis is organised as follows.

Chapter 2 presents the anti-resonant fibres (ARFs) – a class of HC-PCF – suitable alkali vapour filling and performing CPT dark resonance spectroscopy. The ARFs and specially the kagome-lattice ARF (K-ARF) are very attractive to applications involving gas-phase matter, as their large hollow core facilitate the gas diffusion through the fibre length. A historical back ground on ARFs as well as a brief discussion on their guiding mechanism is given, followed by an in-depth characterisation of K-ARFs use in this thesis. The fibres studied in this thesis were characterised regarding their propagation loss and bend loss at Cs D lines wavelengths ($852\ nm$ and $894\ nm$).

Chapter 3 describes a new interconnection method between solid core fibres and HC-PCFs with dissimilar core sizes. By exploiting the multimode interference present in graded index fibres, I model and demonstrate interconnection between standard SMFs to HC-PCFs with large hollow core sizes.

In chapter 4, I theoretically and experimentally demonstrate the coherent population trapping mechanism. I present the main equations that explain the effect and discuss the main line broadening mechanisms, as well as methods to control them. I present a few useful mathematical models that can provide insights on how the Cs vapour interacts with the bulk reference cell and K-ARF geometry. This chapter also presents a full characterisation of millimetre-size reference cells, filled with differ buffer gas pressures. The diffusive character of the Cs vapour in the reference cells is modelled and compared to the actual measured CPT line-width for a range of buffer gas pressures.

In chapter 5 I describe the vacuum chamber designed and built to fill K-ARFs with Cs-vapour and the optical apparatus used to perform high resolution spectroscopy in-situ. The chapter comprehends of a full description of the ultra-high vacuum system designed and built at the National Physical Laboratory and optical system required to investigate the HC-PCF filling and perform high resolution spectroscopy of CPT dark resonance. I describe the use of different longitudinal magnetic field generators (required to obtain magnetic *insensitive* CPT resonances). I

theoretically and experimentally study two different geometries of magnetic field generator (solenoid and a pair of Helmholtz coils), presenting the advantages and disadvantage of each geometry. Finally, I characterise the filling of K-ARFs, introducing a simple physical model capable of predicting the atomic density inside the hollow core fibres when the optical intensity level is varied.

I demonstrate for the first-time spectroscopy of CPT dark resonance in K-ARFs in chapter 6. I characterised the contrast and line-width of the dark resonance as a function of the input laser power, magnetic field strength and polarisation state of light for HC-PCFs and micrometre scale capillaries filled with pure-Cs vapour. In this chapter I also demonstrate the use of a mixture of buffer gas as a technique to narrow the CPT dark resonance observed from the atoms located inside the HC-PCFs and capillaries. I report narrowing of two orders of magnitude for K-ARF with hollow core diameter of $125\ \mu m$. I also report a minimum line-width of $50\ kHz$ for the same K-ARF and$\sim 11\ kHz$ for a capillary with inner diameter of $305\ \mu m$, for a buffer gas mixture of 65% of N_2 and 45% Ar, with total pressure of $\sim 400\ torr$. The results reported in this chapter are four times better than the narrowest atomic feature line measured in alkali vapours in HC-PCFs and represent the state-of-the-art for narrowed atomic features in HC-PCFs filled with thermal alkali-vapours.

Conclusions and future work are presented in chapter 7.

1.3 References

[1] J. Vanier and C. Audoin, The Quantum Physics of Atomic Frequency Standards, v.1. IOP Publishing, 1989.

[2] S. Knappe, “MEMS Atomic Clocks,” *Compr. Microsystems*, pp. 571–612, Jan. 2008.

[3] S. Knappe et al., “A chip-scale atomic clock based on 87Rb with improved frequency stability,” Opt. Express, vol. 13, no. 4, pp. 1249–1253, 2005.

[4] J. Kitching, L. Hollberg, S. Knappe, and R. Wynands, “Compact atomic clock based on coherent population trapping,” Electronics Letters, vol. 37. p. 1449, 2001.

[5] L. A. Liew, S. Knappe, J. Moreland, H. Robinson, L. Hollberg, and J. Kitching, “Microfabricated alkali atom vapor cells,” Appl. Phys. Lett., vol. 84, no. 14, pp. 2694–2696, 2004.

[6] C. T. Jacques Vanier, *The Quantum Physics of Atomic Frequency Standards: Recent Developments*. CRC Press, 2015.

[7] M. V. Balabas *et al.*, “High quality anti-relaxation coating material for alkali atom vapor cells,” *Opt. Express*, vol. 18, no. 6, p. 5825, Mar. 2010.

[8] M. A. Hafiz et al., “Characterization of Cs vapor cell coated with octadecyltrichlorosilane using coherent population trapping spectroscopy,” J. Appl. Phys., vol. 117, no. 18, p. 184901, May 2015.

[9] F. Benabid, J. C. Knight, G. Antonopoulos, and P. S. J. Russell, “Stimulated Raman scattering in hydrogen-filled hollow-core photonic crystal fiber.,” Science, vol. 298, no. 5592, pp. 399–402, 2002.

[10] B. Debord et al., “Ultra-Large Core Size Hypocycloid-Shape Inhibited Coupling Kagome Fibers for High-Energy Laser Beam Handling,” Lightwave Technology, Journal of, vol. 33, no. 17. pp. 3630–3634, 2015.

[11] P. Londero, V. Venkataraman, A. R. Bhagwat, A. D. Slepkov, and A. L. Gaeta, “Ultralow-Power Four-Wave Mixing with Rb in a Hollow-Core Photonic Band-Gap Fiber,” *Phys. Rev. Lett.*, vol. 103, no. 4, p. 043602, Jul. 2009.

[12] A. D. Slepkov, A. R. Bhagwat, V. Venkataraman, P. Londero, and A. L. Gaeta, “Spectroscopy of Rb atoms in hollow-core fibers,” *Phys. Rev. A*, vol. 81, no. 5, p. 053825, May 2010.

[13] A. D. Slepkov, A. R. Bhagwat, V. Venkataraman, P. Londero, and A. L. Gaeta, “Generation of large alkali vapor densities inside bare hollow-core photonic band-gap fibers.,” Opt. Express, vol. 16, no. 23, pp. 18976–18983, 2008.

[14] S. Ghosh, A. R. Bhagwat, C. K. Renshaw, S. Goh, A. L. Gaeta, and B. J. Kirby, “Low-Light-Level Optical Interactions with Rubidium Vapor in a Photonic Band-Gap Fiber,” *Phys. Rev. Lett.*, vol. 97, no. 2, p. 023603, Jul. 2006.

[15] C. Perrella, P. S. Light, J. D. Anstie, T. M. Stace, F. Benabid, and A. N. Luiten, “High-resolution two-photon spectroscopy of rubidium within a confined geometry,” Phys. Rev. A, vol. 87, p. 13818, 2013.

[16] P. S. Light, F. Benabid, F. Couny, M. Maric, and A. N. Luiten, “Electromagnetically induced transparency in Rb-filled coated hollow-core photonic crystal fiber,” *Opt. Lett.*, vol. 32, no. 10, p. 1323, May 2007.

[17] C. Perrella, P. S. Light, J. D. Anstie, F. N. Baynes, F. Benabid, and A. N. Luiten, “Two-color rubidium fiber frequency standard,” Opt. Lett., vol. 38, no. 12, p. 2122, Jun. 2013.

[18] C. Perrella, P. S. Light, S. A. Vahid, F. Benabid, and A. N. Luiten, “Engineering Photon-Photon Interactions within Rubidium-Filled Waveguides,” *Phys. Rev. Appl.*, vol. 9, no. 4, p. 044001, Apr. 2018.

[19] T. D. Bradley *et al.*, "Ground-state atomic polarization relaxation-time measurement of Rb filled hypocycloidal core-shaped Kagome HC-PCF," *J. Phys. B At. Mol. Opt. Phys.*, vol. 49, no. 18, p. 185401, Sep. 2016.

[20] S. Okaba *et al.*, "Lamb-Dicke spectroscopy of atoms in a hollow-core photonic crystal fibre," *Nat. Commun* 5, 4096, Jun. 2014.

[21] F. Poletti, "Nested antiresonant nodeless hollow core fiber," Opt. Express, vol. 22, no. 20, pp. 23807–23828, 2014.

[22] X. M. Zheng et al., "In-situ dwell-time measurement of Rb at the inner-wall coated-surface of HC-PCF," in Conference on Lasers and Electro-Optics, 2018, p. SM3L.4.

[23] X. M. Zheng et al., "Narrow electromagnetically induced transparencies in Rb confined large-core core inner-wall coated Kagome HC-PCFs," in Conference on Lasers and Electro-Optics, 2018, p. SM3L.3.

[24] M. Zhu, L. S. Cutler, J. E. Berberian, J. F. DeNatale, P. A. Stupar, and C. Tsai, "Narrow linewidth CPT signal in small vapor cells for chip scale atomic clocks," in *Proceedings of the 2004 IEEE International Frequency Control Symposium and Exposition, 2004.*, pp. 100–103.

[25] J. Vanier, "Atomic clocks based on coherent population trapping: a review," Appl. Phys. B, vol. 81, no. 4, pp. 421–442, 2005.

Chapter 2 Hollow Core Fibre Technology Suitable for Light-Matter Interactions

Foreword

Hollow Core Anti-Resonant Fibres, or simply ARFs, were firstly introduced by Benabid and his co-workers, in 2002 [1]. Due to their unique and advantageous geometry (capable of supporting large hollow-cores) and optical properties (propagation losses typically below 1dB/m and low density of guided modes), ARFs and their counterpart – Hollow-Core Photonic Band-Gap Fibres (HC-PBGFs) – have been at the centre of the latest developments in gas and alkali vapour-filled HC-PCFs. Among the studies so far reported, groups have demonstrated application of HC-PCFs for non-linear effects [2]–[4], frequency combs [5], four-wave mixing [6], photon-photon interactions [7], [8] Rydberg atoms [9], electromagnetically induced transparency [10]–[12], coherent population trapping [13] and single-photon quantum memories. [14]

ARFs have a natural advantage over HC-PBGFs for applications that require wavelength tunability and large hollow core size. This advantage emerges from the fact that ARFs support large hollow core sizes, with diameters larger than $100\ \mu m$, whilst offering broadband guidance, over an octave span and wider [15]. Recently, better understanding of fabrication processes and the anti-resonance (AR) guidance have led to a drop in propagation loss below $10\ dB/km$ [16], [17], with theoretical predictions of an ultimate overall loss below $10^{-2}\ dB/km$ [18], [19]. Hayes et al. have demonstrated the first laboratory-level use of ARFs for short-haul data transmission [20].

In this chapter, I briefly introduce ARFs and discuss the historical evolution of this fibre design since first demonstration. I present the most iconic geometries and discuss currently understanding of its guidance mechanism and loss mechanism of ARFs. I comment on the use of ARFs as gas and, especially, vapour cells for atom-light interactions.

For the scope of my project, three fibres were designed and fabricated at the ORC facilities by Dr T. Bradley and Dr N. Wheeler. I performed most of the optical measurements other than propagation loss and a bend loss measurements that were performed by Dr Bradley. His contribution is indicated throughout the chapter. These fibres were later used for in-fibre atomic spectroscopy and CPT line width control experiments. Those experiments and the underlying theory are discussed in chapter 4, 5 and 6.

2.1 Hollow Core Anti-Resonant Fibres

The first ARF geometry demonstrated was the Kagome-lattice ARF (K-ARF) [1]. Figure 2.1 (a) is a scanning electron microscope image of a typical K-ARF. The uncertainty regarding its guidance mechanism generated a number of studies proposing and demonstrating advances in optical losses and potential applications [15], [18], [21]–[27]. In particular, Fevrier introduced a ground-breaking and greatly simplified geometry that shed light on the role of the cladding microstructure and the hidden aspects of the AR guidance mechanism [15]. Fevrier's work, the introduction of the negative curvature design in core walls and Argyros' square-lattice ARFs were the turning points that led research groups to demystify the guidance mechanism found in Kagome-lattice microstructure [15], [21], [28]. Scanning electron microscope images of a HC-PBGF and a selection of ARFs, with different cross-sections, are shown in Figure 2.1.

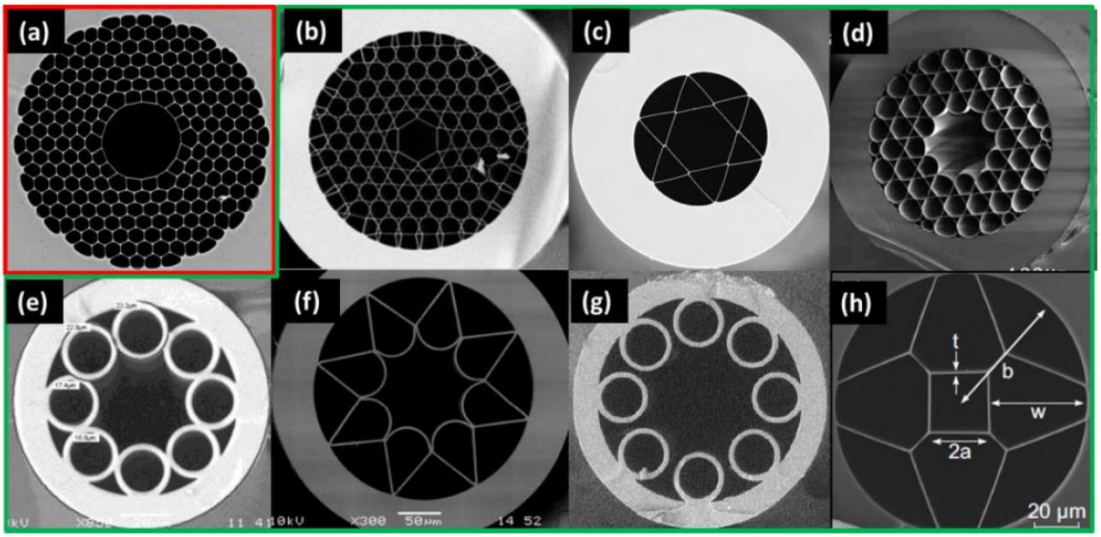

Figure 2.1: Scanning Electron Microscopies of HC-PCFs. (a) HC-PBGF; (b) K-ARF; (c) Hexagram-ARF; (d) Hypocycloid core K-ARF; (e) Negative Curvature ARF; (f) Negative curvature ARF, also; (g) Nodeless Negative curvature ARF; (h) Double Cladded ARF. Extracted from [18].

Debord et al. have nicely demonstrated the beneficial effect of adding the hypocycloid core wall and increasing its curvature in K-ARFs [29] The hypocycloid tends to decrease the coupling between hollow core guided modes and the leaky cladding modes, supported at the microstructure nodes. It improves the spectral response of the ARF by diminishing the presence of additional resonances and ultimately expanding the spectral transmission window. Debord et al. have also demonstrated the role of subsequent Kagome lattice layers in attenuating leakage losses [30]. Bradley et al. have analysed the modal content of K-ARFs and have demonstrated that such fibre designs support a few modes [31]. Prof Fetah Benabid's group at the University of Limoges currently holds the record for minimum loss of $\sim 8\ dB/km$, achieved in a nodeless ARF (with cross-section similar to Figure 2.1 (g)) [17]. Prof F. Poletti and Dr Belardi have suggested an improved version of the nodeless ARF

with a nested element within each microstructured ring that provides a reduction of propagation loss by a few orders of magnitude (below $0.001\ dB/km$) and maximised intermodal differential loss, which leads to an effective single mode guidance [18], [19]. Such loss figures and reduced modality would make ARF an ideal platform for short and long-haul data transmission. Hayes et al. have provided the first demonstration of the use of nodeless ARF for short haul data transmission [20].

In the next section, I introduced a simplified model that may explain the underlying physical phenomenon of AR guidance and the source of losses.

2.1.1 The Anti-Resonant Guidance Mechanism

In order to maintain historical coherence, I refer to K-ARF as Kagome-Lattice HC-PCFs only in this section. The Kagome lattice fibre was demonstrated without prior knowledge of its underlying guidance mechanism…

…and that is the beauty of science; sometimes it gives us a gem to decipher.

Since the first demonstration of Kagome-Lattice HC-PCF in 2002 [1], the guidance mechanism present in this class of HC-PCF has been a subject of intense debate within the scientific community. Couny et al. introduced the concept of inhibited coupling following an extensive analysis of the Kagome lattice microstructure, breaking it down into unit cells and observing its associated resonant optical modes and coupling strengths to the air-guided core modes [5]. Their hypothesis considered that coupling between resonant modes (resonant unit cells) and hollow core modes dictates the confinement strength.

Février et al. reported that the underlying guidance mechanism might rely only on the surrounding core geometry and subsequent microstructure elements only contributed to increasing the confinement loss [15]. Simulations comparing the confinement loss of a simple concentric ring against a four-layered Kagome-lattice microstructure are presented in Figure 2.2. The simplistic ring design showed a confinement one order of magnitude lower, compared to the Kagome-Lattice geometry. Février et al. also pointed out that additional core-concentric rings decrease the confinement loss [15], indicating that the guidance mechanism is related to anti-resonance, similar to Bragg-fibre designs [32].

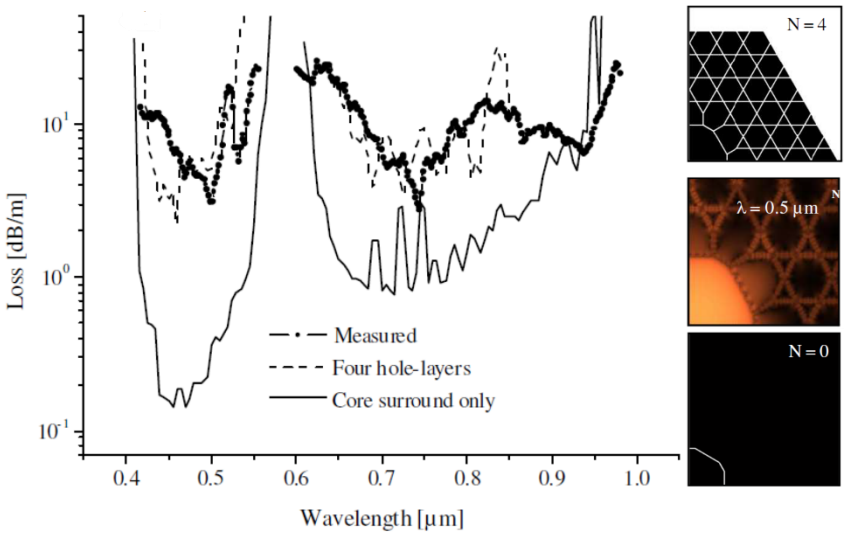

Figure 2.2: Confinement loss comparison of a ring fibre design and a four-layered Kagome-Lattice HC-PCF. One ring fibre showed confinement loss lowed by one order of magnitude relative to the Kagome-Lattice geometry. Experimental data from a four-layered Kagome-Lattice HC-PCFs is also shown in the plot (black dots). Extracted and adapted from [15].

In Kagome-Lattice HC-PCFs, although the radial struts and nodes are necessary for structural purposes, they degrade the optical performance of the fibre. The introduction of the hypocycloid core walls in Kagome-Lattice HC-PCFs corroborated with the fact that the microstructure cannot have a central role in terms of optical properties, as the negative curvature tends to isolate the hollow core modes from the microstructure [21], [29]. Nevertheless, Debord et al. have shown that the Kagome-lattice microstructure has a secondary role and does improve fibre loss when the HC-PCF is bent [30].

In general, the spectral response of a typical ARF can be depicted as low loss spectral windows (fundamental and higher order windows) separated by discrete high loss spectral regions (core-clad resonances) [18], [19], [28], [32]. The high loss spectral positions, λ_m, are roughly defined by the following expression,

$$\lambda_m = \frac{2t}{m}\sqrt{n_{si}^2 - 1}\,, \qquad \text{Eq. 2.1}$$

where t is the core wall thickness, $m \geq 1$ is the resonance order index and n_{si} the core wall refractive index. For silica ARFs, $\lambda_m \sim 2t/m$. This expression can be interpreted as a spectral tuning law, allowing ARFs to be designed to guide at a given wavelength of choice. The transmission window width, analogous to the free spectral range, can be derived from Eq. 2.1 as

$$\Delta\lambda_{m+1} \equiv \lambda_m - \lambda_{m+1} = \frac{\lambda_m}{m+1}, \qquad \text{Eq. 2.2}$$

for $m \geq 1$. Note that the fundamental transmission window does not have a defined width and the higher order window widths are directly proportional to the red-end wavelength and inversely proportional to their order index. Figure 2.3 shows the spectral response of a nodeless ARF with three resonances (2nd, 3rd and 4th) and three transmission windows (2nd, 3rd and 4th orders) visible over the plot range.

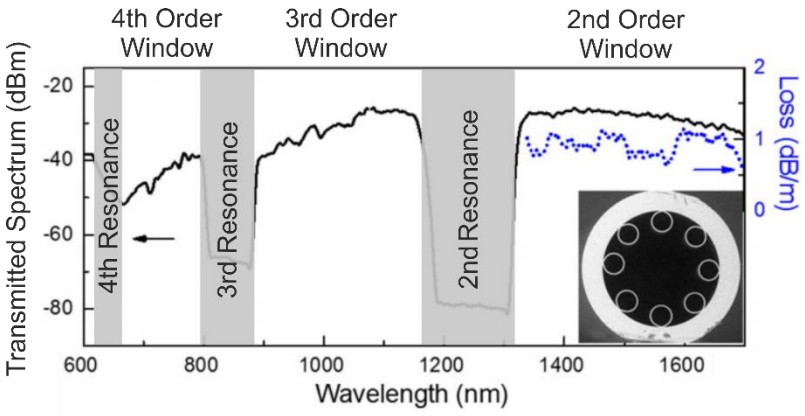

Figure 2.3: Example of spectral response of a nodeless ARF. Three transmission windows and three high loss resonances are present in the spectrum. The first resonance is out of range, as the wall thickness is $t \sim 1.2\ \mu m$, which yields $\lambda_1 \sim 2.4\ \mu m$, according to Eq. 2.1. Extracted and adapted from [33].

Traditionally, Eq. 2.1 emerges from the phase interference caused by multiple reflections that happen at the inner and outer core-wall surfaces [32]. However, it does not fully explain the loss mechanism at a given spectral region. Argyros et al. designed a square-lattice ARF and demonstrated that by approximating the struts to infinite-long slab waveguides, Eq. 2.1 can be derived directly from the dispersion of the TM_m and TE_m modes supported by the core walls [28]. The resonant wavelengths are also the cut-off wavelengths of each TM_m and TE_m mode. At these wavelengths, the modes are weakly guided and over-expanded and their phase velocities are very close to vacuum speed of light. These three conditions are fundamental to amplify the coupling between the core-wall guided modes (cladding modes) and hollow core guided modes (air-guided modes). Therefore, near the cut-off, core guided modes are likely to couple into cladding modes, greatly increasing the confinement loss. Far from the cut-off regions, the core-walls act as anti-resonant reflectors, as described in [32]. Mode coupling between hollow core modes and modes supported by nodes and struts with different thickness increases the overall loss and reduce the width of the transmission windows.

In terms of loss mechanism, ARFs are prone to confinement loss and, secondarily, to surface scattering loss [18]. The confinement loss mechanism is mainly related to coupling between core guided modes and modes supported by the microstructure's struts and the continuum of radiation modes [18]. The confinement loss can be improved with better ARF designs, decreasing the field overlap with nodes and struts that do not provide a *positive* contribution to the AR guidance mechanism [15], [18]. Surface scattering loss is inherently connected to the surface roughness and can be decreased by minimising the fraction of power that overlaps the core wall. This can be achieved by designing ARFs with large hollow core size [18].

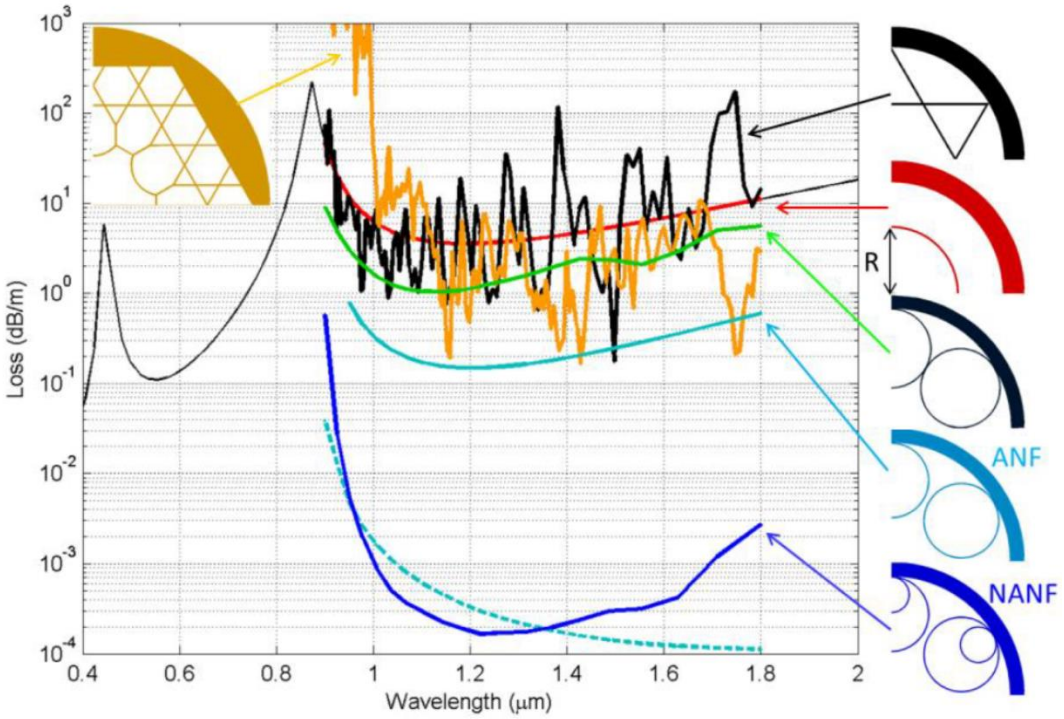

Figure 2.4: Propagation loss simulation comparison of five different ARF designs. All fibres had the same core-wall thickness and hollow core diameter. K-ARF (orange trace) and simplified ARF (black trace) perform similarly. The introduction of the negative curvature in the core –wall and its resonance cleansing property is clearly observed by comparing the orange and black lines to the green line (ARF with a hypocycloid core). The introduction of nodeless element microstructure (light blue trace) and nested elements (blue trace) improves the fibre propagation loss by one and four order of magnitude. Note that the nested nodeless element ARF (NANF) has it propagation loss of the same order as the surface scattering (dashed light blue). Extracted from[18].

ARFs are generally thought to support a few modes. Bradley et al. have thoroughly studied the modality of K-ARFs with different geometries via the Spectral and Spatial imaging technique and observed up to 7 *LP-like* mode groups [31]. They have also observed the excitation of exotic hexagonally symmetric modes during the study [34]. Newkirk et al. have also performed similar experiments with nodeless ARFs and reported observing up to 4 *LP-like* mode groups [33].

Prof Francesco Poletti and Dr Walter Belardi have exploited the combination of negative curvature and multiple concentric rings to design the *ideal* ARF geometry [18], [19]. The nested anti-resonant nodeless hollow core fibre (NANF) may hold the key to achieving ultra-low loss hollow core optical transmission. Theoretical models predicted overall confinement loss figures as low as $\sim 10^{-2}\ dB/km$ for a NANF with a hollow core diameter of $50\ \mu m$. Moreover, the intermodal differential loss can be engineered in this geometry and used to obtain effective single mode operation [18]. Figure 2.4 shows the propagation loss of five different ARFs with the same core-wall thickness and core diameter. Note that the K-ARF, the simplified ARFs with a core wall with and without negative curvature as well as an ideal glass-air Bragg-fibre has propagation loss figures of the same order. An order of magnitude improvement is obtained when the nodeless structure is introduced and three orders of magnitude when the nested nodeless microstructure is considered.

In the next section, I focus the discussion on ARFs for photon-atom interactions.

2.1.2 Hollow Core Anti-Resonant Fibres for Atom-Light Interactions

HC-PCFs are a very versatile photonic platform for atom-light interactions because of the existence of low loss guided modes within a hollow core, where it can filled with gas phase specimens (atoms or molecules) in order to obtain an active medium. Prof Ian Walmsley's group at Oxford University has developed a photon-level memory using a K-ARF filled with Rb vapour [14] and Prof Andre Luiten's group at the University of Adelaide has studied various aspects and applications of thermal Rb vapour-filled K-ARFs [7], [8]. Prof Hidetoshi Katori's group at the University of Tokyo was the first group to demonstrate cold Rb atom trapped in an optical lattice inside a K-ARF and they hold the record for the narrowest atomic feature measured in atoms found within a hollow core ($\sim 8\ kHz$) [35]. Prof Alexander Gaeta's group has also contributed in understanding the spectroscopy of Rb-vapour in HC-PBGFs and has developed methods to control the atomic vapour density in HC-PBGFs [36], [37].

HC-PBGFs and ARFs, in particular, represent very attractive HC-PCF geometries as the spectral properties of such fibres can be tailored to meet certain requirements for optimised atom-light interactions. Transmission bands in HC-PBGFs can be spectrally tuned by changing the size and distance between neighbour 'rods' [38], [39]. For ARFs, the transmission windows and core-clad resonances have well-defined positions determined simply by the hollow core-wall thickness, as described by Eq. 2.1, described previously in this chapter.

The hollow core shape and diameter also play important roles in exploiting quantum effects that require long-lived atomic coherence times and low pressures ($< 10^{-2}\ torr$) in atomic vapours [13], [40]–[46]. The average time of flight of atoms at low pressure is directly proportional to the

diameter of the hollow core and inversely proportional to the thermal speed of the atoms. Wall collisions ultimately leads to spectral broadening of atomic transitions [45], [46]. In other words, the larger the HC-PCF's core, the longer the coherence time and the weaker the associated broadening mechanism. **Therefore, the design of HC-PCFs for atomic vapour spectroscopy impacts the resonance line width.** Please refer to chapter 4 for detailed information on spectral broadening mechanisms defined by the vapour cell's geometry and vapour dynamics.

Due to their simplified guidance mechanism, where in most of the cases only the core wall and innermost microstructure play significant roles, ARFs represent ideal candidates for atomic-vapour experiments and devices in HC-PCFs. Debord et al. have, for example, demonstrated K-ARFs with hollow core diameter as large as $105\ \mu m$ with minimum loss of $0.1\ dB/m$, at a wavelength of $1.3\ \mu m$ [47].

2.2 Kagome Lattice Anti-Resonant Fibres for Cs-Filling

One of the main tasks of my project, as detailed in Chapter 1, was to design and fabricate HC-PCFs with optimised optical guidance at the Cs D1 and D2 lines ($894\ nm$ and $852\ nm$). The use of these lines is clarified in Chapter 4, where I describe the CPT effect I wish to exploit in HC-PCFs filled with Cs vapour. Although nodeless ARFs show a vast improvement in guidance, as discussed in previous the sections, their fabrication methods are still being perfected. K-ARFs, on the other hand, follow a more mature fabrication technique and, for this reason were chosen to be the fibre platform of choice for confining Cs-vapour in this project.

The fabrication team at the ORC's microstructured optical fibre group designed and fabricated three K-ARFs with different hollow core sizes and with guidance properties optimised for the Cs D-lines. A brief summary of the fabrication procedure and optical specifications are provided in the following sections. The fibres discussed in this section and used for spectroscopy in the following chapters were designed and fabricated by Dr Thomas Bradley and Dr Natalie Wheeler.

2.2.1 Fabrication Summary

K-ARFs are fabricated via a stack-and-draw process similar to more conventional PCFs and it is composed of three main stages described below. The procedure described below is somewhat oversimplified and it is included here only to give an overall picture of the fabrication process.

- **Preform**: A number of millimetre-size elements (tubes and rods) with different diameters is stacked following a design plan to form a lattice. Also, a predetermined number of elements is removed to form a defect at the centre of the stack that will define the hollow

core in the following steps. Once prepared, the assembly is placed tightly inside a larger tube (jacket).

- **Cane**: The preform is drawn once using a fibre drawing tower. The result is a millimetre-sized structured tube (called as cane). This stage is fundamental to consolidate the bond between the many capillary elements and between the outermost capillary elements and the outer jacket tube. Failed bonds ultimately result in distorted microstructure in the final stage (fibre drawing), which can impact the optical performance of the final fibre.
- **Fibre drawing:** The cane fabricated in the previous stage is then placed inside another jacket tube and it is drawn once again using a fibre drawing tower. Differential pressure in different regions of the cane (microstructure layers, hollow core, etc.) can be required to obtain the target microstructure expansion, hollow core wall shape and final diameter.

Table 2.1: Geometrical specifications of the K-ARFs fabricated for Cs-vapour filling.

K-ARF	Core Diameter (µm)	Microstructure Diameter (µm)	Outer Diameter (µm)	First Core-Clad Resonance (nm)	Average Propagation Loss at 894 nm (dB/m)	Average Propagation Loss at 1.55 µm (dB/m)
K65	~65	~202	~296	~1100	0.40	0.15
K92	~92	~204	~301	~700	0.12	0.15
K125	~125	~222	~300	~980	1.30	0.50

The geometrical specifications of the three K-ARF fabricated for this project are listed in Table 2.1. K65, K92 and K125 are K-ARFs with hollow core diameters of $65\ \mu m$, $92\ \mu m$ and $125\ \mu m$, respectively. The outer diameter of every fibre was set to $300\ \mu m$ in order to ensure compatibility with the filling system (discussed in chapter 4). The spectral response of $1.5\ m$ long samples and optical microscope images of their cross-sections are shown in Figure 2.5. K65 exhibits first core-clad resonance at a wavelength of $\sim 1100\ nm$ and K125, at $\sim 980\ nm$, while K92 has its first resonance at a wavelength of $\sim 700\ nm$. Therefore, K65 and K125 guide the Cs D lines ($894\ nm$ and $852\ nm$) in their respective second order transmission windows, whilst K92 guides just at the blue end of the fundamental window. In the following, I discuss the propagation and bend loss measurements taken for each fibre.

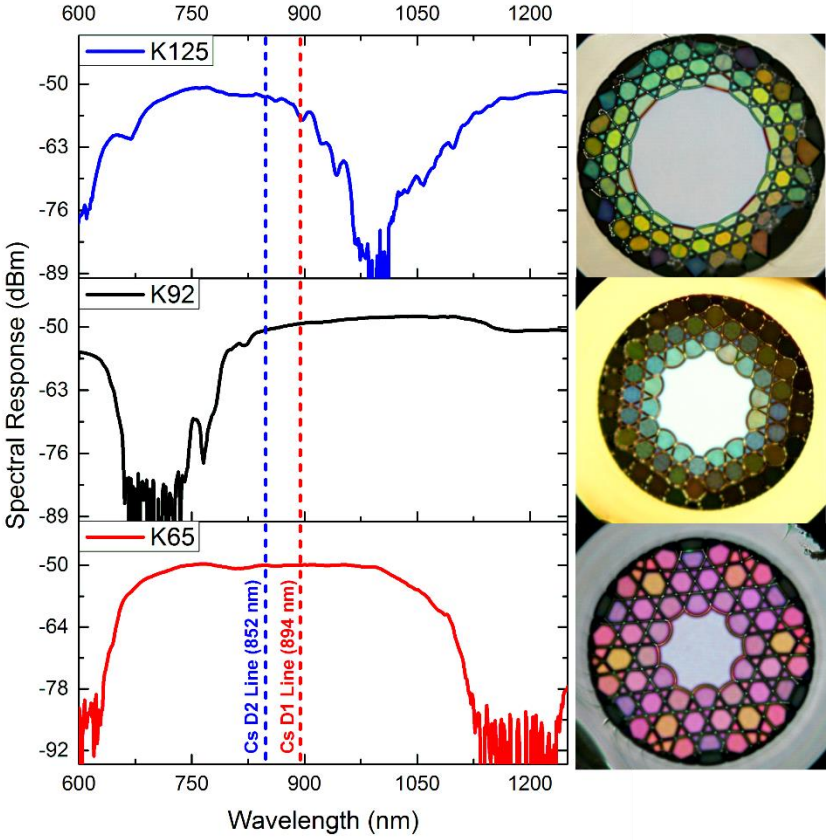

Figure 2.5: Spectral response of the three K-ARFs fabricated for Cs-filled HC-PCFs spectroscopy. K65, K92 and K125 have hollow core diameter of $65\ \mu m$, $92\ \mu m$ and $125\ \mu m$, respectively. All fibres guide at the Cs D-lines range ($850\ nm$ to $900\ nm$) K65 and K125 guide such wavelengths at their second order transmission window and K92 at its fundamental window. Optical microscope images of each fibre cross-section are shown on the right side of their associated transmission spectrum.

2.2.2 Optical Performance

Each K-ARF had its propagation loss measured via the cut-back technique. This measurement is based on a spectral response comparison of different lengths (one long and one short). Considering a fibre under test (FUT) with total length $(X + Y)$ – described in Figure 2.6(a) –, the power attenuation happened throughout the length Y can be inferred by subtracting the spectral power distribution of length X from length $(X + Y)$. The propagation loss, thus, can be inferred at a given wavelength by dividing the corresponding power attenuation at the fibre section by its length. As the cut-back measurement indicates the total loss of the segment analysed, it is necessary to minimise the excitation of higher order modal content and also to avoid bend loss by loosely coiling the FUT. Modality control can be realised by matching the mode field of the launch fibre to the fundamental mode of the FUT.

K92 was characterised using a white-light source and excitation via an endlessly single mode PCF (ESM) (NKT photonics LMA-15) launch fibre with a mode field diameter of about $13\ \mu m$ at $1550\ nm$ and $\sim 12.5\ \mu m$ at $894\ nm$. K65 and K126 showed higher optical loss, requiring use of a powerful light source. A Fianum super-continuum source and a graded-index patch cord were used to characterise both fibres. All spectra were recorded using a Yokogawa AQ-6315B Optical Spectrum analyser (OSA). All fibres were prepared in loose coils with minimum diameter of $40\ cm$, in order to minimise curvature loss. Measurement parameters as well as the fibre's propagation loss at $894\ nm$ and $1550\ nm$ are listed in Table 2.2 and the propagation loss as function of the wavelength for K-ARFs K65, K92 and K125 are shown in Figure 2.6(b),(c) and(d), respectively.

Table 2.2: Optical specification of K-ARFs fabricated for Cs-filled fibre Spectroscopy

K-ARF	Core Diameter (µm)	Light Source	Launch Fibre	Total Length (m)	Cut-back Length (m)	Propagation Loss at 894 nm (dB/m)	Propagation Loss at 1.55 µm (dB/m)
K65	~ 65	Super-Continuum	GIF 125	~ 16	~ 12	0.41 ± 0.01	0.15 ± 0.01
K92	~ 92	White Light Lamp	ESM-15	~ 35	~ 30	0.12 ± 0.01	0.15 ± 0.01
K125	~ 125	Super-Continuum	GIF 125	~ 29	~ 26	1.10 ± 0.01	1.14 ± 0.01

K125 was cut-back from $\sim 29\ m$ to $\sim 3\ m$ and has the highest loss amongst the three K-ARFs at both wavelengths ($894\ nm$ and $1550\ nm$) of $1.10\ dB/m$ and $1.14\ dB/m$, respectively. Although this fibre possesses the largest core, its core walls are not hypocycloids and the leakage loss (coupling to resonant modes supported by struts and radiation modes) can be greater across the whole spectrum. K65 has an intermediate performance among the K-ARFs analysed and showed a propagation loss of $0.41 \pm 0.01\ dB/m$ and $0.15 \pm 0.01\ dB/m$ at $894\ nm$ and $1550\ nm$, respectively, for a section of $\sim 12\ m$, cut from a $\sim 16\ m$ sample. At $1550\ nm$, K65 matched the propagation loss for K92. K92, however, showed better performance at $894\ nm$, with a propagation loss of $0.12 \pm 0.01\ dB/m$. Such a low value may be attributed to the fact that K92 possesses a hypocycloid core wall and hollow core diameter 41% larger than the K65. The loss measured in K92 was related to a $\sim 30\ m$ section, cut back from a $35\ m$ long sample. Dr Bradley supported my work in performing the K92 cut-back measurement.

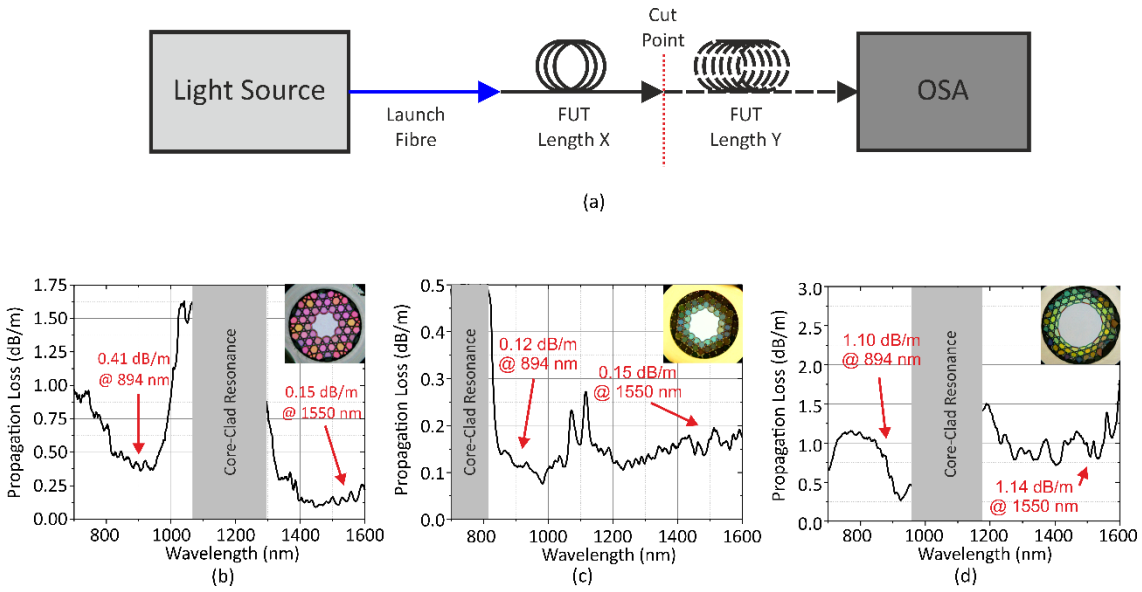

Figure 2.6: (a) Diagram of a typical cut-back measurement. The fibre under test (FUT) has two well defined segments with length X and Y. The loss at segment Y is inferred by comparing the spectra of lengths $(X + Y)$ and Y. The propagation loss of the fibre can then be estimated as the loss at the segment divided by its length. A suitable choice of launch fibre and Optical spectral analyser (OSA) can be required for optimised light injection and spectral range. The propagation loss of K65 (b), K92 (c) and K125 (d). K125 has relatively poor optical performance as a result of absence of hypocycloid core wall. K92, on the other hand, has optimised performance at both wavelengths of $894\ nm$ and $1550\ nm$. Optical microscope images of each fibre are shown as insets for each graph.

The K-ARFs were also characterised regarding their bend losses. In order to do so, $3.5\ m$ of each fibre was taken and placed into a bending rig comprising various loops with diameters ranging from $8\ cm$ to $40\ cm$, around which the fibre can be bent. The experimental diagram is depicted in Figure 2.7(a). A white light source and the Yokogawa AQ-6315B OSA were used in this experiment and the launch fibre was a custom-made LMA – a solid core SMF at a wavelength of $1.55\ \mu m$ and with mode field diameter of $\sim 18\ \mu m$, at the same wavelength.

Bend loss in ARFs manifests itself in two ways: overall attenuation caused by power leakage and coupling to resonant modes supported by the microstructure. This is a direct result of the mode displacement towards the microstructure expected for curved waveguides of any kind [30], [48].

The bend loss as function of bend radius, for a selection of wavelengths and for K65, K92 and K125 are shown in Figure 2.7(b), (c) and (d), respectively. K92 outperformed fibres K65 and K125 at wavelengths of $1.30\ \mu m$ and $1.55\ \mu m$, with bend losses below $0.12\ dB/cm$ up to bends with radii as small as $6\ cm$. Fibres K125 and K65 performed similarly at wavelengths of $1.30\ \mu m$ and $1.55\ \mu m$, with bend losses below $0.25\ dB/cm$ for bends with radius larger than $8\ cm$.

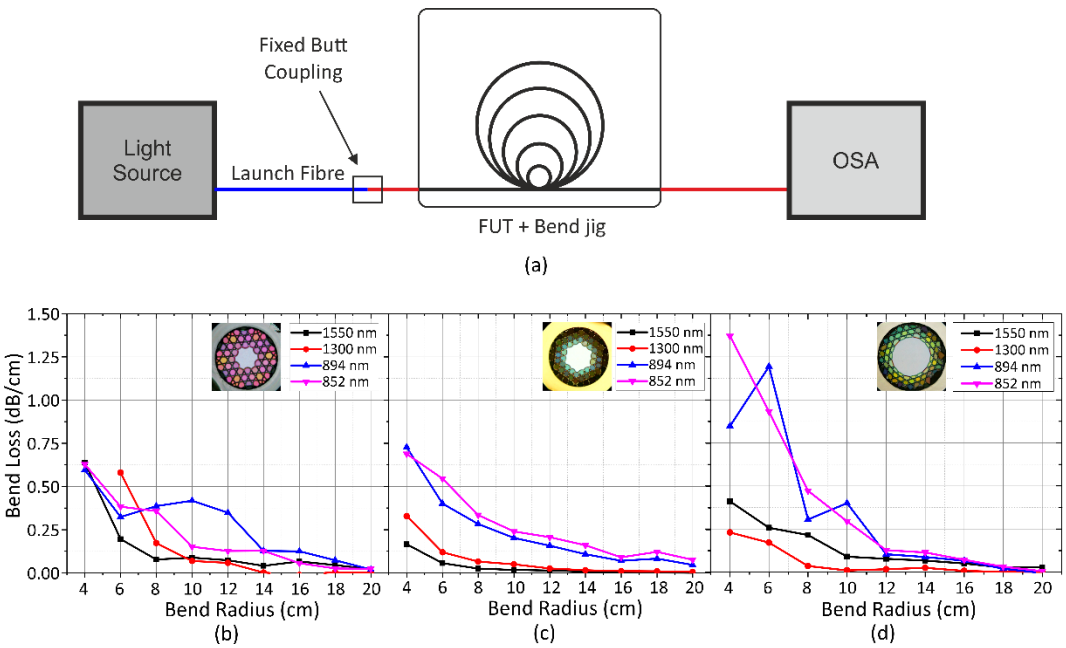

Figure 2.7:(a) Bend loss measurement diagram. A bend jig, with discreet bend radii, was used with a white light source and OSA to measure the fibre under test (FUT) optical response when bent. Bend loss for fibres (a) K65, (b) K92 and, (c) K125. All fibres showed bend loss as low as $0.55\ dB/cm$, for bend radii larger than $8\ cm$. Anomalous loss regime for fibres K65 and K125 can indicate coupling to high loss cladding modes at given bend radius.

At D-lines (wavelength of $852\ nm$ and $894\ nm$), fibres K125 and K92 performed similarly, with losses below $0.50\ dB/cm$ for bends with a radius larger than $8\ cm$. K65 showed anomalous behaviour at a wavelength of $894\ nm$. The bend loss increased and reached a local maximum of $0.40\ dB/cm$, at a bend radius of $10\ cm$. It, then, decreased systematically to $0.32\ dB/cm$ at a bend radius of $6\ cm$ and, then, it rapidly increased to $0.6\ dB/cm$, for a bend radius of $4\ cm$. This indicates that, during the course of the measurement, the light traveling through the K-ARF experienced coupling between strong and high loss cladding modes at given bend radii. Fibre K125 also presented oscillatory behaviour of the bend loss at a wavelength of $894\ nm$, which can also indicate the same loss mechanism taking place. I received the support of Dr Bradley, who measured the bend loss of K-ARF K65.

2.3 Conclusion

In this chapter, I have presented the concept of the ARF, discussing its origins, including the evolutional aspects towards an ideal microstructure as well as the numerous attempts to explain the underlying guidance mechanism and inherent optical loss mechanisms. The discussion covered the initial observation of the AR guidance mechanism, found in Kagome-lattice [1], to the latest iteration of the ARF geometry [18], [27].In summary, the AR guidance mechanism is related to the existence of modes supported by the core walls and the associated coupling to hollow core guided

modes. It is also understood that the propagation loss in ARFs is dominated by confinement loss and surface scattering loss. Over the past five years, the propagation loss has decreased by about two orders of magnitude ($\sim 10\ dB/km$, in the present days) as the result of the identification and realisation of number of geometries capable of increasing the confinement strength, especially related to the introduction of hypocycloid core walls [21].

For alkali vapour filled HC-PCFs applications, ARFs have fundamental advantages over their HC-PCFs counterparts. The simplified guidance mechanism allows ARF to support hollow cores with diameters larger than $100\ \mu m$ with propagation losses as low as $0.5\ dB/m$. This capability is ideal for atom-light interactions that are prone to short coherence times (transit-time broadening – covered in chapter 4), of which is mainly governed by the average time of flight of atoms. For this reason, ARFs (and, historically, K-ARFs) have been at the centre of the study of alkali-vapour atom-photon effects in fibres [13], [14], [35], [43].

The main goal of this project is to define new routes using HC-PCFs for the miniaturisation of Cs-vapour fibre cells for frequency and time applications. The microstructured optical fibre group at the ORC designed and fabricated three K-ARFs with different hollow core diameters ($65\ \mu m$, $92\ \mu m$ and $125\ \mu m$). Those fibres were geometrically and, therefore, optically optimised to guide at the Cs D lines ($852\ nm$ and $894\ nm$). The fibres were characterised in terms of their propagation loss and bend loss. The losses at the Cs D lines for the three K-ARFs were no greater than $\sim 1.10\ dB/m$, with minimum of $\sim 0.10\ dB/m$. Bend losses at the same wavelengths were no greater than $\sim 0.5\ dB/cm$ for bend radii larger than $8\ cm$. Although the propagation loss figures are somewhat larger, compared to the state-of-the-art ARFs ($\sim 10\ dB/km$), they will not impact the fibre cells performance as the study focusses on just short sections of K-ARFs ($\sim 10\ cm$).

A potential shortcoming of using large hollow core ARF concerns its interconnection to standardised fibre technology (solid core fibres). Therefore, the next chapter is devoted to the development of mode field adapters for interconnecting solid-core fibres to HC-PCFs and their potential application to fibre reference cells. Discussions on in-fibre Cs spectroscopy can be found in chapter 5 and 6.

2.4 Chapter References

[1] F. Benabid, J. C. Knight, G. Antonopoulos, and P. S. J. Russell, “Stimulated Raman scattering in hydrogen-filled hollow-core photonic crystal fiber.,” Science, vol. 298, no. 5592, pp. 399–402, 2002.

[2] P. S. J. Russell, P. Hölzer, W. Chang, a. Abdolvand, and J. C. Travers, “Hollow-core photonic crystal fibres for gas-based nonlinear optics,” *Nat. Photonics*, vol. 8, no. 4, pp. 278–286, 2014.

[3] M. F. Saleh *et al.*, "Theory of Photoionization-Induced Blueshift of Ultrashort Solitons in Gas-Filled Hollow-Core Photonic Crystal Fibers," *Phys. Rev. Lett.*, vol. 107, no. 20, p. 203902, Nov. 2011.

[4] J. C. Travers, W. Chang, J. Nold, N. Y. Joly, and P. St. J. Russell, "Ultrafast nonlinear optics in gas-filled hollow-core photonic crystal fibers [Invited]," *J. Opt. Soc. Am. B*, vol. 28, no. 12, p. A11, Dec. 2011.

[5] F. Couny, F. Benabid, P. J. Roberts, P. S. Light, and M. G. Raymer, "Generation and photonic guidance of multi-octave optical-frequency combs," *Science*, vol. 318, no. 5853, pp. 1118–1121, Nov. 2007.

[6] P. Londero, V. Venkataraman, A. R. Bhagwat, A. D. Slepkov, and A. L. Gaeta, "Ultralow-Power Four-Wave Mixing with Rb in a Hollow-Core Photonic Band-Gap Fiber," *Phys. Rev. Lett.*, vol. 103, no. 4, p. 043602, Jul. 2009.

[7] C. Perrella, P. S. Light, T. J. Milburn, D. Kielpinski, T. M. Stace, and A. N. Luiten, "Anomalous two-photon spectral features in warm rubidium vapor," *Phys. Rev. A*, vol. 94, no. 3, p. 033403, Sep. 2016.

[8] C. Perrella, P. S. Light, S. A. Vahid, F. Benabid, and A. N. Luiten, "Engineering Photon-Photon Interactions within Rubidium-Filled Waveguides," *Phys. Rev. Appl.*, vol. 9, no. 4, p. 044001, Apr. 2018.

[9] G. Epple et al., "Rydberg atoms in hollow-core photonic crystal fibres.," Nat. Commun., vol. 5, no. May, p. 4132, 2014.

[10] F. Benabid, P. Light, F. Couny, and P. Russell, "Electromagnetically-induced transparency grid in acetylene-filled hollow-core PCF.," Opt. Express, vol. 13, no. 15, pp. 5694–5703, 2005.

[11] F. Couny, P. S. Light, F. Benabid, and P. S. J. Russell, "Electromagnetically induced transparency and saturable absorption in all-fiber devices based on 12C2H2-filled hollow-core photonic crystal fiber," Opt. Commun., vol. 263, no. 1, pp. 28–31, Jul. 2006.

[12] P. S. Light, F. Benabid, F. Couny, M. Maric, and A. N. Luiten, "Electromagnetically induced transparency in Rb-filled coated hollow-core photonic crystal fiber," *Opt. Lett.*, vol. 32, no. 10, p. 1323, May 2007.

[13] M. A. Gouveia et al., "Coherent Population Trapping in Cs-filled Kagome Hollow Core Fibers," in Conference on Lasers and Electro-Optics, 2018, p. JTh2A.42.

[14] M. R. Sprague et al., “Broadband single-photon-level memory in a hollow-core photonic crystal fibre,” Nat. Photonics, vol. 8, no. 4, pp. 287–291, 2014.

[15] S. Février, B. Beaudou, and P. Viale, “Understanding origin of loss in large pitch hollow-core photonic crystal fibers and their design simplification,” *Opt. Express*, vol. 18, no. 5, p. 5142, Mar. 2010.

[16] N. V. Wheeler *et al.*, “Low-loss Kagome hollow-core fibers operating from the near- to the mid-IR,” *Opt. Lett.*, vol. 42, no. 13, p. 2571, Jul. 2017.

[17] B. Debord *et al.*, “7.7 dB/km losses in inhibited coupling hollow-core photonic crystal fibers,” in *Conference on Lasers and Electro-Optics*, 2016, p. JTh4C.8.

[18] F. Poletti, “Nested antiresonant nodeless hollow core fiber,” Opt. Express, vol. 22, no. 20, pp. 23807–23828, 2014.

[19] W. Belardi and J. C. Knight, “Hollow antiresonant fibers with reduced attenuation,” *Opt. Lett.*, vol. 39, no. 7, p. 1853, Apr. 2014.

[20] J. R. Hayes et al., “Antiresonant Hollow Core Fiber with Octave Spanning Bandwidth for Short Haul Data Communications,” in Optical Fiber Communication Conference Postdeadline Papers, 2016, p. Th5A.3.

[21] Y. Y. Wang, N. V. Wheeler, F. Couny, P. J. Roberts, and F. Benabid, “Low loss broadband transmission in hypocycloid-core Kagome hollow-core photonic crystal fiber,” *Opt. Lett.*, vol. 36, no. 5, p. 669, Mar. 2011.

[22] A. D. Pryamikov, A. S. Biriukov, A. F. Kosolapov, V. G. Plotnichenko, S. L. Semjonov, and E. M. Dianov, “Demonstration of a waveguide regime for a silica hollow - core microstructured optical fiber with a negative curvature of the core boundary in the spectral region > 3.5 μm,” Opt. Express, vol. 19, no. 2, pp. 1441–1448, 2011.

[23] W. Belardi and J. C. Knight, “Effect of core boundary curvature on the confinement losses of hollow antiresonant fibers,” *Opt. Express*, vol. 21, no. 19, p. 21912, Sep. 2013.

[24] A. N. Kolyadin, A. F. Kosolapov, A. D. Pryamikov, A. S. Biriukov, V. G. Plotnichenko, and E. M. Dianov, “Light transmission in negative curvature hollow core fiber in extremely high material loss region,” Opt. Express, vol. 21, no. 8, pp. 9514–9519, 2013.

[25] J. R. Hayes, F. Poletti, M. S. Abokhamis, N. V. Wheeler, N. K. Baddela, and D. J. Richardson, “Anti-resonant hexagram hollow core fibers,” *Opt. Express*, vol. 23, no. 2, p. 1289, Jan. 2015.

[26] W. Belardi and J. C. Knight, “Hollow antiresonant fibers with low bending loss,” Opt. Express, vol. 22, no. 8, pp. 10091–10096, 2014.

[27] B. S. Mubassira et al., “Lotus-Shaped Negative Curvature Hollow Core Fiber With 10.5 dB/km at 1550 nm Wavelength,” J. Light. Technol. Vol. 36, Issue 5, pp. 1213-1219, vol. 36, no. 5, pp. 1213–1219, Mar. 2018.

[28] A. Argyros, S. G. Leon-Saval, J. Pla, and A. Docherty, “Antiresonant reflection and inhibited coupling in hollow-core square lattice optical fibres.,” Opt. Express, vol. 16, no. 8, pp. 5642–5648, 2008.

[29] B. Debord et al., “Hypocycloid-shaped hollow-core photonic crystal fiber Part I: arc curvature effect on confinement loss.,” Opt. Express, vol. 21, no. 23, pp. 28597–608, 2013.

[30] M. Alharbi et al., “Hypocycloid-shaped hollow-core photonic crystal fiber Part II: cladding effect on confinement and bend loss.,” Opt. Express, vol. 21, no. 23, pp. 28609–16, 2013.

[31] T. D. Bradley *et al.*, “Modal content in hypocycloid Kagomé hollow core photonic crystal fibers,” *Opt. Express*, vol. 24, no. 14, p. 15798, Jul. 2016.

[32] N. M. Litchinitser, A. K. Abeeluck, C. Headley, and B. J. Eggleton, “Antiresonant reflecting photonic crystal optical waveguides.,” Opt. Lett., vol. 27, no. 18, pp. 1592–1594, 2002.

[33] A. Van Newkirk *et al.*, “Modal analysis of antiresonant hollow core fibers using S^2 imaging,” *Opt. Lett.*, vol. 41, no. 14, p. 3277, Jul. 2016.

[34] B. M. Trabold, D. Novoa, A. Abdolvand, and P. S. J. Russell, “Selective excitation of higher order modes in hollow-core PCF via prism-coupling,” *Opt. Lett.*, vol. 39, no. 13, p. 3736, Jul. 2014.

[35] S. Okaba *et al.*, “Lamb-Dicke spectroscopy of atoms in a hollow-core photonic crystal fibre,” *Nat. Commun* 5, 4096, Jun. 2014.

[36] A. D. Slepkov, A. R. Bhagwat, V. Venkataraman, P. Londero, and A. L. Gaeta, “Spectroscopy of Rb atoms in hollow-core fibers,” *Phys. Rev. A*, vol. 81, no. 5, p. 053825, May 2010.

[37] A. D. Slepkov, A. R. Bhagwat, V. Venkataraman, P. Londero, and A. L. Gaeta, “Generation of large alkali vapor densities inside bare hollow-core photonic band-gap fibers.,” Opt. Express, vol. 16, no. 23, pp. 18976–18983, 2008.

[38] F. Poletti, M. N. Petrovich, D. J. Richardson, and M. J. Li, “Hollow-core photonic bandgap fibers: Technology and applications,” *Nanophotonics*, vol. 2, no. 5–6. Walter de Gruyter GmbH, pp. 315–340, 01-Dec-2013.

[39] T. A. Birks, D. M. Bird, T. D. Hedley, J. M. Pottage, and P. S. J. Russell, “Scaling laws and vector effects in bandgap-guiding fibres,” *Opt. Express*, vol. 12, no. 1, p. 69, Jan. 2004.

[40] T. D. Bradley *et al.*, “Ground-state atomic polarization relaxation-time measurement of Rb filled hypocycloidal core-shaped Kagome HC-PCF,” *J. Phys. B At. Mol. Opt. Phys.*, vol. 49, no. 18, p. 185401, Sep. 2016.

[41] X. Zheng et al., “Ground-state population relaxation dynamics of polarized Rb atoms in Kagome HC-PCF,” in Conference on Lasers and Electro-Optics, 2016, p. SM2H.8.

[42] X. M. Zheng et al., “In-situ dwell-time measurement of Rb at the inner-wall coated-surface of HC-PCF,” in Conference on Lasers and Electro-Optics, 2018, p. SM3L.4.

[43] X. M. Zheng et al., “Narrow electromagnetically induced transparencies in Rb confined large-core core inner-wall coated Kagome HC-PCFs,” in Conference on Lasers and Electro-Optics, 2018, p. SM3L.3.

[44] M. R. Sprague *et al.*, “Efficient optical pumping and high optical depth in a hollow-core photonic-crystal fibre for a broadband quantum memory,” *New J. Phys.*, vol. 15, no. 5, p. 055013, May 2013.

[45] J. Vanier and C. Audoin, The Quantum Physics of Atomic Frequency Standards, v.1. IOP Publishing, 1989.

[46] W. Happer, “Optical Pumping,” *Rev. Mod. Phys.*, vol. 44, no. 2, pp. 169–249, Apr. 1972.

[47] B. Debord et al., “Ultra-Large Core Size Hypocycloid-Shape Inhibited Coupling Kagome Fibers for High-Energy Laser Beam Handling,” Lightwave Technology, Journal of, vol. 33, no. 17. pp. 3630–3634, 2015.

[48] A. W. Snyder and J. D. Love, Optical Waveguide Theory. Chapman & Hall, 1995.

Chapter 3 Towards Interconnections between Dissimilar Optical Fibres for Stand-Alone HC-PCFs Photonic Cells

Foreword

In the previous chapter, I have discussed in depth HC-PCF technology applied to photonic cells. The two main advantages of a fully fibrerised reference cell over their commercial counterparts (bulk cells) are the reduced footprint and ease of integration with standard fibrerised devices. Therefore, this new piece of technology has the potential to reduce the overall size of optical systems while minimising the use of complex free-space optical assemblies.

Although HC-PCFs technology is still under development, it already offers advantages over standard solid fibre primary solutions – such as for power delivery applications [1], gas references and non-linear effects in gases [2]–[4]. However, compatibility between HC-PCF technology and standardised optical systems (solid core fibres) still poses a key challenge towards the broad acceptance and optical performance of fibrerised photonic cells. The mode field mismatched between SMF and HC-PCFs supported modes, resulted from the large hollow core sizes found in HC-PCFs, is the main cause of optical losses when splicing solid-to-hollow core fibres. Moreover, the mechanical strength of the splice is key to maintain the photonic cell in operation (leak-free).

Mode field adapters could provide a solution for interconnecting HC-PCFs to standard optical fibres. In summary, these optical devices are special fibre sections that have the role of reshaping the incoming beam in order to maximise the optical transition between fibres with different mode field properties (different mode shape and effective diameter). Several groups have investigated the use of MMF fibre sections and their intrinsic spatial multimodal beating to overcome high optical losses between solid SMFs with dissimilar core sizes [5] and with PCFs [6]–[8]. Other groups took a different route to achieve beam reshaping and studied the effects of adiabatically tapering down the HC-PCFs ends to achieve better mode field matching between HC-PCFs guided modes and the SMF FM [9], [10].

In this chapter, I present a comprehensive study on the interconnection of dissimilar fibres using mode field adaptors (MFAs) based on graded index fibres (GIFs) section. I take advantage of the parabolic shaped GIF core to obtain coherent modal beating and thus achieve beam expansion or compression. I present theoretical models for GIF based MFAs, presenting the necessary and sufficient condition to obtain beam expansion and compression and discussing the efficiency of the device in some important scenarios. I also present a proof-of-concept experiment using solid core fibres and HC-PCFs and examine the performance limitations of the current state of the art. At the

end of this chapter, I summarise the prospects and future work required to obtain stand-alone fibre reference cells.

3.1 Spatial Multimodal Effects for Beam Expansion and Compression

Spatial and spectral (S^2) mode beating are effects inherently present in multi-mode media, intrinsically connected to mode content excitation and its evolution. MFAs based on spatial multimode interference (SMMI) take advantage of a well-known mode-beating pattern to obtain either beam expansion or compression. This pattern is defined by the geometrical parameters of the multi-mode medium, as well as the initial condition of the optical signal (mode shape and spatial phase distribution) injected into the MMF section. In the next section, I discuss the physical principle of SMMI, indicate its main features and present methods to engineer the modal content for MFA applications.

3.1.1 Spatial and Spectral Mode Interference Principle

Let us assume a simple interconnection between two optical fibres, F_1 and F_2, where F_1 is single-mode and F_2 is multi-mode – supporting N_2 modes around λ. Figure 3.1 depicts the proposed interconnection. Under the scalar fields approach, the only mode supported by F_1 has a normalised transversal field distribution of the form $\varphi^{(1)}(\boldsymbol{x})$, with $\boldsymbol{x} \equiv (x, y)$. For F_2, each supported mode has a normalised transversal distribution $\varphi^{(2)}_{l,m}(\boldsymbol{x})$. Here, I also sub-label the modes according to their azimuthal order number, l, and radial order number, m; similar to the linear polarisation notation ($LP_{l.m}$). I also force the modes of F_2 to be orthogonal by pairs. In other words, $\int d^2\boldsymbol{x}\, \varphi^{(2)}_{l,m}(\boldsymbol{x})\varphi^{*(2)}_{l',m'}(\boldsymbol{x}) \equiv e_0^{l,m} e_0^{*l',m'} \delta_{l,l'}\delta_{m,m'}$, where $\delta_{n,n'}$ is the Kronecker delta symbol and $e_0^{l,m}$ is the electric field strength, in V/m, associated to the mode with indices (l, m).

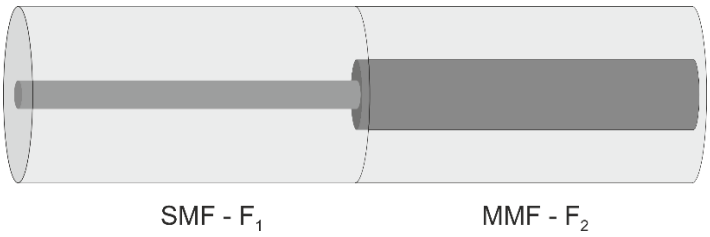

Figure 3.1: Interconnection between two dissimilar fibres, F_1 and F_2, where the first is assumed to be single-mode and the second multi-mode.

The mode evolution, $\psi(\boldsymbol{x}, z, t)$, at any longitudinal position $\Delta z = z - z_0$, along F_2 can be described as follows

$$\psi(\boldsymbol{x}, z, t) = \sum_{l,m}^{N_2} a_{l,m}\, \varphi_{l,m}^{(2)}(\boldsymbol{x}) e^{i(\beta_{l,m}\Delta z - \omega t)}, \qquad \text{Eq. 3.1}$$

where,

$$a_{l,m} \equiv \iint_{\Omega} d^2x\, \varphi^{*(2)}_{l,m}(\boldsymbol{x}) \varphi^{(1)}(\boldsymbol{x}'), \qquad \text{Eq. 3.2}$$

is the coupling coefficient between the fundamental mode and mode with index l, m at the interface $z = z_0$ with $\boldsymbol{x}' \equiv (x - x_0, y - y_0)$ and integrated over the infinite surface Ω defined at the plane $z - z_0 = 0$; note also that $a_{l,m} \in \mathbb{C}$. Here I define (x_0, y_0) as the coordinates of the centre of cross-section of fibre F_2. If, for instance, I assume $\boldsymbol{x}' \to \boldsymbol{x}$, the coupling coefficients with $l \neq 0$ are trivial, as $\int d\theta \cos l\theta = 2\pi\, \delta_{0,l}$, and only modes with $l = 0$ symmetry can be excited. This assumption is valid if, and only if, the F_1 and F_2 cores are axially aligned. The mode evolution, thus, can reduce to only modes in the sub-space $l = 0$, with M being the number of total elements in this sub-space. The general shapes of a few $LP_{0,m}$ modes are depicted in Figure 3.2.

The intensity at any given point z is $\langle P \rangle = \frac{c}{2} \int d^2x \varepsilon\, \psi(\boldsymbol{x}, z, t) \psi^*(\boldsymbol{x}, z, t) \sim \sum_m^M \frac{c\varepsilon}{2} |a_{0,m}|^2$, where ε is the permittivity of the medium and c is the speed of light. Note that, ideally, no fast oscillations in the intensity spectrum are expected, as no information on phase (propagation constant) is retrieved; only perhaps a slow varying component can be present as a result of the spectral dependency of the fibre's mode shape that impacts the coupling coefficient value. The power spectrum can also be affected by the dispersion and absorption properties of the medium.

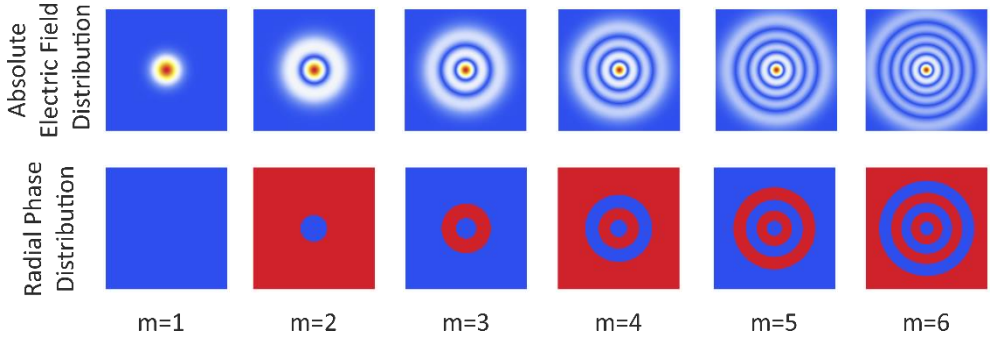

Figure 3.2: Absolute electric field and phase distributions of the first few $LP_{0,m}$ modes. The radial order number is indicated below each mode.

Spatial beating is present according to Eq. 3.1. As the time dependency manifests itself as a global phase, I have excluded that from the following analysis. Assuming that the fundamental mode of F_2 carries most of the power, Eq. 3.2 can be rewritten as follows,

$$\psi(\boldsymbol{x}, z) \sim a_{0,1}\left(\varphi_{0,1}^{(2)}(\boldsymbol{x}) + \sum_{m=2}^{M} \frac{a_{0,m}}{a_{0,1}} \varphi_{0,m}^{(2)}(\boldsymbol{x}) e^{i\Delta\beta_m \Delta z}\right), \qquad \text{Eq. 3.3}$$

where $\Delta\beta_m \equiv \beta_{0,m} - \beta_{0,1}$.

Eq. 3.3 is the key result sought in this section and shows four important relations under this approximation:

i. Modal beatings manifested by pairs of modes
ii. The phase information in the MMF fibre section dictates the spatial mode evolution.
iii. Each mode's mode field diameter (MFD) and coupling coefficient contributes to define the global maximum expansion and global minimum compression.
iv. Increasing the number of supported modes can help decrease the overall interconnection loss.

In summary, a suitable choice of MMF section is fundamental to achieve optimised mode expansion and compression. The multi-mode medium should support a minimum number of modes that contribute to the effect and it is key that the propagation constant difference, $\Delta\beta_m$, should be such that all excited modes interfere at a well-defined length L_{MFA}. This yields an optimised compressed and expanded image of the input mode, depending on the initial coupling condition.

Graded-index solid multi-mode fibres are the most suitable commercially available solution for MMI-based MFA interconnections. They can support a number of LP_{0m}-like modes; moreover, their key feature is that, in parabolic-shaped GIFs, the propagation constant difference between neighbour modes ($\beta_{l,m+1} - \beta_{l,m}$) is constant [11], [12]. This condition is ideal for achieving the maximum multi-modal interference, hence, the maximum beam expansion and compression [5], [6]. In the next section, I introduce the GIF geometry and its main features.

3.1.2 Graded-Index Fibres Applied as Mode Field Adapters

Graded-index fibre is a class of solid core optical fibres that possesses a radial refractive index profile following a smoothly varying and well-defined distribution. This feature is key to engineering mode properties such as the number of supported modes, the mode shapes and dispersion properties (propagation constant and group velocity) [12]. Generally, a GIF core refractive index profile can be modelled following a power law function as follows – in cylindrical coordinates $\boldsymbol{x} = (\rho, \theta, z)$,

$$n^2(\rho) = n_0^2\left[1 - 2\Delta\left(\frac{\rho}{a}\right)^{\gamma}\right], \qquad \text{Eq. 3.4}$$

where n_0 is the refractive index at the centre of the core, a is the core radius and $\Delta \equiv (n_0^2 - n_{cl}^2)/n_0^2$, with the cladding refractive index defined as n_{cl}. The power law γ defines the resultant profile, as shown in Figure 3.3(a). Note that when $\gamma = 2$, the profile manifests itself as a parabolic shape and in the limit $\gamma \to \infty$, it manifests itself as a step-index core.

The propagation constant of GIFs with a power-law close to $\gamma \sim 2$ has a closed form in the Wentzel-Kramers-Brillouin (WKB) approximation [11]–[13]

$$\beta_{l,m}(\gamma) = k_0 n_0 \sqrt{1 - \frac{NA^2}{n_0^2}\left(\frac{2m + l - 1}{\sqrt{\frac{\gamma}{4 + 2\gamma}}\, NAk_0 a}\right)^{\frac{2\gamma}{2+\gamma}}}, \qquad \text{Eq. 3.5}$$

where $NA \equiv \sqrt{n_0^2 - n_{cl}^2}$ is the fibre's numerical aperture and $k_0 \equiv 2\pi/\lambda$ is the wave vector in vacuum. This expression can be expanded and further simplified by assuming that the second term inside the square root is much smaller than the unity. Under this assumption, the propagation constant expression takes the form

$$\beta_{l,m}(\gamma) \approx k_0 n_0 - \frac{k_0 NA^2}{2n_0}\left(\frac{2m + l - 1}{\sqrt{\frac{\gamma}{4 + 2\gamma}}\, NAk_0 a}\right)^{\frac{2\gamma}{2+\gamma}}. \qquad \text{Eq. 3.6}$$

Note also that, for $\gamma \to 2$ and $l = 0$, this expression yields,

$$\beta_{l,m} \to \beta_0 - m\Delta\beta, \qquad \text{Eq. 3.7}$$

with $\beta_0 \equiv k_0 n_0 + NA/(n_0 a)$ and $\Delta\beta \equiv 2NA/n_0 a$. Eq. 3.7 tells us that GIF can indeed be applied as an MFA as its various modes beat harmonically if the power law coefficient γ is chosen to be around 2. Note also that $\Delta\beta_m = \beta_{0,m} - \beta_{0,1} = (1 - m)\Delta\beta$, for $m > 1$, and Eq. 3.3 can indeed be seen as an expansion of harmonic orthogonal functions (or modes). **This is a key result that makes GIFs ideal candidates for MFA applications.**

To validate Eq. 3.5, Eq. 3.6 and Eq. 3.7, I have simulated the commercially available GIF50 (Thorlabs) using the finite element method (FEM) software COMSOL with regards of its modal propagation constants and compared these with the analytical solutions of Eq. 3.5, calculated using Wolfram

Mathematica, for the five $LP_{0,m}$ modes supported by this fibre. The parameters used were $NA = 0.2, \gamma = 2.17, n_{cl} = 1.444, a = 25\ \mu m$ and for $\lambda = 1.55\ \mu m$. Those parameters are available from the Thorlabs website and are also referenced in [5]. The FEM eigenvalue convergence was set to 10^{-6}.Figure 3.3(c) shows the propagation constant as a function of radial mode order m for the first five $LP_{0,m}$ modes. The linear behaviour of the GIF propagation constant decrease with the mode order as Eq. 3.7 indicates. The propagation constant calculated by the FEM agreed with the analytical solution from Eq. 3.5 at the 10^{-5} level. I also included the data of a step-index MMF (SIMMF) with the same parameters as the GIF50 for comparison. Figure 3.3(b) depicts the geometry of GIF50 and SIMMF used in the simulations. For SIMMF, it is easy to see that the propagation constant difference is not constant between adjacent pairs, as it is for GIFs. This behaviour has serious implications on the global maximum expansion and compression achieved on SIMMF and this will be discussed in the following sections of this chapter.

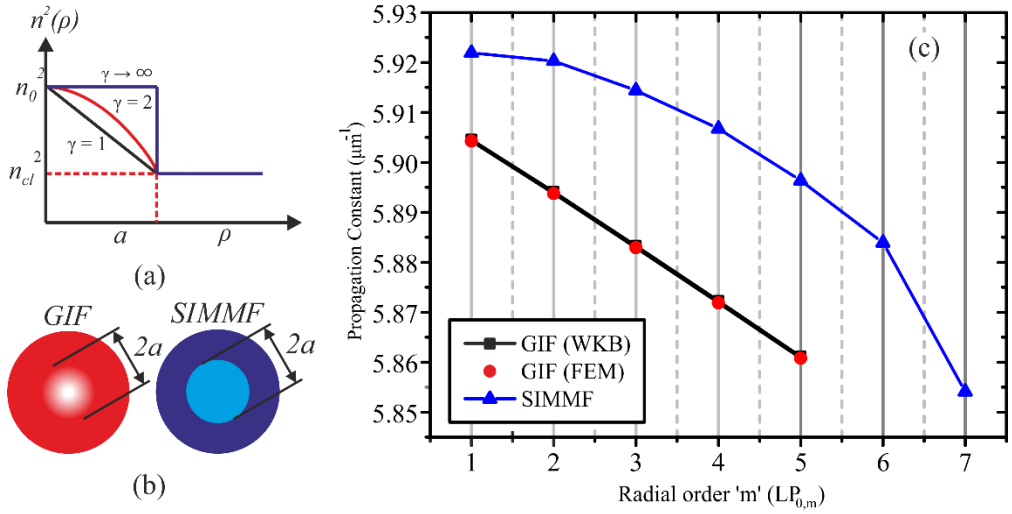

Figure 3.3: (a) Associated refractive index profiles for three cases of power-law γ: 1,2 and ∞. Note that when $\gamma \to \infty$, the profile tends to the step-index shape. (b) GIF and SIMMF's geometry. (c) Propagation constants of five first LP modes of GIF and seven first modes of SIMMF for $l = 0$ mode order. The fibre's parameters were NA = 0.2 and $\gamma = 2.17$ for GIF and NA=0.2 for SIMMF. Both fibres have a 50μm core diameter. A comparison between the analytical expression obtained by the WKB method and a finite element method (FEM) yields a convergence at the 10^{-5} level, which is being mainly limited by accuracy of the numerical model. SIMMFs' propagation constants were extracted from [5].

Although Eq. 3.7 states that $\beta_{0,m}$ varies linearly as a function of the radial mode order m when $\gamma \to 2$ and simulations have also indicated it, if γ deviates from 2 by an amount $\delta\gamma$, I should expect an associated error, $\delta\beta$. This associated error has the form, to a first order approximation, as follows

$$\delta\beta(m) \approx (2m-1)\left(\frac{NA}{4n_0 a}\right)\ln\left(2\frac{2m-1}{NAk_0 a}\right)\delta\gamma. \qquad \text{Eq. 3.8}$$

Eq. 3.8 was obtained from a first order Taylor expansion of Eq. 3.6, for $\gamma \to 2$. It indicates that the propagation constant difference increases non-linearly as a function of the radial mode order m. It has important implications in GIF based MFAs as $\gamma \neq 2$ implies in a dephasing mechanism. Moreover, as the total phase information depends on the length L_{MFA} of the GIF in use, it is expected that the total dephase increases with the length and, therefore, restricting the use of GIF to short sections.

To picture the dephasing effect and beam expansion, I have simulated using Wolfram Mathematica the field propagation of a system composed of a single-mode fibre (standard SMF-28) spliced to GIF50. I have only considered the five $LP_{0,m}$ supported modes in the GIF50, assuming that both fibres are axially aligned, and therefore, only LP_{0m}-like modes take part in the effect. The SMF parameters were: $NA = 0.115$, $n_{cl} = 1.444$, core radius of $4.1\ \mu m$ and MFD of $10\ \mu m$ at $\lambda = 1.55\ \mu m$, following the SMF's specifications available online. Thorlabs' GIF50 specifications used for this simulation were the same mentioned previously in this section. The simulation was performed under a scalar field approach and Laguerre-Gauss functions were used as they best describe the modes in GIFs with a parabolic shape ($\gamma = 2$) [12].

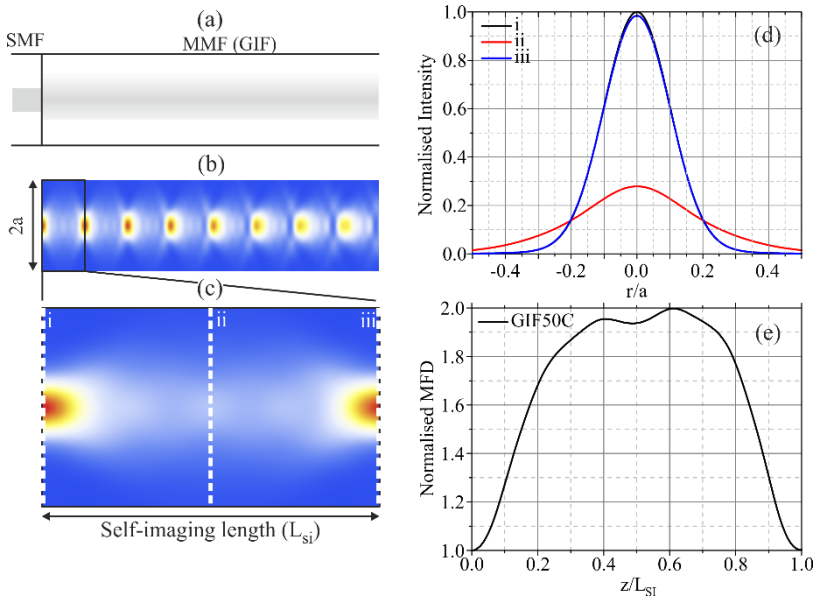

Figure 3.4: (a) Geometry: SMF splice to a typical GIF. (b) Mode evolution along the propagation axis. Dephasing effects decrease the coherence between beating modes, resulting in poor self-image (SI) formation. This effect is period along the propagation axis. (c) First interactional section. the mode's expansion and compression throughout the length can be observed. (d) Normalised intensity at three different positions i) input, ii) phase-shifted image, iii) self-image. The positions are depicted in (c). (e) MFD evolution of the mode superposition at the GIF50. Note that the mode finds its maximum around 0.6 L_{SI}, where L_{SI} defines the self-imaging length.

Figure 3.4 (a) depicts the proposed simulated interconnection. Figure 3.4 (b) shows the field evolution throughout the multi-mode medium (GIF section). The main characteristic observed here is the lensing phenomenon that happens in a graded-index medium. This is a result of the various modes interfering coherently at given points. They interfere with each other and reconstruct the initial mode (SMF mode shape) at a given period, as depicted in Figure 3.4 (d). The spatial period for re-imaging is called the self-imaging length L_{SI}, and it is indicated in Figure 3.4 (c). Note also that there is a phase-shifted image, located at $L_{SI}/2$ that produces an expanded beam. That length is the L_{MFA}. The MFD, calculated as the beam width at $1/e^2$ from the central value, is shown in Figure 3.4 (e). Note that in this configuration, the GIF works as a beam expander. I will discuss the fundamental mechanism that allows me to define whether the GIF will can be used as beam expander and compressor in the following sections. Dephasing phenomena, as indicated by Eq. 3.8 and discussed in this section is also present. As I have used $\gamma = 2.17$ for this simulation, one can easily notice in Figure 3.4 (b) that the reimaging quality decreases as the signal travels through the GIF section. It can be attributed to as the accumulated dephasing ($\delta\beta z$) parameter that shifts the beating points for each mode participant in the effect.

Most of the commercially available GIFs have a power-law coefficient, γ, around 2. They are sometimes intentionally tuned to a different value in order to achieve different modal properties, such as a tailored differential group velocity [11], [12]. In the next section, I explore the use of GIFs lengths as MFAs.

3.2 Mode Field Adapters

In this section, I described the MMF-based MFA theory using GIFs and demonstrate the use of MFAs in some specific cases such as a proof-of-concept using single mode, solid core, large mode area fibres and the use of MFAs in interconnections between single-mode solid fibres and HC-PCFs. I discuss the advantages and drawbacks of this technology and the methods necessary to obtain low loss interconnections between fibres with different geometries and guiding mechanisms (SMF, SIMMFs and HC-PCFs).

3.2.1 Single-Mode to Single-Mode fibre interconnections

Single-mode to single-mode (SM to SM) dissimilar solid fibres' interconnection is perhaps the simplest and most straight-forward use of mode field adapters. Hofmann et al. have studied the use of GIFs as field adapters to interconnect SMFs with dissimilar core size [5]. The results reported in this section confirm Hofmann's experiments and should be seen as a proof-of-concept and stepping stone for SMF to HC-PCFs low loss interconnections using MFAs.

In the next sections I derive the power transmission equation for dissimilar SMFs interconnection using a section of GIF. I demonstrate the use of GIF as MFA by interconnecting a SMF (MFD = $\sim 10\ \mu m$) to a LMA fibre (MFD = $\sim 18\ \mu m$), with a minimum loss below 0.1dB.

3.2.1.1 Simplified Model

Let us assume the following geometry: F_1 spliced to F_2 spliced to F_3, as depicted in Figure 3.5. Let us also assume that F_1 and F_3 are SMF, albeit with different core sizes, and F_2 being a GIF section. Eq. 3.1 and Eq. 3.2 describe the coupling of an incoming signal from a SMF into a MMF. Let us assume then a second coupling between the GIF and an SMF after the signal has travelled a distance L in the multi-mode medium.

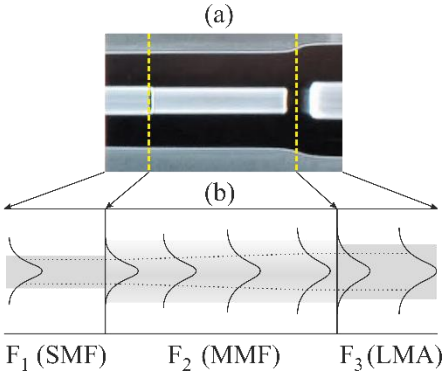

Figure 3.5: Description of a MFA device. (a) Snapshot of a GIF section spliced to two dissimilar SMF. (b) Device diagram indicating the signal direction and expected mode expansion.

The field distribution at the interface F_2 to F_3 can be written as an expansion of the modes in F_2, according to Eq. 3.2, as follows,

$$\psi^{(3)}(\boldsymbol{x}) = \sum_{m=1}^{M} a_{0,m}^{(1)}\, e^{i\beta_m L} \varphi_{0,m}^{(2)}(\boldsymbol{x}), \qquad \text{Eq. 3.9}$$

where L is the length of the fibre F_2. The superscript index over $a_{0,m}$ indicates that those coupling coefficients refer to the first interface. Considering that the fibre F_3 supports only one mode, the coupling coefficient $a_{0,m}^{(2)}$ between the guided modes between F_2 and F_3, at the second interface, are expressed as follows,

$$a_{0,m}^{(2)} = \iint_{\Omega} d^2x \varphi^{*(3)}(\boldsymbol{x}) \varphi_{0,m}^{(2)}(\boldsymbol{x}'). \qquad \text{Eq. 3.10}$$

Taking into account the coupling at the interface F_1 to F_2 (Eq. 3.1 and Eq. 3.2) and considering GIF power law $\gamma \sim 2$, after some algebra, Eq. 3.9 can be rewritten and the normalised transmission T has the following form,

$$T \equiv |\psi(\boldsymbol{x})|^2 = \left| a^{*(2)}_{0,1}\, a^{(1)}_{0,1} + \sum_{m=2}^{M} a^{*(2)}_{0,m}\, a^{(1)}_{0,m} e^{-i(m-1)\Delta\beta L} \right|^2 . \qquad \text{Eq. 3.11}$$

Here I have labelled the coupling coefficients with index (1) and (2) to indicate the first and second fibre interfaces (splice points), respectively. It is clear that Eq. 3.11 is an expansion of harmonic waves with a fundamental spatial frequency $\Delta\beta$. Hence, the fundamental *period* is $2\pi/\Delta\beta$ and should match the self-imaging length, L_{SI}, which was defined in the previous section. The mode field adapter length is found at the phase inversion point, $L_{SI}/2$. Also, as defined previously, $\Delta\beta \equiv 2NA/n_0 a$. Thus,

$$L_{MFA} = \frac{\pi}{\Delta\beta} \sim \frac{\pi n_0 a}{2NA}, \qquad \text{Eq. 3.12}$$

is the approximated mode field adapter length. In other words, L_{MFA} defines the minimum length of GIF that will optimise the coupling between dissimilar fibres. The optimised coupling will only happen if, and only if, the expanded (or compressed) optical beam at the GIF section has similar MFD to the collection fibre (F_3). In addition, note that this expression is a function only of the GIF geometry; therefore, it is invariant, in principle, to the coupling mechanism and mode excitation. The coupling mechanism can induce phase fluctuations to each and every mode excited, since the fields are described as complex functions. This phase can displace the beating of certain modes, incurring a dephasing process and, thus, decreasing the overall efficiency of the device. **Eq. 3.12 is one of the key results sought in this section and can be seen as a design rule for GIFs-based MFAs.**

The coefficients $a^{(1)}_{0,m}$ carry the information on whether the GIF will be an expander or compressor adapter. The underlying mechanism that dictates the phase difference between odd and even modes at the coupling interface. This phase is defined by the pair of incoming mode shapes and mode coupling. The overlap integral of both modes yields the sign carried by coupling coefficient. In the following, I list the general phase information needed to achieve:

- **Expansion,** If $a^{(1)}_{0,m} > 0$, $\forall\, m$;
- **Compression,** if $a^{(1)}_{0,2m-1} > 0$ and $a^{(1)}_{0,2m} < 0$, $\forall\, m$;

Those conditions are not strict rules; however they were defined based on observations of the sign of $a^{(1)}_{0,2m}$ coupling integral (Eq. 3.2) as a function of the MFD of the incoming beam. In fact, this inversion happens when the incoming beam width (MFD_{in}) is comparable to the GIF's fundamental mode MFD, defined as $MFD_{FM} \equiv 2\sqrt{a\lambda/\pi NA}$. This leads us to a second design rule

for MFAs based on GIF's geometrical parameters solely, and I state: **GIFs generally expand incoming beams if $MFD_{in} < 2\sqrt{a\lambda/\pi NA}$ and compress if $MFD_{in} > 2\sqrt{a\lambda/\pi NA}$.**

In the next section I demonstrate the use of GIFs as MFAs and validate Eq. 3.11 and Eq. 3.12.

3.2.1.2 Proof-of-Concept

To demonstrate the efficiency of MFAs based on GIFs, the *Microstructured Optical Fibres group* at the *ORC* built a precision cleaver capable of cleaving solid core fibres with $5\ \mu m$ resolution. The cleaving system is shown in Figure 3.6 (a).

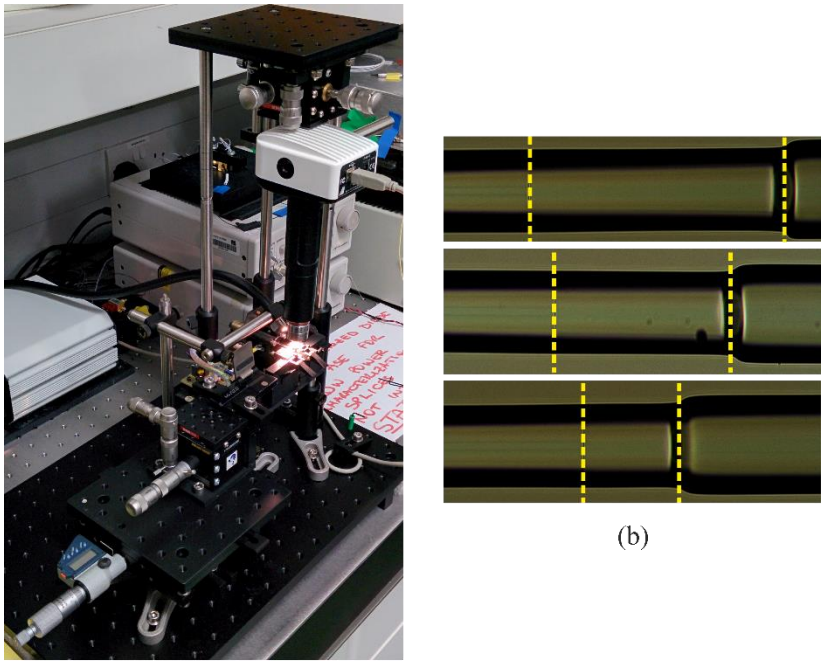

(a) (b)

Figure 3.6: (a) Picture of the precision cleaving system built at the ORC. (b) Example of segments of GIF50 spliced to SMF and LMA. The length of GIFs, from the bottom to the top, are: 170, 292 and 415µm.

The experiment described in the following was performed by me and had the goal of investigating the interconnection loss of a standard SMF-28 ($MFD_{SMF} \sim 10\ \mu m$) to a home-made LMA fibre ($MFD_{LMA} \sim 18\ \mu m$) using a suitable section of GIF. The two GIFs investigated in this experiment were the Thorlabs GIF50 and GIF625. The fibre specifications are found in Table 3.1. Figure 3.6 (b) shows three examples of the GIFs spliced to SMF and LMA. Note that the GIFs were cleaved with different lengths and that the LMA fibre has a larger outer diameter compared to standard fibres ($125\ \mu m$). The refractive indices profile of each GIF and LMA fibres were measured and are shown in Figure 3.7. The GIF profiles were fitted to estimate the power law coefficient, the values of which listed in Table 3.1.

The LMA's parameters were tuned to match the experimental measurements of the MFD ($\sim 18\ \mu m$) at $\lambda \sim 1.55\ \mu m$. I have had to define an effective core radius for this fibre as its core

profile index is complex and cannot be simply approximated to a step-index distribution, as can be seen in Figure 3.7 (c).

Table 3.1: Core radius, Numerical Aperture, power-law coefficient, number of modes, cut-off wavelength, effective core radius and simulated FM-MFD used for proof-of-concept experiment

Fibre	Core Radius (µm)	NA	γ	Number of modes (LP_{0m})	LP_{11} cut-off wavelength	Eff. Core Radius (µm)	Simulated FM MFD (µm) @ 1.55µm
SMF-28	4.1	0.115	– –	1	$\sim 1.25\ \mu m$	– –	9.9
LMA	9.4	0.069	– –	1	$\sim 1.48\ \mu m$	8.3	17.9
GIF50	25.0	0.200	1.95	5	– –	– –	15.7
GIF625	31.2	0.275	1.88	9	– –	– –	14.9

The experiment was run as follows: two lengths of SMF and LMA were spliced to various sections of GIF (GIF50 and GIF625) and the insertion loss was monitored. The fibre's interconnection geometry is indicated in Figure 3.8 (a). The light source was a diode laser at $1.55\ \mu m$ with an output power of about 1mW. Splicer recipes were tailor-made to minimise deformations to the optical fibre while yielding strong bonds and the cleave angles were kept below 2°.

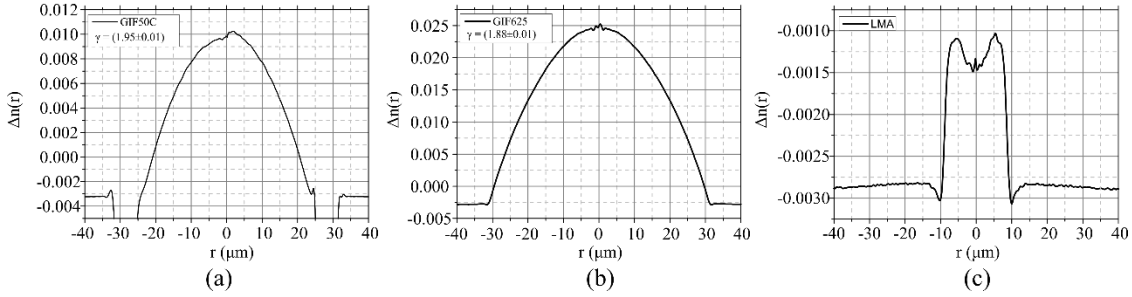

Figure 3.7: Refractive-index profile of commercial (Thorlabs) (a) GIF50, (b) GIF625 and custom-made (c) LMA. The power law coefficient γ of the GIF50 and GIF625 are: (1.95±0.01) and (1.88±0.01), respectively.

Figure 3.8 (b) shows the transmission loss (in dB) as a function of the length of the GIF for GIF50 and GIF625. The minimum loss of under 2% was observed at about $300\ \mu m$ for GIF50 and $260\ \mu m$ for GIF625. The experimental data agrees very well with the model predictions from transmission function (Eq. 3.11) and with the predicted L_{MFA} (Eq. 3.12) of $\sim 260\ \mu m$ and $\sim 290\ \mu m$ for GIF625 and GIF50, respectively. Moreover, Figure 3.8 (c) depicts the overlap integral (Eq. 3.2) for each $LP_{0,m}$ mode excited at the SMF-GIF interface for GIF50 and GIF625. The fields were solved under the scalar fields approach [11]. Note that the even modes ($LP_{0,2m}$) yielded negative overlap integrals and also that SMF MFD is smaller than both GIFs FM MFDs (Figure 3.8 (d)). This corroborates with the fact that GIFs are beam expanders if the incoming beam is smaller than the

GIFs FM, as discussed in this section. Figure 3.8 (d) also indicates that the maximum expansion achieved by the pairs SMF-GIF50 and SMF-GIF625.

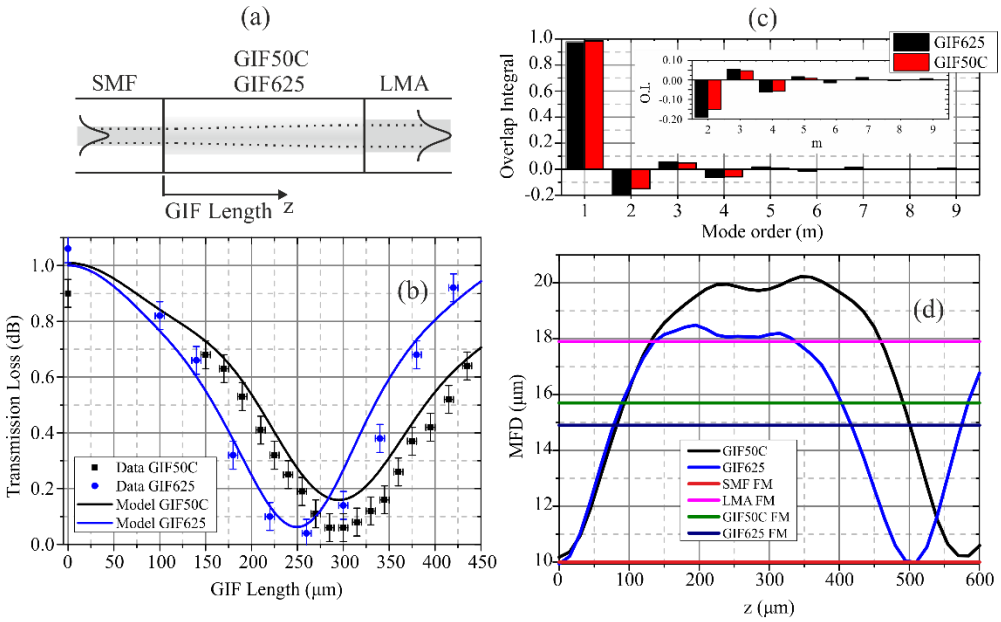

Figure 3.8: (a) MFA geometry considered for proof-of-concept demonstrations. (b) Device's transmission loss as a function of the GIF length. Simulation for GIF50C (black curve) and for GIF625 (blue curve). Experimental data follows the same colours and are displayed as squares for GIF50C and circles for GIF625. (c) Calculated overlap integrals for both GIFs, considering the SMF FM as the input mode. Note that even order modes are negative for both GIFs. (d) Mode field diameter evolution of the mode superposition traveling through the GIF. Simulated MFD of GIFs FM and SMF and LMA are indicated in the graph.

Although GIF50 and GIF625 performed well as MFAs for the SMF-LMA pair, it is helpful to expand the concept for larger output MFDs. In the next section, I define a route to obtain larger expansion or compression by engineering the GIFs geometry

3.2.1.3 Mode Field Adapters with Large Mode Fields

In the last sections I have defined a set of design-rules that can guide one when defining the GIF geometry to a given MFA. These parameters depend only on the GIF specifications such as core size and numerical aperture (NA) and wavelength of operation. Yet, as discussed in the previous chapters, fibre cells have better performance if they possess ultra-large cores and, thus, large mode-field distributions. Thus, it is necessary to understand whether GIF-based MFAs can cope with large mode-field excitation. In this section I discuss the impact on the MFA performance caused by the GIF's core size, number of modes and power-law coefficient γ.

A. GIF Core Size

Let us assume a set of GIFs with different core sizes but the same NA and study the effects of core size changes on the expanded MFD. The GIFs' specifications chosen for this theoretical study are listed in Table 3.2.

Table 3.2: Core radius, Numerical Aperture, power-law coefficient, number of modes, cut-off wavelength, effective core radius and Mode field diameter at L_{MFA} for GIF designs to be used as MFAs for large mode fields.

Fibre	Core Diameter (µm)	NA	γ	Number of modes LP_{0m}	L_{MFA} (µm)	MFD at L_{MFA} (µm)
GIF100	100	0.29	2.0	15	~400	27.5
GIF125	125	0.29	2.0	19	~500	34.1
GIF150	150	0.29	2.0	22	~600	40.1
GIF175	175	0.29	2.0	26	~700	48.0
GIF200	200	0.29	2.0	30	~800	54.7
GIF225	225	0.29	2.0	33	~900	61.7
GIF250	250	0.29	2.0	37	~1000	68.4

The MFD evolution of each fibre was simulated for a SMF fundamental mode incoming beam at wavelength of $1.55\ \mu m$ and it is depicted in Figure 3.9 (a). The simulation conditions were similar to the one presented in the previous section. An important feature observed in the simulations is that the expansion strength scales linearly with the GIF core size. Figure 3.9 (b) shows that the expanded MFD as a function of the core diameter $(2a)$ follows a linear trend with fitting angular coefficient of ~ 0.27 and this defines an empirical scaling law for GIF-based MFAs. The insertion loss was also computed for the range of GIFs simulated. I have considered a Gaussian-like mode as the mode target for excitation and varied its MFD from $25\ \mu m$ to $60\ \mu m$. The insertion loss as function of the target mode MFD is shown in Figure 3.9 (c) for a selection of GIFs with different core diameter ($100\ \mu m$, $125\ \mu m$, $150\ \mu m$ and $200\ \mu m$). If I fix an insertion loss budget of 0.25dB, I can define operation ranges for each GIF-based MFA. For instance, GIF100 has optimised performance when interconnecting SMF to LMA fibre with a MFD ranging from $25\ \mu m$ to $35\ \mu m$, then GIF150 takes over and has an insertion loss within the budget for output MFDs from $35\ \mu m$ to $60\ \mu m$. Therefore, with only two GIF designs, it is possible to cover a wide range of target MFDs from $25\ \mu m$ to $60\ \mu m$.

In this simulation I only considered the excitations of the $LP_{0,m}$ mode group. Therefore, the loss reported here can be interpreted as a fundamental limit and indicates the maximum efficiency of the device in its most optimised geometry (concentrically-aligned fibres). The main sources of losses are non-concentric fibre alignment and angled end-faces [14], [15]. It is well-known that cleave angles and radially-displaced cores induce the excitation of modes of any symmetry $(LP_{l,m})$ [15] and it could become a critical parameter when preparing the MFAs. Residual stress and large outer diameter can influence the mechanical cleaving tension [14] and impact the end-face quality,

resulting in the excitation of modes that do not participate in the effect [15]. Those modes would not only decrease the power carried by the $LP_{0,m}$ modes – thus decreasing the maximum expansion.

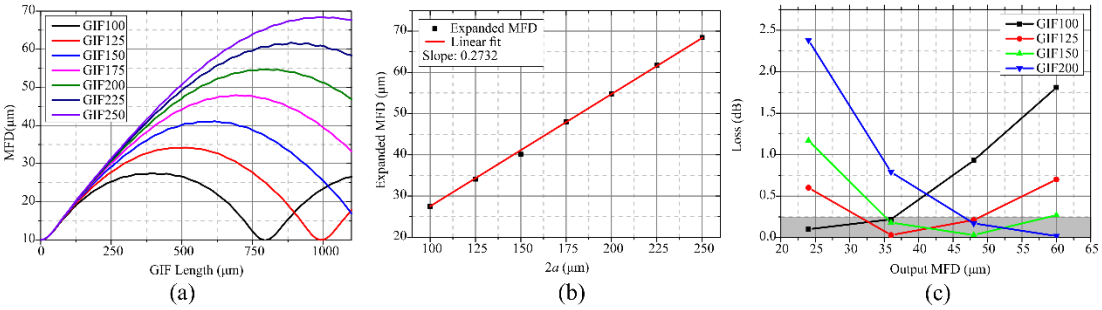

Figure 3.9: (a) MFD evolution as function of the GIF length for various GIF with different core size. Geometric parameters listed in Table 3.2. (b) MFD at L_{MFA} as function of the core diameter. Note that the MFD increases linearly with the diameter. (c) Transmission loss for various GIF (100,125,150 and 200) as a function of the output MFD. Note that with this arrangement of fibres, it is possible to interconnect to any fibre whose FM MFD range from 25 to 60μm with a loss as small as 0.25dB.

B. Number of Modes $(LP_{0,m})$

In order to identify the impact of the number of modes, I have simulated a set of GIFs with different modality but that match the supported mode's shape. It was possible by changing the core size and NA by a given amount to maintain the modes' shape, however increasing the modal content in the process. The parameters used for the simulation are listed in

Table 3.3. The NA was varied in steps of 0.02 from 0.1 to 0.34. The core size was tuned according to the linear function $a(NA) = 115NA$, for which any fibre with NA and $a(NA)$ would have a fundamental mode with a MFD of $15\ \mu m$. This also ensures that the other subsequent modes have the same shape, as fields described by Laguerre-Gauss functions are invariant to geometrical changes if, and only if, the quantity a/NA is constant [12]. The output MFD was varied from $20\ \mu m$ to $25\ \mu m$ in steps of $1\ \mu m$ and the fibre geometry was optimised to have a minimum loss for output MFD of $22\ \mu m$.

Modality is thus seen to have a clear impact on the expansion coefficient and the insertion loss. The expansion coefficient reaches its maximum with 7 modes, as depicted in Figure 3.10 (a). Additional higher order modes provide a secondary contribution to the expansion with a variation below 0.3%. The insertion loss as a function of the number of supported modes for a number of target MFDs is shown in Figure 3.10 (b). Although the minimum loss varied according to the target MFDs, the global minimum is found between 7 and 8 modes and increase monotonically as the number of modes is increased.

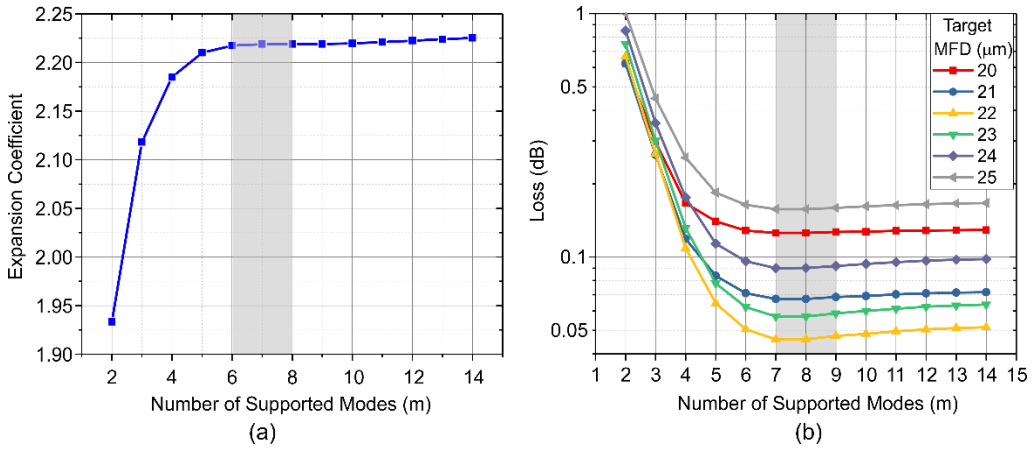

Figure 3.10: (a) Expansion coefficient as function of the number of supported modes. The expansion stabilised at ~ 2.22 for six or more supported $LP_{0,m}$ being taken into account. (b) Insertion loss as function of the number of supported modes for a selection of target output MFD from $20\ \mu m$ to $25\ \mu m$. The loss decreases rapidly as modes are added from two to six, where it stabilises. A global minimum is found when eight modes are considered.

Table 3.3: Fibre parameters used to study the impact of modality on the MFA efficiency

NA	Core Radius (µm)	Number of modes (LP_{0m})
0.1	11.50	1
0.12	13.80	2
0.15	17.25	3
0.18	20.70	4
0.2	23.00	5
0.22	25.30	6
0.24	27.60	7
0.26	29.90	8
0.28	32.20	9
0.29	33.35	10
0.3	34.50	11
0.32	36.80	12
0.33	37.95	13
0.34	39.10	14

In summary, eight $LP_{0,m}$ yields the maximum expansion, while minimising the insertion loss, for the proposed geometry. The additional higher modes should not impact the maximum expansion; however, they do increase the insertion loss.

C. Power-Law Coefficient γ

In the previous sections, I have demonstrated that, if $\gamma \neq 2$, a dephasing mechanism can arise from the anharmonic form of Eq. 3.7 with a correction term $\delta\beta(m)$, as defined in Eq. 3.8 and should impact the self-imaging quality at points defined by $L_{SI} = \pi k n_0 a/NA$, with $k \in \mathrm{N}$. The field transmission, defined by Eq. 3.11, can be rewritten considering the first order correction and has the following form,

$$T \sim \left| a^{*(2)}_{0,1} a^{(1)}_{0,1} + \sum_{m=2}^{M} a^{*(2)}_{0,m} a^{(1)}_{0,m} e^{-i[(m-1)\Delta\beta + \delta\beta(m) - \delta\beta(1)]L} \right|^2 . \qquad \text{Eq. 3.13}$$

Eq. 3.13 indicates that the mode beating length is displaced by an amount,δL,

$$\delta L \sim -\frac{\pi}{(\Delta\beta)^2}[\delta\beta(m) - \delta\beta(1)] \sim -\frac{L_{MFA}^2}{\pi}[\delta\beta(m) - \delta\beta(1)], \qquad \text{Eq. 3.14}$$

with $L_{MFA} \sim \pi n_0 a/2NA$. Eq. 3.8 also tells us that $\delta\beta(m) \propto L_{MFA}^{-1}$ and, thereby, $\delta L \propto L_{MFA}$. This asymptotic analysis tells us that dephasing phenomenon $\delta\beta$ caused by $\gamma \neq 2$ increases with modality and with the MFA length. Thus, it is necessary to minimise modality and MFA length simultaneously in order to weaken the dephasing effect caused by $\delta\gamma \neq 0$.

To analyse the impact of $\gamma \neq 2$ over a GIF with an optimised number of modes ($N_m = 8$), I have simulated a GIF MFA section with $a = 30\ \mu m$, $NA = 0.26$, $L_{MFA} = 267\ \mu m$ and with γ ranging from 1.80 to 2.2 by steps of 0.05. The launch mode was identical to an SMF-28 mode with a target output MFD ranging from $20\ \mu m$ to $25\ \mu m$ at $\lambda = 1.55\ \mu m$. The MFA was optimised for a target output MFD of $22\ \mu m$.

Figure 3.11 shows the insertion loss as function of the power-law coefficient γ. Although the loss variation is noticeable, its maximum amplitude was of just $\sim 0.018\ dB$, $\sim 0.02\ dB$ and $\sim 0.03 dB$ for target MFDs of $20\ \mu m$, $22\ \mu m$ and $25\ \mu m$, respectively.

In summary, GIFs-based MFAs can theoretically expand mode fields and the associated expansion coefficient be tuned by control of the GIFs geometrical attributes (core size and NA). In principle, any level of expansion and compression can be achieved by tuning both the core size and numerical aperture. Attention has to be paid to the quality of the refractive index profile, number of supported modes and the overall size of the MFA, as each of these attributes, together with cleave quality, splice and alignment are crucial parameters that can potentially compromise the performance of the MFA, if not carefully controlled.

In the next section, I generalise MFA theory for single-mode to multi-mode fibre interconnections, aiming for minimised coupling loss and reduced modal content excitation.

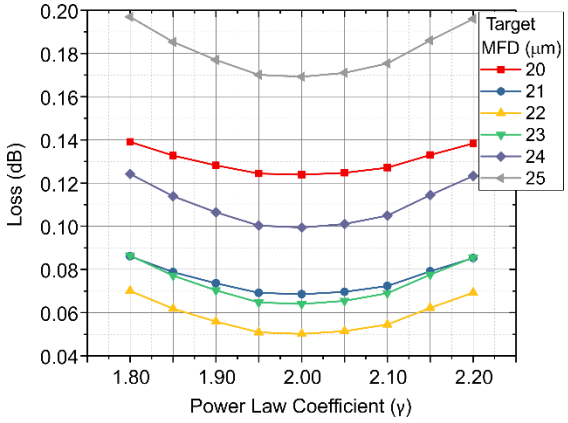

Figure 3.11: Insertion loss as function of the power law coefficient γ for a selection of target output MFDs ranging from $20\ \mu m$ to $25\ \mu m$. The GIF simulation parameters were $a = 30\ \mu m$, $NA = 0.26$, $L_{MFA} = 267\ \mu m$. The minimum loss is found at $\gamma = 2$ and increases as $|\delta\gamma| > 0$, indicating dephasing as a loss mechanism. Note that the GIF specifications were tuned to yield minimum loss for target MFD of $22\ \mu m$.

3.2.2 Single-Mode to Multi-Mode Fibre Interconnections using Mode Field Adapters

SMF to MMF is an important scenario to study as HC-PCFs are inherently MMFs, supporting at least a few modes [16], [17]. Those HC-PCFs frequently have mode sizes much larger than standard telecom fibres – as discussed in chapter 2 – making the use of field adapters for mode expansion and compression necessary in order to minimise optical losses. In the case of HC-PCF cells, optimised mode launches decrease the MMI caused by large mode content excitation and, thereby, improve the SNR of spectroscopy lines of atomic vapours found within the HC-PCF.

In the next two sections, I generalise the GIF-based MFA theoretical model for interconnections between SMF and MMF of any kind and describe the theory of fully-connectorised SMF to MMF to SMF patch cord arrangements, discussing the general aspects such as expected loss and MMI intrinsic to the MMF medium and the mode content excited.

3.2.2.1 Generalised Model for Fibre Interconnections Using Mode Field Adapters

Let us assume the configuration composed of a SMF-28 fibre spliced to a given GIF and then to a generic MMF and, after a length Z, the end of MMF is spliced to a GIF and then back to a SMF, as pictured in Figure 3.12 (a). This can be seen as a MMF patch cord with SMF connectors.

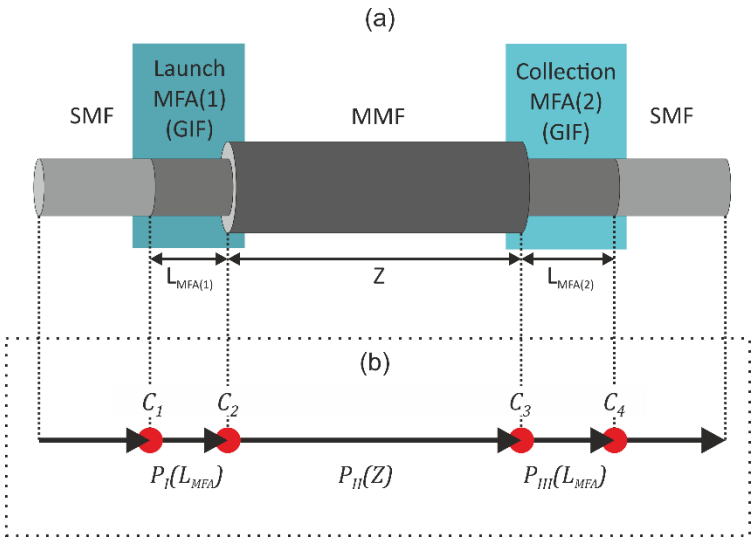

Figure 3.12: (a) SMF to MMF interconnection using GIF-based MFAs. (b) Interaction diagram used to picture each physical phenomenon taking place for the proposed geometry. C_n and P_k are related to the coupling propagator matrices. Red dots describe the coupling points and arrows describe the system evolution.

Unlike in the analysis performed in the previous sections, I make use of a matrix formalism to study the present geometry.

Let C_n be the coupling matrix at the n-th interaction point and $P_k(z)$ be the propagator of the k-th fibre section with length z. Each interaction point and fibre section are indicated in the diagram found in Figure 3.12 (b). The coupling matrix C_n is an $N_i \times N_{i+1}$ matrix where its elements describe the coupling between the n-th mode of fibre F_{i+1} and the n-th mode of fibre F_i, with N_i and N_{i+1} are the number of modes of fibres F_i and F_{i+1} taking part in the effect, respectively. Each element c_{nm} of C_n is calculated according to the overlap integral, in the scalar fields approximation,

$$c_{nm} = \iint_{\Omega} d^2x \varphi_m^{*\,(i)}(\boldsymbol{x}) \varphi_n^{(i+1)}(\boldsymbol{x}'). \qquad \text{Eq. 3.15}$$

where $\varphi_n{}^{(i)}(\boldsymbol{x})$ and $\varphi_m{}^{(i+1)}(\boldsymbol{x})$ are the n-th and m-th modes from fibres F_i and F_{i+1}. The propagator, $P_i(z)$, is a $N_i \times N_i$ diagonal matrix with elements,

$$p_{nn} = e^{i\beta_n z - \alpha_n z}, \qquad \text{Eq. 3.16}$$

where β_n and α_n are the n-th mode's propagation constant and attenuation coefficient, respectively. This matrix carries both the phase information and the propagation loss of each mode. The coordinate z can have two values: L_{MFA}, for propagations through GIFs, and Z for propagation

through MMF. The product $C_{i+1}P_n(L_{MFA})C_i$ describes the underlying mechanism of the MFA for either expansion or compression. Initially, I will focus on the first section of the proposed geometry that involves the launch MFA and derive an expression for GIF-based MFA interconnection of SMF to MMF.

Let us also assume that SMF, MFA(1) and MMF share the same z-axis. This simplifies the calculations as only the LP_{0m} modal sub-space takes part in the effect and this is a fundamental condition to achieve mode launch and collection at the GIF section, as discussed in details in the past sections. In order to model the coupling between SMF and MMF, mediated by a GIF (MFA) section. Let us assume that the numbers of modes with $l = 0$ are N and M for GIF and MMF, respectively. The coupling matrices C_1 and C_2 are $N \times 1$ and $M \times N$ matrices and the only propagator, $P_I(L_{MFA(1)})$, is a diagonal matrix with elements $p_{ij}^{(I)} = \delta_{ij}e^{i\beta_j^{(I)}L_{MFA(1)}}$, where β_j is the propagation constant of the j-th supported mode in the GIF. In this propagator, I neglected the propagation loss coefficient, as $L_{MFA(1)} \ll 1/\alpha_n^{(I)}$. The excitation strengths of the MMF's modes,b_m^{MMF}, are a function of $c_{n1}^{(1)}$, $c_{nm}^{(2)}, \beta_n^{(I)}$ and $L_{MFA(1)}$ and are obtained by calculating the following expression,

$$\boldsymbol{b}^{(\boldsymbol{MMF})} = C_2 \cdot P_I\left(L_{MFA(1)}\right) \cdot C_1. \qquad \text{Eq. 3.17}$$

Note that $\boldsymbol{b}^{(\boldsymbol{MMF})}$ is a vector with M components and each component defines the coupling strength of its associated mode.

The inner product $\langle \boldsymbol{\varphi}^{(\boldsymbol{MMF})}(\boldsymbol{x}, z), \boldsymbol{b}^{(\boldsymbol{MMF})} \rangle$ describes the mode evolution of the modal content excited at the MFA-MMF interface, and $\boldsymbol{\varphi}^{(\boldsymbol{MMF})}(\boldsymbol{x}, z) = (\boldsymbol{\varphi}_{01}^{(\boldsymbol{MMF})}(\boldsymbol{x})e^{i\beta_{01}z}, \dots, \boldsymbol{\varphi}_{0M}^{(\boldsymbol{MMF})}(\boldsymbol{x})e^{i\beta_{0M}z})$. This result shows that regardless of the launch conditions at the MFA-MMF interface, there will always be a probability of exciting LP_{0m} modes and a percentage of power can be transferred to these modes. Therefore, it is expected to observe MMI in SMF-MMF-SMF patch cords and, in order to gauge the impact of MMI in the overall loss, it is necessary to analyse the second section of the proposed geometry.

Let us assume again that all fibre sections share the same frame of reference and that GIF has N' LP_{0m} modes and assume $\boldsymbol{b}'^{(MMF)}$ as a generic excitation coming from the MMF section. The coupling matrices C_3 and C_4 are are $N' \times M$ and $1 \times N'$ matrices, respectively and the propagator $P_{III}\left(L_{MFA(1)}\right)$ is also a diagonal matrix with terms $p_{ij}^{(III)} = \delta_{ij}e^{i\beta_j^{(III)}L_{MFA(2)}}$. Here I again neglected the attenuation coefficient assuming that the GIF section is not long enough to induce propagation losses. The SMF coupling coefficient, $b^{(SMF)}$ has the closed expression as follows,

$$b^{(SMF)} = C_4 \cdot P_{III}\left(L_{MFA(2)}\right) \cdot C_3 \cdot \boldsymbol{b}'^{(MMF)} = c_{11}^{(4)}\left(\sum_k^M b'^{(MMF)}_k c_{jk}^{(3)}\right) + \sum_{m=2}^{N'} c_{1m}^{(4)}\left(\sum_k^M b'^{(MMF)}_k c_{mk}^{(3)}\right) e^{-im\Delta\beta L_{MFA(2)}}. \quad \text{Eq. 3.18}$$

I can infer directly from Eq. 3.18 the existence of MMI features in the energy transferred to the SMF FM. The MMI effect is identified as the sum, $\sum_k^M b'^{(MMF)}_k c_{jk}^{(3)}$, and describes the coupling of multiple modes of the MMF section to the various modes supported by the GIF. Note that each element of $\boldsymbol{b}'^{(\boldsymbol{MMF})}$ have a different phase as it carries information of the excitation strength and phase of each mode excited at the GIF-MMF interface and propagated through the MMF section.

Finally, I can define the full-power transmission function based on coupling matrices C_1 to C_4 and propagators $P_I\left(L_{LMA(1)}\right)$, $P_{II}(Z)$ and $P_{III}\left(L_{MFA(2)}\right)$. The propagator $P_{II}(Z)$ describes the mode evolution throughout the MMF section and is also a diagonal matrix with elements $p_{ij}^{(II)} = \delta_{ij} e^{i\beta_j^{(II)} Z - \alpha_j Z}$. The power transmission function, therefore, is given by the following expression,

$$T = \left|C_4 \cdot P_{III}\left(L_{MFA(2)}\right) \cdot C_3 \cdot P_{II}(Z) \cdot C_2 \cdot P_I\left(L_{MFA(1)}\right) \cdot C_1\right|^2. \quad \text{Eq. 3.19}$$

Eq. 3.19 describes the spectral response of the geometry proposed in Figure 3.12 (a) and is the key result sought in this section. The transmission efficiency of this geometry is closely connected to the ability to minimise the excitation of higher order modes at the MMF section or, mathematically, when $\sum_k^M b_k^{(MMF)} e^{-i\beta_k Z} c_{jk}^{(3)} \rightarrow b_1^{(MMF)} c_{j1}^{(3)}$. This would suppress the MMI element and the system would behave similarly to a SMF-SMF-SMF interconnection mediated by MFAs.

In the next section I simulate the device and discuss the results and implications of them.

3.2.2.2 Single-Mode to Multi-Mode to Single-Mode Interconnections: Device Efficiency and Limitations

To investigate the advantages and limitations of the SMF-MMF-SMF patch cord, I have simulated Eq. 3.19 for the geometry proposed in Figure 3.12 (a) and discussed in detail in the last section. Five GIF geometries were considered for these calculations, as listed in Table 3.4. The system considered was a symmetric one, i.e., the launch and collection MFAs were made of the same GIF and length. The simulation was performed at $\lambda = 1.55\ \mu m$. This guarantees that large MMI periods can be taken into account.

Table 3.4: GIF Core Diameter, Numerical Aperture, Power-Law coefficient, Number of modes, MFA optimum length and optimised Mode field diameter at MFA used for simulating SMF-MMF-SMF interconnections mediated by MFAs.

Fibre	Core Diameter (μm)	NA	γ	Number of modes LP_{0m}	L_{MFA} (μm)	MFD at L_{MFA} (μm)
GIF50	50	0.20	1.95	5	~290	22
GIF85	85	0.27	2.0	12	~360	29
GIF125	125	0.27	2.0	17	~530	43
GIF150	150	0.27	2.0	21	~630	51
GIF200	200	0.27	2.0	27	~840	68

The SIMMF's core radius and NA were tuned to match the MFD range where each GIFs has its operation optimised, i.e., around the expanded MFD, listed in Table 3.4. The modality was kept fixed at three, as ARFs generally support only a couple of LP_{0m}-like modes [17]. The SIMMF fields were obtained under the scalar fields approach and they are combinations of Bessel functions [15]. Their associated propagation constant were obtained analytically by solving the Eigen-value equation for SIMMF for each geometry considered [15].

The SIMMFs' lengths were varied from $10.5m$ to $10.51\,m$, in steps of $50\,\mu m$, to assess the efficiency and the existence of MMI. The average loss and its standard deviation were computed for each pair (GIF, SIMMF) by analysing the loss as a function of length (Z). The standard deviation holds the information regarding the MMI present in the signal and it is key to define the ultimate efficiency of the proposed device.

Figure 3.13 shows the insertion loss as a function of the SIMMF FM-MFD for the five devices considering the GIF-based MFAs listed in Table 3.4. It is noticeable that strong MMI takes place when the FM-MFD is larger than the MFA target MFD. This results from stronger coupling into higher order modes of the SIMMF which influences the efficiency of the collection MFA. In addition, all simulated scenarios achieved a minimum loss of $0.6 \pm 0.2\,dB$ at the target MFD of each GIF. This result defines the minimum loss expected from a fully-connectorised SMF-MMF-SMF patch cords.

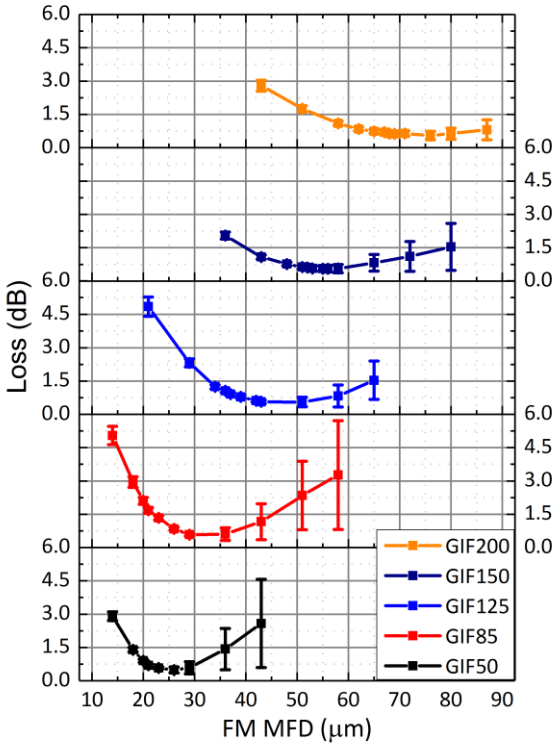

Figure 3.13: Simulated minimum loss as a function of the SIMMF FM-MFD for a set of GIF-based MFAs. Minimum loss of $(0.6 \pm 0.2)\ dB$ was estimated for all configurations. The GIF specifications are listed in Table 3.4. GIF lengths were considered to be L_{MFA}, defined in Eq. 3.12.

In order to understand the results presented in Figure 3.13, I have selected three special cases (geometry X, Y and W) where the target MFA MFD is larger, equal and small than the SIMMF FM-MFD. The parameters used in each geometry are listed in Table 3.5. Figure 3.14 shows the average loss – (a), (c) and (e) – and standard deviation – (b), (d), and (f) – as a function of the output MFA length and for a selection of input MFA lengths.

I can infer directly from Figure 3.14 (a) that the geometry X was poorly designed as the maximum loss of $\sim 2.9\ dB$ achieved at the L_{MFA}. It reflects that there is a strong mismatch at the launch MFA-SIMMF interface and that second MFA is acting as a beam expander rather than a compressor, as a result of the FM MFD being smaller than the GIF FM MFD ($\sim 15\ \mu m$). The standard deviation is shown in Figure 3.14 (b). A minimum deviation as low as $0.3\ dB$ indicates weak higher order excitation in the SIMMF section. Geometry Y is the optimised configuration when using GIF50 as the MFA, with a minimum loss of $\sim 0.7\ dB$ and a minimised deviation of only $\sim 0.2\ dB$, as indicated in Figure 3.14 (c) and (d). Geometry W is an extreme case, when the SIMMF FM-MFD is much larger than the MFA target MFD (about two times as large). It is easy to note the high MMI in this case, resulting in high loss figures, Figure 3.14 (e), and large deviation (Figure 3.14 (f)). The peaks found

at $L{\sim}240\ \mu m$ and $L{\sim}340\ \mu m$ are related to the phase-inverted higher order modes in the collection MFA that minimise the compression, resulting in additional loss.

Table 3.5: Geometry parameters and main results obtained with the SMF-MMF-SMF interconnections mediated by MFAs.

Case	MFA used	MFA Length (µm)	MFA target MFD (µm)	SIMMF FM-MFD (µm)	Min. Avg. Loss (dB)	Min. S. Dev.(dB)
X	GIF50	~290	22	14	1.80	0.24
Y	GIF50	~290	22	21	0.50	0.30
W	GIF50	~290	22	43	2.50	0.30

In this section, I have presented the theoretical and experimental aspects of the GIF-based MFA applied interconnection between dissimilar fibres. An analytical model for SMF to SMF interconnections were derived, a proof-of-concept experiment was performed to validate the model. Analytical models predicted that the GIFs geometry could be designed to maximise expansion while minimising modal content in order to minimise interconnection losses. GIF-based MFA was also studied for interconnecting fibres with different modality, where a fully-connectorised patch cord was considered and simulated for a wide range of SIMMF supporting a FM with an MFD from $15\ \mu m$ to $80\ \mu m$. The nature of the interconnections and the inherent MMI present in the SIMMF section led to a minimum insertion loss of $0.6 \pm 0.2\ dB$, regardless of the patch cord geometry. This can be considered as a fundamental limit for SMF-MMF-SMF interconnections with minimised MMI, mediated by MFAs.

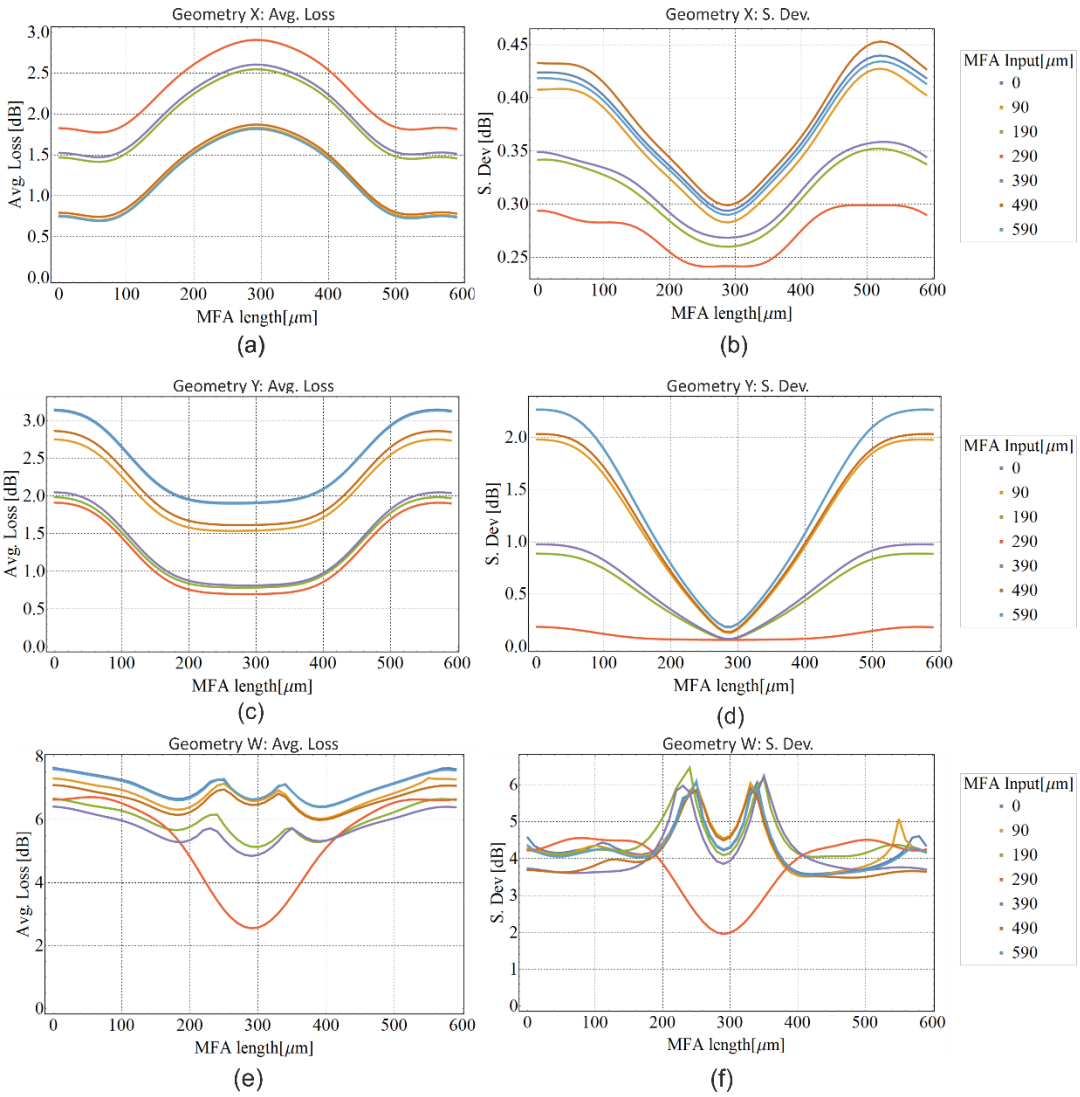

Figure 3.14: Average loss (a), (c) and (e) and standard deviation (b), (d) and (f) as functions of the output GIF length for three different geometries (X, Y and W). Each curve in each graph represents the average loss and standard deviation of different input MFA lengths. Geometrical parameters and minimum average loss and standard deviation are found in Table 3.5.

3.2.3 Solid-to-Hollow Core Fibre Interconnections

In the past sections of this chapter, I have discussed in details the underlying physical mechanism in GIF-based MFA, demonstrated experimentally its working principle and the suitability of employing this device for interconnecting optical fibres with large fundamental mode mismatch and minimised higher order modes excitation.

In this section, I discuss the experimental aspects of interconnecting SMF to HC-PCFs using MFAs. Interconnections between solid core fibres and HC-PCFs are not realised through conventional splicing programmes. The micro and sometimes, nanoscale microstructure geometry of HC-PCFs requires extra care when arc-fusion splicers are used, as heat can damage the core surroundings,

causing microstructure recession and therefore inducing propagation loss at the splice point. Wooler et al. have developed a cold splices technique for arc-fusion splicer with induced loss as low as $0.16\ dB$ for HC-PCF to HC-PCF and HC-PCF to LMA [18], [19].

3.2.3.1 Hollow Core Fibre Splice Technique and Practical Challenges

Non-standard splice techniques based on Fusion splicers for HC-PCFs should fulfil at least two conditions:

- The electric arc is powerful enough to create bonds between both fibre ends
- The electric arc is weak enough and the exposure time is fast enough to not cause any damage to the microstructure.

The balance between both conditions is key to obtain long lasting and low loss splices between HC-PCFs and solid core fibres. Wooler et al. have developed a technique for arc-fusion splices that involves three stages: tack, sweep and pulse [18], [19]. This technique proved efficient to splice HC-PCFs to HC-PCFs and HC-PCFs to solid fibres with insertion losses as low as $0.2\ dB$ [18]. The technique is based on a powerful, but short, electric arc to create a solid bond between both fibre ends. A weak arc sweeps around the joint in order to correct any imperfections (cracks) found on the fibres' outer surface. The cleaving process can create those cracks and impact the joint mechanical strength and stability of the joint [14]. Finally, an electric arc pulse train is applied over the joint to consolidate the bond. By tuning the arc exposure and intensity at each stage as well as the number of pulses, one is able to obtain bonds with minimised damage to HC-PCFs with a variety of microstructures.

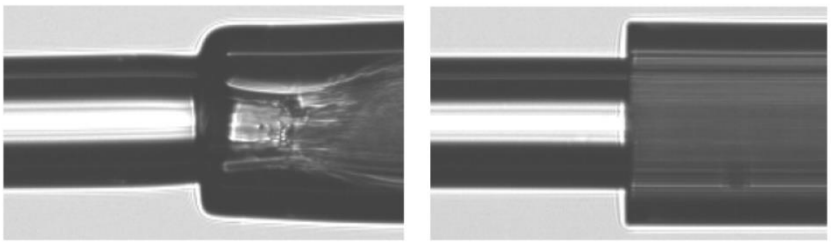

Figure 3.15: (a) $125\ \mu m$ solid core fibre spliced to HC-PBGF using standard SMF recipe. (b) $125\ \mu m$ solid core fibre spliced to HC-PBGF using cold splice technique. Figures adapted from [18].

Powerful electric arc power and long exposure can cause the microstructure to recess [18]. Such recession impacts the guiding mechanism and results in high loss caused by mode scattering at the splice point. Figure 3.15(a) shows the result of using standard SMF recipes to splice SMF to HC-PBGFs. The HC-PBGF microstructure was heavily damaged by the exposure to a powerful electric arc. Figure 3.15(b) shows a cold, but stable, splice between SMF and HC-PBGF. Note that both fibre

ends do not show any sign of damage caused by the splice technique. Wooler et al. reported splice loss in the region of $0.2\ dB$ to $0.5dB$ [18] and those figures match with laboratory observations reported in the next section. I bring the attention to a fundamental loss related to the nature of each fibres. As the splice is performed between a solid and a hollow core fibre, back reflection of $\sim 0.18\ dB$ is expected. Therefore, cold splices have a global minimum loss of $\sim 0.18\ dB$.

The size of the fibres being spliced also plays an important role in the joint stability and ultimate strength. The bonding strength is directly proportional to the contact surface area of each fibre ends. Since HC-PCFs possess a large portion of their cross-section formed by air-holes, the area of contact useful for splicing is diminished and generally is found at the region just outside the microstructure, as shown in Figure 3.16.

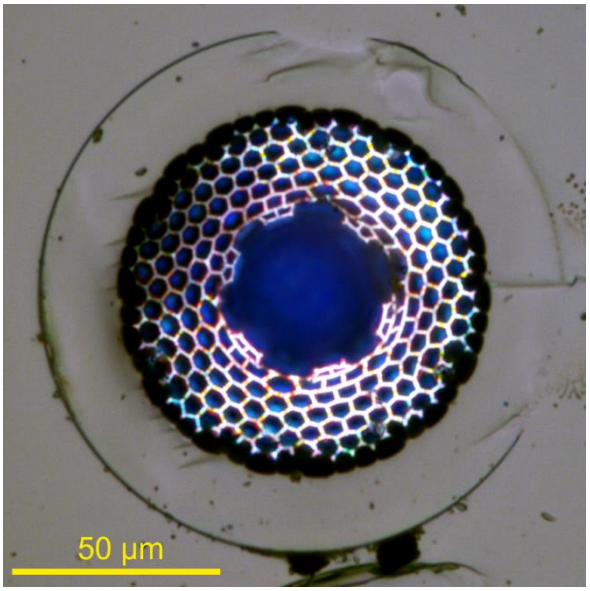

Figure 3.16: Cross-section of a broken splice between a HC-PBGF and a standard telecom fibre using cold splice technique. Note that a layer of SMF was left over the microstructure, showing that the fibres were indeed attached to each other. The contact surface area between both ends is about 50% of the SMF cross-section area.

The scenario is more challenging for K-ARFs especially developed for alkali filling, as those fibres were designed to have large hollow cores, with a microstructure outer diameter exceeding $150\ \mu m$. To obtain robust and stable splices, it is required that the MFA section has an outer diameter much larger than the K-ARF microstructure diameter and, ideally, the same size as the K-ARF outer diameter. By matching both fibres outer diameters, the bond strength is maximised and the splice condition can be dictated by the splice technique and splicer machine conditions solely.

Figure 3.17 shows the end-face of a GIF with outer diameter of $\sim 290\ \mu m$ that was a cold-spliced to a K-ARF (Fibre B, discussed in chapter 2). Parts of the K-ARF jacket and microstructure remained attached to the GIF. It indicates that the splice technique is effective and yield consolidated bonds.

Although cold splices can indeed yield low loss joints, their ultimate strength is very low. The splice point is very delicate and can break simply on handling and its ultimate strength normally is below $50\ gf$. By encapsulating the splice point using splice protectors, the ultimate strength vastly improves and laboratory measurement indicates that it can be as high as $1500\ gf$, with an increased loss of $0.15\ dB$. These figures were obtained by operating a CT-105 Fujikura cleaver, varying the applied tension. Figure 3.17 also shows that the GIF end face was partially damaged during cleaving. The existence of a mist hackle area indicates that cleaving tension was set too high for the given fibre geometry [14].

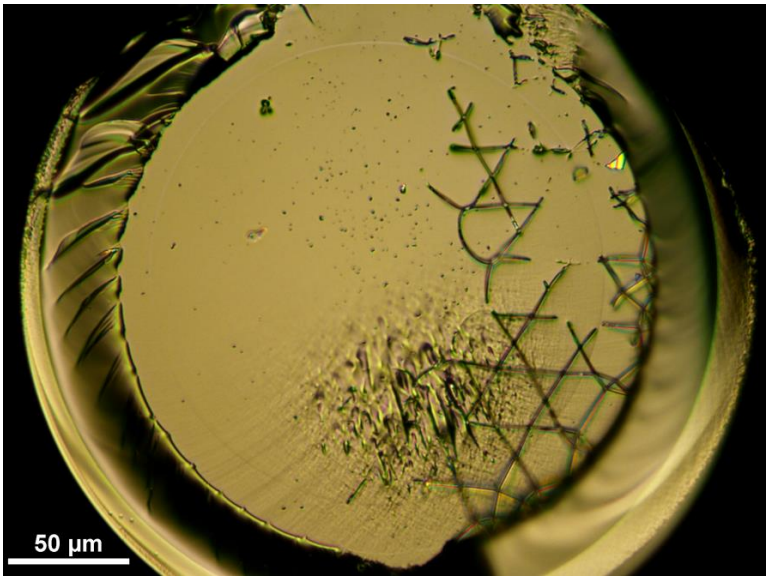

Figure 3.17: Cross-section of a broken splice of a K-ARF to a $\sim 290\ \mu m$ GIF using cold splice technique. Part of the K-ARF (microstructure and silica jacket) remained at the GIF end.

3.2.3.2 Hollow Core Fibres Patch-Cords

Full-connectorisation of HC-PCFs in general has been one of the key aspects to be addressed to broad the acceptance of HC-PCFs and devices based on this technology and numerous groups have tried to interconnect such fibres to standard fibres using various techniques and processes. Yablon et al. and Ouyang et al. studied a similar geometry composed by a coreless fibre followed by a GIF section interconnecting an SMF to a PCFs (solid core). Both groups reported a similar coupling loss figures ($\sim 0.5\ dB$) for a single interconnection [6], [7]. Wheeler et al and Zheng et al. investigated tapering the ends of K-ARFs in order to match the fibres outer diameter and decrease the mode mismatching between SMF and K-ARF. Wheeler et al. reported a minimum coupling loss of $0.6\ dB$ and $\sim 2.25\ dB$ for $\sim 40\ \mu m$ and $\sim 70\ \mu m$ core diameter K-ARFs, respectively [9]. Zheng et al. obtained comparable coupling loss figures ($0.48\ dB$) and the main advantage of the method presented is that the hypocycloid was maintained throughout the tapering process [10]. I bring the reader's attention to the fact that none of these studies addressed the problem of fully-interconnecting, end-to-end, a section of HC-PCFs to standard SMFs. They only reported on light

injection through tapered HC-PCFs. When used as a collection configuration (where the light travels from the HC-PCFs to the SMF), Zheng has reported a loss penalty as high as $3.5\ dB$ [10]. Such high loss is related to the modal content excited in the HC-PCF section and MMI that affects the mode quality and coupling to the SMF FM. In this section I report the experimental findings when using GIF-based MFAs for interconnection between HC-PCFs and SMFs.

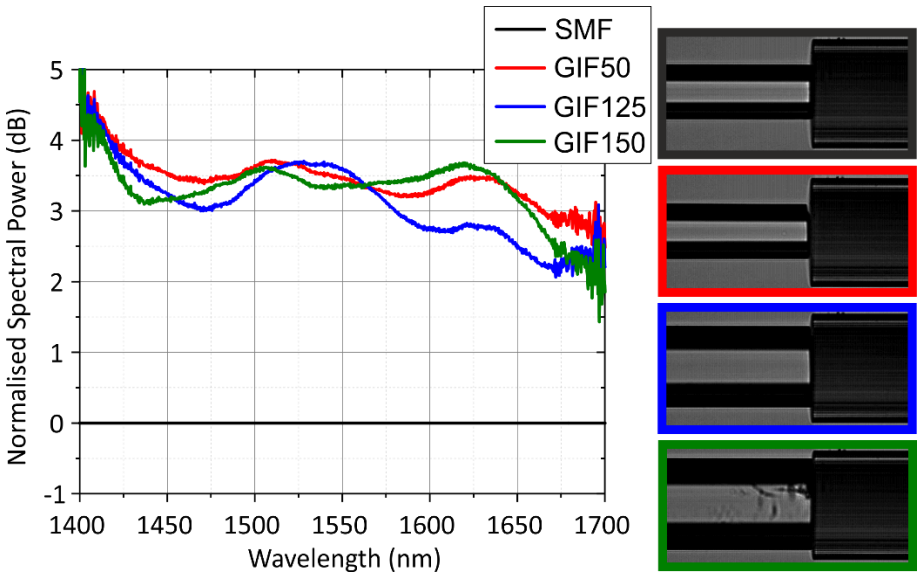

Figure 3.18: Normalised spectral response for four different light injection configuration using SMF and three GIFs (50,125 and 150). GIF assisted signal launch showed at least 3 dB improvement over SMF.

I have investigated initially the launch efficiency of MFAs mediating between SMFs and HC-PCFs. In this experiment, I varied the GIF used as the MFA and the signal was launched from SMF to the HC-PCF. The HC-PCF was a K-ARF with a hollow core diameter of $\sim 41\ \mu m$. Its main geometrical parameters and optical properties are found in Table 3.6 (K-ARF(1)). The GIFs used were the Thorlabs GIF50, with $NA = 0.20$, and the Fibreware GIF125 and GIF150, with $NA = 0.27$. All GIFs were spliced to an SMF connector and cleaved to their associated L_{MFA} lengths, found in Table 3.4. The transmission power from a white light source was recorded using the Yokogawa AQ-6315B OSA. Four launching conditions were considers using SMF and GIFs 50, 125 and 150. Figure 3.18 shows the normalised spectral response of each case. The power injected in the HC-PCFs doubled its value when GIFs were used, compared to SMF. This indicates that the optical signal coming out of the GIFs has very little divergence angle, as small as the K-ARF's acceptance angles. This shed light on another important aspect of GIFs that is its lensing mechanism and collimating capability [20].

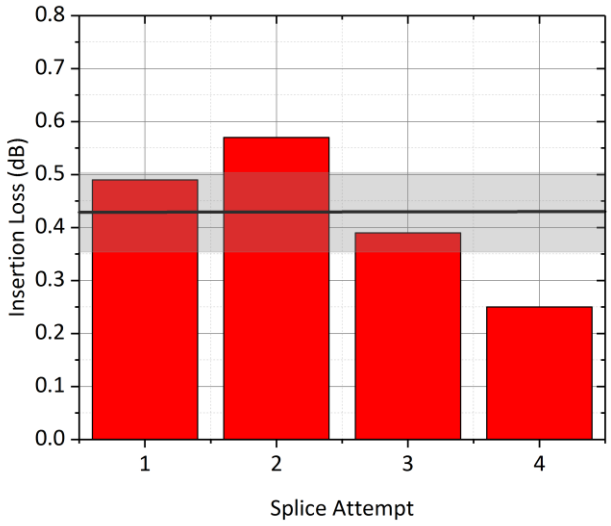

Figure 3.19: Splice loss for a SMF-MFA-HC-PCF joint. The GIF was carefully chosen to match the K-ARF FM MFD and its geometry. An average loss of $0.4 \pm 0.1\ dB$ was inferred from the experiment data.

A cold splice recipe was fine tuned to splice a $\sim 15\ m$ long K-ARF to a GIF125 MFA. Five splice attempts were performed monitoring to insertion loss using a diode laser at $1.55\ \mu m$ with $1\ mW$ output power. The GIF125, with $NA = 0.27$, was the most suitable choice as it theoretically yields an expanded field with a MFD of $\sim 36\ \mu m$, which is only $\sim 5\ \mu m$ larger than the expected FM-MFD of the chosen K-ARF. An average insertion loss of $0.4 \pm 0.1\ dB$ with minimum of observable loss of $0.25\ dB$ was observed during the experiment. The splice histogram is shown in Figure 3.19. The losses observed are likely connected to the splice procedure and coupling losses.

In order to study the full-connectorisation of HC-PCFs, Three HC-PCFs geometries were chosen. They consist of one HC-PBGF and two K-ARFs (1, 2). Geometry and optical specifications are listed in Table 3.6 and their cross-section are shown in Figure 3.20. The GIF geometry was chosen based on expected FM-MFD of each HC-PCF and its microstructure outer diameter. Their geometrical and expected MFA specifications are also listed in Table 3.6. In this same table, I have highlighted with two different colours the key specifications used to design the GIF. For instance, patch-cord using HC-PBGF requires a GIF that produces expanded MFDs of $20\ \mu m$ and have outer diameters as larger as $90\ \mu m$. For this scenario, the GIF50, with $NA = 0.20$ and outer diameter of $125\ \mu m$ is the best match. For patch-cord based on K-ARF(2), it was required a GIF with expanded MFD of $54\ \mu m$ and outer diameter as larger as $190\ \mu m$. GIF200, with $NA = 0.27$ and outer diameter of $290\ \mu m$ was suitable match for the K-ARF geometry chosen.

Table 3.6: Patch-cord specifications

Patch-cord	Length (m)	HC Diameter (µm)	HC-PCF Microstructure Diameter (µm)	Loss at $1.55\ \mu m$ (dB/km)	Expected HC-PCF FM-MFD (µm)	GIF Core Diameter (µm)	GIF Outer Diameter (µm)	NA	L_{MFA} (µm)	MFD at L_{MFA} (µm)
HC-PBGF	~10	~30	~90	~3.8	~21	~50	~125	0.20	~290	~21
K-ARF(1)	~14	~41	~155	~160	~31	~125	~185	0.27	~530	~36
K-ARF(2)	~25	~72	~190	~279	~54	~200	~290	0.27	~840	~68

All patch cords were prepared and the measurement was performed as follows:

- HC-PCFs ends were cleaved using the CT-105 Fujikura cleaver;
- Large outer diameter GIFs were cleaved using a precision cleaver built around the CT-101 Fujikura cleaver;
- Fibres were spliced using tailor-made recipes for FITEL S184PM-SLDF(v.2) splicer;
- A laser diode at $1.55\ \mu m$ with $1\ mW$ power was used to characterise the patch-cord. Insertion loss was measured by comparing the power before and after the patch-cord.
- Photo-detector noise floor is $0.01\ dB$.

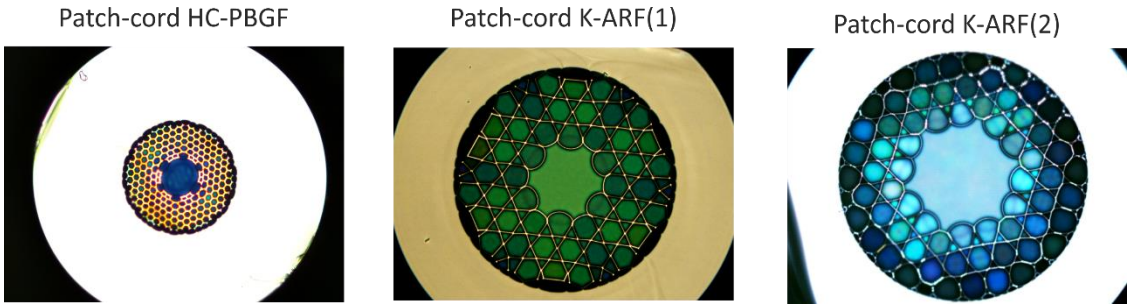

Figure 3.20: Cross-section of the three HC-PCFs used to assembly patch-cords A to D, listed in Table 3.6. left: HC-PBGF. Centre and right: K-ARF(1) and (2).

Fibre end-face angles, measured by the splicer machine, were kept below 2° to minimise losses and excitation of higher order modes associated to tilted end-faces [14], [15]. The recipes were optimised to minimise damage to the microstructure of the HC-PCF. All GIFs listed in Table 3.6 are commercially-available fibres from FIBREWARE (GIF125 and GIF200) and Thorlabs (GIF50). The refractive index profiles were measured and are shown in Figure 3.21. The power law coefficient γ varied considerably (~ 0.2) from sample to samples, with absolute value of 1.96, 1.81 and 1.78 for GIF50, GIF125 and GIF200, respectively.

Two identical HC-PBGF patch cords were prepared using GIF50 MFAs at each end and spliced to SMF connectors. The MFA preparation and splice to SMF connector yielded losses below $0.01\ dB$

in all cases. Note that the propagation loss at the HC-PBGF should be below $0.1\ dB$ for a $10\ m$ sample and, thus, negligible for this study. MFA to HC-PBGF splices were characterised separately, where the launch MFA to HC-PBGF had an associated insertion loss of $(0.55 \pm 0.05)\ dB$. After the second splice, the patch-cord had insertion loss of $(2.3 \pm 0.2)\ dB$. This figure is about two times greater than the theoretical prediction of $(0.9 \pm 0.2)\ dB$, which includes the patch-cord theoretical insertion loss ($0.55\ dB$) and back-reflection losses ($0.36\ dB$). Higher-order modes excited at the HC-PBGF section and high splice loss are the main causes for such disparity. The direction of the light launch was swapped and a variation of only $0.1\ dB$ was observed. It may indicate that both splices are similar in terms of splice loss; hence, the insertion loss observed is related to the mode content excited at the HC-PBGFs solely.

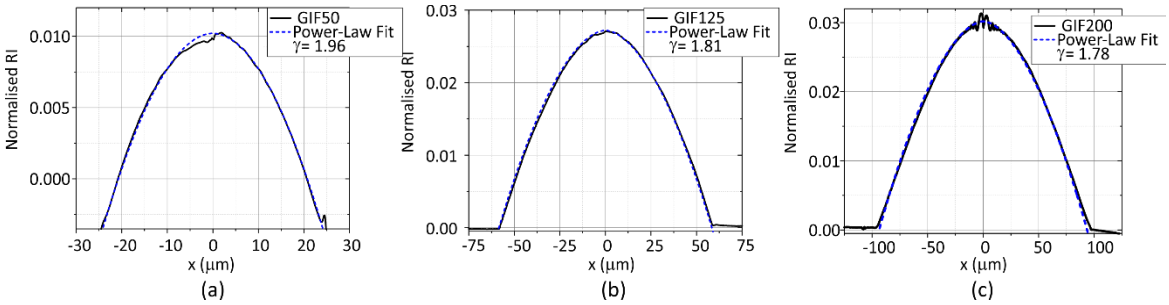

Figure 3.21: Refractive index profile of (a) GIF50, (b) GIF125 and (c) GIF200. Power-law coefficients were obtained fitting the data and are 1.96, 1.81 and 1.78, respectively.

The patch-cords made using K-ARF(1) and K-ARF(2) presented high insertion loss over $5\ dB$. Such high loss figure can be related to the quality of the GIF used. In Figure 3.21(b) and (c), one can readily infer that the refractive index profiles of GIF125 and GIF200 deviate from the ideal parabolic shape. It results in strong dephasing between the numerous $LP_{0,m}$ modes participating in the effect, changing the value of L_{MFA} and the maximum beam compression and expansion that the GIF can produce. It is required further investigation in this subject.

3.3 Conclusion

In this chapter, I have demonstrated the use of MFA based on GIFs to interconnect HC-PCFs to standard solid core fibres. I discussed and derived theoretical assumptions and expression and defined a route to design MFAs considering the geometry and mode shape of the fibres to be spliced to. MFAs offer an alternative solution to interconnect standard SMF to HC-PCFs with only commercially available solutions (parabolic shape GIFs) and without the need to post-processing HC-PCFs in order to minimise optical losses.

A proof-of-concept using dissimilar SMFs was performed and validated the MFA properties of GIFs. This study confirmed the finding reported in [5]. I also presented a detailed theoretical model

considering the GIF geometry parameters such as core radius, NA, refractive index shape and modality, drawing conclusions from the impact of each parameter over the efficiency of the MFA.

I theoretically studied the special case of full connectorisation of MMFs using MFAs. Models have indicated an intrinsic minimum of loss of $0.6 \pm 0.2\ dB$ for any patch-cord (SMF-MMF-SMF), with optimised field adaptors in each joint. Finally, I discussed splicing methods for HC-PCFs and performed the experiment of assembling a patch-cord using HC-PCFs and SMF, mediated by suitable MFAs. I observed insertion loss of $2.3 \pm 0.2\ dB$ when using a HC-PBGF and $50\ \mu m$ core diameter GIF as MFA. This figure is about two times greater than the theoretical prediction of $0.9 \pm 0.2\ dB$ and can be further decreased by employing fine tuning the splice recipe to reduce associated splice damage.

3.4 References

[1] Y. Chen et al., "First Demonstration of Low Loss, Bend Insensitive 37-Cell Hollow-Core Photonic Bandgap Fiber at 1µm for High Power Delivery Applications," in Conference on Lasers and Electro-Optics, 2016, p. STu4P.1.

[2] F. Benabid, F. Couny, J. C. Knight, T. A. Birks, and P. S. J. Russell, "Compact, stable and efficient all-fibre gas cells using hollow-core photonic crystal fibres.," Nature, vol. 434, no. 7032, pp. 488–491, 2005.

[3] F. Benabid, P. Light, F. Couny, and P. Russell, "Electromagnetically-induced transparency grid in acetylene-filled hollow-core PCF.," *Opt. Express*, vol. 13, no. 15, pp. 5694–5703, 2005.

[4] P. S. J. Russell, P. Hölzer, W. Chang, A. Abdolvand, and J. C. Travers, "Hollow-core photonic crystal fibres for gas-based nonlinear optics," Nat. Photonics, vol. 8, no. 4, pp. 278–286, 2014.

[5] P. Hofmann, A. Mafi, C. Jollivet, T. Tiess, N. Peyghambarian, and A. Sch??lzgen, "Detailed investigation of mode-field adapters utilizing multimode-interference in graded index fibers," J. Light. Technol., vol. 30, no. 14, pp. 2289–2297, 2012.

[6] A. D. Yablon and R. T. Bise, "Low-loss high-strength microstructured fiber fusion splices using GRIN fiber lenses," IEEE Photonics Technol. Lett., vol. 17, no. 1, pp. 118–120, 2005.

[7] D. Ouyang, S. Ruan, C. Guo, and H. Wei, "Low loss splicing between double-clad fiber and photonic crystal fiber using graded index fiber lens," J. Light. Technol., vol. 32, no. 14, pp. 2524–2530, Jul. 2014.

[8] D. Ouyang et al., “Theoretical and experimental analysis of splicing between the photonic crystal fiber and the conventional fiber using grin fibers,” Appl. Opt., vol. 51, no. 36, p. 8516, Dec. 2012.

[9] N. V. Wheeler, M. D. W. Grogan, P. S. Light, F. Couny, T. A. Birks, and F. Benabid, “Large-core acetylene-filled photonic microcells made by tapering a hollow-core photonic crystal fiber,” Opt. Lett., vol. 35, no. 11, p. 1875, Jun. 2010.

[10] X. Zheng, B. Debord, L. Vincetti, B. Beaudou, F. Gérôme, and F. Benabid, “Fusion splice between tapered inhibited coupling hypocycloid-core Kagome fiber and SMF,” *Opt. Express*, vol. 24, no. 13, p. 14642, Jun. 2016.

[11] K. Okamoto, *Fundamentals of Optical Waveguides*. Elsevier Inc., 2006.

[12] A. Ghatak and K. Thyagarajan, Introduction to fiber optics. Cambridge: Cambridge University Press, 1998.

[13] J. J. Ramskov Hansen and E. Nicolaisen, “Propagation in graded-index fibers: comparison between experiment and three theories,” *Appl. Opt.*, vol. 17, no. 17, p. 2831, Sep. 1978.

[14] A. D. Yablon, *Optical fiber fusion splicing*. Springer, 2005.

[15] A. W. Snyder and J. D. Love, Optical Waveguide Theory. Chapman & Hall, 1995.

[16] D. Gray et al., “Real-Time Modal Analysis via Wavelength- Swept Spatial and Spectral Imaging,” IEEE Photonics Technol. Lett., vol. 28, no. 9, pp. 1034-1037, 2016.

[17] T. D. Bradley *et al.*, “Modal content in hypocycloid Kagomé hollow core photonic crystal fibers,” *Opt. Express*, vol. 24, no. 14, p. 15798, Jul. 2016.

[18] J. Wooler et al., “Overcoming the Challenges of Splicing Dissimilar Diameter Solid-Core and Hollow-Core Photonic Band Gap Fibers,” in Workshop on Specialty Optical Fibers and their Applications, 2013, p. W3.26.

[19] J. Wooler et al., “Robust Low Loss Splicing of Hollow Core Photonic Bandgap Fiber to Itself,” in Optical Fiber Communication Conference/National Fiber Optic Engineers Conference 2013, 2013.

[20] S. H. Wang, C. J. Tay, C. Quan, and H. M. Shang, “Collimating of diverging laser diode beam using graded-index optical fiber,” *Opt. Lasers Eng.*, vol. 34, no. 2, pp. 121–127, 2000.

Chapter 4 Introduction to Coherent Population Trapping in Alkali Thermal Vapours

Foreword

In this chapter, I describe the theoretical and experimental aspects of coherent population trapping (CPT). The effect was first reported in 1976 by Alzetta et al who observed decreasing in the fluorescence of Sodium vapour [1]. Its main characteristic is the decreased absorption (or fluorescence) in an atomic vapour when two photons are simultaneously resonant in a lambda configuration, as depicted in Figure 4.1.

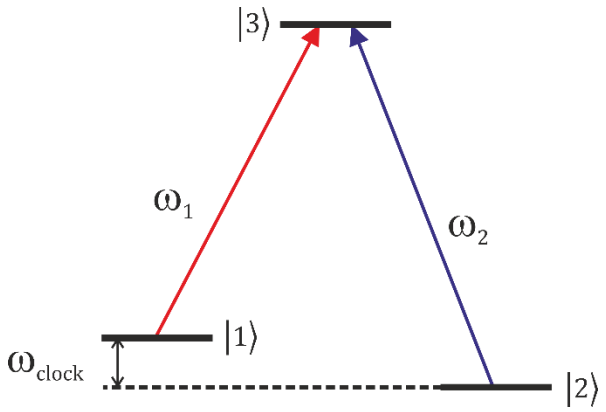

Figure 4.1: Lambda configuration used to obtain coherent population trapping.

In the past few decades the effect has been exploited in atomic frequency and time reference technology [2]–[4]. The fundamental condition to achieve CPT is a frequency matching condition of the two resonant photons. It can be interpreted as an indirect optical measurement of the, dipole forbidden, clock transition of alkali atoms, since the frequency matching condition is $\omega_2 - \omega_1 = \omega_{clock}$. In practical terms, the microwave clock transition frequency of Cs ($9.192.631770\ GHz$) can be indirectly measured by the difference of the two photon (laser) frequencies. The transparency effect manifests as a Lorentzian peak with line width sometimes below kHz regime, making this effect very attractive for ultra-stable frequency and time references.

This chapter is divided into two main parts, concerning theoretical aspects and literature review and experimental observations. Section 4.1 introduces the Cs atomic structure and properties related to the transitions used to achieve CPT. Section 4.2 presents the CPT effect in its qualitative and quantitative aspects. This section contains a theoretical description with equations useful to model the effect. Line broadening mechanisms are discussed and methods to control them, such as buffer gas addition [5]–[7] and anti-relaxation coatings [8], are suggested with theoretical models. Finally, section 4.3 analyses the experimental aspects of CPT. The experimental apparatus

is presented, followed by two experiments that I performed, involving a pure-Cs vapour container and a series of buffer gas added Cs-vapour cells. The latter is companied with a mathematical modelling, as an attempt to methodically demonstrate the roles of the numerous broadening mechanisms present in CPT.

4.1 Caesium Atomic Structure and Transition Lines

Caesium is a soft alkali metal and the most reactive element in the periodic table. It has atomic number 55 and its stable isotope is the ^{133}Cs, with molar mass $132.905\ kg/mol$. It has, therefore, 55 electrons and its electronic distribution is shown in Figure 4.2.

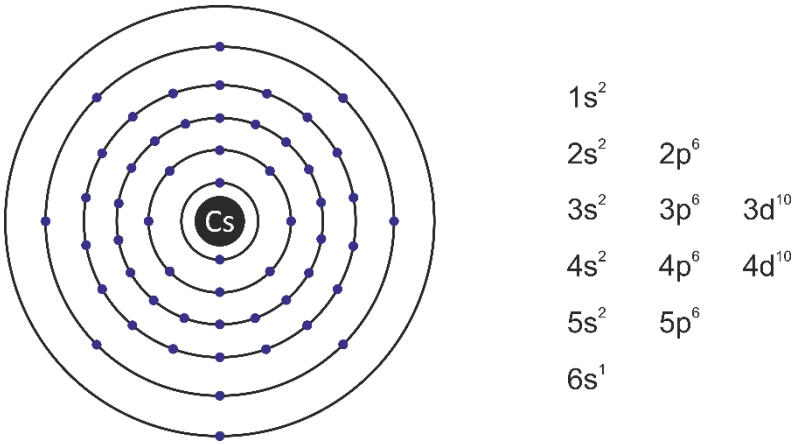

Figure 4.2: Caesium electronic distribution.

For the scope of this project, I will focus on the atomic structure of the ^{133}Cs D lines and most specifically on the D1 line. There are two main lines, D1 $\left(6^2S_{1/2} \rightarrow 6^2P_{1/2}\right)$ at $894\ nm$ and D2 $\left(6^2S_{1/2} \rightarrow 6^2P_{3/2}\right)$ at $852\ nm$, with natural line-width of $\sim 4.5\ MHz$ and $\sim 5.2\ MHz$, respectively [9]. D1 and D2 line fold into four and six hyperfine transitions, according to each hyperfine level total angular momentum, F. Note also that those transitions have $(2F+1)$ Zeeman sublevels if the atoms are subject to magnetic fields. The ground state to ground state transition (the so-called clock transition), $6^2S_{1/2}\ F=3 \rightarrow 6^2S_{1/2}\ F=4$, is in the microwave range with exact frequency of $\omega_{rf} = 9.192631770\ GHz$. This transition is currently the primary standard for the second and its stability is measured in Cs fountains atomic clocks, with normalised precision $\sigma_\omega/\omega_{rf} < 10^{-15}$ [10]. The two excited states, $6^2P_{1/2}\ F=\{3,4\}$, that compose the D1 line are separated by $\sim 1.1\ GHz$ and the four excited states, $6^2P_{3/2}\ F=\{2,3,4,5\}$ that compose the D2 line are separated by $\sim 150\ MHz$ $(F=2\ \rightarrow F=3)$, $\sim 200\ MHz$ $(F=3 \rightarrow F=4)$ and $\sim 250 MHz$ $(F=4\ \rightarrow F=5)$ [9]. The D lines transitions diagram is depicted in Figure 4.3 (a) with a sub-doppler hyperfine spectroscopy of the $6^2S_{1/2}\ F=4 \rightarrow\ 6^2P_{1/2}\ F'=\{3,4\}$ transitions.

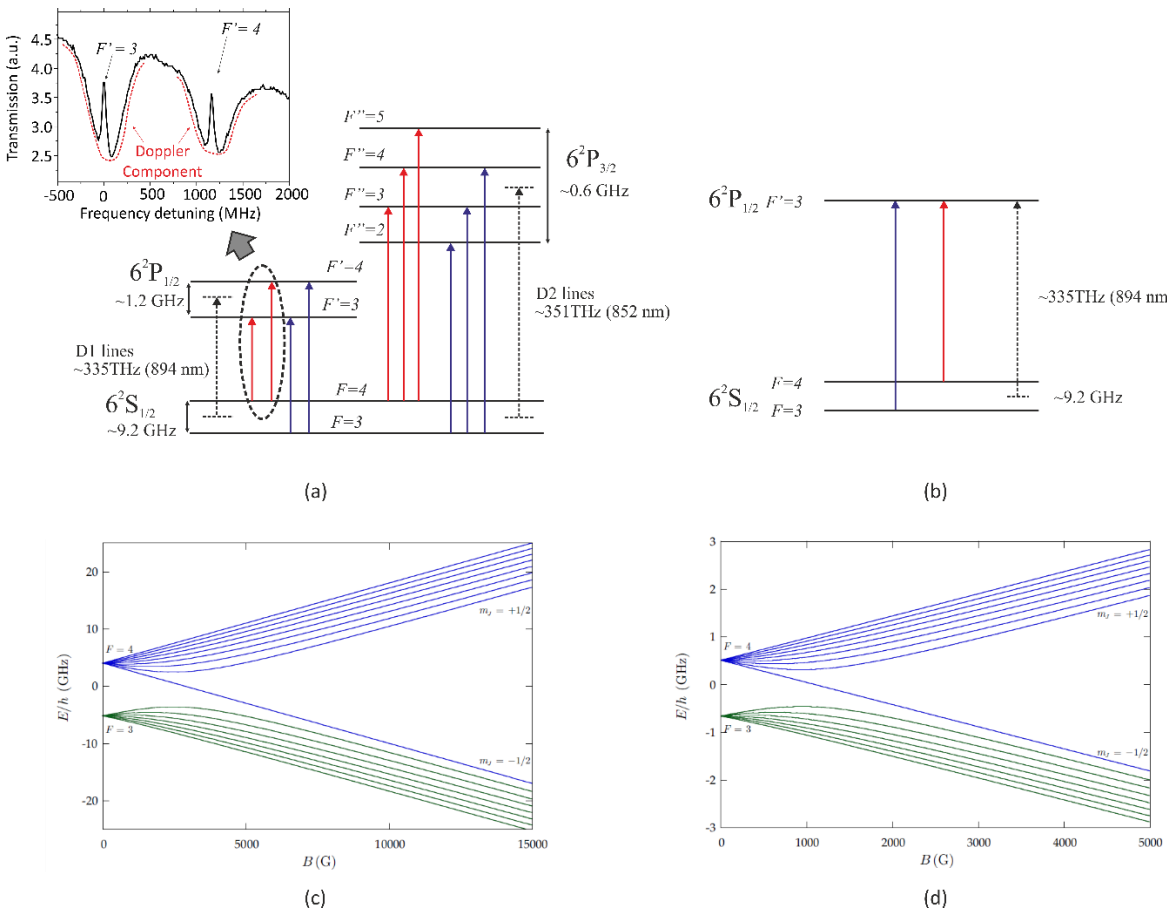

Figure 4.3: (a) Caesium D lines diagram and sub-Doppler pump-probe spectroscopy of $6^2S_{1/2}F = 4 \rightarrow 6^2P_{1/2}F' = \{3,4\}$ transitions. (b) D1 lines lambda configuration used for coherent population trapping spectroscopy in this study. Energy as a function of the magnetic field strength for (a) the ground state $6^2S_{1/2}$ $F = \{3,4\}$ and (d) for the excited state $6^2P_{1/2}$ $F = \{3,4\}$. Graphs shown in figures (c) and (d) were extracted from [9]. Note that $10\ G = \ 1\ mT$.

The transitions chosen for coherent population trapping (CPT) spectroscopy present throughout the chapters of this thesis are the $6^2S_{1/2}(\ F = \{3,4\}, m_F = 0) \rightarrow 6^2P_{1/2}(\ F' = 3, m_F = \pm 1)$, where m_F is the z-projection of the total angular momentum F. The CPT mechanism will be discussed in detail in this chapter. The choice of the given Zeeman transition pair was made based on the optical properties of this pair of transitions, although it is possible to obtain CPT resonance in $6^2S_{1/2}$ $F = \{3,4\} \rightarrow 6^2P_{1/2}$ $F' = 4$ and with the D2 lines as well. At strong magnetic fields ($B \gg 100\ mT$), where the hyperfine number F and m_F are no longer good quantum numbers, the energy of the Zeeman states varies as a function of the magnetic field strength, as depicted in Figure 4.3 (c) and (d). At weak fields ($B \ll 100\ mT$), the hyperfine quantum numbers F and m_F are good numbers and Zeeman states with $m_F = 0$ become insensitive to external magnetic fields. The $m_F = 0$ ground states are imperative to minimise the frequency dependency over weak magnetic field fluctuations. Transitions pairs formed with states with $m_F \neq 0$ are sensitive to magnetic field fluctuations, For the scope of this thesis, only CPT with $\sigma^{\pm}$ transitions were studied. This is a direct

result of the proposed experimental setup where the longitudinal magnetic field is collinear with the optical signal, of which only allows $\sigma^{\pm}$ transitions to be studied. Details on the experimental setup can be found in section 4.3 and chapter 6 of this thesis.

Table 4.1 Cs D1 line angular momentum coupling strengths (Clebsch-Gordan Coefficients) for $\sigma^{\pm}$ and π transitions between $6^2S_{1/2}(F; m_F = 0) \rightarrow 6^2P_{1/2}(F; m_{F'} = m_F + \Delta m)$[9]

Transition type	$F = 3 \rightarrow F' = 3$	$F = 4 \rightarrow F' = 3$	$F = 3 \rightarrow F' = 4$	$F = 4 \rightarrow F' = 4$
$\sigma^+(\Delta m = +1)$	$-\sqrt{1/8}$	$\sqrt{1/8}$	$-\sqrt{5/24}$	$\sqrt{5/24}$
$\sigma^-(\Delta m = -1)$	$\sqrt{1/8}$	$\sqrt{1/8}$	$-\sqrt{5/24}$	$-\sqrt{5/24}$
$\pi\ (\Delta m = 0)$	0	$\sqrt{1/3}$	$\sqrt{1/3}$	0

Table 4.1 shows the angular momentum coupling coefficients of $\sigma^{\pm}$ and π transitions for the D1 line pairs $6^2S_{1/2}\ F = \{3,4\} \rightarrow 6^2P_{1/2}\ F' = \{3,4\}$. Note that regardless of the handedness of the σ transition $(\sigma^{\pm})$ chosen, the transition pairs $F = \{3,4\} \rightarrow F' = 3$ and $F = \{3,4\} \rightarrow F' = 4$ have absolute strengths of ~ 0.35 and ~ 0.45, respectively. This symmetry does not hold for the D2 lines, however. It is also noteworthy that π-transitions are forbidden between states with same total angular momentum F. Therefore, CPT is not observable with any π transition configuration using states with $\Delta F = 0$. For D2 lines, transitions of each pair $F = \{3,4\} \rightarrow F' = \{3,4\}$ have a different angular momentum strength, as listed in the Table 4.2.

Table 4.2 Cs D2 line angular momentum coupling strengths (Clebsch-Gordan Coefficients) for $\sigma^{\pm}$ and π transitions between $6^2S_{1/2}(F; m_F = 0) \rightarrow 6^2P_{3/2}(F; m_{F'} = m_F + \Delta m)$ [9]

Transition type	$F = 3 \rightarrow F' = 3$	$F = 4 \rightarrow F' = 3$	$F = 3 \rightarrow F' = 4$	$F = 4 \rightarrow F' = 4$
$\sigma^+(\Delta m = +1)$	$\sqrt{3/16}$	$\sqrt{1/48}$	$\sqrt{25/336}$	$\sqrt{7/48}$
$\sigma^-(\Delta m = -1)$	$-\sqrt{3/16}$	$\sqrt{1/48}$	$\sqrt{25/336}$	$-\sqrt{7/48}$
$\pi\ (\Delta m = 0)$	0	$\sqrt{1/18}$	$-\sqrt{5/42}$	0

Table 4.3 Cs D1 line transition strengths for $6^2S_{1/2}(F) \rightarrow 6^2P_{1/2}\ (F')$ [9]

$F = 3 \rightarrow F' = 3$	$F = 4 \rightarrow F' = 3$	$F = 3 \rightarrow F' = 4$	$F = 4 \rightarrow F' = 4$
1/4	7/12	3/4	5/12

So far, one can conclude that the set of transitions $6^2S_{1/2}\ (F = \{3,4\}, m_F = 0) \rightarrow 6^2P_{1/2}(\ F' = 3, m_F = \pm 1)$ and $6^2S_{1/2}\ (F = \{3,4\}, m_F = 0) \rightarrow 6^2P_{1/2}(\ F' = 4, m_F = \pm 1)$ are equally suitable for CPT, in terms of the angular momentum coupling coefficients. The first pair of transitions, however, has an important advantage over the second with respect to transition strength. Table 4.3 lists the strengths of each transition $6^2S_{1/2}\ (F = \{3,4\}) \rightarrow 6^2P_{1/2}(\ F' = \{3,4\})$. At first glance, one can notice that both pairs are unbalanced by a factor of 3. The transition pair $F = \{3,4\} \rightarrow F' = 3$ is more efficient, since its average strength is 16% greater than the second pair. Therefore, the optimum transition pair for CPT is indeed $6^2S_{1/2}\ (F = \{3,4\}, m_F = 0) \rightarrow 6^2P_{1/2}(\ F' = 3, m_F = \pm 1)$.

The handedness of circularly polarised light plays an important role as it defines the transition type between σ^+ and σ^-. CPT with σ-transitions can be achieved with any polarisation of light, since any polarisation of light can be decomposed as between a combination of left-handed and right-handed polarisations.

Caesium atoms couple to external magnetic fields through the angular momentum operator and the coupling mechanisms have different descriptions, depending on the magnetic field strength [9]. For simplicity, and the case of this study, let us consider the field being homogeneous and parallel to the quantisation axis. For weak fields, the total angular momentum (electronic orbital and spin and nuclear spin) conserved and the atomic levels splits as a linear function of the magnetic field strength [9],

$$\Delta E^{Zeeman} \equiv \mu_B g_F m_F B_z, \qquad \text{Eq. 4.1}$$

where μ_B is the Bohr magneton, g_F is a coupling coefficient and B_z is the magnetic field strength. The total angular momentum g-factor, g_F, can be approximated as follows [9],

$$g_F \approx g_J \frac{F(F+1) - I(I+1) + J(J+1)}{2F(F+1)}, \qquad \text{Eq. 4.2}$$

and,

$$g_J \approx 1 + \frac{J(J+1) - L(L+1) + S(S+1)}{2J(J+1)}, \qquad \text{Eq. 4.3}$$

where $\hat{F} = \hat{J} + \hat{I}$ is the total angular momentum operator and $\hat{J} = \hat{L} + \hat{S}$ is the total electronic angular momentum operator and $\hat{I}$, $\hat{L}$ and $\hat{S}$ are the nuclear spin, orbital and spin operators, respectively. For Cs, the nuclear spin is $7/2$ [9]. Eq. 4.3 is an approximated expressions obtained by considering that the electron spin and electron orbital g-factors were approximately 2 and 1, respectively [9]. Eq. 4.2, in turn, is obtained by inferring that $g_j \gg g_I$ [9]. This assumption is valid at weak magnetic field regime ($B \ll 100\, mT$), where F and m_F are *good* quantum numbers. For strong magnetic fields, the orbit and spin operators decouple and the energy level shift is still a linear function of the magnetic field, however in this case described by the contributions of each angular momentum operator. This is the so-called the hyperfine Pashen-Back regime and it is described by the following equation [9],

$$\Delta E^{PB} \approx \mu_B B_z \left(g_J m_J + g_I m_I\right), \qquad \text{Eq. 4.4}$$

where m_J and m_I are the z-projection of the J and I operators and g_I the g-factor is related to the nuclear spin and is obtained experimentally, $g_I \sim 3.9 \times 10^{-4}$. This regime is only observable at magnetic fields $B \gg 100\ mT$ [9].

The problem of intermediate magnetic fields, however, has no general solution except in the case for $(2F+1)$ ground states of the D transition. The Breit-Rabi formula models the energy gap variation as a function of the external magnetic field. For the $6^2S_{1/2}(F=3\,, m_F=0) \rightarrow 6^2S_{1/2}(F=4\,, m_F=0)$ transition, the Breit-Rabi formula is [9],

$$\Delta\omega_{rf} \approx \left(\frac{{g_J}^2 \mu_B^2}{2\hbar \Delta E_{hfs}}\right) B_z^2, \qquad \text{Eq. 4.5}$$

where and $g_J\left(6^2S_{1/2}\right) \sim 2$ and $\Delta E_{hfs} = (I+1/2)h \cdot 2.2981579425\ GHz$ is the ground-state hyperfine splitting of Cs D lines with $I = 7/2$ [9]. Eq. 4.5 is very important as it estimates the frequency uncertainty caused by magnetic field instability in magnetic 'insensitive' transitions $(m_F = 0 \rightarrow m_F = 0)$.

4.2 Coherent Population Trapping in Alkali Thermal Vapours

Coherent population trapping (CPT) is a quantum interference phenomenon that occurs when two transitions with a common excited state are pumped simultaneously in a so-called lambda-configuration (see Figure 2.1) [4]. It manifests itself in alkali vapours as a reduced fluorescence within an optically pumped atomic ensemble. It was first reported in 1976 by Alzetta et al in Sodium vapour [1]. The minimised fluorescence translates into induced transparency (dark resonance) in the transmitted optical signal and it takes place if, and only if, the frequency difference of the two photons is equal to that associated to the ground-state splitting energy. The frequency matching condition therefore guarantees access to optical dipole-forbidden transitions without the use of RF cavities and establishes CPT as an alternative quantum effect for clock and microwave frequency reference applications [2], [11]. Moreover, because of the nature of the effect, the dark resonances can have line width of the order of tens of Hz in alkali vapours [6].

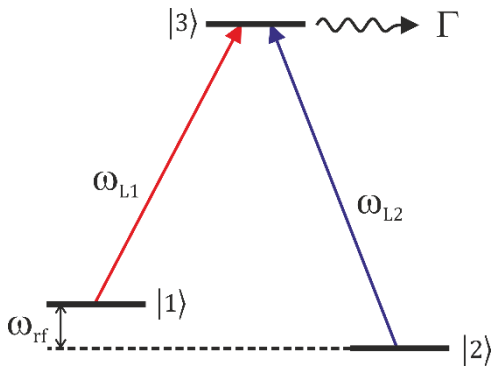

Figure 4.4: Lambda configuration for CPT. Transitions $|1\rangle \rightarrow |3\rangle$ and $|2\rangle \rightarrow |3\rangle$ are optical dipole allowed and $|1\rangle \rightarrow |2\rangle$ is forbidden. A transparency peak in the transmitted optical signal manifests when $\omega_{L2} - \omega_{L1} = \omega_{rf}$. Atoms at excited state $|3\rangle$ relaxes at rate Γ.

Generally, the dark resonance is impacted by three main effects: 1) optical power broadening; 2) Doppler effect and; 3) Atomic collisions [4]. Optical power broadening is present in CPT as a direct result of the presence of coherences (related to the transitions $|1\rangle \rightarrow |3\rangle$ and $|2\rangle \rightarrow |3\rangle$, depicted in Figure 2.1) with a power dependency through the Rabi frequency Ω_{ij},

$$\Omega_{ij} \equiv \frac{1}{\hbar} E_\lambda(\boldsymbol{x}) \langle i | \hat{\boldsymbol{d}} \cdot \hat{\boldsymbol{e}}_\lambda | j \rangle, \qquad \text{Eq. 4.6}$$

where the $\hat{\boldsymbol{d}} \equiv q\hat{\boldsymbol{r}}$ is dipole operator, with q being the elementary charge and $\hat{\boldsymbol{r}}$ the position operator. $E_\lambda(\boldsymbol{x})$ and $\hat{\boldsymbol{e}}_\lambda$are the electric field distribution and polarisation vector associated to the resonant photon. Temperature plays an important role as it is a measurement of the motion of the vapour constituents, which are subject to inhomogeneous and homogeneous broadening processes such as Doppler effect, collisions and mean time of flight. The latter is closely related to the optical beam size. Methods to control and minimise the impact of the aforementioned effects on the dark resonance are detailed in this chapter.

In the following, I introduce a simplified three-level model that qualitatively explains the CPT mechanism and how it manifests itself in the atomic level structure.

4.2.1 Simplified Three-Level Model

Let us consider the three-level system as described in Figure 2.1 and we follow the description found in reference [12]. Let us also assume that the $|1\rangle \rightarrow |3\rangle$ and $|2\rangle \rightarrow |3\rangle$ transitions are optical dipole allowed and $|2\rangle \rightarrow |1\rangle$ is forbidden. Two monochromatic and coherent electromagnetic fields (EMFs) with frequency ω_{L1} and ω_{L2} are dipole coupled to the transitions $|1\rangle \rightarrow |3\rangle$ and $|2\rangle \rightarrow |3\rangle$, respectively, with an associated Rabi frequency as described by Eq. 4.7. The Hamiltonian of the system can be described – in the semi-classical approximation – as follows,

$$\hat{H} = \hat{H}_0 + \hat{H}_D + \hat{\mathcal{L}}, \qquad \text{Eq. 4.7}$$

where $\hat{H}_0 = \sum E_i |i\rangle \langle i|$ is the unperturbed Hamiltonian with E_i being the associated energy of each level. $\hat{H}_D = -\hbar\Omega_{13}|1\rangle\langle 3| - \hbar\Omega_{23}|2\rangle\langle 3| + c.c.$ is the dipole interaction term and $\hat{\mathcal{L}} = -i\hbar\Gamma|3\rangle\langle 3|$ is the upper state relaxation operator. Under the time dependent perturbation and rotating wave approximations, the time-dependent solution, $|\psi\rangle(t) = \sum a_i(t)|i\rangle$, has the following form, in the Schrödinger picture,

$$|\psi\rangle(t) = \left(\frac{\Omega_{13}}{\Omega}\right)|D\rangle + \left(\frac{\Omega_{23}}{\Omega}\right)|B\rangle\, e^{-(\Omega^2/\Gamma)t}, \qquad \text{Eq. 4.8}$$

with $\Omega \equiv \sqrt{\Omega_{13}^2 + \Omega_{23}^2}$ is the normalised two-photon Rabi frequency. The states $|D\rangle$ and $|B\rangle$ are the eigenstates of $\hat{H}$ and are labelled as dressed states as they are combinations of the two ground states $|1\rangle$ and $|2\rangle$, solutions of $\hat{H}_0$, and depend directly on the EMF intensity. Under this assumptions, they have the form,

$$\begin{cases} |D\rangle = \dfrac{1}{\Omega}(\Omega_{23}|1\rangle - \Omega_{13}|2\rangle) \\ |B\rangle = \dfrac{1}{\Omega}(\Omega_{13}|1\rangle + \Omega_{23}|2\rangle) \end{cases}. \qquad \text{Eq. 4.9}$$

While the two EMFs are mutually resonant to each transition, the atomic structure is slightly modified, where the transitions $|1\rangle \rightarrow |3\rangle$ and $|2\rangle \rightarrow |3\rangle$ are no longer accessible. Instead, the two ground states become superposed and form a different basis $\{|D\rangle;|B\rangle\}$. Eq. 4.8 says that, if the system evolves through a time frame $\tau \gg \Gamma/\Omega^2$, the resultant state tends asymptotically towards $|\psi\rangle(t \rightarrow \tau) \sim (\Omega_{12}/\Omega)|D\rangle$, of which, in theory, is non-radiative. **In this regime, the atomic population would be trapped at a non-resonant (dark state – $|D\rangle$), causing the transitions $|1\rangle \rightarrow |3\rangle$ and $|2\rangle \rightarrow |3\rangle$ to become transparent, as no optical driven promotion nor recombination of electrons is allowed between the states in the lambda-configuration. Mostly important, the frequency matching condition allows us to have access to frequency ω_{rf} related to the energy gap between $|1\rangle$ and $|2\rangle$.**

Eberly also pointed out that if the EMFs are incoherent relative to one another, the state evolution would merely be a linear combination of the two ground states $|1\rangle$ and $|2\rangle$, and therefore the CPT process will no longer take place [12]. This represents the first distinction between CPT and electromagnetically induced transparency (EIT) to be pointed out in this chapter. Both effects have similarities, as both produce an induced transparency. However, the theoretical assumptions and

experimental setups are different. Perhaps the main difference between these effects is that EIT does not require that the two transitions are pumped with coherent EMFs. Also in EIT, the transitions are pumped at different rates (unbalanced lambda configuration), where one transition is strongly driven while the other is weakly driven by their associated EMFs.

The qualitative analysis presented in this section helps one to depict the underlying mechanism and physical phenomenon that takes place in the CPT process. It fails, however, to give a clear indication of the signal shape and physical and geometrical parameters that can influence the dark resonance properties. Also, it does not cover the effects of interacting particles nor magnetic field splitting neither motion of the atoms participating to the effect. In the next section, I discuss a more comprehensive model that can provide a broader understanding of the effect and its limitations.

4.2.2 Density Matrix Approach and Three-Level Model

In the last section, I discussed the qualitative aspects of the CPT phenomenon at the single particle level. In order to fully appreciate the CPT effect in its many aspects, we need to analyse the optical response of an ensemble of atomic vapour in the presence of a pair of resonant, or quasi-resonant, EMF, relative to the transitions participating to the lambda-configuration. Figure 4.5 shows the three-level configuration used to model CPT. In this case, we consider the decay rates from the excited state $|m\rangle$ to each ground state $|\mu\rangle$ and $|\mu'\rangle$ to be Γ_1 and Γ_2, respectively. Relaxation of the ground states are also considered, at a rate of γ between states $|\mu\rangle$ and $|\mu'\rangle$. The relaxation rate models the homogeneous broadening processes such as collisions and other dephasing effects that can take place in the ensemble.

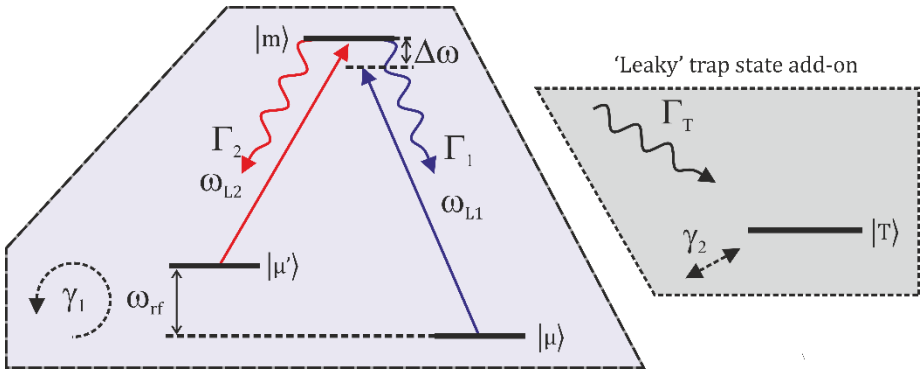

Figure 4.5: Lambda configuration for CPT model. Transitions $|\mu\rangle \rightarrow |m\rangle$ and $|\mu'\rangle \rightarrow |m\rangle$ are optical dipole allowed and $|\mu\rangle \rightarrow |\mu'\rangle$ is forbidden. Γ_1 and Γ_2 are the spontaneous decay rates of $|m\rangle \rightarrow |\mu\rangle$ and $|m\rangle \rightarrow |\mu'\rangle$ transitions and the ground state population relaxes at rate γ_1. A leaky trap state can be considered with Γ_T spontaneous decay from $|m\rangle$ to $|T\rangle$ and ground state relaxation γ_2. ω_{L1} and ω_{L2} are the quasi resonant laser frequencies and ω_{rf} is the ground state to ground state transition frequency.

A fourth state, $|T\rangle$, can be considered and plays the role of a 'trap' state, with a decay rate from $|m\rangle$ of Γ_T. This extra state is important if modelling CPT when the conservation of angular momentum leads to optical pumping to a non-interacting state (case of circularly polarised EMFs). Including the trap state into the analysis, however, increases the complexity of the model that can only be solved numerically [4], [13].

The three-level model discussed in this section was firstly introduced by Vanier et al. and subsequently used widely by many research groups [3], [14], [15]. The problem described in Figure 4.5 can be solved using a density matrix approach [16], as described by Vanier et al [4]. We assume the population of the states to be $\rho_{\mu\mu}$, $\rho_{\mu'\mu'}$, ρ_{mm} and ρ_{TT}, and the associated coherences $\rho_{\mu\mu'}$, $\rho_{\mu m}$ and $\rho_{\mu' m}$. The Liouville's equation for the interaction is given by,

$$\partial_t \hat{\rho} = -\frac{i}{\hbar}\left[\hat{H}_I, \hat{\rho}\right] - \hat{\mathcal{L}}\hat{\rho}, \qquad \text{Eq. 4.10}$$

where $\hat{H}_I$ is the interaction Hamiltonian and $\hat{\mathcal{L}}$ models the decay rates and relaxation phenomena. The coherences elements are assumed to have solutions of the form[4],

$$\rho_{\mu\mu'}(z,t) = \delta_{\mu\mu'}(z,t)e^{i(\omega_{L1}-\omega_{L2})t}, \qquad \text{Eq. 4.11}$$

$$\rho_{\mu m}(z,t) = \delta_{\mu m}(z,t)e^{i\omega_{L1}t}, \qquad \text{Eq. 4.12}$$

$$\rho_{\mu' m}(z,t) = \delta_{\mu' m}(z,t)e^{i\omega_{L2}t}, \qquad \text{Eq. 4.13}$$

with ω_{L1} and ω_{L2} being the angular frequencies of the EMFs. Note also that $\Delta\omega = \omega_{L1} - \omega_{L2} - \omega_{rf}$. Eq. 4.10 can be expanded in its various terms and it has the form, if replacing the suitable terms with those from Eq. 4.11, Eq. 4.12 and Eq. 4.13 [4] ,

$$\partial_t \rho_{mm} = -\Omega_{\mu m} Im\left(\delta_{\mu m}\right) - \Omega_{\mu' m} Im\left(\delta_{\mu' m}\right) - (\Gamma_1 + \Gamma_2)\rho_{mm}, \qquad \text{Eq. 4.14}$$

$$\partial_t \rho_{\mu'\mu'} = \Omega_{\mu' m} Im\left(\delta_{\mu' m}\right) + \Gamma_2 \rho_{mm} - \left(\frac{\gamma}{2}\right)\left(\rho_{\mu'\mu'} - \rho_{\mu\mu}\right), \qquad \text{Eq. 4.15}$$

$$\partial_t \rho_{\mu\mu} = \Omega_{\mu m} Im(\delta_{\mu m}) + \Gamma_1 \rho_{mm} - \left(\frac{\gamma}{2}\right)(\rho_{\mu\mu} - \rho_{\mu'\mu'}), \quad \text{Eq. 4.16}$$

$$\partial_t \delta_{\mu m} + \left[\Gamma_1 + i(\omega_{L1} - \omega_{m\mu})\right]\delta_{\mu m} = i\left(\frac{\Omega_{\mu m}}{2}\right)(\rho_{mm} - \rho_{\mu\mu}) - i\left(\frac{\Omega_{\mu' m}}{2}\right)\delta_{\mu\mu'}, \quad \text{Eq. 4.17}$$

$$\partial_t \delta_{\mu' m} + \left[\Gamma_2 + i(\omega_{L2} - \omega_{m\mu'})\right]\delta_{\mu' m} = i\left(\frac{\Omega_{\mu' m}}{2}\right)(\rho_{mm} - \rho_{\mu'\mu'}) - i\left(\frac{\Omega_{\mu' m}}{2}\right)\delta_{\mu'\mu}, \quad \text{Eq. 4.18}$$

$$\partial_t \delta_{\mu\mu'} + \left[\frac{\gamma}{2} + i(\omega_{L1} - \omega_{L2} - \omega_{\mu\mu'})\right]\delta_{\mu\mu'} = i\left(\frac{\Omega_{\mu m}}{2}\right)\delta_{m\mu'} - i\left(\frac{\Omega_{\mu' m}}{2}\right)\delta_{\mu m,} \quad \text{Eq. 4.19}$$

$$Tr(\hat{\rho}) = 1, \quad \text{Eq. 4.20}$$

Here I have defined the transition frequencies as ω_{ij}, with $i,j = \{\mu, \mu', m\}$, and note that $\omega_{rf} = \omega_{\mu\mu'}$. Eq. 4.14 to Eq. 4.20 describes the CPT effect considering the homogeneous broadening mechanisms. In the next section I will discuss the main broadening mechanisms that takes place in CPT and its implications. The set of equations just presented does not have an analytical solution for any given time t, however they can be simplified and an analytical expression can be derived from it [4]. The simplifications are:

- Solutions are considered only in the steady-state, where $\partial_t \hat{\rho} \to 0$
- Lasers frequencies are resonant with the transitions.
- The two EMFs and the two transition strengths lead to equal Rabi frequency: $\Omega_{\mu m} = \Omega_{\mu' m} = \Omega$.
- The decay rates from $|m\rangle$ to $\{|\mu\rangle, |\mu'\rangle\}$ are the same: $\Gamma_1 = \Gamma_2 = \Gamma/2$.
- The populations in the ground states are much larger than in the excited state and tend to equilibrium: $\rho_{\mu\mu}(eq.) = \rho_{\mu'\mu'}(eq.) = 1/2$.

After some algebra, the population ρ_{mm} at the excited state $|m\rangle$ can be expressed as a function of the ground-to-ground state coherence $\delta_{\mu\mu'}$, as follows,

$$\rho_{mm} = \frac{\Omega^2}{\Gamma^2}\left[1 + 2Re(\delta_{\mu\mu'})\right]. \quad \text{Eq. 4.21}$$

The coherence $\delta_{\mu\mu'}$ has a closed expression of decay and relaxation rates and Rabi frequency, as follows:

$$Re(\delta_{\mu\mu'}) = -\left(\frac{\Omega^2}{2\Gamma}\right)\left(\frac{1}{\frac{\gamma}{2}+\frac{\Omega^2}{\Gamma}}\right)\left\{1+\left[\Delta\omega/\left(\frac{\gamma}{2}+\frac{\Omega^2}{\Gamma}\right)\right]^2\right\}^{-1}. \qquad \text{Eq. 4.22}$$

From Eq. 4.22, one can readily identify that $Re(\delta_{\mu\mu'})$ is a Cauchy-like (Lorentzian) spectral distribution. Together with Eq. 4.23, one can define the fluorescence and power absorbed through the CPT mechanism. The fluorescence power emitted, P_{fl}, can be estimated as [4],

$$P_{fl} = \hbar\bar{\omega}\Gamma N\rho_{mm}, \qquad \text{Eq. 4.23}$$

where N is the number of interacting atoms, $\overline{\omega}$ is the average photon frequency of the transitions $|\mu\rangle \rightarrow |m\rangle$ and $|\mu'\rangle \rightarrow |m\rangle$ and $\hbar$ is the normalised Planck constant. The power absorbed in a length L is [4],

$$\Delta P_{abs} = \int_0^L \hbar\bar{\omega}(\Gamma+\gamma)n(z)\rho_{mm}dz, \qquad \text{Eq. 4.24}$$

with $n(z)$ being the linear atomic density. Therefore, the total power detected after the ensemble is,

$$P(z) = P_0 - \Delta P_{abs} \sim P_0 - \hbar\bar{\omega}(\Gamma+\gamma)\bar{n}L(1-\Im), \qquad \text{Eq. 4.25}$$

where $\bar{n}$ is the average atomic density over the length L. The term $\Im$ was introduced for compactness. It carries the information on the resonance strength and shape and has the form,

$$\Im = \left(\frac{\Gamma}{4}\right)\left(\frac{I}{I_{sat}}\right)\left[\frac{\gamma}{2}+\left(\frac{\Gamma}{2}\right)\left(\frac{I}{I_{sat}}\right)\right]^{-1}\left\{1+\left\{\frac{\Delta}{\left[\frac{\gamma}{2}+\left(\frac{\Gamma}{2}\right)\left(\frac{I}{I_{sat}}\right)\right]}\right\}^2\right\}^{-1}. \qquad \text{Eq. 4.26}$$

Here, I replaced the term $2(\Omega/\Gamma)^2$ with the term (I/I_{sat}), where I is the EMF intensity and I_{sat} the associated saturation intensity of the transition in use [9]. From Eq. 4.26, I can readily infer that, for a homogeneously distributed ensemble, in absence of inhomogeneous broadening mechanism, the line-width (full-width at half-maximum – FWHM) of the dark resonance varies linearly with the laser intensity, as well as decay and relaxation rates and has the form,

$$FWHM_{CPT} = \frac{1}{\pi}\left(\frac{\gamma}{2} + \left(\frac{\Gamma}{2}\right)\left(\frac{I}{I_{sat}}\right)\right)\ [Hz]. \qquad \text{Eq. 4.27}$$

The line-width of the dark-resonance is therefore dictated by the relaxation rate γ_1 and linearly varies linearly with the EMF intensity applied. In summary, the line-width can be tailored by controlling the relaxation rates, i.e. decreasing dephasing phenomena such as transit-time and rate of collisions.

The dark-resonance amplitude, for weak EMFs, has the form,

$$Amplitude = \hbar\bar{\omega}(\Gamma + \gamma)\bar{n}L\left(\frac{\left(\frac{\Gamma}{4}\right)\left(\frac{I}{I_{sat}}\right)}{\frac{\gamma}{2} + \left(\frac{\Gamma}{2}\right)\left(\frac{I}{I_{sat}}\right)}\right), \qquad \text{Eq. 4.28}$$

Eq. 4.25 to Eq. 4.28 are the key results sought in this section. They are useful in understanding the CPT process and the impact that parameters such as decay rates, transition strength and relaxation rates have on the dark resonance shape and amplitude. This model does not predict the effects of having unbalanced transitions (EMFs with different power), neither the thermodynamic implications of the atomic vapour over the dark resonance shape and its behaviour. It also does not predict the behaviour of CPT amplitude at high EMF power regime. This can be done by adding a 'leaky' trap into the model, as shown in Figure 4.5. A discussion on this model can be found here [4], [17] and in the following sections and chapters.

In the following sections, I discuss the impact of unbalanced optical transitions and the main resonance broadening mechanisms that take place with CPT in alkali vapour.

4.2.3 Resonance Broadening Mechanisms

There are two categories of broadening mechanisms that can take place in the atomic ensemble: homogeneous and inhomogeneous. I discuss each category in the following.

I. Homogeneous Broadening Mechanism

In the previous section, I have described the CPT model considering damping relaxation rates and spontaneous decay. Both elements fall within the homogeneous broadening effect as they happen for each and every participating atom. The list of effects below is a selection of the most important damping mechanisms that take place in micrometric size vapour cells. The list, therefore, is non-exhaustive.

- **Natural Line-width** is connected to the Heisenberg uncertainty principle and limits the minimum achievable linewidth to the fundamental uncertainty in the energy levels [16]. It has the form,

$$\Delta \mathrm{E} \sim \frac{\hbar}{2\tau_{nat}}, \qquad \text{Eq. 4.29}$$

- **Spontaneous decay**, Γ, is directly related to the physical properties of the optical transition and EMF's polarisation. The transition coupling coefficient and conservation of angular momentum also play important roles in the population recombination rates and strength [4].
- **Transit-time broadening** is related to the time-of-flight of atoms within the EMF [18] and it dictates the interaction time for the effect to take place. If we consider an EMF beam with a width of w_0, the time-of-flight τ_{tt} that atoms can interact with the EMF can be estimated as **[4],**

$$\tau_{tt} \propto \frac{w_0}{v_{th}}. \qquad \text{Eq. 4.30}$$

where v_{th} is the vapour thermal velocity.

- **Spin-exchange broadening** is connected with the dephasing mechanism that takes place when polarised atoms collide with each other or with the vapour cell's walls and they are, in principle, different mechanisms. Atom-atom collisions causes spin exchange, as a result of the conservation of angular momentum. It relaxes with time constants (population and coherence) [4], [18],

$$\tau_x^{(1)} = \frac{1}{n\bar{v_r}\sigma_x}, \qquad \tau_x^{(2)} \sim \left(\frac{8I+4}{6I+1}\right)\tau_x^{(1)}, \qquad \text{Eq. 4.31}$$

where n is the volumetric atomic density, $\bar{v_r}$ is the average relative speed, σ_x is the spin-exchange cross-section and I is nuclear spin of the atom. The calculated spin-exchange cross-section, for Cs, is $2.82 \times 10^{-14} cm^2$, at $300\ K$, and $2.77 \times 10^{-14} cm^2$, at $407\ K$ [4].

- **Relaxation on the container walls** can happen as a result of numerous processes. Atoms upon contact to the container walls can bounce or bind to [4], [18]. As a result of electric charge found at the wall, atoms can be *confined* at its vicinity in a Van-der-Waals type of potential [4]. The dwell time of the atoms interacting with the walls is,

$$\tau_{dwell} \sim \tau_0 e^{\frac{E_a}{k_B T}}, \qquad \text{Eq. 4.32}$$

where τ_0 is related to the vibrational period of the atoms at the wall's surface and E_a is the bond energy [18]. During the time the atoms are found trapped at the vicinity of the walls, they are prone to random perturbations (thermal agitation) that leads to depolarisation. Generally, E_a is of the order of $0.1\ eV$ and $\tau_0 \sim 10^{-12}\ s$ [18]. The total time, τ_{wall}, spent by atoms between consecutive depolarisations is,

$$\tau_{walls} \sim \tau_{dwell} + \eta \tau_{free}, \qquad \text{Eq. 4.33}$$

where $\tau_{free} \sim 4V/v_{th}S + \tau_0$ is the time between consecutive elastic collisions with the walls, with V and S being the internal volume and surface of the container, respectively, and η is the number of elastic collision an atom does before binding to the walls.

The effects described in this section will be revisited throughout this thesis when necessary and modifications to the models introduced when required.

II. Inhomogeneous Broadening Mechanism

This class of broadening mechanism covers effects that take into account the properties of each atom participating to the effect. **Doppler broadening** belongs to this class as it depends on the speed of each atom of the ensemble taking part to the effect.

Let us consider that the atom's centre of mass follows classical trajectories, the vapour dynamics leads to a Doppler shift as atoms can travel on different paths at different speeds. The Doppler shift only considers trajectories parallel to the EMF. The shift, in the first order, is

$$\omega' = \left(1 + \frac{v_{\parallel}}{c}\right)\omega, \qquad \text{Eq. 4.34}$$

where $v_{\parallel}$ is the velocity component parallel to the EMF trajectory towards the observer (detector), c is the speed of light, ω' is the observed frequency and ω is the absolute frequency. The atoms' centre of mass dynamics can be classically modelled by the one dimensional Maxwell-Boltzmann distribution of velocity [4]. The velocity distribution regarded to component parallel to the traveling EMF has the form,

$$g(v_{\parallel})dv_{\parallel} = \sqrt{\frac{m}{2\pi k_B T}} e^{-\frac{mv_{\parallel}^2}{2k_B T}} dv_{\parallel}, \qquad \text{Eq. 4.35}$$

where k_B is the Boltzmann constant, m is the atomic mass and T is the temperature. Under the transformation of variable $v_{\parallel} = (\omega' - \omega)(c/\omega)$, Eq. 4.35 can be modified and a spectral distribution, $g'(\omega' - \omega)$, around the absolute frequency arises as a direct result of the vapour dynamics and can be understood as a broadening effect. This transformation is useful to define the line broadening caused exclusively by the motion of the atoms. The line-width (FHWM) of the distribution $g'(\omega' - \omega)$ is,

$$FWHM_{Doppler} = \frac{\omega_0}{2\pi}\sqrt{\frac{8\ln(2)\, k_b T}{mc^2}}. \qquad \text{Eq. 4.36}$$

The Maxwell-Boltzmann distribution also provides us with information of the thermal velocity of the atoms. The thermal velocity is defined as the mean-value of the obtained from the three dimensional Maxwell-Boltzmann distribution and has the form [4],

$$v_{th} = \sqrt{\frac{8k_b T}{\pi m}}. \qquad \text{Eq. 4.37}$$

The thermal velocity is fundamental to estimate the time-of-flight of the atoms and their associated transit-time broadening. This effect was covered in the homogeneous broadening mechanism.

The contribution of a given inhomogeneous broadening mechanism, $H(\omega' - \omega)$, to an existing atomic feature, $IH(\omega')$ is computed via the convolution integral described in the following the equation,

$$\mathcal{F}(\omega) = \int_0^{\infty} H(\omega' - \omega)\, IH(\omega') d\omega'. \qquad \text{Eq. 4.38}$$

This process can be repeated if a second inhomogeneous mechanism takes place. Eq. 4.38 can have a complex form and lead to non-integrable functions. The Voigt profile, for example, is a convolution between the Cauchy and Gaussian distributions and, as a result of the complex form of the Gaussian function, it does not have a closed form expression. Transition lines, when considering only homogeneous broadening processes, is modelled by the Cauchy distribution [4], [9].

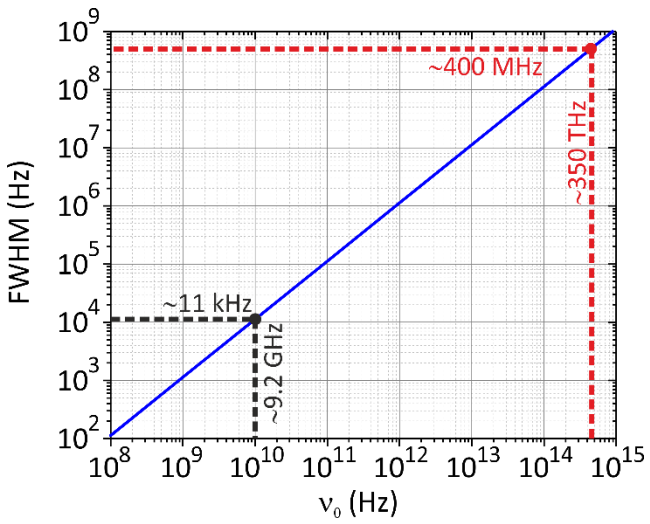

Figure 4.6: Example of residual Doppler FWHM as a function of the transition frequency for Cs vapour at $330\ K$ (Eq. 4.36). It shows expected line-width of $\sim 11\ kHz$ for $\nu_{rf} \sim 9.2\ GHz$ (D Line microwave ground state splitting) and $\sim 400\ MHz$, for $\nu_0 \sim 350\ THz$ (D1 lines).

Eq. 4.38 indicates that if the $FWHM_{IH} \gg FWHM_H$, then $H(\omega' - \omega) \to \delta(\omega')$, where $\delta(\omega')$ is the Dirac delta distribution and, thereby, $\int_0^\infty \delta(\omega' - \omega)\, IH(\omega') d\omega' = IH(\omega)$. Therefore, if $FWHM_{Doppler} \gg FWHM_{CPT}$, then the line-width presented in the spectral distribution $\mathcal{F}(\omega)$ tends asymptotically to $FWHM_{Doppler}$, also called as the residual Doppler broadening. Figure 4.6 shows the expected $FWHM_{Doppler}$ (Eq. 4.36) as a function of the transition frequency $\nu_0 \equiv \omega_0/2\pi$ for Cs vapours at $330\ K$. It indicates that the residual Doppler width limits the minimum line-width to $FWHM_{\mathcal{F}} \sim 11\ kHz$, which can be regarded as a fundamental line-width, for CPT performed in a pure Cs vapour containers.

4.2.4 Line-Width Control and their Implications

Up to this point, I have discussed the CPT process, the underlying physical effects and have given a number of theoretical expressions that are useful to understand the role of relaxation and decay rates as well as the effect of the motion of the atom in the vapour phase. The theoretical predictions of $FHWM$ of $\sim 11\ kHz$ for a pure-Cs reference cell put CPT as an ideal candidate for high resolution spectroscopy compared to other methods such as saturation spectroscopy and EIT. However, other potential applications, such as metrology, require ultra-narrow transition lines. Frequency and atomic time references rely on ultra-stable and ultra-narrow atomic transitions as they effectively improve locking efficiency and, thus, the overall device stability [2]. Many groups have investigated methods to narrow CPT resonance beyond the residual Doppler broadening and to control relaxation parameters such as atom-wall collisions. The next two sections, therefore, are devoted

to two main methods to control homogeneous broadening caused by atom-walls collisions, time of flight and inhomogeneous broadening caused by residual Doppler broadening.

4.2.4.1 Anti-Relaxation Coatings

In section 4.2.3, I have briefly discussed the mechanism of relaxation on the container walls. The underlying physical phenomena involves the physical binding of alkali atoms to the Van-der-Waals like potential formed by charges distributed on the surface of the walls [18]. During the period the atoms are 'trapped', random fluctuations take place and the atom depolarise [4], [18].The total time, τ_{walls}, is modelled according Eq. 4.33 and recalled in the following,

$$\tau_{walls} \sim \tau_{dwell} + \eta\tau_{free}, \qquad \text{Eq. 4.33}$$

where τ_{dwell} and τ_{free} are the time the atoms spend trapped on the walls and between two elastic collisions, respectively. The parameter η is the number of elastic bounces between consecutive atomic depolarisations. By tailoring the charge distribution on the container wall, one can decrease the interaction with the alkali atoms, reducing the Van-der-Waals attraction force and in turn increasing the number of elastic bounces [19]. Such engineering step can be obtained by using, for instance polymeric carbohydrates. Ramsey proposed the use of long-chain polymeric compounds as coatings for Alkali vapour containers as an attempt to increase the atomic polarisation lifetime [20]. Bouchiat and Brossels reported that a Paraffin $[CH_3(CH_2)_nCH_3]$ coating can support $\eta \sim 10^4$ on a Rb vapour cell [21]. Balabas et al. demonstrated that alkenes $[C_nH_{2n+1}]$ coated Cs vapour cells can hold an atomic polarisation for up to $\eta \sim 10^6$ bounces [22]. Recently, Hafiz et al. reported a silane-coated Cs vapour cell that led to 37 elastic bounces [19]. Although it leads to a rather reduced number of bounces, silanes are very interesting compounds as they can withstand temperatures up to 170 ℃, while Paraflint and alkanes have lower operational temperature below 100 ℃ [19].

In CPT, Hafiz et al. reported dark resonance as narrow as $2\ kHz$ for OTS coated Cs alkali cell and its application as a time reference with a fractional stability of the order of 10^{-13} over a $1\ s$ integration time [19]. Figure 4.7 is a comparison between the dark resonance of the Cs D1-lines from a pure-Rb cell and a silane coated Cs Cell. Note also that the narrowed dark resonance obtained via an anti-relaxation coating sits on the top of a Doppler broadened pedestal.

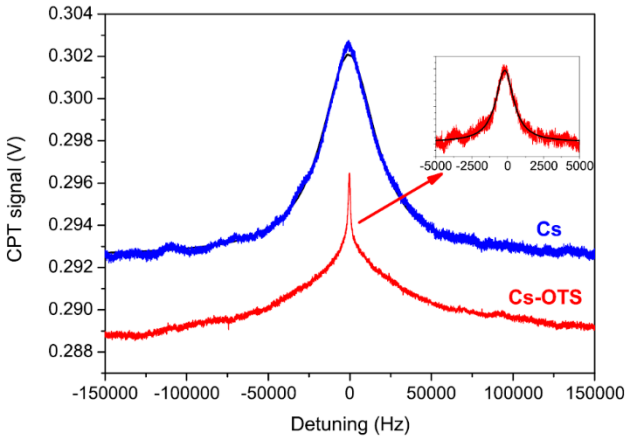

Figure 4.7: Comparison of CPT dark resonance obtained from a pure-Cs cell (blue trace) and silane coated Cs cell (red trace), showing a line-width reduction of about 25 times, from $\sim 38\ kHz$ (pure Cs) to $\sim 1.5\ kHz$ (coated cell). Both cells were at $303\ K$ and both spectroscopy measurements were taken for the same optical power of $100\ \mu W$. Extracted from [19]

Corsini et al. did a very comprehensive study on alkene-coated Rb cells obtaining a line-width as narrow as $\sim 110\ Hz$ [23]. They also measured the Van-der-Waals interaction related frequency shift of the hyperfine clock transition of the Rb D1 lines. The Van-der-Waals interaction distorts the electronic cloud of the atoms and thus shift the transitions. They reported a negative shift of $\sim 210\ Hz$ from the clock transition frequency [23].

Coatings have also been investigated for HC-PCF cell technology. The first demonstration of an HC-PCF with an inner coating was reported by Ghosh et al. for a Rb-filled HC-PBGF with hollow core diameter of $6\ \mu m$ and internally coated with Octadecyldimethylmethoxysilane $[(C_{25}H_{46}OSi)]$ and reported EIT with a peak width of $\sim 60\ MHz$ [24]. The polymer coating, together with light induced atomic desorption [25], were used to increase the vapour pressure within the hollow core [24]. Later, Light et al. showed EIT with a line-width as narrow as $\sim 6\ MHz$ in K-ARFs with a hollow core diameter of $11\ \mu m$, coated with polydimethylsiloxane $[(C_2H_6OSi)_n]$ and filled with Rb vapour [26]. Recently, Zheng et al. have reported an ultra-narrow line-width for EIT of $\sim 150\ kHz$ in a K-ARF coated with silane and filled with Rb vapour [27].

4.2.4.2 Buffer Gas

The addition of an inert gas, also referred to as a buffer gas, into a given alkali-loaded container modifies the atoms' motion and can be used to minimise the effect of two important relaxation parameters that dictate the minimum CPT line-width [4].

The choice of gases is based on two main conditions: i) the buffer gas specimen does not form stable molecules with Cs – i.e., the alkali atoms must not react chemically with the buffer gas ; ii) the interaction between the buffer gas specimen and Cs atoms must be weak [4]. Those two conditions

guarantee that the addition of buffer gas to the atomic ensemble does not alter strongly the energy structure level of Cs. Formation of stable molecules between buffer gas and Cs would change the atomic structure of Cs, shifting its transitions. Weak interaction between buffer gas and Cs atoms can be achieved by selecting atomic and molecular gases made of specimens with low polarizability (non-polar specimen). This guarantees that the weak interaction between the buffer gas and Cs atoms would lead to weak relaxation caused by spin-exchange interactions [4]. A variety of gases has been used for this purpose such as N_2, Ar, Ne, Kr and Xe.

The increased number of buffer gas particles in the system reduces the mean-free path of alkali atoms within the vapour cloud and, thus, increase the transit-time and atom-wall collision induced homogeneous broadening processes. Moreover, the constant change of direction caused by consecutive collisions decreases the residual Doppler broadening, as the atoms slow down with the interaction with buffer gas atoms. This effect is also known as Dicke narrowing [28]. Firstenberg et al. have published a theoretical description of the narrowing process considering the average path that atoms can take in the classical picture [28].

Buffer gases affect the CPT line-width through homogeneous and inhomogeneous broadening mechanisms. At lower applied pressure ranges, it can decrease the rate of diffusion and, thus, the Residual Doppler width, buffer gas broadens the dark resonance through inelastic collisions between gas molecules (atoms) and the alkali vapour [4], [18]. Moreover, as a direct result of the binding process that buffer gases and alkali atoms are subject to, it is expected to induce distortions in the atomic structure. This distortions affects the transition frequencies causing them to shift [4], [7], [29]. In this section, I will discuss both line-width and resonance shift caused by the addition of buffer gas in a container housing alkali vapour.

I. Line-width Control

In order to obtain a more insightful view on the impact of buffer gas on vapour dynamics and its contribution to inhomogeneous broadening mechanism, let us assume a buffer gas and alkali vapour in a container with a radius R and length L and solve the problem of alkali vapour diffusion in a medium composed of a buffer gas at high pressure. The atomic density, $n(r,z,t)$, evolution within the container can be modelled by the diffusion equation [4], [18],

$$\begin{cases} \partial_t n = -D\nabla^2 n, \\ n(R,z,t) = 0 \\ n(r,L,t) = 0 \\ n(r,z,0) = n_0 \end{cases}, \qquad \text{Eq. 4.39}$$

with D being the homogeneous diffusion coefficient and n_0 the atomic density at $t = 0$. The problem can be solved in cylindrical coordinates considering the Dirichlet boundary conditions

given also in Eq. 4.39. Under this assumptions, the local atomic density variation $\Delta n(r,z,t) = n(r,z,t) - n_0$, as a function of the time, has the following distribution,

$$\Delta n(r,z,t) = \sum_m \sum_l A_{l,m} e^{-\gamma_{BG}^I t} J_0\left(\frac{\alpha_m}{R} r\right) \sin\left[\frac{(2l-1)\pi}{L} z\right], \quad \text{Eq. 4.40}$$

where $J_0(x)$ is the Bessel function of the first kind and

$$\gamma_{BG}^I = D\left[\left(\frac{2.405}{R}\right)^2 + \left(\frac{\pi}{L}\right)^2\right], \quad \text{Eq. 4.41}$$

is the buffer gas relaxation rate, α_m is the m-th root of $J_0(\mathrm{r})$, $A_{l,m}$ is a normalisation constant and m and l are integers. Note that the density distribution has an exponentially decaying form. This decay rate will reflect an uncertainty in the atomic transition frequencies. The spectral distribution associated with the atomic density diffusing through the container can be obtained by calculating its Fourier transform. It leads to an association of Cauchy distribution and each element of this association is related to a diffusion mode. The spectral response is therefore,

$$\Delta n(r,z,\omega) \propto \sum_m \sum_l A_{l,m}^* \left(\frac{1}{\pi \gamma_{BG}^I}\right)\left[1 + \left(\frac{\omega - \omega_0}{\gamma_{BG}^I}\right)^2\right]^{-1}, \quad \text{Eq. 4.42}$$

where $A_{l,m}^*$ is a normalisation constant. Finally, if one replaces Eq. 4.26 and Eq. 4.42 in Eq. 4.38, considering only the first diffusion mode $(l,m) = (1,1)$ and taking into account that the convolution of two Cauchy distributions is also a Cauchy distribution, the dark resonance line-width with addition of buffer gas has the following form,

$$FWHM_{CPT} \approx \left[2\gamma_{BG}^I + \gamma_1 + \left(\frac{\Gamma}{2}\right)\left(\frac{I}{I_{sat}}\right)\right], \quad \text{Eq. 4.43}$$

Therefore, the CPT line-width, at the presence of buffer gas, can be approximated through a direct association of all broadening mechanisms. As a first approximation, one can approximate the diffusion coefficient varies inversely proportional to the buffer gas pressure. Under this condition [4],

$$D \to \frac{D_0 p_0}{p}, \quad \text{Eq. 4.44}$$

where p is the buffer gas pressure and D_0 is the diffusion coefficient at pressure p_0 (conventionally set at $760\ torr$).

The buffer gas contribution to the line-width broadening via homogeneous processes results directly from alkali atom and buffer gas molecule (atom) collisions. At each collision, the traveling alkali atom binds to a buffer gas specimen for a characteristic time. During the interaction, the electronic cloud is subject to distortions caused by attractive Van-der-Waals forces and repulsive forces. This interaction, at a first approximation, can be modelled using the Lennard Jones (12-6) potential [4]. Those distortions shift the atomic transitions, increasing the transition uncertainty thus the line-width [4], [18]. Spin-orbit interaction is also expected, however the associated shift is of second order compared to the transition distortions [4]. The relaxation time can be modelled according the following expressions [4],

$$\gamma_{BG}^{H} = \frac{p}{p_0} N_0 \bar{v_r} \sigma_2, \qquad \text{Eq. 4.45}$$

where N_0 is the Loschmidt constant and σ_2 is the associated coherence cross-section, which is determined experimentally [4], [18]. The population cross-section, σ_1, was suppressed here as it is normally one to two orders of magnitude smaller than the coherence cross-section [4].

Finally, one can define the total contribution of the buffer gas to the CPT line-width. It can be modelled considering both inhomogeneous and homogeneous broadening mechanism as follows,

$$\gamma_{BG}^{total} = \gamma_{BG}^{H} + \gamma_{BG}^{I} = \frac{D_0 p_0}{p}\left[\left(\frac{2.405}{R}\right)^2 + \left(\frac{\pi}{L}\right)^2\right] + \frac{p}{p_0} N_0 \bar{v_r} \sigma_2, \qquad \text{Eq. 4.46}$$

Note that Eq. 4.46 carries the information of the container (radius and length, for a cylindrical shaper), the buffer gas and alkali atom specifications and system pressure. Temperature is also a factor which is implicitly present in the diffusion coefficient and relative velocity. The effect of 'thin' and 'tight' containers is expressed in the first RHS term, where the geometry of the container becomes an important factor governing the atomic diffusion and, hence, dark resonance line-width. Eq. 4.46 also indicates the existence of a sweet-spot, as the first RHS term decreases with the pressure while the second term increases. The optimised pressure and minimum line-width are obtained by minimising Eq. 4.46 and the solutions have the following closed form expressions,

$$p_{opt} \sim \left(\frac{2.405}{R}\right)\sqrt{\frac{D_0}{N_0 \bar{v_r} \sigma_2}}\ p_0, \qquad \text{Eq. 4.47}$$

$$\min\left(\gamma_{BG}^{total}\right) \sim 2\left(\frac{2.405}{R}\right)\sqrt{D_0 N_0 \bar{v}_r \sigma_2}. \qquad \text{Eq. 4.48}$$

Note that the optimised pressure and minimum line-width scale with the inverse of the container radius. This dictates a potential limitation on the line-width in 'tight' containers, where radial confinement plays a very important role in the diffusion of the alkali vapour in a buffer gas-rich environment.

Figure 4.8 shows the FHWM (Eq. 4.46) as a function of the pressure for Cs-vapour in an N_2 rich medium at $330\ K$. Five values of radius were considered: $30\ \mu m$, $60\ \mu m$, $120\ \mu m$, $0.5\ mm$ and $1\ mm$ and all containers were $10\ cm$ long. In fact, the length was varied during the simulation and no change was observed. This was expected as $R^{-1} \gg L^{-1}$ for all cases considered. The diffusion coefficient was set to be $0.3\ cm^2/s$ and the coherent cross-section was considered to be $5 \times 10^{-23}\ cm^2$. Note that for lower pressure values ($p < 10^3\ torr$), the expected line-width for all the containers is dictated only by the atomic diffusion. As the curves approach their minimum, the collisional interaction takes over and this limits the line-width for higher pressure values.

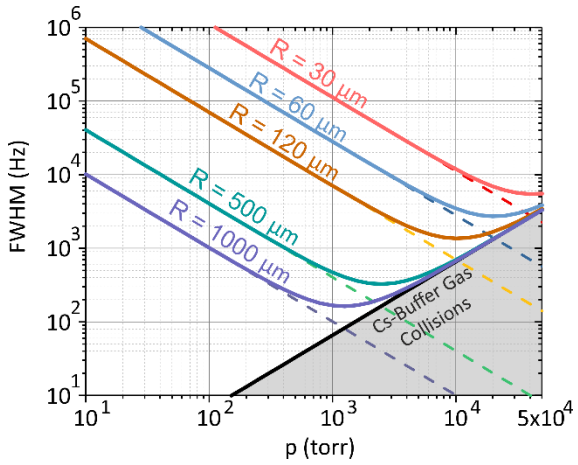

Figure 4.8: Simulated expected FWHM for Cs vapour in presence of N_2 for a set of $10\ cm$ long cylindrical containers with radius of $30\ \mu m$, $60\ \mu m$, $120\ \mu m$, $0.5mm$ and $1\ mm$. Temperature set to $330\ K$ and diffusion and coherence cross-section were set to be $0.3\ cm^2/s$ and $5 \times 10^{-23}\ cm^2$. Two main regimes are present: purely inhomogeneous and purely homogeneous broadening. At lower pressures inhomogeneous (diffusion related) broadening governs the effects, while homogeneous (alkali-buffer gas collisions) broadening takes over at higher pressure.

II. Frequency shift

Buffer gases also shift the central frequency of the dark resonances as a result of the distortions caused by the binding mechanism between the alkali atoms and the buffer gases molecules (atoms) [4].

The pressure shift is temperature dependent and it can be described by the empirical quadratic equation as follows [4], [29],

$$\Delta\nu(T) = p_{ref}\left[\beta + \delta\left(T - T_{ref}\right) + \varepsilon\left(T - T_{ref}\right)^2\right], \qquad \text{Eq. 4.49}$$

where p_{ref} and T_{ref} are the reference pressure and temperature. Coefficients β, δ and ε are empirical parameters to be determined experimentally [4], [29].

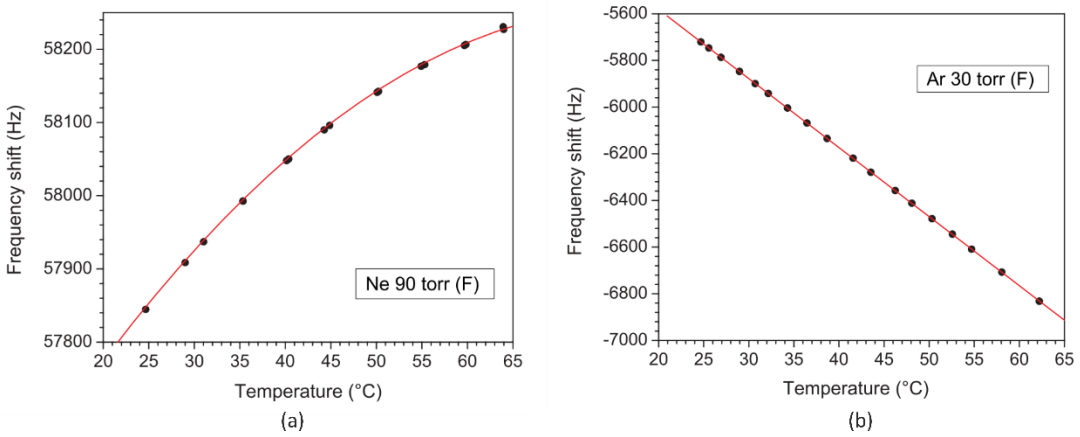

Figure 4.9: Central frequency shift as a function of the temperature for Cs vapour mixed with $90\ torr$ of Ne (a) and $30\ torr$ Ar (b). The containers is cylindrical, with radius of $\sim 20\ mm$ and at least $15\ mm$ long. Cs atoms and Ne interaction leads to a positive shift while, with Ar, it leads to a negative shift. Extracted and adapted from [29].

Two examples of Cs-loaded containers with a buffer gas are depicted in Figure 4.9 for, (a) $90\ torr$ of Ne and (b) $30\ torr$ of Ar. The frequency shift resulted from the Cs-buffer gas interaction is different for each species. Neon atoms interacts with Cs and modify the hyperfine ground state splitting towards high frequencies. Interaction with argon, on the other hand, yields a negative shift. This difference in gradients is regarded due to the nature of the interaction that takes place between the atoms. In the Lennard Jones (12,6) potential picture, large buffer gas atoms tend to have a stronger contribution from dipole forces, while smaller buffer gas atoms have stronger contribution from repulsive forces [4], [29]. This leads to a difference in sign in the observable frequency shift gradient [4]. This property of the buffer gas inducing pressure shifts with opposite sign is useful to minimise the temperature dependency of the resonance frequency. This factor is imperative in obtaining stable atomic reference cells that can operate in a wide range of temperatures. Kozlova et al. initially studied the operation of a Cs and Neon reference cell at the inversion temperature (maximum shift) [7]. At this point, the central frequency of the dark resonance is less sensitive to temperature variations, since the gradient shift is close to zero [7]. The same authors studied a mixture of the gases in order to tune the inversion point to a different

operation temperature for a mixture of N_2 and Ar [29]. This was obtained by summing up the frequency shift contribution for each gas, $\Delta\nu^{N_2}/p_{N_2}$ and $\Delta\nu^{Ar}/p_{Ar}$, and then minimising the pressure shift at the inversion point and solve it for $r = p_{Ar}/p_{N_2}$. The result is the following closed form expression for the partial pressure (p_{Ar} and p_{N_2}) as function of the pressure shift coefficients as well as T_{inv}, [29]

$$r = \frac{p_{Ar}}{p_{N_2}} = -\frac{\delta_{N_2} + 2\varepsilon_{N_2}\left(T_{inv} - T_{ref}\right)}{\delta_{Ar} + 2\varepsilon_{Ar}\left(T_{inv} - T_{ref}\right)}. \qquad \text{Eq. 4.50}$$

4.3 Coherent Population Trapping in Reference Vapour Cells

In this section, I describe CPT spectroscopy in pure Cs cells with a mixture of buffer gases. The main objective of this section is to clarify key experimental challenges and trends that are present in fibre cells.

I initially describe the experimental setup, covering its main features and specifications. I proceed to define the dark resonance spectroscopy characterisation parameters (line-width and contrast). Data analysis is then performed for pure Cs vapour cells and Cs vapours with a buffer gas mixtures considering different temperature and buffer gas pressures.

4.3.1 Experimental Setup and Characterisation Parameters

The experimental setup used for CPT dark resonance spectroscopy of Cs D lines is shown in Figure 4.10(a). The system is composed by a $894\ nm$ external cavity diode laser (ECDL) ($\sim 1\ mW$ output, and nominal line-width of $\sim 100 kHz$), an electro optical modulator (EOM) (Photline, model: NIR-MPX-LN-10) and an RF signal generator (Keysight E8257D) with a frequency range up to $20\ GHz$ and an RF power up to $25\ dBm$. The setup has two main optical arrangements, one for laser locking and a second for dark resonance spectroscopy. A beam splitter is used to send 50% of the signal to each optical arrangement.

The laser locking setup used is a typical Sub-Doppler pump-probe spectroscopy with two co-propagating beams (reference and control) and with a third counter-propagating beam (probe), co-aligned with the control beam [30]. This technique is useful to obtain Doppler-free transition, as shown in Figure 4.10(b). The three beams travel through a paraffin coated Cs reference cell and the signals are detected by a balanced photodetector (Thorlabs, model: PDB210A). The DL pro controller receives the signal and an error function is generated by the built-in locking module, as described in Figure 4.10(a).

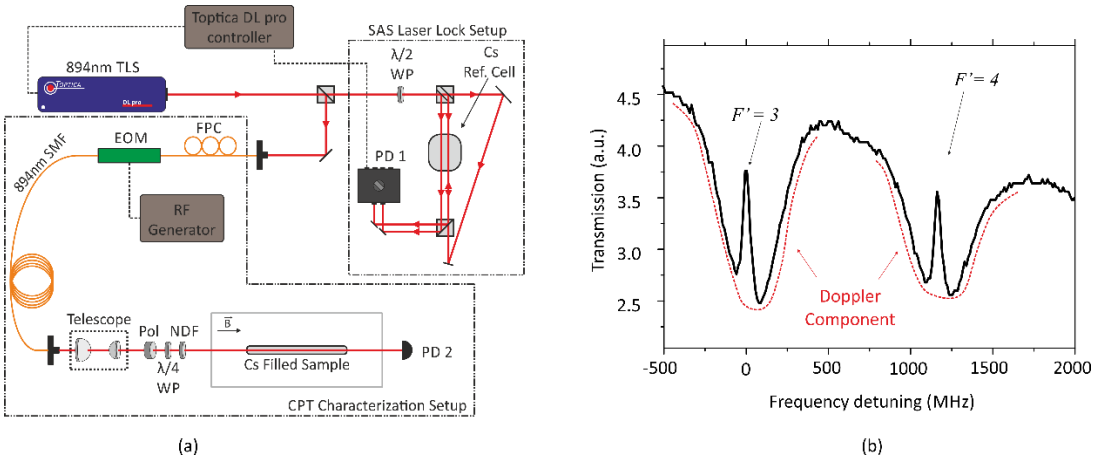

Figure 4.10: (a) CPT characterisation rig. The system is composed by a $894\ nm$ toptica DL-pro (ECDL), Keysight RF generator (model E8257D) and an electro optical modulator (EOM) (Photline). A saturation absorption spectroscopy is in place to lock the laser at the $6^2S_{1/2}F = 4 \rightarrow 6^2P_{1/2}F = 3$ transition. The EOM modulates the laser at $9.2\ GHz$ and where the first side band will be resonant to the $6^2S_{1/2}F = 3 \rightarrow 6^2P_{1/2}F = 3$ transition. Polarisation is set and maintained by the pair polariser (Pol) and quarter wave-plate ($\lambda/4$ WP) the signal interacts with the Cs atoms in the reference cell and is detected by the photodetector (PD). The reference cell is kept inside a long solenoid and then inside a mu-metal cage. (b) Example of saturation absorption spectroscopy at $6^2S_{1/2}F = 4 \rightarrow 6^2P_{1/2}F = \{3,4\}$ transitions. Note the Doppler-free feature inside the Doppler broadened profile.

The second part of the system is the CPT investigation arm, also described in Figure 4.10(a). The optical signal is sent through an optical fibre from the laser to the EOM where its frequency is modulated at the exact Cs clock transition frequency, $\omega_{rf} = 2\pi\ 9.192{,}631{,}770\ GHz$, and swept around this frequency by the amount $\Delta\nu$, as depicted in Figure 4.11(a). A collimating lens fibre connector (Thorlabs, model F260APC-850) is attached to the fibre-end. The exiting beam has nominal diameter of $3.31\ mm$. The free space signal pass through a linear polariser and a quarter wave-plate. The signal then travels across the reference cell and is detected by a Si detector (Thorlabs, PDA360A). The electric signal from the photodector is then analysed by a $60\ MHz$ oscilloscope with maximum dynamic range of $48\ dB$ (8-bit vertical resolution). A telescope arrangement can be placed just after the collimating connector in order to manipulate the beam diameter.

The reference cell was placed inside a long solenoid and then inside a mu-metal cage in order to shield the system from external magnetic fields. The cell was wrapped in aluminium foil and heaters were place around it together with a set of type-K thermocouples.

The response of the EOM to the applied RF power was characterised using a tunable Fabry-Perot cavity with a frequency range of $\sim 18\ GHz$. The laser signal, with the modulation on and with $\Delta\nu =$

0, was launch into the cavity and the RF power was varied from $0\ dBm$ to $25\ dBm$ and the power at the carrier and the two first side bands ($q = \pm 1$) were computed. The normalised power at the carrier and side bands versus the RF power is plotted and shown in Figure 4.11 (b). It was observed that the two side bands and the carrier equalise at RF power around $19\ dBm$. At first glance, this should be the optimum point to operate the RF generator in order to have equal power at each transition. However, I decided to operate at $\sim 18\ dBm$ in order to minimise the excitation of higher order side bands ($|q| > 1$).

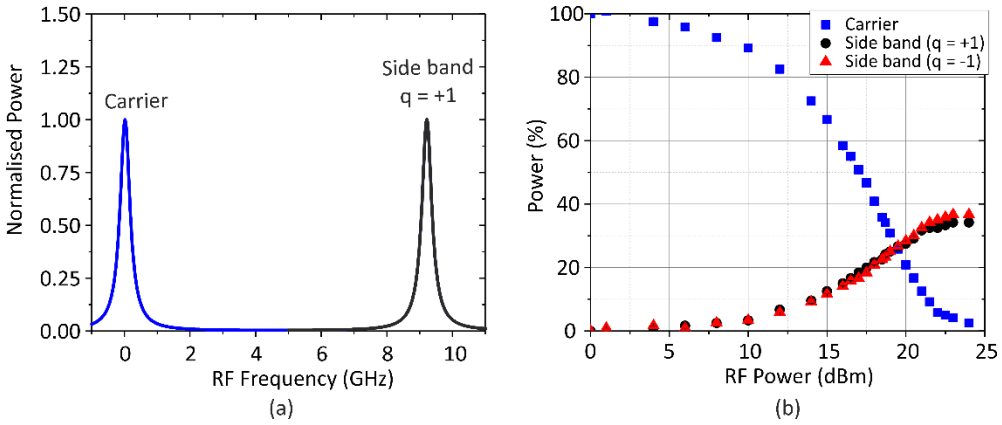

Figure 4.11: (a) Description of the EOM carrier and side bands. The carrier is locked at the $6^2S_{1/2}F = 4 \rightarrow 6^2P_{1/2}F = 3$ transition while the side band is modulated around $\sim 9.2\ GHz$ by the amount $\Delta\nu$. (b) Power at the carrier and side bands ($q = \pm 1$) as a function of the RF power. Note that the power at each component (carrier and side bands) equalise at $P_{RF} \sim 19\ dBm$.

The measuring method used throughout this study was the so-called continuous method, where the laser frequency is modulated continuously about the $6^2S_{1/2}F = 3 \rightarrow 6^2P_{1/2}F = 3$ transition. The measured CPT peak was analysed concerning its line-width and contrast. The centre frequency was also analysed depending on the experiment considered. The line-width is considered to be the full-width at half-maximum (FWHM) value and the contrast is the peak amplitude normalised according to the following equation,

$$A_c = \frac{Peak\ amplitude}{Background\ signal}, \qquad \text{Eq. 4.51}$$

where the background signal is the radiation signal detected by photo-detector altogether with the CPT signal. In the following sections I discuss the experimental results obtained from a pure Cs reference cell and a group of cells containing a combination of buffer gas and Cs vapour.

4.3.2 Dark Resonance Line-Width and Contrast in a Pure Cs Reference Cell

Initially, let us assume the simplest scenario of CPT spectroscopy in a pure Cs vapour reference cell. The experiment was performed using the setup described in the previous section and with an $80\ mm$ long a pure Cs vapour cell with diameter of $50\ mm$. The analysis considered three main aspects: laser input power, beam width and temperature.

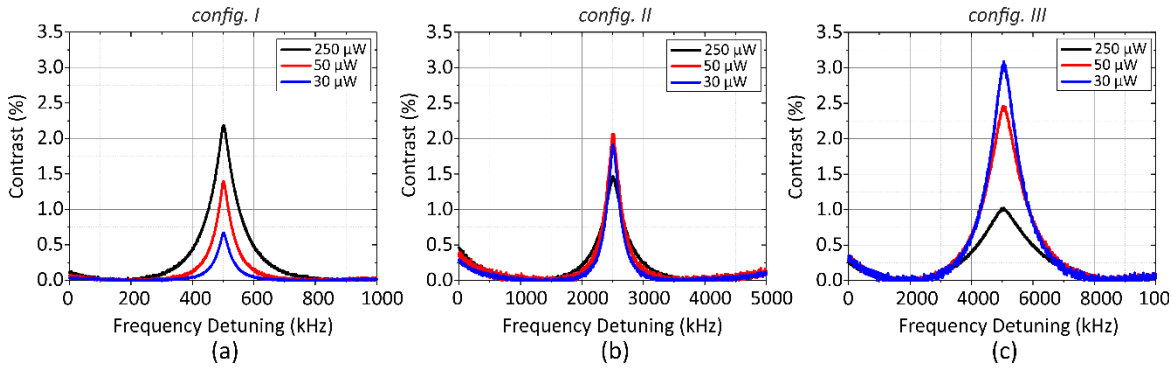

Figure 4.12: Dark resonance comparison for a selection of laser input power ($30\ \mu W$, $50\ \mu W$ and $250 \mu W$) for the three configurations, (a) I, (b) II and (c) III. The variation of the beam spot diameter increased the power broadening.

I focused the analysis on only the $(F = 3, m_F = 0) \rightarrow (F = 4, m_F = 0)$ resonance. A longitudinally homogeneous magnetic field was applied using a $250\ mm$ long solenoid with a diameter of $8\ mm$, made with a $1\ mm$ thick copper wire and with no spacing between turns. The longitudinal component of the field varies linearly as a function of the applied current with estimated gradient $dB_z/di = 0.18\ mT/A$. Also, the current was tuned to guarantee that the magnetic sensitive dark resonances were spectrally shifted to avoid overlapping between resonances with different orders.

Table 4.4 Experimental parameters used to investigate CPT in Pure Cs reference cells.

Configuration	I	II	III
Laser Power	2µW to 250 µW	2µW to 250 µW	2µW to 250 µW
Beam diameter	~3.3 mm	~2.5 mm	~1.7 mm
Beam Area reduction (compared to I)	NA	~45%	~75%
Telescope setup	NA	f_1 = 100 mm f_2 = 75 mm	f_1 = 100 mm f_2 = 50 mm
Temperature	21 C to 42 C	21 C	31 C
Magnetic Field	~0.5 mT	~0.9 mT	~1.7 mT

The dark resonance was characterised for a laser input power varying from 2 μW to ~250 μW and for three beam diameters (I~3.3 mm, II~2.5 mm and III~1.7 mm). The beam-width compression was obtained by a suitable choice of lenses assembled in a telescopic arrangement. Finally, the temperature was varied only for configuration I and kept constant for configurations II and III. The experimental parameters are listed in Table 4.4.

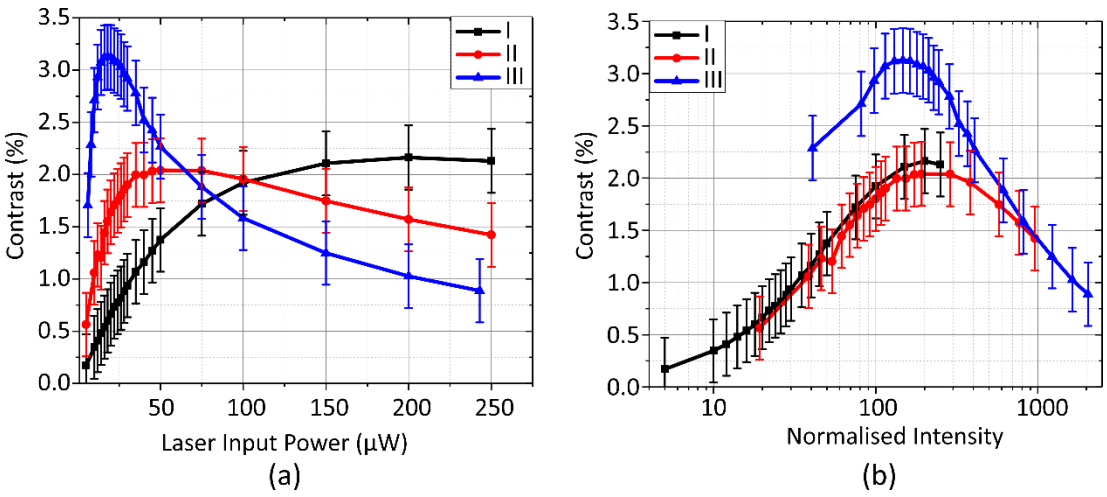

Figure 4.13: Contrast as a function of the laser input power and (a) normalised intensity (b) for configurations I, II, III. The beam width was tuned in each case with nominal values of 3.3 mm, 2.5 mm and 1.7 mm, respectively. The experiment parameters are listed in Table 4.4. The change in temperature between configurations I, II and III indicates the atomic density dependency over the temperature and its relationship with contrast.

Figure 4.12 shows the dark resonance shape evolution for three laser input power and for the three configurations I, II and III. Note that the contrast increased from $30\ \mu W$ to $50\ \mu W$ and to $250\ \mu W$ for configuration I while it presented a more complex behaviour for configurations II and III. Primarily, the main aspect observed in the contrast behaviour is the existence of a maximum. This complex behaviour is explained by including a trap state to the lambda configuration, as briefly point out in previous sections [17]. Secondly, it is noteworthy the impact that decreasing the beam diameter had over the CPT line-width and, at first glance, contrast behaviour. The contrast behaviour as a function of laser input power is showed in Figure 4.13(a). Note that as the beam width is decreased (configuration II and III), the maximum contrast shifted towards weak input power. This reflects only the effect of increased intensity for each case and, by changing the axis to the intensity, the shift disappears – as depicted in Figure 4.13(b). Also, as a consequence of the high current applied to the solenoid, the configuration III stabilised thermally at $31\ C$. The $10\ C$ difference from configurations I and II increased the contrast by more than 1% and it is resulted by the increased number of atoms participating in the effect driven by temperature changes.

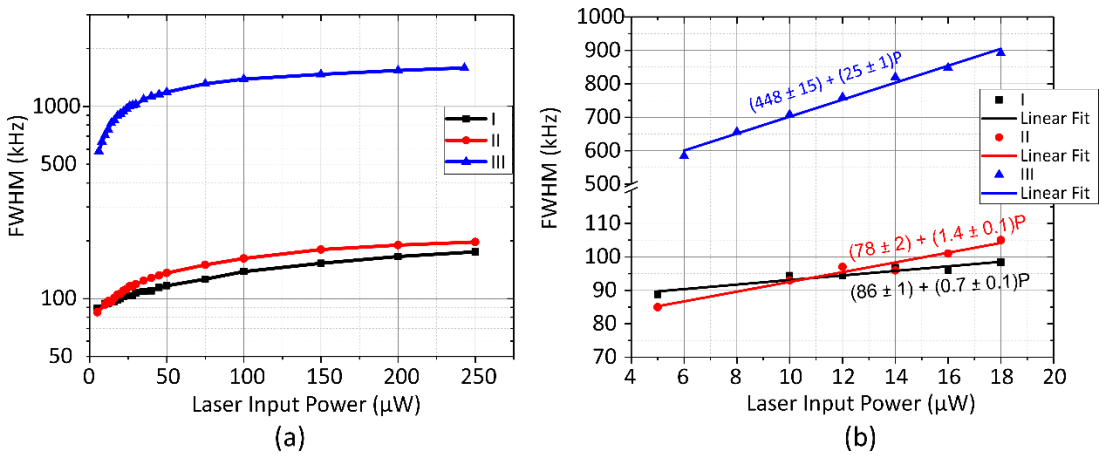

Figure 4.14: (a) Line-width as a function of the laser input power. Transit-time broadening and laser power broadening are the two main broadening effects governing the line-width response for the three configurations of beam width studied. (b) Line-width regime at low power range. The linear fitting coefficients indicated that the configuration I and II are limited by the transit time broadening, while power broadening is still the stronger broadening mechanism in configuration III.

The line width data also showed different trends with respect to different beam widths. The FWHM response as a function of the laser input power is depicted in Figure 4.14(a). As one can see, the resonance broadens as a function of power, since the beam intensity scales with the square of the beam diameter. For the configurations I and II, transit time broadening governs the line-width behaviour in the low laser power regime, while for configuration III, power broadening and the transit-time give rise to main broadening mechanisms. According to Eq. 4.37, the average thermal velocity of Cs at $20\ C$ and $31\ C$ is $218\ m/s$ and $222\ m/s$, respectively. The broadening component associated with the atomic time of flight are, according to Eq. 4.30, $66\ kHz$, $87\ kHz$ and $128\ kHz$, respectively to configurations I, II and III. This is confirmed by the analysis of the line width dependency over power in the low power range ($2\ \mu W$ to $20\ \mu W$), depicted in Figure 4.14(b). Linear fitting showed linear coefficient of $(78 \pm 2)\ kHz$ and $(86 \pm 1)\ kHz$, respectively to configurations I and II. Those number are close to the estimated from the transit time broadening for each case, as previously mentioned. Interestingly, the angular coefficients are $(0.7 \pm 0.1)\ kHz/\mu W$ and $(1.4 \pm 0.1)\ kHz/\mu W$, respectively for each case, and this is a direct result from the increased beam intensity of in configuration II, compared to I.The linear fitting of configuration III indicated, as shown in Figure 4.14(b), linear coefficient about 3.5 times larger than the transit time estimative. This indicates that the line-width behaviour is governed by transit-time and, strongly, by power broadening. It also indicates that, although appearing linear at the first glance, the range analysed is actually just part of the full non-linear trend. In fact, the line-width of the CPT dark resonance in pure-Cs cells is non-linear, as described in [19], [31]. Brazhnikov et al. have theoretically demonstrated that the CPT line-width, in the high intensity regime follow a non-linear trend [31],

$$FWHM_{I \gg I_{sat}} \propto \sqrt{I/I_{sat}}, \qquad \text{Eq. 4.52}$$

4.3.3 Line Width as a Function of the Buffer Gas Pressure

To experimentally analyse the buffer gas effects on the dark resonance, I have measured four geometrically identical Cs reference cells with a mixture of 29% of Argon and 71% of Nitrogen, for four different total pressures ($1\ torr$, $10\ torr$, $70\ torr$, $120\ torr$). The partial pressure of each gas was tuned in order to provide maximum shift and minimum temperature dependency at $\sim 70\ C$. The cells are $50\ mm$ long and have a diameter of $1\ mm$.

The experimental apparatus was identical to that discussed in section 4.3.1 and 4.3.2. A telescope arrangement was used to compress the beam below the cell's inner diameter and to avoid cladding propagation in the cell's walls. The telescope was composed of two lenses with focal length of $f = 100\ mm$ and $f = 25\ mm$, respectively. The cells were arranged in a circular sample holder and placed inside a $30\ cm$ long solenoid with properties similar those used in the previous section. The cell holder and solenoid were placed inside a μ-metal cage to minimise the impact of external magnetic fields. Two values of magnetic field strength were used. For cells B, C and D, the field strength was set to $64 \pm 1\ \mu T$, while for cell A, it was set to $160 \pm 1\ \mu T$. This difference in magnetic field strength was necessary as the CPT dark resonance observed in cell A was broader than for cells B, C and D.

Table 4.5 Cs cells nominal specifications and experimental parameters

Cell	*A*	*B*	*C*	*D*
Inner Diameter	$1\ mm$	$1\ mm$	$1\ mm$	$1\ mm$
Buffer Gas Mixture	29% Ar 71% N_2	29% Ar 71% N_2	29% Ar 71% N_2	29% Ar 71% N_2
Total Pressure	$1\ torr$	$10\ torr$	$70\ torr$	$120\ torr$
Laser Power	$7.5\ \mu W$ *to* $80\ \mu W$	$7.5\ \mu W$ *to* $80\ \mu W$	$7.5\ \mu W$ *to* $80\ \mu W$	$7.5\ \mu W$ *to* $80\ \mu W$
Temperature	$38 \pm 1\ C$	$38 \pm 1\ C$	$38 \pm 1\ C$	$38 \pm 1\ C$
Magnetic Field	$160 \pm 1\ \mu T$	$64 \pm 1\ \mu T$	$64 \pm 1\ \mu T$	$64 \pm 1\ \mu T$

As discussed in the previous sections, the buffer gas not only reconditions the line-width but also cause a frequency shift. In the experiment described in this section, however, I only focused on the general behaviour of the line width and contrast for the cells listed in Table 4.5. This table also lists the cell specifications and experimental parameters.

The contrast of each cell's dark resonance response as a function of the laser input power is shown in Figure 4.15(a). At first glance, one notices that the maximum contrast varies as a function of the buffer gas pressure, shifting towards lower laser input power as the pressure is increased. This

response is analogous to the influence of beam width, albeit through a different mechanism and it indicates indirectly that the line width has changed for each cell at different pressures. This response can be a direct result when the contributions from transit-time and residual Doppler broadenings mechanisms are decreased, as discussed in section 4.2. This hypothesis is confirmed by analysing the line width as a function of the laser input power, as shown in Figure 4.15(b). In the absence of a buffer gas, the atomic time of flight should lead to a transit-time broadened resonance, Eq. 4.30, with FWHM of $\sim 230\ kHz$. Therefore, at first glance, one can conclude that even at $1\ torr$ of pressure, the buffer gas is already changing the atomic dynamics and decreasing the line width already below the transit-time limit. As the total pressure is increased, the linewidth is further decreased up to $10\ kHz$, for a cell with buffer gas pressure of $120\ torr$.

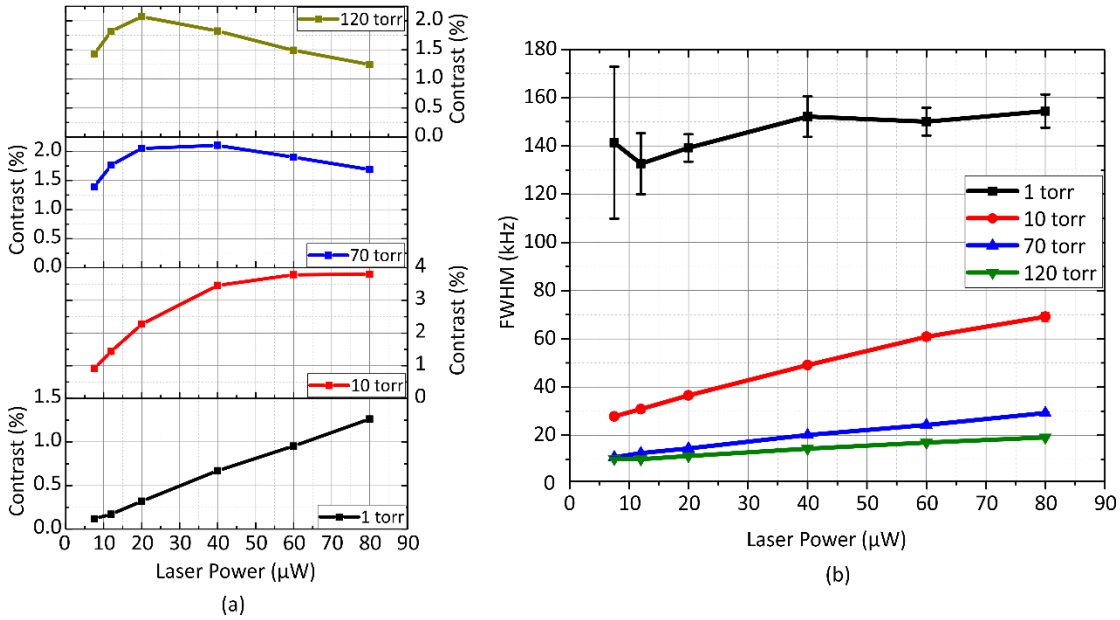

Figure 4.15: (a) CPT dark resonance contrast as a function of the laser input power for the four reference cells filled with Cs vapour and 29% of Ar and 71% N_2 buffer gas with total pressure of $1\ torr$ (black line), $10\ torr$ (red line), $70\ torr$ and $120\ torr$. Note that maximum contrast shifts towards weaker laser power, as the pressure is increased. (b) Dark resonance line width as a function of the laser input power. The line width decreasing is a direct result of the presence of buffer gas and its total pressure.

By analysing the line width response as a function of the laser input power and various pressure values, one can conclude that power broadening and atomic density diffusion through the buffer gas can be used to actively tailor the dark resonance shape. In order to investigate the line width dependency for the set of cells studied, I developed a simple model assuming four broadening mechanisms considered. The model assumptions included the two broadening mechanisms caused by the buffer gas – diffusive, γ_{BG}^{I}, and Cs-buffer gas atomic collisions, γ_{BG}^{H} –, power broadening, γ_P, and transit-time broadening γ_{tt}. Since the transit-time and the atomic diffusion broadening are

effects linked, I hence postulated an effective line width, γ_{eff}, which is the inverse of the harmonic sum of γ_{BG}^{I} and γ_{tt},

$$\frac{1}{\gamma_{eff}} = \frac{1}{\gamma_{BG}^{I}} + \frac{1}{\gamma_{tt}}. \qquad \text{Eq. 4.53}$$

As hypothesised, this effective line width should model the dark resonance line shape transitioning from transit time broadening to diffusive broadening. Note that the model also predicts the two asymptotic limits, where $\gamma_{eff} \rightarrow \gamma_{BG}^{I}$, if $\gamma_{BG}^{I} \ll \gamma_{tt}$ and $\gamma_{eff} \rightarrow \gamma_{tt}$, if $\gamma_{BG}^{I} \gg \gamma_{tt}$. The expected dark resonance line width is therefore a sum of the various broadening mechanism and has the form,

$$FWHM_{CPT} \sim 2\left(\gamma_{eff} + \gamma_{BG}^{H} + \frac{\gamma_P}{2}\right). \qquad \text{Eq. 4.54}$$

The data presented in this section was fitted using Eq. 4.30, Eq. 4.41 and Eq. 4.45 into Eq. 4.53 and Eq. 4.54. Power broadening, γ_P, diffusion coefficient, D_{eff}, and cross-section σ_{eff} were fitting parameters and the transit time decay rate was set to be $220\ kHz$. The relative velocity term present in Eq. 4.45, $\overline{v_r}$, was considered to be $\sqrt{2}v_{th}$, with $v_{th} \sim 220\ m/s$.

Table 4.6 Simulation parameters for Buffer gas effect on the CPT dark resonance line shape.

Model	***X***	***Y***	***V***	***W***
$D_{eff}\ (cm^2/s)$	0.09	0.09	0.09	0.09
$\sigma_{eff}\ (10^{-22}\ cm^2)$	3	3	3	3
γ_P **(kHz)**	7	10	20	30
γ_{tt} **(kHz)**	220	220	220	220
Laser Power	$7.5\ \mu W\ to\ 80\ \mu W$	$7.5\ \mu W\ to\ 80\ \mu W$	$7.5\ \mu W\ to\ 80\ \mu W$	$7.5\ \mu W\ to\ 80\ \mu W$

The fitting and set parameters are listed in Table 5.1. The diffusion coefficient and cross-sectional parameters were considered to be effective parameters as the cells were filled with a mixture of buffer gases and, although those parameters were obtained by adjusting the curves over the data, they were estimated to have the same order of magnitude of those found in the literature, and obtained experimentally[4].

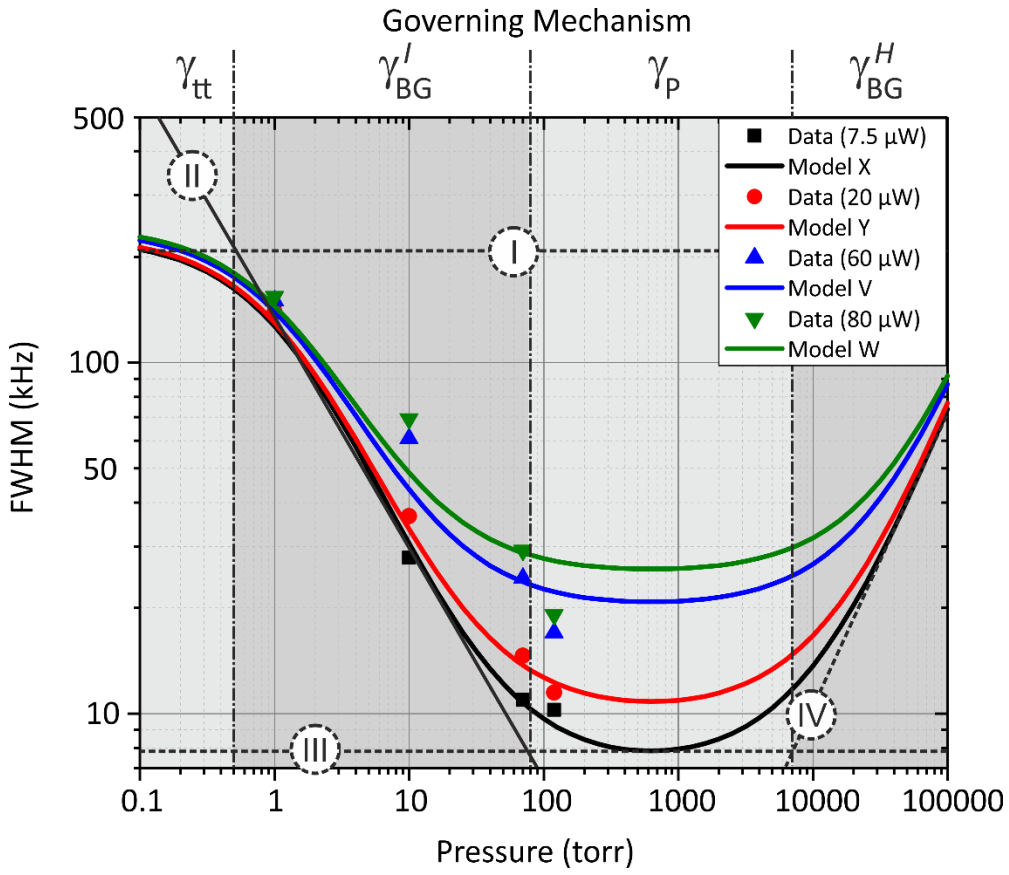

Figure 4.16: Line-width as a function of the buffer gas pressure applied for a selection of laser input power. Points define the experimental data and the solid lines the model described by Eq. 5.2. Four main regimes can be defined from the broadening mechanism limits I,II,III and IV. The limits are defined by the transit-time broadening, diffusion broadening, power broadening and Cs-buffer gas collisions, respectively.

Eq. 4.54 was plotted against the experimental data, using the parameters listed in Table 4.6, as depicted in Figure 4.16. There are four main limits present and identified in Figure 4.16. The region above the limit I is the transit-time broadening threshold. This line dictates that, in the absence of a buffer gas, the line width should lie within that region, i.e., $FWHM \geq 2\gamma_{tt}$. The second region is the area limited below limit II. This limit dictates the minimum line width observable and is governed by diffusion broadening (or narrowing) mechanism. No observable line-width should exist below this line. The limit III defines the lower limit for the line width and power broadening is the governing mechanism at this range. Finally, limit IV is due to the Cs-BG collisions and limits the line width in the high-pressure regime. One can stipulate, for $p < 1\ torr$, the minimum linewidth is dictated mainly by transit time broadening. For $1\ torr < p < 100\ torr$, diffusion broadening (narrowing) is the governing mechanism. For $100\ torr < p < 10000\ torr$, power broadening is the governing effect. One can find the global minimum line-width at this range. For $p > 10000\ torr$, the main broadening mechanism is the Cs-buffer gas collisions.

By analysing the theoretical model against the experimental data, one can safely conclude that the buffer gas pressure can be further reduced. The analysis also points out that the laser power caused associated broadening of at least $7\ kHz$. Theoretical predictions using the fitting parameters indicates that the FWHM can be decreased to $\sim 800\ Hz$, for a buffer gas pressure of 360 $torr$ and in the absence of power broadening.

4.4 Conclusion

In this chapter I have described the atomic structure of Cs and discussed the choice between the D lines transition candidates and the selection of the ideal ones for coherent population trapping spectroscopy. The CPT process was described and a three level model using a density matrix approach was presented and solved analytically.

I have discussed the main broadening mechanisms (homogeneous and inhomogenous), defined expressions useful to model the various mechanisms involved. Methods to control the line shape were discussed, involving the use of buffer gases and anti-relaxation coatings. The diffusion of alkali atoms in a buffer gas rich environment was solved and expressions for the line-width were derived.

This chapter also included an experimental description of the effect and two studies that involved pure-Cs cells and buffer gas filled cells. These studies shed light on the main aspects of the broadening mechanisms present, such as transit-time broadening, power broadening and diffusion broadening, when buffer gas is present with the Cs vapour.

The Cs vapour behaviour in the presence of a buffer gas led to an experimental and theoretical study, where I analysed the dark resonance line-width as a function of pressure. The cells were filled with Cs vapour and $29\%\ Ar$ and $71\%\ N_2$ and for four nominal pressures ($1\ torr$, $10\ torr$, $70\ torr$ and $120\ torr$). The theoretical modelling fitted the experimental data and the measured fitting parameters were of the order of magnitude of those experimentally measured and found in reference [4]. The ultimate line-width measured for a $50\ mm$ long cell and with a diameter of $1\ mm$ was $\sim 10 kHz$, for a total pressure of $120\ torr$. Theoretical predictions indicated the line-width could be further decreased to $\sim 800\ Hz$, if the buffer gas pressure is raised to $360\ torr$.

4.5 Chapter Reference

[1] G. Alzetta, A. Gozzini, L. Moi, and G. Orriols, “An experimental method for the observation of r.f. transitions and laser beat resonances in oriented Na vapour,” *Nuovo Cim. B Ser. 11*, vol. 36, no. 1, pp. 5–20, Nov. 1976.

[2] S. Knappe, “MEMS Atomic Clocks,” *Compr. Microsystems*, pp. 571–612, Jan. 2008.

[3] J. Vanier, “Atomic clocks based on coherent population trapping: A review,” Appl. Phys. B Lasers Opt., vol. 81, no. 4, pp. 421–442, 2005.

[4] J. Vanier and C. Audoin, The Quantum Physics of Atomic Frequency Standards, v.1. IOP Publishing, 1989.

[5] M. Erhard and H. Helm, “Buffer-gas effects on dark resonances: Theory and experiment,” Phys. Rev. A - At. Mol. Opt. Phys., vol. 63, no. 4, p. 043813, 2001.

[6] S. Brandt, A. Nagel, R. Wynands, and D. Meschede, “Buffer-gas-induced linewidth reduction of coherent dark resonances to below 50 Hz,” Phys. Rev. A - At. Mol. Opt. Phys., vol. 56, no. 2, pp. 1063–1066, 1997.

[7] O. Kozlova, R. Boudot, S. Guerandel, and E. de Clercq, “Temperature Dependence Cancellation of the Cs Clock Frequency in the Presence of Ne Buffer Gas,” Instrumentation and Measurement, IEEE Transactions on, vol. 60, no. 7. pp. 2262–2266, 2011.

[8] M. Abdel Hafiz et al., “Spectroscopy and hyperfine clock frequency shift measurements in Cs vapor cells coated with octadecyltrichlorosilanes (OTS),” in 2015 Joint Conference of the IEEE International Frequency Control Symposium & the European Frequency and Time Forum, 2015, pp. 33–36.

[9] D. Steck, “Cesium D Line Data,” Notes, pp. 1–31, 2008. URL: https://steck.us/alkalidata/cesiumnumbers.1.6.pdf

[10] K. Szymaniec, S. N. Lea, K. Gibble, S. E. Park, K. Liu, and P. Głowacki, “NPL Cs fountain frequency standards and the quest for the ultimate accuracy,” *J. Phys. Conf. Ser.*, vol. 723, p. 012003, Jun. 2016.

[11] J. Vanier, “Atomic clocks based on coherent population trapping: a review,” Appl. Phys. B, vol. 81, no. 4, pp. 421–442, 2005.

[12] J. H. Eberly, “Transmission of dressed fields in three-level media,” Quantum Semiclassical Opt. J. Eur. Opt. Soc. Part B, vol. 7, no. 3, pp. 373–384, Jun. 1995.

[13] J. Vanier, M. W. Levine, D. Janssen, and M. J. Delaney, “On the use of intensity optical pumping and coherent population trapping techniques in the implementation of atomic frequency standards,” IEEE Trans. Instrum. Meas., vol. 52, no. 3, pp. 822–831, 2003.

[14] J. Vanier, A. Godone, and F. Levi, “Coherent population trapping in cesium: Dark lines and coherent microwave emission,” Phys. Rev. A, vol. 58, no. 3, pp. 2345–2358, Sep. 1998.

[15] A. Godone, F. Levi, S. Micalizio, and J. Vanier, “Dark-line in optically-thick vapors: Inversion phenomena and line width narrowing,” *Eur. Phys. J. D*, vol. 18, no. 1, pp. 5–13, 2002.

[16] C. Cohen-Tannoudji, B. Diu, and F. Laloë, “Quantum Mechanics Vol. I,” Wiley-VCH. 1977.

[17] J. Vanier, M. W. Levine, D. Janssen, and M. Delaney, “Contrast and linewidth of the coherent population trapping transmission hyperfine resonance line in 87 Rb: Effect of optical pumping,” *Phys. Rev. A*, vol. 67, no. 6, p. 065801, Jun. 2003.

[18] W. Happer, “Optical Pumping,” *Rev. Mod. Phys.*, vol. 44, no. 2, pp. 169–249, Apr. 1972.

[19] M. A. Hafiz et al., “Characterization of Cs vapor cell coated with octadecyltrichlorosilane using coherent population trapping spectroscopy,” J. Appl. Phys., vol. 117, no. 18, p. 184901, May 2015.

[20] N. F. Ramsey, “Resonance Experiments in Successive Oscillatory Fields,” Rev. Sci. Instrum., vol. 28, no. 1, p. 57, 1957.

[21] M. A. Bouchiat and J. Brossel, “Relaxation of Optically Pumped Rb Atoms on Paraffin-Coated Walls,” *Phys. Rev.*, vol. 147, no. 1, pp. 41–54, Jul. 1966.

[22] M. V. Balabas *et al.*, “High quality anti-relaxation coating material for alkali atom vapor cells,” *Opt. Express*, vol. 18, no. 6, p. 5825, Mar. 2010.

[23] E. P. Corsini, T. Karaulanov, M. Balabas, and D. Budker, “Hyperfine frequency shift and Zeeman relaxation in alkali-metal-vapor cells with antirelaxation alkene coating,” *Phys. Rev. A*, vol. 87, no. 2, p. 022901, Feb. 2013.

[24] S. Ghosh, A. R. Bhagwat, C. K. Renshaw, S. Goh, A. L. Gaeta, and B. J. Kirby, “Low-Light-Level Optical Interactions with Rubidium Vapor in a Photonic Band-Gap Fiber,” *Phys. Rev. Lett.*, vol. 97, no. 2, p. 023603, Jul. 2006.

[25] A. Burchianti, A. Bogi, C. Marinelli, E. Mariotti, and L. Moi, “Light-induced atomic desorption and related phenomena,” Physica Scripta, vol. T135. p. 014012, 2009.

[26] P. S. Light, F. Benabid, F. Couny, M. Maric, and A. N. Luiten, “Electromagnetically induced transparency in Rb-filled coated hollow-core photonic crystal fiber,” *Opt. Lett.*, vol. 32, no. 10, p. 1323, May 2007.

[27] X. M. Zheng et al., “Narrow electromagnetically induced transparencies in Rb confined large-core core inner-wall coated Kagome HC-PCFs,” in Conference on Lasers and Electro-Optics, 2018, p. SM3L.3.

[28] O. Firstenberg, M. Shuker, A. Ben-Kish, D. R. Fredkin, N. Davidson, and A. Ron, “Theory of Dicke narrowing in coherent population trapping,” Phys. Rev. A - At. Mol. Opt. Phys., vol. 76, no. 1, p. 013818, 2007.

[29] O. Kozlova, S. Guérandel, and E. De Clercq, “Temperature and pressure shift of the Cs clock transition in the presence of buffer gases: Ne, N2, Ar,” Phys. Rev. A - At. Mol. Opt. Phys., vol. 83, no. 6, p. 062714, 2011.

[30] D. W. Preston, “Doppler-free saturated absorption: Laser spectroscopy,” Am. J. Phys., vol. 64, no. 11, p. 1432, 1996.

[31] D. V. Brazhnikov, G. Coget, M. A. Hafiz, V. Maurice, C. Gorecki, and R. Boudot, “Analytical Expressions of the Dark Resonance Parameters in a Vacuum Vapor Cell,” IEEE Trans. Ultrason. Ferroelectr. Freq. Control, vol. 65, no. 6, pp. 962–972, Jun. 2018.

Chapter 5 Experimental Apparatus and Kagome-Lattice Anti-Resonant Fibres Filled with Cs Vapour.

Foreword

The design and assemble of the experimental setup is of utmost importance for obtaining stable atomic densities within the HC-PCF and ultimately performing high resolution atomic spectroscopy in the atomic vapour cloud found within the HC-PCF. A thorough assessment of the main system parameters and geometry is fundamental to minimise secondary sources of noise on the target measurement. In atomic reference measurements, for example, the sensitivity of atomic resonance over temperature and magnetic field changes makes these two parameters to be controlled precisely.

For the purpose of my project, a complex apparatus was design containing an ultra-high vacuum chamber, magnetic field generators, heating system and optical assemblies. This apparatus was designed and built focusing on maximising the filling rate of hollow core fibre samples and to be compliant to high resolution absorption spectroscopy and coherent population trapping spectroscopy of Cs D-lines.

This chapter has the goal of discussing two key elements of the experimental apparatus necessary to perform CPT spectroscopy in Cs filled HC-PCFs. The chapter layout is as follows. I initially present the ultra-high vacuum system that I designed and built at the National Physical Laboratory. A description of the optical system built around the system is also given, discussing the various parameters and adaptations that the system requires in order to obtain efficient coupling in HC-PCFs with different core diameters and it is followed by a brief description of the sample preparation. The next section concerns the magnetic field generator and the field quality. Two geometries are discussed: extra-long homogenous magnetic fields using solenoids and a set of two pairs of Helmholtz coils. This section contains simulations and experimental demonstrations and focussed discussions of both geometries applied to high resolution spectroscopy. The last section of this chapter is related to fibre filling and the experimental aspects of absorption spectroscopy in Cs filled HC-PCFs.

For the UHV design task, I received technical support from Prof Patrick Gill and Dr Thomas Bradley. Dr Mohsin Haji built the vacuum pump setup and advised me during the construction of the UHV chambers. I was entirely in charge of design and construction of the heating system, optical apparatus and magnetic field generators.

5.1 Ultra-High Vacuum Apparatus and Sample Preparation

The use of vacuum systems is required for alkali vapour filling in order to avoid contamination and unwanted reactions. Caesium is the most reactive metal known and reacts to atmospheric air in two ways. It can react with water vapour present in the air or form a superoxide in the presence of oxygen molecules. Nitrogen molecules act as a buffer gas, decreasing the reaction with water vapour and oxygen. However, they can cause broadening of the atomic lines as a result of collisions between caesium and nitrogen molecules, as discussed in chapter 4.

In the next section I present the UHV setup built for CPT spectroscopy in HC-PCFs filled with Cs vapour.

5.1.1 Ultra-High Vacuum Fibre Filling Setup

The UHV system was designed and built for the purpose of performing CPT spectroscopy in-situ. The system can be separated into two main parts: sample chamber assembly and auxiliary chambers. Figure 5.1(a) shows a 3D concept of the sample chamber. This chamber is composed of two chambers (1) connected by a $\sim 5\ cm$ long feedthrough (2). The two chambers (1) connect the fibre sample region to the auxiliary chambers and they have auxiliary cavities that are useful for inspecting the Cs vapour build-up in the main chamber during filling. The feedthrough has eight holes that extend through the pair. Each hole accommodates a fibre sample, as it is shown in Figure 5.1(b), and it will be described later in this chapter. The samples are found within a $7.5\ mm$ radius from the centre of the feedthrough. The chamber (1) is made of non-magnetic stainless steel and the feedthrough (2) is made of titanium. Additional parts, such as bolts and viewports, were also made from either non-magnetic steel or titanium. Non-magnetic metals and alloys are required to minimise distortions in the magnetic field that are externally applied in the volume around the feedthrough and chambers. Figure 5.1(c) shows the assembled part with view ports and loaded with fibre samples.

The auxiliary chambers have the role of connecting the sample chamber to the vacuum pump system and also to the Cs dispenser, buffer gas inlet and pressure gauges. The buffer gas inlet is a needle valve responsible for controlling the flux of gas to the UHV assembly. A 3D concept image of the full UHV setup and an actual picture of the system are shown in Figure 5.2(a) and (b), respectively.

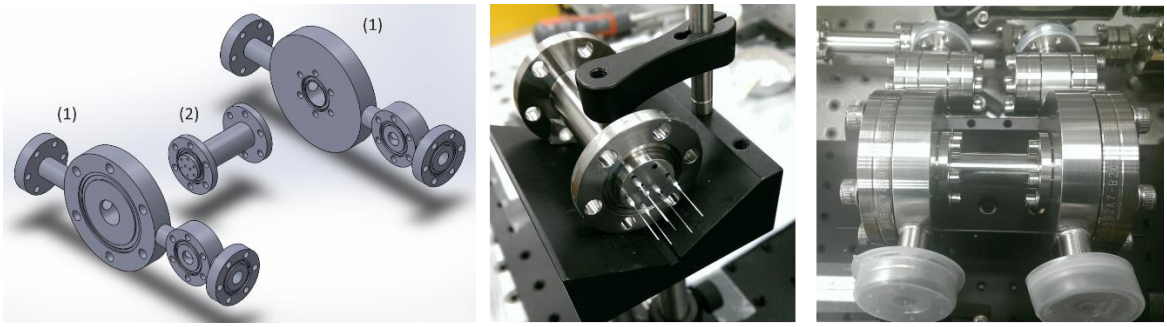

(a) (b) (c)

Figure 5.1:(a) 3D concept of the sample chambers assembly. It is composed of two parts: (1) main chambers and (2) sample holder feedthrough. The assembly is completed with view ports. All parts are non-magnetic grade metals and alloys. (b) Sample holder being loaded with fibres. Note that it has the capability to support up to eight samples. (c) Picture of the actual sample chambers assembled and ready to be connected to the auxiliary chambers of the UHV system.

Heaters and temperature sensors were placed across the system. The heaters were organised into different circuits in order to obtain local control of the temperature. A magnetic field generator was placed around the sample chambers. A first iteration of the generator was based on a tightly coiled solenoid. A later and final iteration of the generator was based on a more sophisticated arrangement of Helmholtz coils. In terms of pressure range, the UHV pump system can evacuate the UHV assembly down to $10^{-8}\ torr$.

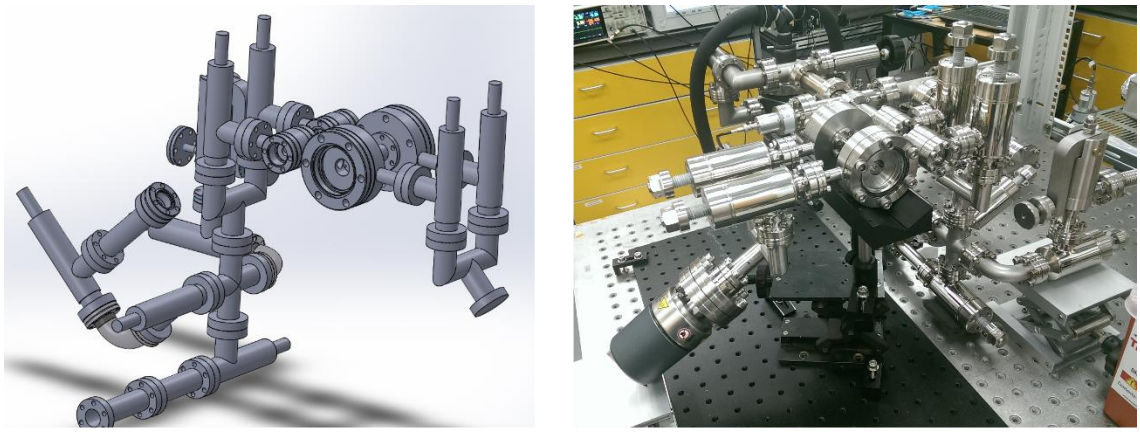

(a) (b)

Figure 5.2: 3D concept (a) and a picture (b) of the full UHV assembly used for in-situ CPT spectroscopy in HC-PCFs

5.1.2 Optical Setup

The optical setup used to observe the Cs D1 lines and perform CPT spectroscopy within the hollow core fibre is similar to that described in chapter 4 and an optical assembly was built around the UHV

fibre filling setup, as depicted in Figure 5.3. The laser signal is sent to the UHV setup through a fibre link (single mode at $\lambda = 890\ nm$) and its power is split using a 90%-10% fibre coupler, where 90% of the signal is sent to the **fibre spectroscopy setup** and the remaining power is sent to the **filling inspection setup**.

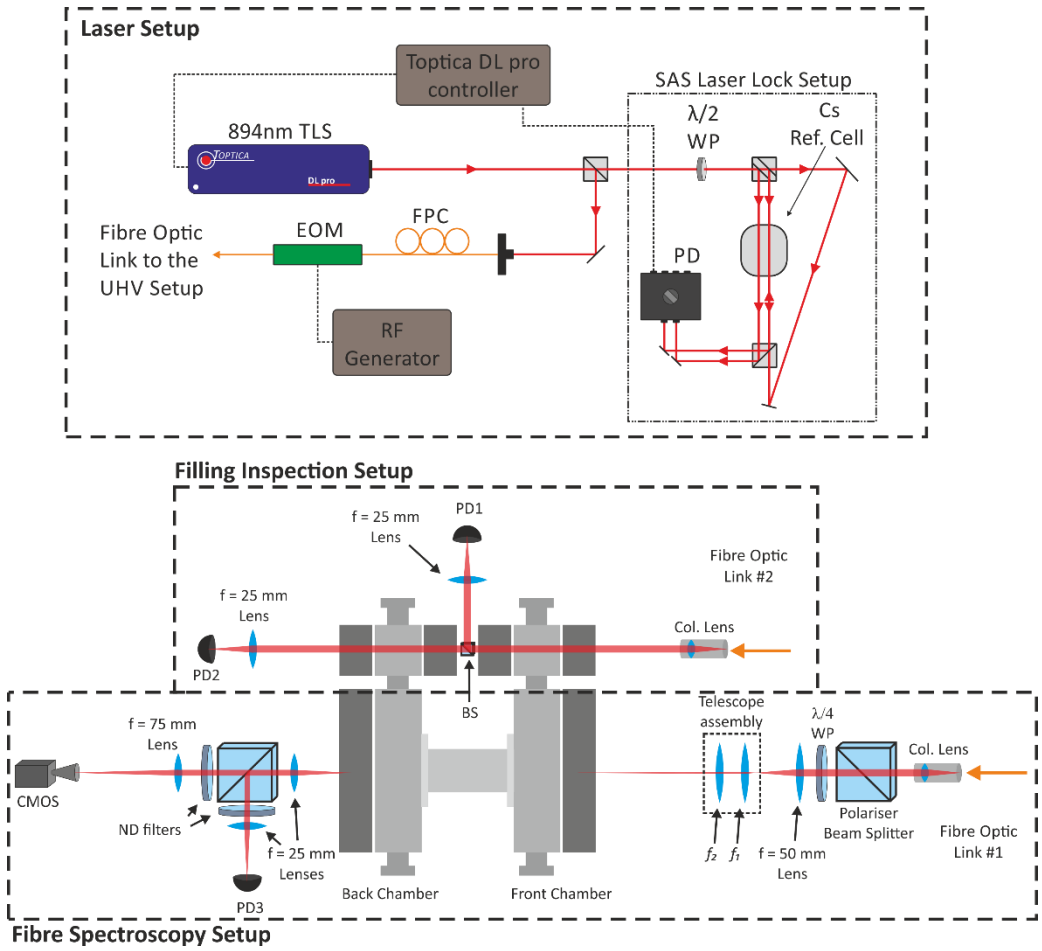

Figure 5.3: Diagram of the laser system and optical setups around the UHV chambers. The laser setup is the same described in chapter 4. The laser setup is composed by a $894\ nm$ Toptica laser, Keysight RF generator (model E8257D) and an electro optical modulator (EOM) (Photline). A saturation absorption spectroscopy is in place to lock the laser at the $6^2S_{1/2}F = 4 \rightarrow 6^2P_{1/2}F = 3$ transition. The EOM modulates the laser at $9.2\ GHz$ and where the first side band will be resonant to the $6^2S_{1/2}F = 3 \rightarrow 6^2P_{1/2}F = 3$ transition. The laser signal is sent to the UHV chamber via fibre link and the signal is divided using a 90%-10% fibre coupler. 10% of the signal is used in the filling inspection setup and the remaining 90% is directed to the fibre spectroscopy setup. Nomenclature used: TLS: tunable laser system; WP: wave plate; PD: photo detector; FPC: fibre polarisation controller; EOM: electro-optic modulator; BS: beam splitter; CMOS: CMOS camera; ND: neutral density.

The laser setup has two main optical arrangements, one for laser locking and a second for dark resonance spectroscopy. A beam splitter is used to send 50% of the signal to each optical

arrangement. This setup is described in details in chapter 4. For more information on it, please refer to section 4.3.1, in chapter 4.

The filling inspection setup is composed of a pair of silicon photo-detectors (thorlabs, model: PDA36A), a pair of $f = 25\ mm$ lenses and a beam splitter. The optical signal is collimated with a collimator fibre connector (Thorlabs, model: F240APC-850) and passes through the first (front) auxiliary chamber. A beam splitter divides the signal and one branch is sent to a photo-detector, while the second branch crosses the second (back) auxiliary chamber and is detected by another photo-detector. This setup has the primary role of indicating that the Cs vapour is building-up inside the chambers. Secondly, it can indicate the existence possible leaks and contaminations present in the chambers.

Table 5.1 Telescope Arrangement Used for Optimised Signal Coupling into Fibre Samples

Parameters	Telescope I	Telescope II
$f_1(mm)$	25	75
$f_2\ (mm)$	75	50
Expected Magnification	~ 14	~ 3
Expected NA	< 0.01	< 0.04
Expected Beam Spot at $f_2\ (\mu m)$	70	15

The fibre spectroscopy setup resembles the CPT characterisation setup described in chapter 4. It comprises a double telescope arrangement with a polariser followed by a quarter wave plate. The polariser and quarter wave plate have the roles of fixing the incoming beam polarisation state to linear and then reselecting the polarisation state of the outgoing beam, respectively. By rotating the wave-plate relatively to the polariser, one can set the outgoing beam polarisation state to be circular, linear or elliptic. The first telescope arrangement is fixed and is composed by a $f \sim 11\ mm$ and a $f \sim 50\ mm$ lens. The second telescope arrangement can be replaced in order to better match the mode field of the optical link fibre to the target fibres. Two combinations of lenses, telescope I and II, were used during the experiments. The lenses specifications and telescope parameters are listed in Table 5.1.Telescope I is composed of a $f \sim 25\ mm$ lens, followed by a $f \sim 75\ mm$ lens. In turn, telescope II is formed by $f \sim 75\ mm$ lens, followed by a $f \sim 50\ mm$ lens. Combined with the first telescope arrangement, telescope I and II magnify the single mode fibre beam ~ 14 times and ~ 3 times, respectively. With the two double telescopes described, I managed to keep the optical signal coupling efficiency over 70%, on average, with a minimum of 50% and a maximum of 95%, for any HC-PCF fabricated for this study and placed in the system. Table 5.1 lists the main parameters for the two telescopes used in for efficient light coupling into the target fibres.

The signal coming out the fibres is collected using a $f = 25\ mm$ lens and the signal is split into two paths, one leads to a photodetector and another that leads to a CMOS camera. The camera is useful for core alignment and for inspecting the mode quality coming out of the fibres in the chamber. A selection of neutral density filters can be used to optimise the detected signal to be within the measurable range of the oscilloscope in use ($\pm\ 2\ V$, for high resolution scan). Both collection and launching optical systems were built over a 3D translation stage assembly with a travel length of $25\ mm$ in each direction.

5.1.3 Fibre Sample Preparation

The system was designed to have up to eight samples. The sample lengths were set according to the viewport-to-viewport distance, as shown in Figure 5.4(a). This distance is approximately $95\ mm$, although its exact value cannot be inferred as the vacuum gasket and tightening procedure can induce uncertainties in the millimetre range. The fibre sample lengths were therefore set to be $\sim 90\ mm$ and gaps between the view port glass surface and the fibre end of at least $2\ mm$ were intentionally left to guarantee that the atoms could flow into the hollow core.

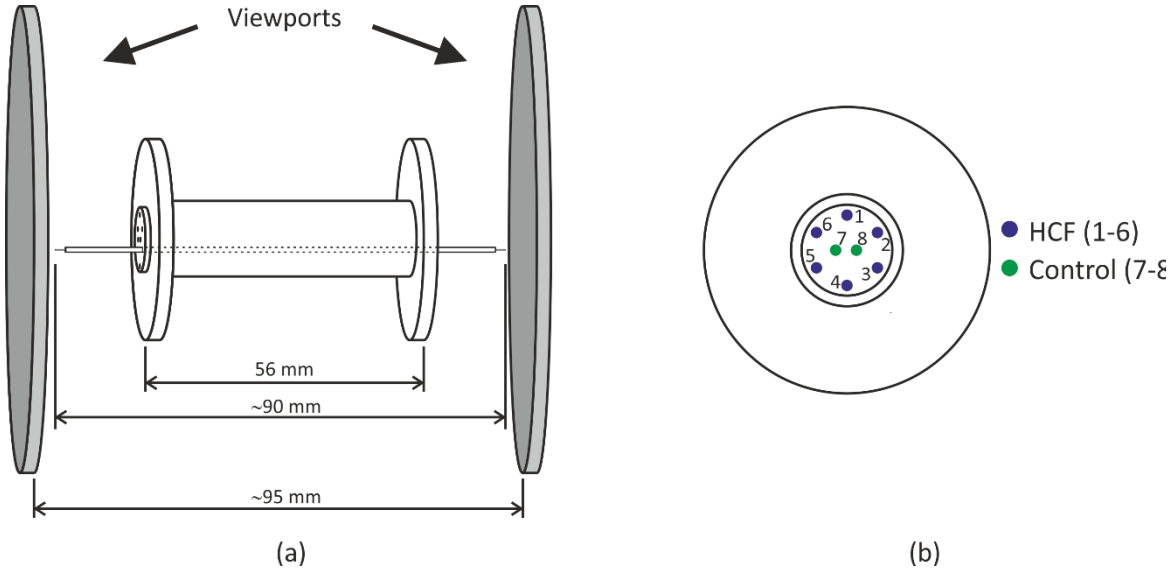

Figure 5.4:(a) Diagram indicating the fibre sample positioning inside the chamber. The samples were $\sim 90\ mm$ long and a gap of $\sim 2\ mm$ between the fibre's end and the viewport internal surface was intentionally left for hollow core filling purposes. In total, six HC-PCFs samples and two control fibres can be loaded in the system. The control fibres are multimode solid core fibres, with core diameter of $200\ \mu m$.

The system was loaded with six HC-PCFs and two control fibres. The HC-PCFs were over sleeved using a $\sim 1.2\ mm$ outer diameter and $\sim 310\ \mu m$ inner diameter capillary, and they were hand cleaved within a millimetre tolerance. The control fibres are multimode, solid core, fibres ($200\ \mu m$ core diameter), and they are useful to estimate the filling status at the gaps. The sample positioning

in the feedthrough is depicted in Figure 5.4(b). In order to increase the mechanical stability of the samples and to restrain the flux of the atomic vapour to flow only through the hollow cores, the samples were glued with UHV compatible epoxy to the feedthrough at only one end.

After loading the samples in the chambers, the UHV assembly was evacuated until it reached a base pressure of $\sim 10^{-8}\ torr$. During this period, the setup was thoroughly checked for leaks at all connections and viewports. Once the system was ready, a Cs ampoule was cracked inside the system and Cs vapour diffused throughout the assembly, initialising the fibre filling process.

The atomic vapour was directed to the fibre chambers using a combination of temperature gradients, decreasing from the Cs dispenser chamber to the fibre chambers. The system was kept with temperatures above $40\ C$, to avoid condensation of the Cs vapour in areas colder than the melting point ($\sim 28\ C$). Any variation of the temperature across the system could impact the filling process.

5.2 Generation of Homogeneous Longitudinal Magnetic field

To complete the description of the apparatus, I must first discuss the two methods to generate homogeneous longitudinal magnetic field around the fibre samples. In the following I discuss the geometry of each magnetic field generator. Its design need to fulfil a very important condition of dark resonance splitting.

5.2.1 Magnetic Field Strength Requirement

To define the magnetic field strength requirements, it is necessary to estimate the magnetic field dependency of the various magnetic-sensitive dark resonance, i.e., resonances composed by ($m_F \neq 0$) ground state sublevels. As discussed in chapter 4, the Cs $6^2S_{1/2}$ $F = \{3,4\}$ hyperfine levels have seven and nine Zeeman sublevels, respectively. However, I can restrict the analysis to first order sublevels $m_F = \pm 1$, as they will have the weakest gradient among all $m_F \neq 0$ sub levels. For dark resonances composed by $m_F = 1$ sublevels, the hyperfine ground state to ground state transition frequency increases by $\sim 2 \times 3.5\ MHz/mT$ [1]. In turn, the transition frequency decreases at the same rate, for the dark resonance composed by $m_F = -1$ sublevels. The higher-order ($m_F > 1$) dark resonances shift, as a function of their order, by $\sim 2m_F 3.5\ MHz/mT$.

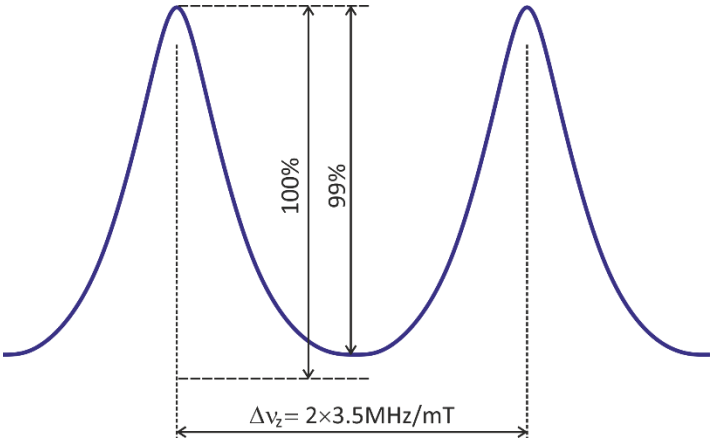

Figure 5.5: Diagram used to estimate the magnetic field strength necessary to separate 0-0 dark resonance from its magnetic sensitive neighbours, unveiling the resonance shape entirely.

Next, I need to estimate the minimum frequency shift necessary to avoid resonance overlap between the 0-0 dark resonance and its neighbouring peaks. This can be done by estimating the transit-time broadened line width of the smallest fibre core I used for CPT spectroscopy. In chapter 2, I have shown the fibre geometries and the smallest core in use is the $65\ \mu m$ hollow core diameter K-ARF. Its transit time broadened line width is $\sim 3.5\ MHz$, for Cs vapour at $60\ °C$. Considering that the dark resonances are Cauchy distributions, one can estimate the shift needed to unveil 99% of the peak by calculating the half-width at 1% of the maximum. Figure 5.5 shows a diagram explaining the methodology used here to estimate the shift required. For Cauchy distribution, the width at 99% of the maximum is $\Delta\nu = \sqrt{99} FWHM/2 \sim 5 \times FWHM$. From this, I can infer that the base width of the Cauchy distribution at 1% of the maximum is about ten times larger than its FWHM. The magnetic field strength required to obtain the fully resolved resonances would cause a shift of $2\Delta\nu \sim 10 \times FWHM$. Considering here the largest transit time broadening line width of $\sim 3.5\ MHz$, present in $65\ \mu m$ hollow core diameter K-ARF, the field required would be,

$$B_{req} = \frac{35\ [MHz]}{2 \times 3.5\ [MHz/mT]} \sim 5\ mT. \qquad \text{Eq. 5.1}$$

In the next section I present the two main geometries used to generate a homogeneous longitudinal magnetic field with a strength of $5\ mT$.

5.2.2 Solenoid Geometry

A three-section solenoid, with a radius of $35\ mm$, coil spacing of $\sim 4\ mm$ and a gap of $\sim 15\ mm$ between each section. Figure 5.6(a) is a picture of the solenoid wound around the fibre chamber and then covered with mu-metal in order to shield the system from external magnetic fields.

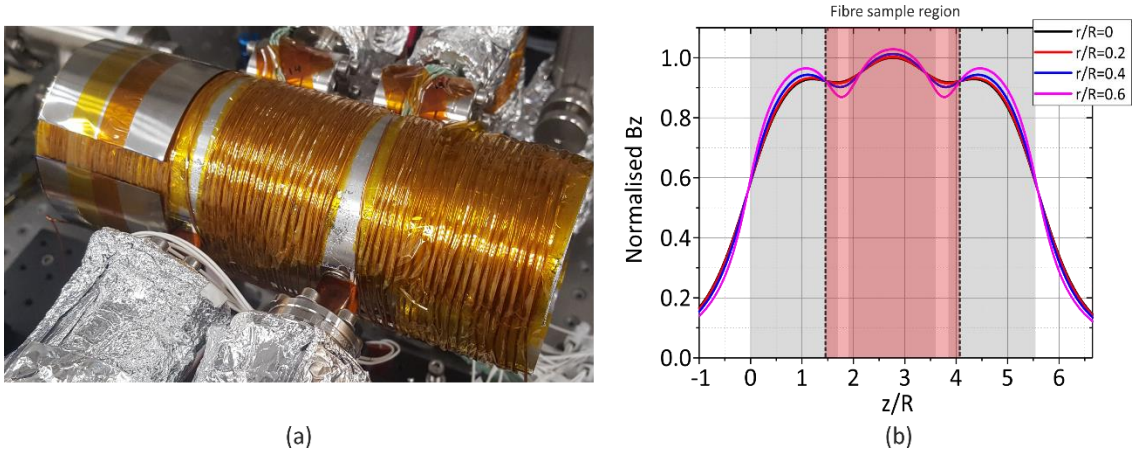

Figure 5.6:(a) Picture of the solenoid used for generating the homogeneous longitudinal magnetic field.(b) Simulated magnetic field z-component.

The field produced by the three-section solenoid was powerful enough to split the atomic transitions over a $21\,MHz$ range, with a current of $8.5\,A$, with experimental and theoretical gradients of $350 \pm 30\,\mu T/A$ and $390\,\mu T/A$, respectively. The experimental gradient was estimated based on observations of the magnetic sensitive dark resonance and the theoretical gradient was obtained by solving the Biot-Savart law, for longitudinal and radial fields, for the proposed geometry [2]. The disparities between experimental and theoretical gradients can be attributed to uneven spacing of the solenoid coils, the existence of two gaps – as depicted in Figure 5.6(a) – and measurement error caused by tilted probe. The field distribution was also simulated, using the following magnetic field component, in cylindrical coordinates,

$$\tilde{B}_x^i(z,r) = \frac{\mu I}{4\pi R}\left(\frac{z-z_i}{R}\right)\int_0^{2\pi} \frac{d\varphi\cos(\varphi)}{\left[\left(\frac{z-z_i}{R}\right)^2+\left(\frac{r}{R}\right)^2+1-2\left(\frac{r}{R}\right)\cos(\varphi)\right]^{3/2}}, \quad \text{Eq. 5.2}$$

$$\tilde{B}_y^i(z,r) = \frac{\mu I}{4\pi R}\left(\frac{z-z_i}{R}\right)\int_0^{2\pi} \frac{d\varphi\sin(\varphi)}{\left[\left(\frac{z-z_i}{R}\right)^2+\left(\frac{r}{R}\right)^2+1-2\left(\frac{r}{R}\right)\cos(\varphi)\right]^{3/2}}, \quad \text{Eq. 5.3}$$

$$\tilde{B}_z^i(z,r) = \frac{\mu I}{4\pi R}\int_0^{2\pi} \frac{d\varphi\left[1-\left(\frac{r}{R}\right)\cos(\varphi)\right]}{\left[\left(\frac{z-z_i}{R}\right)^2+\left(\frac{r}{R}\right)^2+1-2\left(\frac{r}{R}\right)\cos(\varphi)\right]^{3/2}}, \quad \text{Eq. 5.4}$$

where R is the solenoid radius, z_i is the position of each coil of the solenoid, μ is the magnetic permeability and I is the applied current. The final field takes the form,

$$\vec{B} = \sum_{i=1}^{N} \left(\tilde{B}_x^i(z,r)\hat{x} + \tilde{B}_y^i(z,r)\hat{y} + \tilde{B}_z^i(z,r)\hat{z}\right), \qquad \text{Eq. 5.5}$$

the sum of the magnetic fields associated to each coil. The analytical solution of the fields in the three axis for each point of the space require the integration of elliptic functions and were suppressed from this analysis. Instead, the fields were solved numerically.

Figure 5.6(b) shows the simulated longitudinal normalised field strength, as a function of the z-coordinate and for some radial positions The fields were normalised to $\max\left(B_z(z, r = 0)\right)$. The grey areas in the plot indicate the position of each section of the solenoid, containing twenty one turns in each section. The red region indicates where the fibre samples would be found inside the magnetic field. Note that at the region the fibres are located, the field varies spatially within 10% of its maximum value, found at the centre of the solenoid. Also, as the radial position increases, the variation of field become severe and, at $r = 0.6R$, two symmetrical dips manifest. Those dips are inherent to the break of symmetry caused by the two gaps that separate the solenoid into three sections.

The major drawbacks of using solenoids for generating the magnetic field required are the field fringing and the joule heating. Generally, field curvature can be reduced by increasing its radius. The fringing at the centre of the solenoid, however, is also caused by the two gaps. They geometrical restrictions imposed by the UHV chambers design and their size cannot be minimised by any practical means (except redesigning the chamber). The joule heating is an effect inherent to the flow of current in the copper wire and can be reduced by increasing the wire diameter.

During preliminary filling tests, it was noticed an increasing in temperature of the inner region of solenoid, UHV chamber found inside it and in its surroundings, as a result of long periods with the solenoid field on. It led to atomic vapour depletion from fibre chambers, resulting in a reduction of contrast. The filling had to be restated and the chamber had to be amended a number of times, as the large temperature gradient over the viewports caused hair-line fractures in the glass constituents, resulting in leaks and ultimately oxidation of the Cs vapour.

In the next section I discuss the solution found to address the both fringing and heating issues.

5.2.3 Double Helmholtz Coil Design and Characterisation

Another way to obtain homogeneous and longitudinal magnetic fields is by using Helmholtz coils. They are large coils with many turns that generate a longitudinal magnetic field in its centre. The physical description of the magnetic field generated by a Helmholtz coil is modelled by Eq. 5.2, Eq.

5.3 and Eq. 5.4. One of the main characteristics of this accessory is that the spatial width of the longitudinal field is linearly proportional to the coil diameter. The association of two coils produces a homogeneous and longitudinal field, if the distance between the coils is close to the coils radius. For example, to produce a $10\ cm$ long homogeneous field a pair of coils with a radius of $10\ cm$ is required. Helmholtz coils heat up by the joule effect. However, as the coils housing is not be in contact with the UHV system, the oven effect caused by the solenoid is rather diminished.

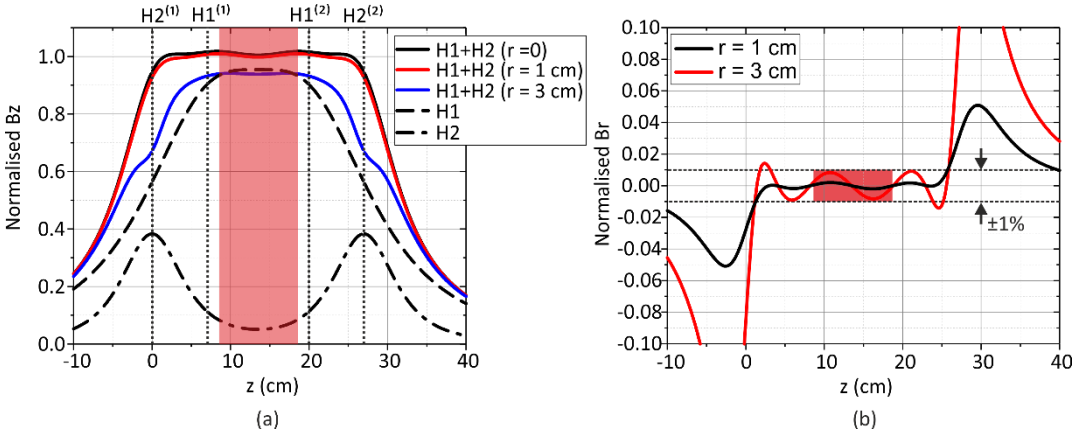

Figure 5.7: (a) Simulated normalised longitudinal magnetic field distribution as a function of the longitudinal coordinate z for the pairs H1 and H2, with parameters listed in Table 5.2, and for radial position $r = 0, r = 1\ cm$ and $r = 3\ cm$. The contributions of each pair are also shown in the graph. (b) Simulated radial magnetic field distribution of the full assembly for radius $r = 1\ cm$ and $r = 3\ cm$. Note that the field fringes within 1% of the value of the maximum longitudinal field within a cylinder with $3\ cm$ of radius. The red box indicates where the fibre samples would be found within the field.

For the scope of this project, I have designed and implemented a Helmholtz assembly with two pairs of Helmholtz coils. The use of two pairs enlarges the homogeneous field region and theoretically and experimentally demonstrated in this section. The radius of each pair coils, inner and outer, was carefully designed following simulation results for maximised field longitudinal homogeneity and minimised radial field component. The design constraints were i) the longitudinal homogenous field should be at least $10\ cm$ long and ii) the distance between the two inner pairs should be larger than $10\ cm$. The first constraint is a direct result of the size of the fibre samples and the second constraint is related to the UHV chamber geometry.

Table 5.2 Helmholtz Design Parameters.

Pair	H1	H2
Radius (cm)	13	6
Distance (cm)	13	27
Number of turns	80	21

The double Helmholtz coil geometry was simulated for various values radii, distance and number of turns. Table 5.2 lists the parameters that yield a $22\ cm$ long homogeneous longitudinal magnetic field. Figure 5.7(a) shows the simulated longitudinal field of the assembly and the contribution of each pair $H1$ and $H2$. The fields were normalised to $\max\big(B_z(z, r=0)\big)$, for the full assembly. Figure 5.7(a) also shows the field variations as the radius is increased. Note that at $r = 3\ cm$ the field fringed at its extremity and centre value decreased of 10% of its total value. Figure 5.7(b) shows the radial field distribution for two radial positions ($r = 1\ cm$ and $r = 3\ cm$). Note that the field varies within 1% of $\max\big(B_z(z, r=0)\big)$. The region marked in red in both plots indicates where the fibre samples would be found for the given assembly. The simulation also indicates that the overall field strength (radial and longitudinal components) at the centre of the assembly increases linearly as a function of the applied current with a gradient $\sim 0.60\ mT/A$.

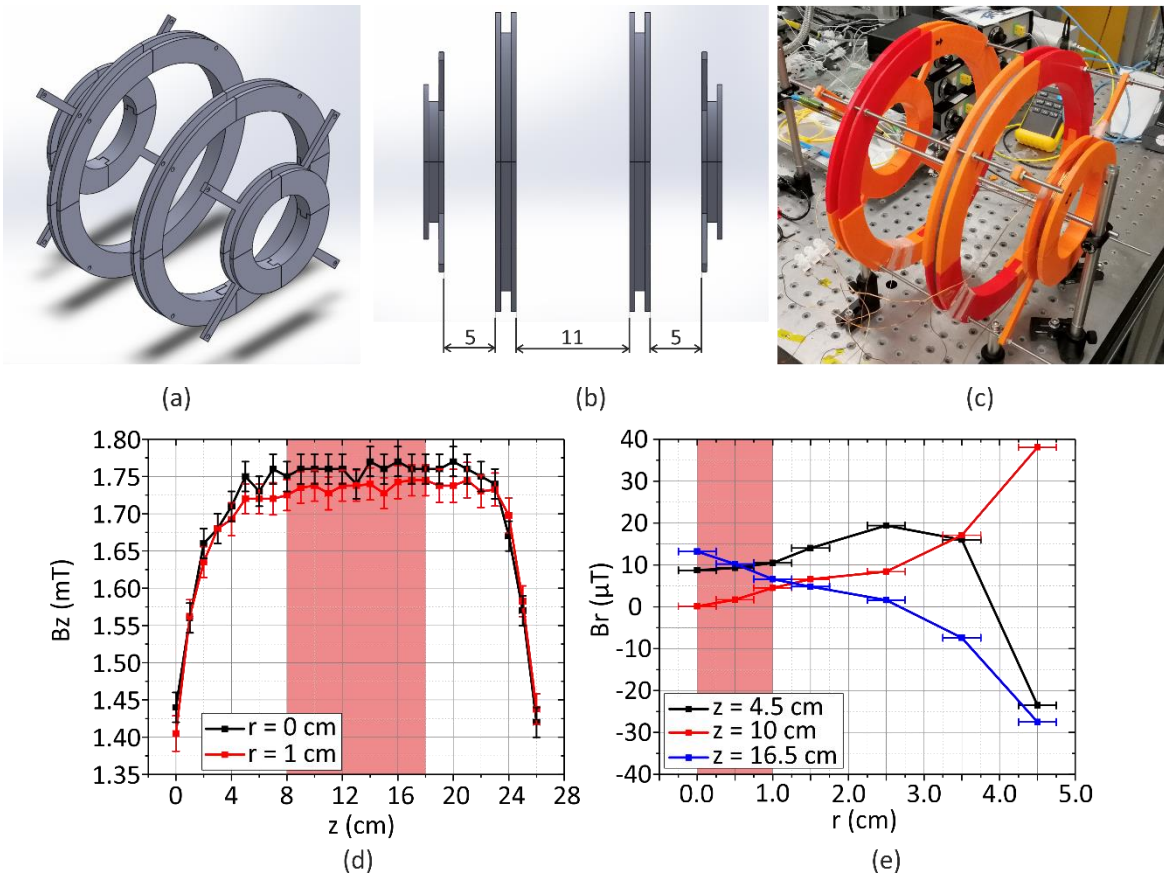

Figure 5.8:(a) 3D sketch of the double Helmholtz coils designed following the parameters found in Table 5.2. (b) Lateral view of the sketch showed in (a) indicating the distance between each coil. Note that the coil supports are $2\ cm$ thick. (c) Photograph of the assembly built in laboratory for characterisation. (d) Longitudinal field component for a current of $3\ A$ passing through each coil and for $r = 0\ and\ r = 1\ cm$. The field showed a flat zone of $\sim 18\ cm$ length and a gradient of $(0.58 \pm 0.01)\ mT/A$.

The double Helmholtz coil setup was built and characterised. The coil supports were 3D printed following the sketch shown in Figure 5.8(a). The thickness of each coil was set to $1\ cm$ and the

distances between each coil are depicted in Figure 5.8(b). Each solenoid was hand-wound, where the first pair has eight layers of ten turns of copper wire and the second, two layers and one turn. The copper wire used had a diameter of $1\ mm$ and the maximum current of operation was $19\ A$. A picture of the coils arrangements is shown in Figure 5.8(c).

The assembly was characterised using a gauss meter, with active probe dimensions of $0.25mm\ \times 0.4\ mm$, and concentrically aligned to the assembly. The longitudinal field generated by the assembly at a passing current of $3\ A$ was characterised for two values of radial position, as shown in Figure 5.8(d). The flat zone of extends over $18\ cm$ and it has gradient of $(0.58 \pm 0.01)\ mT/A$. These values are comparable with the simulated ones, where the flat zone is over $22\ cm$, with a gradient of $0.6\ mT/A$. The measurement at $r = 1\ cm$ is the average of four points found $1\ cm$ distant from the longitudinal axis. It is seen that, inside a cylinder with radius of $1\ cm$, the field flatness is maintained while its overall field strength decreases by an average of $25\ \mu T$. The radial component of the field was also measured, as shown in Figure 5.8(e). It was measured from its centre to its edge for three longitudinal distances from the first coil, $z = 4.5\ cm$, $z = 10\ cm$ and $z = 16.5\ cm$. The measurement shows that the radial field, inside a cylinder of $3\ cm$ radius, varies within $< 1\%$ of the longitudinal maximum value, as expected from the model.

The double Helmholtz geometry, although considerably larger spatially than the solenoid, offers an elongated longitudinal magnetic field and addresses the issue of joule heating, present in the solenoid geometry. The coil assembly was actively used for CPT measurements as it will be discussed in the following chapter.

5.3 Absorption Spectroscopy in Vapour Loaded Kagome Lattice Anti-Resonant Fibres

In this section I discuss the main aspects of fibre filling and absorption spectroscopy performed on the filled samples. Absorption spectroscopy of the Cs D1 line was taken as indicative of the filling status of hollow core fibre samples. The filling evolution is therefore dictated by changes in the absorption depth of the Cs lines at the same power. The absorption depth can be used to estimate the atomic density of atoms in hollow core fibres, as the attenuation depends on the scattering cross-section and the density of atoms [1], [3]. This analysis needs to be performed carefully, as saturation of the transitions is present [1], [4]. No magnetic field was used for absorption spectroscopy as I was interested only in the Doppler-broadened absorption hyperfine lines of Cs $6^2S_{1/2}F = 4\ \rightarrow 6^2P_{1/2}F' = \{3,4\}$

In the next two sections I describe the absorption spectroscopy performed in Cs vapours found within the hollow core and in its surroundings. I also discuss the filling status and estimate the atomic density found in the fibre's hollow core.

5.3.1 D1 Line Spectroscopy of Caesium Vapour Loaded Kagome Lattice Anti-Resonant Fibres and Filling Status

The D1 line spectroscopy of Cs vapour found inside the vacuum chamber and inside the hollow core was measured using a $894\ nm$ Toptica laser operated in scan mode. The optical power range used for spectroscopy was from $1\ \mu W$ to $120\ \mu W$ and this plays an important role on the optical depth and attenuation.

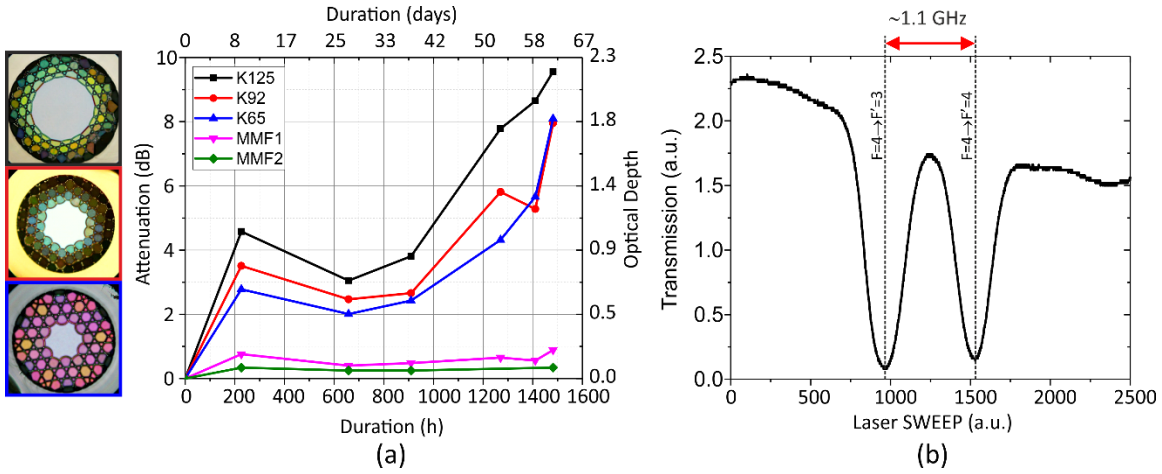

Figure 5.9:(a) Attenuation caused by the transition $6^2S_{1/2}F = 4 \rightarrow 6^2P_{1/2}F' = 3$ as a function of time for the three K-ARFs (K125, K92 and 65 – cross-sections shown on the left) used and for the two control fibres (MMF1 and 2). After a period of ~ 60 days, the fibres were found to have an apparent OD greater than 1.8. (b) Typical D1 line absorption spectroscopy of a Cs vapour found within the hollow core of K125. The laser input power used for computing the attenuation was set to $1\ \mu W$, with optical coupling efficient around $70\ \%$.

The optical attenuation caused by the transition $6^2S_{1/2}F = 4 \rightarrow 6^2P_{1/2}F' = 3$ as a function of time for Cs vapour found in the hollow core and in the laser beam path is shown in Figure 5.9(a), for a laser input power of $1\mu W$ and a coupling efficiency of $\sim 70\%$, on average. The cross section of the K-ARFs are shown on the left side of the plot. These K-ARFs were described in chapter 2. As described in section 5.1, two gaps were intentionally left at each fibre end in order to facilitate filling. They, however, have an associated atomic density that needs to be characterised. Fibres MMF 1 and MMF2 are the control solid core fibres used to estimate the density in the gaps. Note in Figure 5.9(a) that the atomic attenuation increased in the first eight days of filling and slowly decreased for the next twenty days. This decrease is regarded to a crack found in a view port. After repairing the system, the filling was restarted and the attenuation increased rapidly to $10\ dB$ and $8\ dB$ for K125 and K192(65), respectively. The attenuation in the control fibres (MMF1 and 2)

increased to $1\ dB$ in the first week and varied within $0.5\ dB$ for the next sixty days analysed. This qualitative analysis indicates that the K-ARFs were successfully filled. Figure 5.9(b) shows a typical spectroscopic measurement of the D1 line transition measured from the Cs vapour found inside the hollow core of K125.

5.3.2 Optical Power Related Effects

In order to estimate the atomic density found within the fibres' hollow core, one must take into account the effect of high optical intensity on the photon scattering cross-section. For the K-ARFs filled with Cs shown in Figure 5.9(a), the optical intensities within their hollow cores is expected to be 12 to 45 times greater than the saturation intensity associated to the transition analysed (I_{sat}~$1.2\ mW/cm^2$). This can be done by considering the power broadening contribution present in the two-level atom model, where the scattering cross-section, σ_f, can be modelled as follows, [1]

$$\sigma_f = \left(\frac{1}{1+I/I_{sat}}\right)\left[\frac{\sigma_0}{1+4\left(\frac{\Delta\omega}{\Gamma\sqrt{1+I/I_{sat}}}\right)^2}\right], \qquad \text{Eq. 5.6}$$

where I_{sat} is the saturation intensity, estimated to be $\sim 1.2\ mW/cm^2$ and σ_0 is the on-resonance cross-section, defined as [1],

$$\sigma_0 \equiv \frac{\hbar\omega\Gamma}{2I_{sat}}. \qquad \text{Eq. 5.7}$$

If the laser intensity is much larger than the transition saturation intensity, the atomic fluorescence varies asymptotically as a function of I^{-1}. Note also that the cross-section width broadens as a function of $\sqrt{I}$. Eq. 5.6 also leads to an important result that the Doppler broadened cross-section is proportional to $\sqrt{1+I/I_{sat}}$ [5].This result modifies the Beer-Lambert law, as the attenuation coefficient now varies as a function of the applied intensity. Its implications were reported by Siddons et al for rubidium atoms [4] and were observed during fibre filling as well and reported in this section. The general behaviour of the attenuation coefficient for a volume containing an atomic density, n, takes the form [4], [5],

$$\alpha(I) \sim \frac{n\sigma_0}{\sqrt{1+I/I_{sat}}}. \qquad \text{Eq. 5.8}$$

Eq. 5.8 implies that the medium opacity decreases for large optical intensities. Also, note that $\alpha(I) \to n\sigma_0\sqrt{I_{sat}/I}$, if $I/I_{sat} \gg 1$. The intensity variation in an infinitesimal length dL attributed to the fluorescence scattering is,

$$\frac{dI}{dL} = -\alpha(I)\, I\,. \qquad \text{Eq. 5.9}$$

This analysis tell us that the atomic density cannot be estimated from the signal attenuation without considering the intensity dependence of the attenuation constant. At the limit $I \ll I_{sat}$, $\alpha \to n\sigma_0$, Eq. 5.9 becomes the differential form of the Beer-Lambert law.

The discussion above sheds light on two main aspects present in optically pumped transitions beyond the saturation points. They are:

1. $\alpha \neq n\sigma_0$, for $I \gg I_{sat}$.
2. Optical depth (OD) varies as a function of the optical intensity, giving rise to an *apparent optical depth*. This indicates that OD is not a reliable way to gauge the filling conditions of HC-PCFs, as the atomic density and optical intensity can be compensated to produce apparent ODs. **(implication of item 1)**

A filling estimate can be obtained by approximating $dI/dL \to \Delta I/\Delta L$ and defining the normalised attenuation to be $a_N \equiv -\Delta I/I$. Under these assumptions, Eq. 5.9 gives rise to,

$$a_N \sim \frac{\langle n\rangle\sigma_0\Delta L}{\sqrt{1 + I/I_{sat}}}. \qquad \text{Eq. 5.10}$$

Note that a_N is limited to values within the interval $[0,1]$ and $\langle n\rangle$ is the averaged atomic density delimited by the effective volume of the beam path. Figure 5.10(a) and (b) show the attenuation estimated using Eq. 5.10 for a cylindrical beam-path with a diameter of $100\ \mu m$, for two lengths $\Delta L = 4\ mm$ (Figure 5.10(a)) and $\Delta L = 100\ mm$ (Figure 5.10(b)), and for five different atomic densities, $\langle n\rangle = \{1, 10, 50, 100, 500\} \times 10^{13}\ m^{-3}$. The two lengths were conveniently chosen to highlight the impact solely of the gaps in the attenuation picture. At $I < 0.1\ I_{sat}$, the attenuation tends to the value $\langle n\rangle\sigma_0\Delta L$, as expected from Eq. 5.10. At $I > I_{sat}$, the attenuation decreases proportionally to $I^{-1/2}$. It also indicates that the medium opacity is a function of the number of particles. Figure 5.10(b) indicates that at $I/I_{sat} = 10$, the medium is totally opaque for atomic densities higher than $10^{15}\ m^{-3}$ and decreases to $\sim 20\ \%$, $\sim 5\ \%$ and $\sim 0.5\ \%$ for densities of $2 \times 10^{14}\ m^{-3}$, $1 \times 10^{14}\ m^{-3}$ and $1 \times 10^{13}\ m^{-3}$, respectively. Therefore, I defined here as intensity cut-off the intensity level at which the atomic medium changes from opaque to translucent. This behaviour fundamentally impact the CPT spectroscopy in HC-PCFs in two ways:

i. CPT dark resonance is only observed at the translucent regime, where the photon scattering related to the optical transitions do not saturate. Below the power cut-off point, the scattering rate is so great that the probability of having a superposition of dressed states vanishes.

ii. At optically thick media, CPT dark resonance will only be observed at $I \gg I_{sat}$. Therefore, it is expected that the Dark resonance line-width is dominated by power broadening.

This two-element hypothesis is discussed in details in the next chapter, where I demonstrate CPT spectroscopy in Cs filled HC-PCFs.

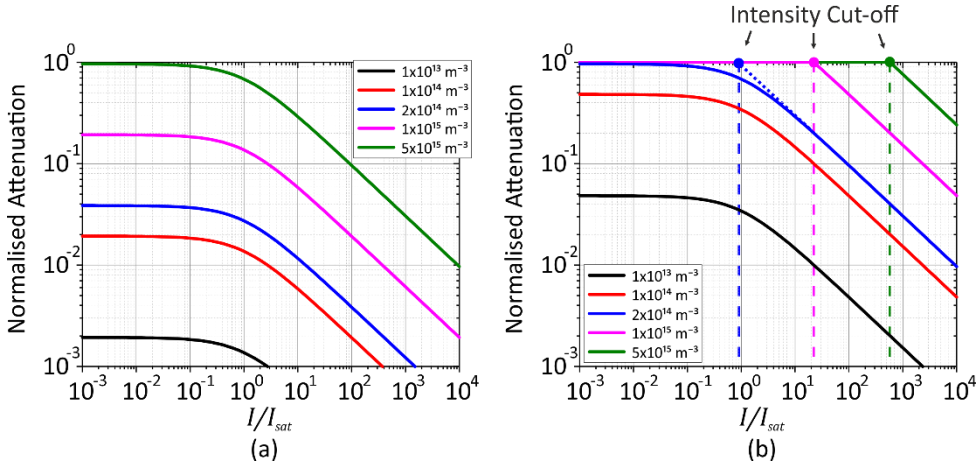

Figure 5.10: Estimated attenuation for the transition $6^2S_{1/2}F = 4 \rightarrow 6^2P_{1/2}F' = 3$ as a function of the input laser power (Eq. 5.10) for a beam path with cross-section with diameter of $100\ \mu m$ and (a) $\Delta L = 4\ mm$ and (b) $\Delta L = 100\ mm$. The atomic density was varied from $\langle n \rangle = 1 \times 10^{13}\ m^{-3}$ to $\langle n \rangle = 5 \times 10^{15}\ m^{-3}$. The scattering cross-section used was the theoretical one (Eq. 5.7), $\sigma_0 = 4.82 \times 10^{-14}\ m^{-2}$, with the saturation intensity of $I_{sat} = 12\ W/m^2$.

In order to confirm the validate Eq. 5.10, the optical attenuation of two K-ARFs and two capillary fibres were characterised as a function of the power. Those samples were loaded in the UHV chamber and Cs filling was started when a base pressure of $\sim 10^{-8}\ torr$ was reached. The temperature around the samples was set at $(48 \pm 1)\ C$ and no magnetic field was applied throughout the optical measurement.

Figure 5.11(a) shows the normalised resonance depth as a function of the optical power for four hollow core structures (K125 and K65) and two capillary fibres C140 and C305, with a core diameter of $140\ \mu m$ and $305\ \mu m$, and a control fibre MMF. Figure 5.11(b) and (c) are the same plot with a contrast depth measured after six days (b) and twenty-one days (c). Maximum contrast indicates that the attenuation is at least $24\ dB$ (limited by the minimum detectable signal by an 8-bit

oscilloscope). Note that, as the power is increased, the medium became less opaque. This is a direct result of the power broadening effect over the scattering cross-section, as demonstrated previously.

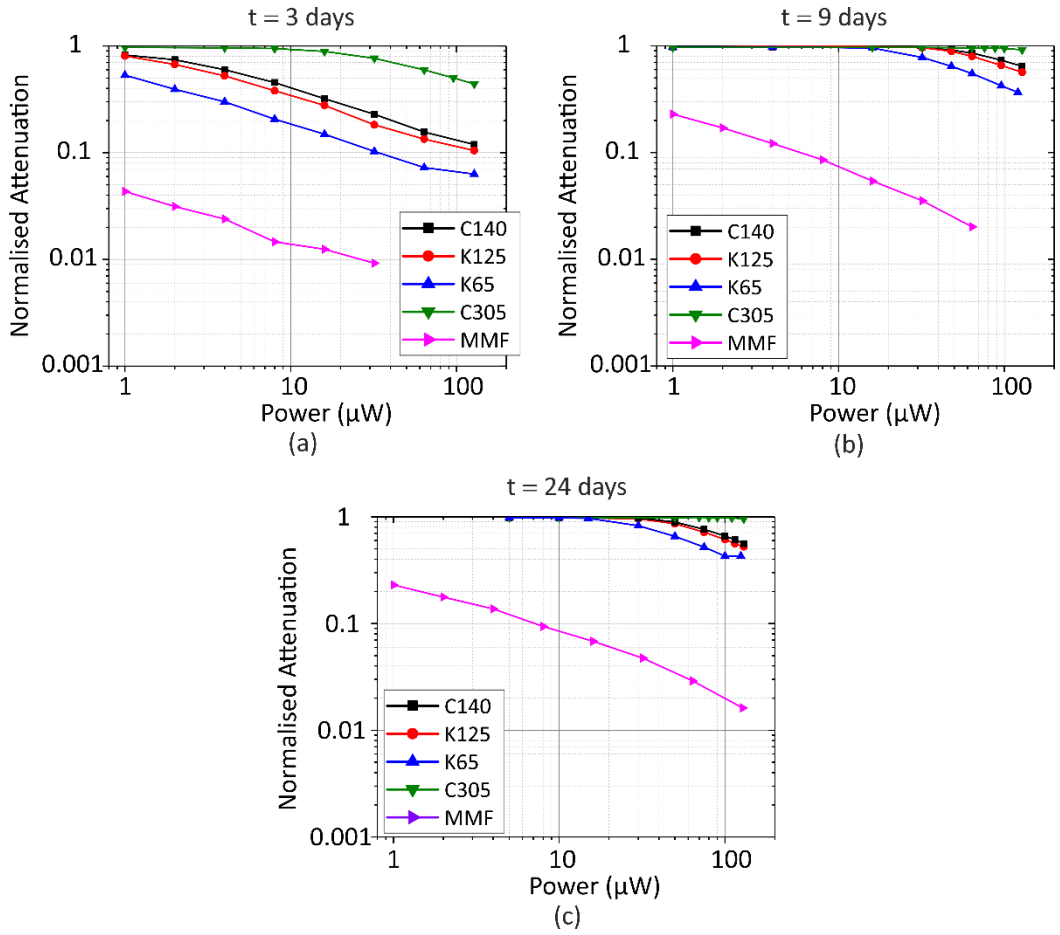

Figure 5.11:(a) Attenuation caused by the transition $6^2S_{1/2}F = 4 \rightarrow 6^2P_{1/2}F' = 3$ as a function of optical power for the two K-ARFs (K125 and K65), two capillaries (C140 and C305), with inner diameter of $140\ \mu m$ and $305\ \mu m$, respectively, and control fibre MMF. (b) and (c) show the same plot with different data set collected six days and twenty-one days after (a). Data set shown in (a) was taken three days after the filling started.

The filling rate can be inferred by comparing the data set from plots Figure 5.11(a), (b) and (c). Note that in nine days of filling, the optical attenuation reached $24\ dB$ for $1\ \mu W$ of input optical power for every hollow core sample (K-ARF and capillary) and only $1.25\ dB$ for the control fibre MMF. This rate is much faster than the one described in Figure 5.9(a) and was obtained by increasing the insulation around the hot areas and decreasing the temperature drastically at the fibre holder. This could only be achieved by replacing the solenoid apparatus with the Helmholtz coils set. By doing so, the fibre feedthrough region was opened to the environment, increasing its heat transfer to the environment and thereby, cooling down the central section of the fibres. The attenuation did not evolve from $t = 9\ days$ to $t = 24\ days$, as shown in Figure 5.11(b) and (c). This indicates that the atomic diffusion stabilised in the chambers and, mostly important, inside the fibres by day 9.

The estimate of the atomic density was made based on the data presented in Figure 5.11(a), (b) and (c) and using Eq. 5.10 and the piece of theory developed here and found in the literature [4], [5]. The curve described by Eq. 5.10 was adjusted to fit to the data set considering a length of $\Delta L = 90\ mm$ for hollow core fibre samples (K-ARFs and capillaries) and $\Delta L = 4\ mm$ for the control fibre (MMF). The optical beam path, ΔL, is defined as the interaction path between atomic vapour and photons. For example, as the interaction path for HC-PCFs their whole extension, it is sensible to define the interaction length to be equal the fibre sample length. In the case of MMF, since it is the case of a solid core fibre, the interaction path is restricted to be only the gaps between the fibre end faces and the inner surface of the viewport, estimated to be $\sim 2\ mm$, in each end. A gap of $2\ mm$ was also considered in every hollow core fibre and capillary at each end. The cross-section and saturation intensity were set to $\sigma_0 = 4.82 \times 10^{-14}\ m^{-2}$ and $I_{sat} = 12\ W/m^2$, respectively, and the average atomic density $\langle n \rangle$ was the tuning parameter. The optical beam diameter was set to be 78% of the hollow core fibre diameter and the 65% of the beam diameter for the MMF [6].

Table 5.3 lists the fixed parameters and the atomic density, tuned to best fit with the experimental data, shown in Figure 5.11(a), (b) and (c). The number of atoms in the hollow core was calculated directly from the atomic density. It was estimated that the atomic densities were around $10^8\ cm^{-3}$ at day three, $10^9\ cm^{-3}$ at day nine and remained stable for the next fifteen days. Figure 5.12(a), (b) and (c) depict the theoretical curves adjusted using the parameters found in Table 5.3 for the fibre samples K65, K125 and the control MMF.

Table 5.3 Estimated average atomic density.

Fibre	Length (mm)	Beam Diameter (μm)	Atomic Density $\langle n \rangle$ $(\times 10^8\ cm^{-3})$			Estimated number of atoms in the hollow core at $t = 24\ days$ $(\times 10^6)$
			$t = 3\ days$	$t = 9\ days$	$t = 24\ days$	
K65	90	~49	9.5	72	78	2.2
K125	90	~97	7.8	48	50	5.3
C140	90	~105	8.2	45	42	5.6
C305	90	~229	15	40	50	31.5
MMF	4	~130	8	40	45	NA

The figures estimated for atomic vapour densities in fibres are closely comparable to reported values found in [7]–[9]. Although the Rb vapour was the atom vapour of choice of some of other groups, the filling mechanism is comparable to Cs vapour and it is expected that they have similar densities at comparable laboratory conditions.

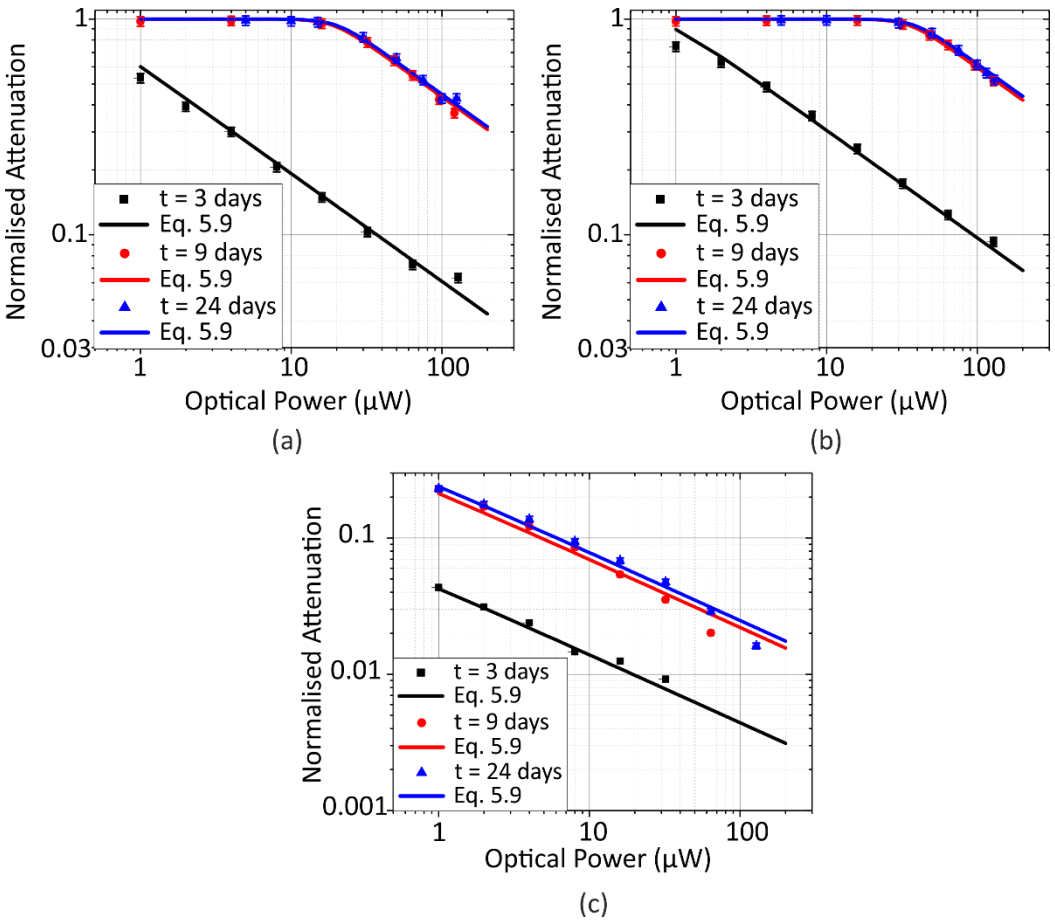

Figure 5.12: Attenuation model adjusted to data set for (a) K65, (b) K125 and (c) MMF. The data set for $t = 3\ days$, $t = 9\ days$ and $t = 24\ days$ are depicted by black squares, red circles and blue triangles, respectively, and the associated model (Eq. 5.10) curves are represented by solid line with respective colours. The error bars are of the same size as the data marker.

Table 5.4 Power Cut-off for opaque-translucent medium in HC-PCFs filled with Cs vapour

Fibre	Length (mm)	Cut-off power (μW)		
		t=3 days	t=9 days	t=24 days
K65	90	< 1	15	15
K125	90	< 1	30	30
C140	90	< 1	30	30
C305	90	< 1	100	> 100
MMF	4	< 1	< 1	< 1

Furthermore, the investigation of the Cs absorption line also indicated the cut-off power at which the atomic medium becomes translucent. Table 5.4 lists the cut-off power in μW for each HC-PCF and capillary sample used for this study. Following the analysis and the hypothesis raised in this chapter, it is expected that CPT dark resonance can only be observed for laser input power values higher than the power cut-off. Therefore, CPT dark resonance can only be present for $P > 15\ \mu W$, for $K65$ and $P > 30\ \mu W$, for K125. It is unlikely to observe dark resonance in $C305$ filled capillary,

since its power cut-off is closer to the maximum input power delivered by the laser system used for this study. A detailed analysis of the CPT dark resonance spectroscopy of the fibre and capillary samples are presented is presented in the next chapter.

5.4 Conclusion

In this chapter I have presented the UHV system designed and built for the purpose of filling HC-PCFs with Cs vapour and performing CPT spectroscopy of the atoms found within the hollow core. I was in charge of the technical design and assembly of the system. I have received technical advice from Prof Patrick Gill, Dr Mohsin Haji and Dr Thomas Bradley in order to complete this task. An optical system was built around the UHV system to comply with optical requirements of high coupling efficiency and light collection.

Longitudinal and homogenous magnetic fields are a requirement for CPT spectroscopy. Two different methods to generate such fields were built and calibrated. I have considered the use of solenoid and Helmholtz coils sets to meet the tight requirements for longitudinally homogeneous and centre strength necessary for success. I have simulated and demonstrated that Helmholtz coils can be designed to produce elongated longitudinal and homogenous fields with a radial field as small as 1% of the longitudinal maximum value. This limit is close to the theoretical value defined in simulations.

I discussed the experimental aspects of fibre filling, showing the increased attenuation in HC-PCFs, compared to solid core fibres. This is a direct result of the atomic vapour ingression in the hollow core, increasing the interaction path – where atoms can interact freely with the photons – by one order of magnitude. I also theoretically described and demonstrated the effect of high optical intensity in the shape and ultimate attenuation of transition lines. A model was derived from which I can extract the information on the atomic density found within the beam path and inside the hollow core.

Finally, I have estimated the atomic density of HC-PCFs and capillaries using the optical attenuation data and fitting to the analytical model described in the references [4], [5]. Through data fitting, I have inferred a Cs vapour density of $\sim 10^8\ cm^{-3}$, for three days of filling, and $\sim 10^9\ cm^{-3}$, for nine days of filling in my current system. Those numbers are close to atomic densities reported for Cs and Rb vapours by other groups [7]–[9]. Power cut-offs were defined to each fibre and capillary sample, according to the theoretical model developed in this chapter. Those figures discriminate the infimum input laser power at which CPT dark resonance is visible. For values below this threshold, the photon scattering is so high that it prevents the atoms to be found in a superposition of dressed states.

5.5 Chapter References

[1] D. Steck, “Cesium D Line Data,” Notes, pp. 1–31, 2008. URL: https://steck.us/alkalidata/cesiumnumbers.1.6.pdf

[2] J. D. Jackson, *Classical Electrodynamics*, 3rd ed. Wiley, 1998.

[3] C. Cohen-Tannoudji, B. Diu, and F. Laloë, “Quantum Mechanics Vol. I,” Wiley-VCH. 1977.

[4] P. Siddons, C. S. Adams, C. Ge, and I. G. Hughes, “Absolute absorption on rubidium D lines: comparison between theory and experiment,” *J. Phys. B At. Mol. Opt. Phys.*, vol. 41, no. 15, p. 155004, Aug. 2008.

[5] D. E. Jones, J. D. Franson, and T. B. Pittman, “Saturation of atomic transitions using subwavelength diameter tapered optical fibers in rubidium vapor,” *J. Opt. Soc. Am. B*, vol. 31, no. 8, p. 1997, Aug. 2014.

[6] D. Marcuse, “Loss Analysis of Single-Mode Fiber Splices,” Bell Syst. Tech. J., vol. 56, no. 5, pp. 703–718, 1977.

[7] C. Perrella, P. S. Light, S. A. Vahid, F. Benabid, and A. N. Luiten, “Engineering Photon-Photon Interactions within Rubidium-Filled Waveguides,” *Phys. Rev. Appl.*, vol. 9, no. 4, p. 044001, Apr. 2018.

[8] T. D. Bradley *et al.*, “Ground-state atomic polarization relaxation-time measurement of Rb filled hypocycloidal core-shaped Kagome HC-PCF,” *J. Phys. B At. Mol. Opt. Phys.*, vol. 49, no. 18, p. 185401, Sep. 2016.

[9] S. Ghosh, A. R. Bhagwat, C. K. Renshaw, S. Goh, A. L. Gaeta, and B. J. Kirby, “Low-Light-Level Optical Interactions with Rubidium Vapor in a Photonic Band-Gap Fiber,” *Phys. Rev. Lett.*, vol. 97, no. 2, p. 023603, Jul. 2006.

Chapter 6 Coherent Population Trapping in Kagome Lattice Anti-Resonant Fibres

Foreword

HC-PCFs are very attractive for gas phase light-matter interactions as they play a double role of housing the atom or molecule in the gas phase while providing maximum interaction between guided photons with the specimen confined in the hollow core. Over the last two decades, prestigious research groups worldwide have investigated the use of HC-PCFs (HC-PBGFs and ARFs) for non-linear effects [1]–[3], frequency combs [4], four-wave mixing [5], photon-photon interactions [6], [7] Rydberg atoms [8], electromagnetically induced transparency [9]–[11] and single-photon quantum memories [12]. For alkali atomic vapour in particular, I highlight the achievements of five main research groups. Prof Ian Walmsley's group at Oxford University has demonstrated a single photon-level memory using Cs-filled K-ARF [12]. Prof Hidetoshi Katori's group at Tokyo University has developed a complex system that could optically trap and cool down Rb atoms and move trapped cold atom clouds inside the hollow core of a K-ARF, demonstrating narrow atomic features with a line-width of $\sim 8\ kHz$ [13]. Prof Alexander Gaeta's group at Cornell University (now at the University of Columbia) and Prof Fetah Benabid's group at the University of Bath (now at the University of Limoges) have extensively studied Rb atomic vapours in HC-PBGFs and K-ARFs, developing and demonstrating passive and active methods to control the atomic density within the hollow core [5], [14]–[19]. Prof Andre Luiten's group at the University of Adelaide has demonstrated the use of Rb-filled K-ARFs for two-photon interactions [6], [7], [20]. Mostly important, they have also demonstrated for the first time a Rb vapour loaded HC-PCF frequency standard, with an atomic feature line-width of $\sim 10\ MHz$ and a fractional frequency stability of $\sim 10^{-11}$ for an integration time of $1\ s$ [21]. The research conducted by the groups led by Prof Gaeta, Prof Luiten and Prof Benabid at their respective institutions serve as a stepping stone for further implementation towards fibrerised and compact reference cells – or, in short, *photonic vapour cells*.

This chapter demonstrates coherent population trapping in K-ARFs, as an alternative to obtain narrow atomic features for time and frequency reference applications. As described in chapter 4, the vapour dynamics impact directly the ultimate line width of CPT dark resonances, where methods to control atomic collisions are required to increase the coherence time and therefore decrease the atomic feature line-width. Prof Benabid's group has extensively studied the effects of anti-relaxation coatings in HC-PCFs Rb filled samples on the dwell-time according to the coating material applied [16]–[19]. Unfortunately, their findings indicate that the complexity of applying a

homogeneous layer of anti-relaxation coating over the inner walls of the K-ARFs decreases the efficiency of the coating, decreasing drastically its anti-relaxation properties.

I demonstrate in this chapter the feasibility of adding a mixture of buffer gas into HC-PCFs samples, filled with Cs-vapour, as a method to increase the coherence time of Cs-vapour. Firstly, I have performed coherent population trapping spectroscopy in the D line hyperfine transitions $6^2S_{1/2}F = \{3,4\} \rightarrow 6^2P_{1/2}F = 3$ to every fibre and capillary samples present in the chamber and filled with pure Cs-vapour. I report the contrast and line-width of the CPT dark resonance as a function of the input laser power, magnetic field and polarisation of light for each sample. The second and most important experiment performed and reported in this chapter, is the coherent population trapping of Cs vapour loaded K-ARFs and capillaries in the presence of buffer gas. The dark resonance measured was characterised as a function of the input laser power and buffer gas back ground pressure. The main results of this thesis is presented in section 6.2 of this chapter.

6.1 Dark Resonance Spectroscopy in Pure Cs Vapour-Loaded Kagome Lattice Anti-Resonant Fibres

The study of CPT in HC-PCFs filled with pure Cs vapour is essential to define the underlying impact of the geometry and vapour dynamics on the dark resonance shape and strength. The characterisation of the CPT dark resonance contrast and line-width can indicate the expected frequency stability of the resonance, when used as a frequency reference. The short-term frequency deviation of a given CPT resonance can be defined as [25],

$$\sigma(t) \approx \frac{1}{\sqrt{2}}\left(\frac{\sqrt{RIN}}{4C_{CPT}}\right)\left(\frac{FWHM_{CPT}}{\nu_{centre}}\right)t^{-1/2}, \qquad \text{Eq. 6.1}$$

where RIN is the relative amplitude noise, C_{CPT} is the CPT resonance contrast, ν_{centre} is the CPT resonance central frequency, t is the averaging time and $FWHM_{CPT}$ is the CPT resonance width. From the expression above, one can infer that the frequency stability is directly proportional to the FWHM of the resonance and inversely proportional its the contrast. Therefore, if one seeks to minimise the deviation function, one needs to minimise the FWHM and maximise the contrast.

In chapter 4, I have described theoretically and experimentally the CPT mechanism. It was demonstrated that the dark resonance line-width and contrast, obtained from pure Cs vapour cells, are governed mainly by temperature, power and optical beam-width. In other words, transit-time, optical power and Doppler effect are the main broadening mechanisms. It is therefore expected that these effect will still be critical for *photonic cells* with micron-metre scale cross section. The diminished hollow core sizes of K-ARFs ($50 - 130\ \mu m$ in diameter), compared to commercially

available reference cells (inner diameters above $1\,mm$ in diameter), affect the dark resonance shape through transit-time broadening and laser power broadening. This is a direct consequence of the short time-of-flight for transiting atoms across the optical mode and the large optical intensities carried by the waveguide modes. Figure 6.1 (a) shows a microscope image of a typical K-ARF microstructure cross-section.

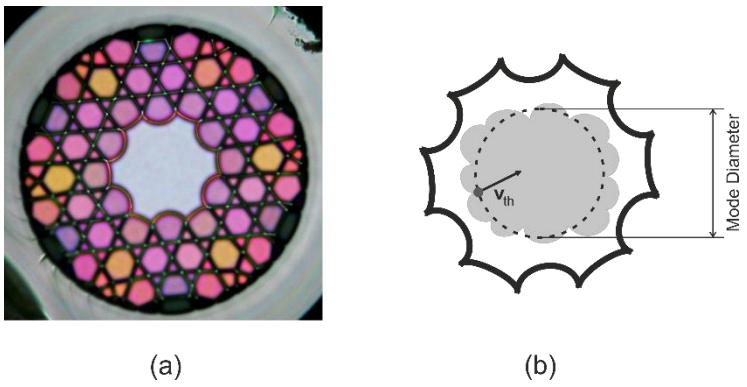

Figure 6.1: (a) Cross-section of a K-ARF with hollow core inner diameter of $\sim 65\,\mu m$. (b) Simplified diagram highlighting the atom dynamics inside the K-ARF's hollow core.

The time-of-flight can be estimated as being the time required for an atom to cross the optical beam path transversally, as shown in Figure 6.1 (b). Assuming that the Cs atoms travels with a thermal velocity v_{th} and that the optical beam is the fundamental mode supported by the K-ARF, with mode field diameter, d_{FM}, the time-of-flight, τ_{tt}, can be defined as,

$$\tau_{tt} \equiv \frac{d_{FM}}{v_{th}}. \qquad \text{Eq. 6.2}$$

Fundamentally, the time-of-flight of atoms is related spectrally to as transit-time broadening, as discussed in chapter 4. The broadening effect is proportional to reciprocal of the time-of-flight, $\gamma_{tt} \sim \frac{1}{\tau_{tt}}\ [Hz]$. It is expected, therefore, that the transit-time broadening will be in the MHz range for Cs vapour at room temperature, enclosed in hollow core fibres with diameter of $100\,\mu m$ and thermal velocity around $200\,m/s$.

Optical power broadening, γ_P, is related to the pumping rate of the hyperfine states participating in the effect. It is generally modelled by the term, $\gamma_P \sim \left(\frac{\Gamma}{2\pi}\right)\left(\frac{I}{I_{sat}}\right)\ [Hz]$, where I and I_{sat} is the beam intensity and the saturation intensity of the transition used in for CPT respectively. For Cs atoms, the D-lines $6^2S_{1/2}F = \{3,4\} \rightarrow 6^2P_{1/2}F = 3$ transitions have theoretical saturation intensities of $\sim 12\ W/m^2$ [26]. Therefore, in order to minimise optical power broadening in photonic cells with hollow core diameter below $100\,\mu m$, the required input laser power is of the order of tens of nW. At such low powers, detection may become a challenge, requiring the use of special techniques to

measure weak signals that are likely embedded in noise. In summary, it is expected that dark resonances observed in Cs vapour filled K-ARFs will present line-widths in the MHz range and strong dependency over the laser input power. In the following I describe in detail the CPT spectroscopy I carried out with the K-ARFs and capillaries I filled with Cs vapour. Please refer to chapter 5 for details regarding the Cs vapour loading and filling measurements.

The CPT dark resonance was measured as a function of the applied magnetic field, optical input power and polarisation state of light for four K-ARFs, two K65 and two K125, with hollow core diameter of $65\ \mu m$ and $125\ \mu m$, respectively. Two capillaries, C140 and C305, were also filled and measured. Table 5.2 lists the main attributes of the fibre samples, temperature and estimated number of atoms in the hollow core of each sample. The use of capillaries in this case can provide further insights on the role of transit-time broadening and power broadening in radially confined micro cells. Because of the complex construction of the vacuum chambers, the temperature could not be varied, with the risk of depleting the atomic density from the hollow core of the K-ARFs and capillaries. The temperature was therefore set to $47\ C$ during filling and kept within $\pm 1\ C$ throughout the measurements.

Table 6.1: Hollow core fibres attributes and filling status by the moment of measurement

Fibre Sample	**K65**	**K125**	**C140**	**C305**
Diameter $(\boldsymbol{\mu m})$	~65	~125	~140	~305
Length $(\boldsymbol{mm})$	~86	~86	~86	~86
Estimated number of atoms $\times \mathbf{10^6}\ \boldsymbol{atoms}$	~2.2	~5.3	~5.6	~31.5
Temperature $(\boldsymbol{C})$	47 ± 1	47 ± 1	47 ± 1	47 ± 1

The samples studied in and reported in this section were filled uninterruptedly for four weeks, as discussed in chapter 5. The filling status of each sample at the end of the filling period is listed in Table 6.1. The magnetic field used for the CPT feature characterisation was generated by the Helmholtz coils set (geometry and characterisation presented also in chapter 5), with a longitudinal field strength ranging from $\sim 0\ mT$ to $\sim 4\ mT$. The laser power was varied from $5\ \mu W$ to $\sim 140\ \mu W$ using a fibre attenuator and the polarisation was set to circular, unless stated otherwise. The light coupling efficiency was kept above 60% to all samples using the telescope arrangement also described in chapter 5.

The dark resonance spectroscopy was observed through the two photon resonance with the Cs D1 line, on transitions $6^2S_{1/2}(F = \{3,4\}, m_F = 0) \rightarrow 6^2P_{1/2}(F' = 3, m_{F'} = \pm 1)$. It was achieved by

modulating the EOM, sweeping the $q = +1$ side-band across the $6^2S_{1/2}(F = 3, m_F = 0) \rightarrow 6^2P_{1/2}(F' = 3, m_{F'} = \pm 1)$ transition, while the carrier was locked on the $6^2S_{1/2}(F = 4, m_F = 0) \rightarrow 6^2P_{1/2}(F' = 3, m_{F'} = \pm 1)$ transition. Figure 6.2(a) and (b) show examples of the dark resonance observed in Cs filled K65 (a) and K125 (b) with the Helmholtz coils switched off (black trace) and with a magnetic field of $B \sim 3.6\, mT$ and $B \sim 1.8\, mT$ (red trace). Note that the dark resonance is asymmetric for the case for $B \sim 0\, mT$. This asymmetry manifests itself as a result of the presence of external magnetic fields (Earth's magnetic field and other sources inside the laboratory), in the absence of a magnetic field shielding assembly around the fibre chambers. This external field was measured about the fibre chambers and its longitudinal component (in the laboratory frame) was less than $0.1\, mT$.

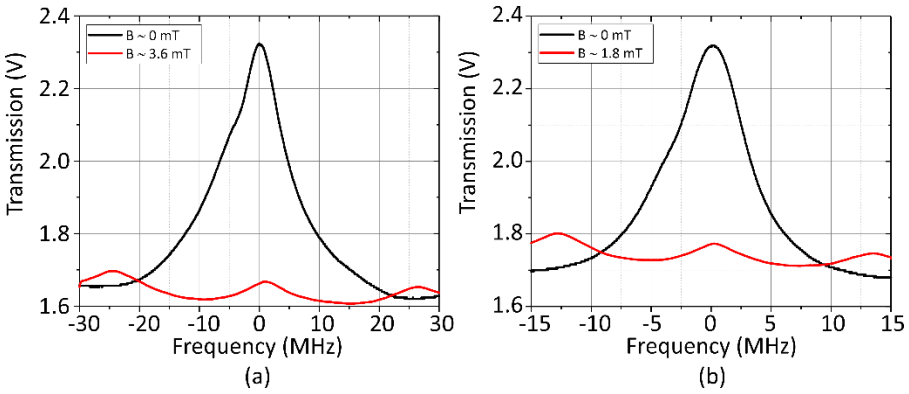

Figure 6.2: Examples of CPT dark resonance observed in (a) K65 and (b) K125 filled with Cs vapour. Black traces depict the dark resonance without applying a controlled magnetic field and the red traces are for applied fields of $\sim 3.6\, mT$ and $\sim 1.8\, mT$. The asymmetry observed in the case of $0\, mT$ is a direct result of the absence of mu-metal shielding and the presence of a weak external magnetic field ($< 40\, \mu T$).

In the following three sections, I discuss the dark resonance response to optical power, magnetic field and polarisation state of the light.

6.1.1 Dark Resonance Response to Optical Power Variation

The dark resonance contrast and line width response to optical power were measured for input laser powers from $5\, \mu W$ to $140\, \mu W$, for two magnetic field values, $\sim 0\, mT$ and a high strength field and for circularly polarised light. The high magnetic field strength was set at the minimum value where the Zeeman splitting was sufficient to resolve the various dark resonance associated with each Zeeman ground hyperfine states $|F, m_F\rangle$, with $F = \{3,4\}$ and $m_F = \{-F, -(F-1), \ldots, -1, 0, 1, \ldots, F-1, F\}$, avoiding resonance overlaps. Two high values were therefore used, $\sim 1.8\, mT$ for samples C305, C140, K125 and MMF, and a stronger longitudinal field of $\sim 3.6\, mT$ for the K65 sample. The latter was required, since the smaller hollow core of K65 fibre yielded broader resonances, as a result of the shorter time of flight and increased beam intensity at same input laser

power. The measurement was taken as follows. Initially the input laser power was set to a given value with the Helmholtz coils turned off. The signal obtained by the direct sweep of the EOM was integrated over 30s to reduce the presence of low frequency noise components and recorded using the 8-bit oscilloscope. The Helmholtz coils were turned on with a given current set to pass through the circuit and the measurement was then repeated for a high magnetic field.

The CPT dark resonance related to the atomic density found at the end gaps (region between the fibre ends and the internal surface of the viewports) was measured and showed diminished contrast compared to values attributed to the HC-PCF and capillary filled samples, as showed in Figure 6.3 (a). As discussed in chapter 4, the CPT contrast is directly related to the number of atoms contributing to the effect. Since the HC-PCFs and capillaries inherently possess longer interaction paths ($\sim 90\ mm$), compared to the short interaction path for end gaps ($\sim 2\ mm$ to $\sim 4\ mm$), it is expected to observe stronger signals from atoms found in within the HC-PCF and capillary beam paths.

The contrast as a function of the input laser power showed slightly different behaviour in the presence and absence of magnetic fields. As shown in Figure 6.3(a) and (c), the CPT dark resonance was only observable from $15\ \mu W$ for K65, $20\ \mu W$ for K125 and C104 and over $80\ \mu W$ for C305. Those values are directly related to the power cut-off, described in chapter 5, and they are a consequence of the atomic density of the medium. For optical power values below the cut-off, the transition absorption is so high that medium becomes opaque at resonant frequencies. The contrast curve as a function of the optical power behaved as expected for CPT dark resonance using circularly polarised light. In this case, it is expected that the contrast increases linearly in the low power range, reaches a maximum and then decreases in the high laser power regime. In the absence of magnetic fields, the maximum contrast observed for K65, K125 and C104 ranged above $40\ \%$ of the back ground signal. This rather large contrast value is a direct result of the presence of various CPT resonances, associated with transitions $|m_F\rangle \rightarrow |m_{F'} = m_F \pm 1\rangle$, with $m_F \neq 0$, superposing upon each other. On the other hand, In the presence of magnetic fields, the maximum contrast reduced to less than $4\ \%$ of the back ground level. This reduction was expected since, at high magnetic fields, only CPT resonances associated with transitions $|m_F = 0\rangle \rightarrow |m_F = \pm 1\rangle$ are seen in the sweep range.

The CPT line-width as a function of power showed a linear trends for all samples, in the absence and presence of magnetic fields, as shown in in Figure 6.3(b) and (d). The line-width behaved as expected in both regimes (with and without magnetic field). The trends showed a strong dependency over optical power, as a result of ultra-high optical intensities being carried through the Cs-filled hollow cores. In terms of absolute values, the CPT dark resonance line-width was in the

few MHz range. Sample K65 showed the broadest lines ($\sim 5\ MHz$ to $\sim 14\ MHz$) This followed our expectations, as K65 possesses the shortest time-of-flight value ($\sim 200\ ns$) among all samples. The second largest was K125, with absolute values ranging from $\sim 4\ MHz$ to $\sim 9\ MHz$, followed closely by C140. C305, which had a diminished signal, was only observable in the high power regime, without applying a strong magnetic field. At detectable ranges, the CPT resonance was around $4\ MHz$.

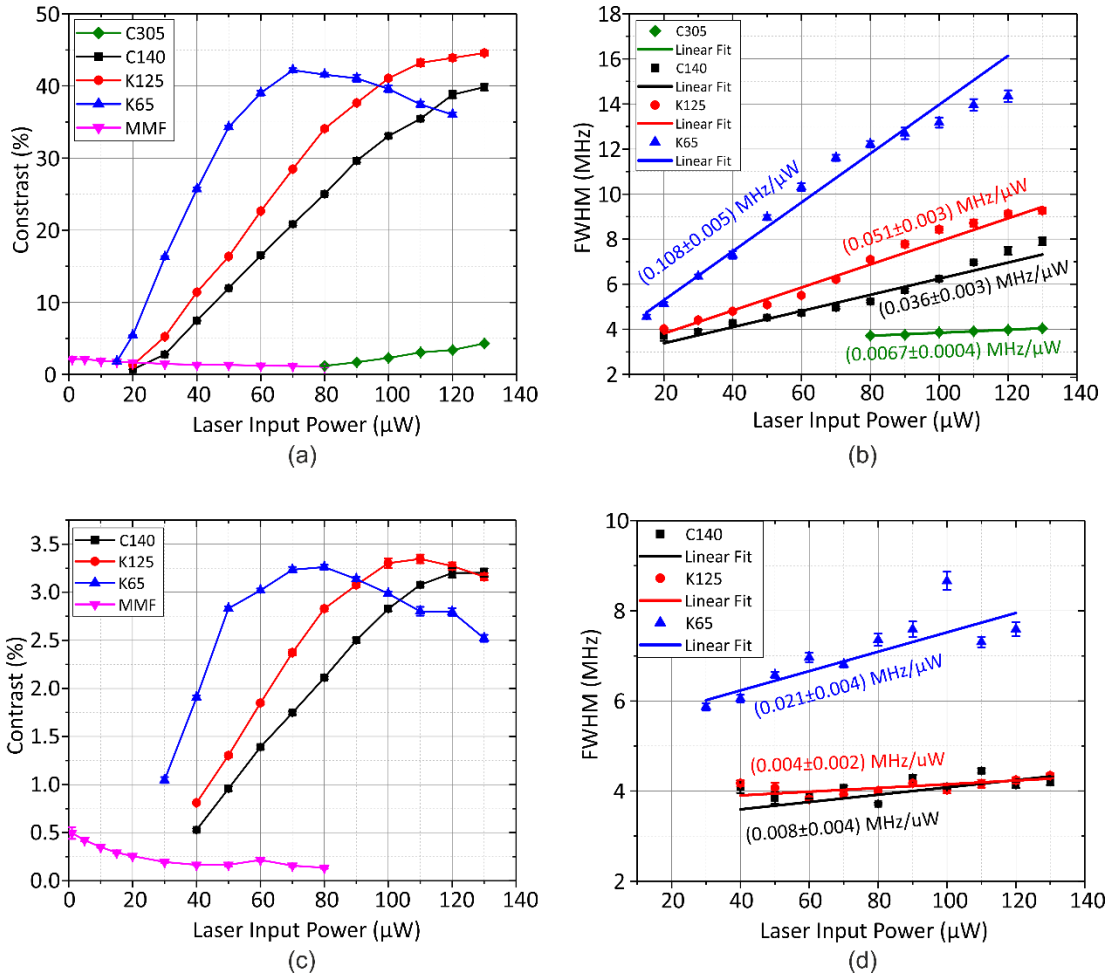

Figure 6.3: CPT dark resonance (a) contrast and (b) line width observed in fibre and capillary samples in absence of a magnetic field. A maximum contrast of above $40\ \%$ was observed for K65, K125 and C140 samples and a line-width that varied linearly with the power in the MHz range. In the presence of high magnetic field strengths, the contrast (c) reduced to maximum below $4\ \%$, while the line width had a decreased dependency on optical power. The magnetic field strength values were $\sim 3.6\ mT$ for K65 and $\sim 1.8\ mT$, for K125, C140, C305 and MMF.

From Figure 6.3(b) and (d), the data set of each sample was fitted and the gradients obtained are listed in Table 6.2. This angular coefficient is the power broadening rate and it was observed that CPT spectroscopy in the presence of magnetic field, the rates were from four times to over one order of magnitude weaker than in the absence of fields. Without an external source of magnetic field, the CPT peaks overlap each other, with a slight asymmetry caused by interference of the

different magnetic sources (earth's natural field and any other weak sources found in the lab). This perturbation is of the order of $100\ \mu T$ and it is enough to distort the dark resonance shape by weakly shifting the various Zeeman sensitive resonances away from the central frequency ($\sim 9.2\ GHz$). Those various peaks are prone to broadening effects such as transit-time and power broadening. The superposition of the various Zeeman sensitive resonances, slightly shifted in frequency according to their associated magnetic quantum number, amplifies the any broadening

Table 6.2: Line-width Power broadening rate with and without external magnetic field.

Sample	Expected transit-time broadening (MHz)	Gradient (kHz/μW)	
		Without Mag. Field	With Mag. Field
K65	~5.00	118 ± 5	21 ± 4
K125	~2.50	51 ± 3	4 ± 2
C140	~2.25	36 ± 3	8 ± 4
C305	~1.00	6.7 ± 0.4	NA

6.1.2 Dark Resonance Response to Magnetic Field Strength and Polarisation of Light Related Effects

In the previous section, I have demonstrated for the first time CPT in HC-PCFs filled with pure Cs vapour and its behaviour with optical power. A preliminary analysis of two values of magnetic field strengths ($\sim 0\ mT$ and $> 1.8\ mT$) showed various differences both in trends and absolute values for both contrast and line-width. In this section, I analyse the CPT behaviour in terms of contrast and line-width as a function of the magnetic field strength and polarisation of the light.

The polarisation of the light is intimately connected with the optical transitions, as they reflect the conservation of the angular momentum. For instance, the combination of atomic states required for the lambda configuration (CPT mechanism) considers the polarisation of light. Transitions between certain combination of hyperfine states, depending on the polarisation state and handedness, do not exist. Because of the experimental apparatus, where I was only able to investigate CPT with magnetic field co-linear to the beam path, only CPT generated with $\sigma^{+/-}$ transitions between Zeeman sub-states were studied. For example, CPT in D1 lines, $6^2S_{1/2}(F = \{3,4\}, m_F) \rightarrow 6^2P_{1/2}(F' = 3, m_{F'})$, have six resonances, for circularly polarised light, and seven resonances, for linearly polarised light. The seven resonances for the case of linearly polarised light is a direct result of the fact that linearly polarised light is an association of circularly polarised light with opposed handedness. Therefore, σ^+ and σ^- transitions are simultaneously driven by linearly polarised light. The missing resonance in the case of circularly polarised light is a direct result of the conservation of angular momentum. For the σ^+ transitions, the pair of hyperfine Zeeman ground states $6^2S_{1/2}(F = 3, m_F = 3)$ and $6^2s_{1/2}(F = 4, m_F = 3)$ do not form a lambda configuration, since there is no $6^2P_{1/2}(F' = 3, m_F = 4)$ state in the hyperfine excited state. Those states have a

secondary role in CPT mechanism as they would act as a trap state, as discussed in chapter 4. The difference in number of resonances depending on the polarisation state of light is easily observed when the longitudinal magnetic field is applied over the atomic ensemble. Figure 6.4(a) and (b) show the various CPT peaks measured from the sample K65 for a series of applied magnetic fields and for circularly and linearly polarised light, respectively. The magnetic quantum numbers m_F of the ground states are used to index each associated resonance and the magnetic field strengths used to obtain each curve are listed between Figure 6.4(a) and (b). Those graphs also show that the resonances shifted linearly with the magnetic field strength, regardless of the polarisation of light used. This behaviour was expected as the central frequency of the CPT resonances is defined by the energy gap between the two hyperfine ground states participating to the lambda configuration. If those states are magnetic field sensitive, i.e. $m_F \neq 0$, their associated energy, energy gap and, therefore, associated frequency will shift linearly as a function of the longitudinal magnetic field strength, in a first order approximation to weak magnetic fields. The resonance formed by $m_F = 0$ hyperfine ground states, or simply the 0-0 resonance, is called magnetic insensitive. This resonance shifts for strong magnetic fields and its shift rate is described by the Breit-Rabi formula, discussed in chapter 4.

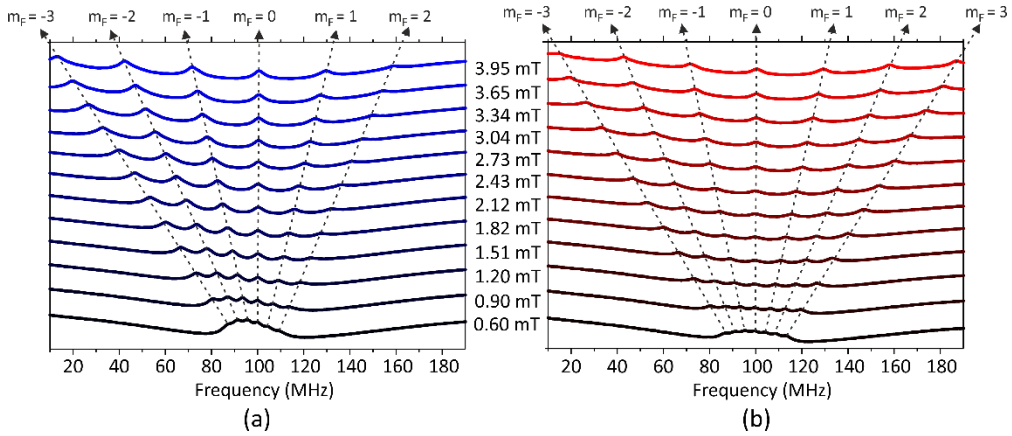

Figure 6.4: CPT dark resonance evolution for a selection of magnetic fields in Cs vapour D1 lines for circularly (a) and linearly (b) polarised light. The magnetic field strengths used are listed between graph and next to each associated curve. Note that linearly polarised light yields seven resonances while circularly polarised yields six resonances. Note also that the resonances frequency shift is linear to the magnetic field, following the Zeeman first order frequency shift. The CPT resonance presented in graphs (a) and (b) were measured from sample K65.

For time and frequency applications, the 0-0 resonance is the natural choice as its central frequency only shifts quadratically as a function of the magnetic field strength, and it is only noticeable in the presence of strong fields. The contrast and line-width of the 0-0 resonance was measured as a function of the magnetic field for a circular polarisation and linear polarisation of light and for a

laser input power of $70\ \mu W$, for fibres K65 and K125. The contrast and line-width observed from fibre K65 are shown in Figure 6.5(c) and (d). The fibre cross-section and a snapshot of the hollow core guide signal are shown in Figure 6.5 (a). In Figure 6.5 (c), note that the contrast decreased monotonically from $\sim 37\%$ (circular polarisation, black trace) and 30% (linear polarisation, red trace) to below $\sim 3\%$ (both polarisations), when the magnetic field was increased from $0\ mT$ to $2.5\ mT$, and increased monotonically to $\sim 4\%$. The line-width response was truncated by a region where the peaks heavily overlap each other (called here the unresolved range). The magnetic field range for unresolved peaks is from $0\ mT$ to $2.5\ mT$. Above $2.5\ mT$, the resonance broadens monotonically for both circular and linear polarisation states of light.

Figure 6.5(b) shows the K125 fibre cross-section and hollow core guided optical signal. The contrast and line-width for linear (red trace) and circular (black trace) are shown in Figure 6.5 (d) and (f). As reported for the K65 CPT contrast, the K125 CPT contrast decreased from $0\ mT$ to $\sim 1.7\ mT$ (both polarisations) and increased from $\sim 1.7\ mT$. The CPT line-width also increased monotonically from $\sim 1.7\ mT$. For values below $\sim 1.7\ mT$, the signal could not be resolved as a result of the overlap between the multiple peaks.

This general behaviour of increasing CPT contrast and line-width for both K65 and K125 samples indicates that there is an underlying relaxation mechanism connected to magnetic field strength and field variations. In this case, atoms freely moving in the atomic ensemble would experience the magnetic field fringing and curvature. According to Vanier and Audoin, if the magnetic perturbation components have a frequency similar to the atomic coherence, it can lead to relaxation of the densities through incoherent transitions [27]. In this experiment, the magnetic field was generated by a pair of Helmholtz coils, however the characterisation presented in chapter 5 only demonstrates the average variation of the field. Temporal instabilities of the current source should only be seen as a secondary effect, since the measurement system averages the signal over at least $30\ s$.

Differences between circularly and linearly polarised light were observed in the analysis. Sample K65 data indicates that the linear polarisation has an advantage over circularly polarised light in terms of line-width, allowing narrower lines in the high magnetic field strength range. This trend was not followed by K125 sample, which exhibited narrowed lines for circularly polarised light. In order to clarify this conflicting observations, I have run a third measurement, now considering circularly and linearly polarised light, but this time varying the optical input power. The results (CPT contrast and line-width as a function of the optical input power, for K65 and K125 filled fibres, and for two magnetic field strengths, $\sim 0\ mT$ and $\sim 3.6\ mT$) are shown in Figure 6.6 (a),(b),(c) and (d). The magnetic field strength, unlike in the first experiment described in the previous section, was

set to the same high value for both K65 and K125 samples. This guarantees that the magnetic field relaxation rate, observed in the previous experiment was set to be the same for both samples.

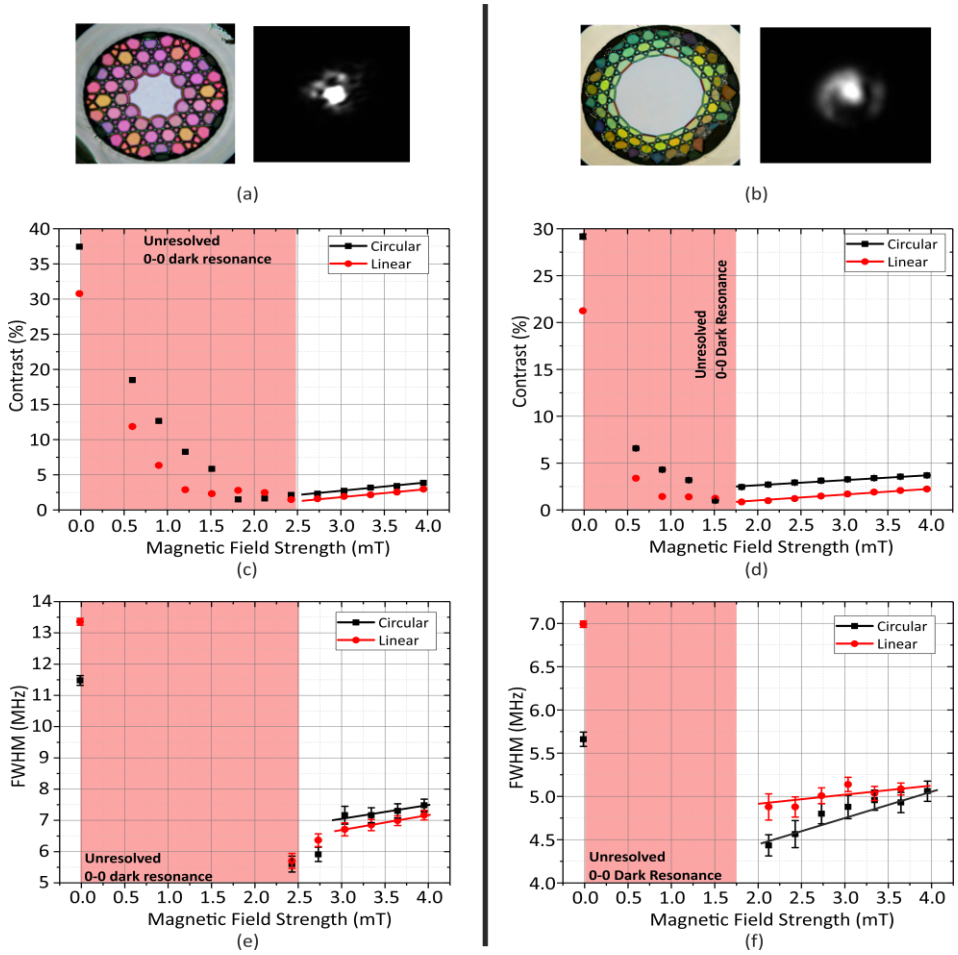

Figure 6.5: Cross-section and optical signal guided in the hollow core of K65(a) and K125(b). CPT contrast (c,d) and line-width (e,f) as a function of the applied magnetic field for K65 and K125 Cs filled samples. Black trace indicates data for circularly polarised light and Red trace, for linearly polarised light.

The CPT contrast for K65 and K125 Cs vapour filled samples showed similar behaviour when the magnetic field generator was turned off. For both K65 and K125 samples, circularly polarised light exhibits a stronger resonance contrast. Interestingly, at high magnetic field strengths, the contrast for K65, Figure 6.6 (a), varied by about $2.5\ \%$ for linearly polarised light, for optical input power varying from $60\ \mu W$ to $130\ \mu W$. For circularly polarised light, the contrast decreases monotonically from $3.7\ \%$ to $2\ \%$, for the same input optical power range. This plateau effect in the CPT contrast for linearly polarised light was expected as there is no trap state present when using this polarisation. For the K125 CPT contrast, Figure 6.6 (b), no plateau effect was observed for linearly polarised light. As this is an intensity related effect, it may be the case that stronger input optical powers are required to reach the range where the contrast stabilises.

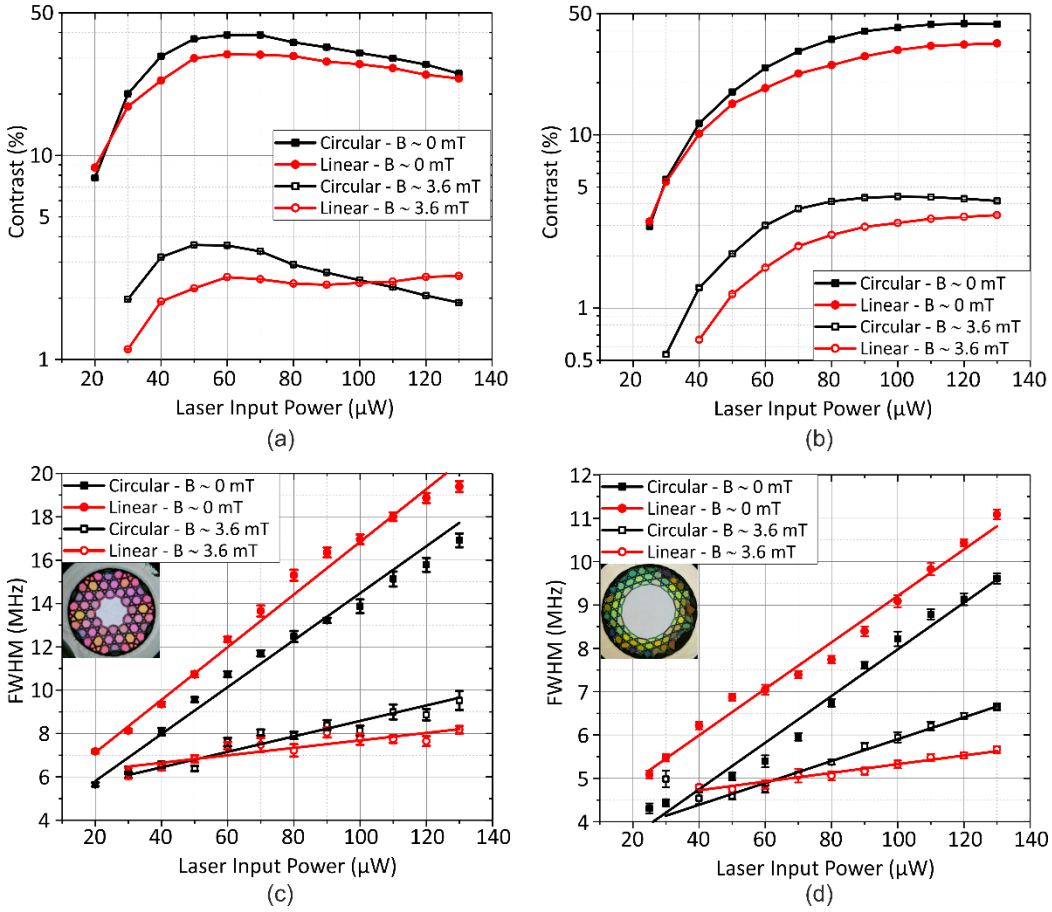

Figure 6.6: CPT contrast (a,b) and line-width (c,d) as a function of the optical input power for K65 and K125 Cs-filled samples, respectively. Red filled circles and black filled squares are the data related to linearly and circularly polarised light, in the absence of a longitudinal magnetic field. Red hollow circles and black hollow squares are the data related to linearly and circularly polarised light, respectively, and for $\sim 3{,}6\ mT$ longitudinal magnetic field applied.

The line-width response for both fibres showed very interesting behaviour for different polarisation states of light and in the high magnetic field regime. In the absence of a longitudinal magnetic field, both K65 and K125 Cs filled responses indicated that circularly polarised light yields a narrower CPT resonance. They also showed a similar optical power broadening rate, as can be inferred in Figure 6.6 (c) and (d), from red filled circles (linear polarisation) and black filled squares (circular polarisation). In the presence of a $\sim 3.6\ mT$ longitudinal magnetic field, the line-width response over power showed different power broadening rates for circularly and linearly polarised light. From the data, we can infer that linearly polarised light is broader in the low optical power range, compared to circularly polarised light, for both fibre sample cases. However, its gradient is also weaker than for circularly polarised light. As a result of the different broadening gradients, the line-width response for circularly and linearly polarised light intercepts at $\sim 50\ \mu W$, for K65, and at $\sim 65\ \mu W$, for K125. This explains the conflicting behaviour found in the previous experiment, where

linearly and circularly polarised light yielded different results for the CPT line-width as a function of the magnetic field strength.

In this section, I have demonstrated for the first time spectroscopy of coherent population trapping resonances in pure Cs-filled HC-PCFs and micrometre-scale glass capillaries. The dark resonance contrast and line-width were studied as a function of the optical input power, applied magnetic field and polarisation state of light. I reported line-widths in the MHz range and contrast over $30\ \%$, in the absence of magnetic fields and below $5\ \%$, in the presence of magnetic fields. The line-width at MHz range is a direct consequence of the transit-time broadening of Cs atoms at $48\ C$.

6.2 Narrowing of CPT Dark Resonances by Adding Buffer Gas in Cs-filled Kagome Lattice Anti-Resonant Fibres

In the previous section, I have described the CPT dark resonance in HC-PCFs and micron-scale capillaries filled with Cs vapour. Resonances with line-width ranging from $4\ MHz$ to $20\ MHz$, as a result of transit-time and optical power broadening, were observed. For time and frequency applications, narrow atomic feature are needed to obtain stable reference signals, as briefly introduced in the beginning of this chapter.

In this section, I demontrate for the first time a study on CPT resonance narrowing by mixing the Cs vapour with a combination of buffer gases. As detailed in chapter 4, a buffer gas slows down the movement alkali atoms through elastic collisions. In this way, the transit-time broadening effect ceases to exist and the CPT resonance line-width is now dictated by vapour diffusion through the buffer gas environment. The CPT line-width can, therefore, be tailor as a function of the buffer gas base pressure. This pressure dictates the number elastic collisions. In the following, I present the experimental description, presenting the buffer gas mixture chosen. I describe the method used to estimate the buffer gas base pressure. I report the measurement of the 0-0 resonance and the line-width and contrast response as a function of input optical power for a set of buffer gas base pressures.

6.2.1 Motivation and Experimental Description

The coherence time in the CPT phenomena is key in obtaining ultra-narrow dark resonances [24], [28], [29]. In alkali vapour cells, the coherence time is directly related with atom dynamics and the cell's geometry, as described in chapter 4. Among the various effects that are associated with relaxation of an atomic ensemble, atom-wall inelastic collisions and time-of-flight of atoms can be considered the main parameters to be controlled. The latter can be minimised by increasing the optical beam size – therefore decreasing the transit-time of atoms – and the former can be

controlled by coating the inner walls of the cell with an anti-relaxation material [18], [30]. The use of a buffer gas mixture addresses both issues, as it slows down the alkali vapour by increasing the number of elastic collisions. This increases the time-of-flight of atoms, while decreasing the probability of atom-walls collisions, since the atoms need to diffuse through an environment populated with inert gas.

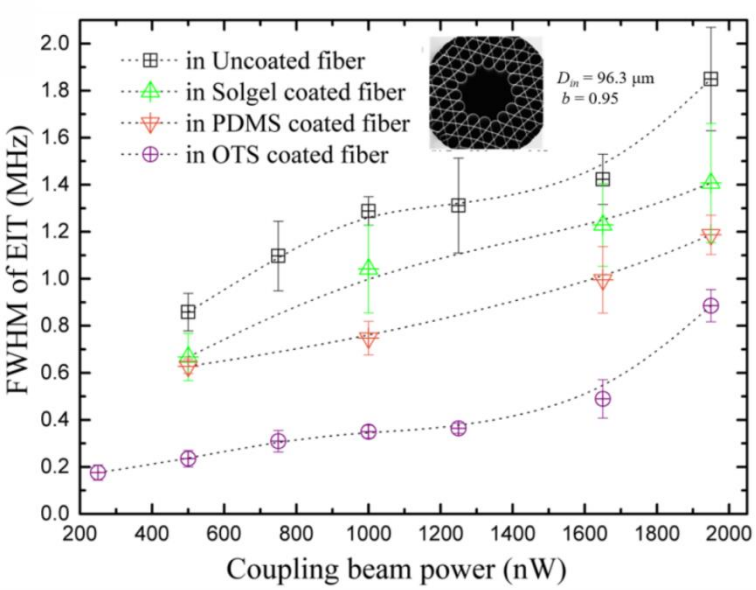

Figure 6.7: EIT line-width response as a function of the input laser power for three different K-ARFs with hollow core inner walls coated with Solgel, PDMS and OTS, and a reference uncoated sample. Note that the OTS coated K-ARF showed FWHM in the range of $200\ kHz$, for laser power of $\sim 250\ nW$. Extracted and adapted from [18].

In fibre reference cells, Prof Benabid's group at the University of Limoges (formerly at the University of Bath) has studied in detail HC-PCFs with hollow core inner walls coated with anti-relaxation materials [11], [16]–[19]. They have demonstrated improvement in the coherence time of Rb filled HC-PCFs by coating its inner core walls with different materials and, in a most recent study published, they reported the observation of sub-MHz line-widths of EIT features in coated HC-PCFs [18]. Figure 6.7 shows the EIT line-width response as a function of the input laser power for four different K-ARFs with a hollow core diameter of $\sim 100\ \mu m$. Note that the OTS coated K-ARF showed almost 4x narrower lines that the uncoated sample, with absolute line-width values varying from $\sim 200\ kHz$ to $\sim 1\ MHz$. Although no measurement of the contrast has been reported, this result is a major breakthrough in fibre reference cells technology. However, the photonic cells are still subject to a very delicate HC-PCFs post processing, involving homogeneously coating the inner hollow core walls of HC-PCFs with a polymer. This process is time consuming, poorly reproducible and can be subject to degradation over time.

The experiment detailed in this section was designed to address the challenge of controlling relaxation phenomena by adding a buffer gas mixture. With this technique, it is expected to obtain kHz level CPT line-width in HC-PCFs filled with Cs vapour. In chapter 4, I have defined an analytical expression for the diffusion of Cs atoms through a buffer gas environment and derived its associated relaxation rate as,

$$\gamma_{BG}^{I} = D\left[\left(\frac{2.405}{R}\right)^{2} + \left(\frac{\pi}{L}\right)^{2}\right] \qquad \text{Eq. 6.3}$$

where D is the homogeneous diffusion coefficient and R and L are the container radius and longitudinal length, respectively. Unlike the case for bulk vapour cells, where the radius and length are of the same order, HC-PCFs have a rather diminished cross-section, where for the case of this experiment, the ratio L/R is approximately 10^3. In this regime, the diffusion of atoms is dictated only by the cross-section.

In order to have a clear picture of the benefits of using buffer gas mixtures in Cs vapour filled HC-PCFs, let us assume the contribution of three broadening effects: atom diffusion (γ_{BG}^{I}), Eq. 4.41, transit-time (γ_{tt}), Eq. 4.30, and atom-atom collisions (γ_{BG}^{H}), Eq.4.45. As discussed in chapter 4, it was hypothesised that the diffusion and transit-time contributions leads to an effective relaxation, γ_{eff}, defined as,

$$\frac{1}{\gamma_{eff}} = \frac{1}{\gamma_{BG}^{I}} + \frac{1}{\gamma_{tt}}. \qquad \text{Eq. 6.4}$$

Thus, the total contribution of these three broadening mechanism is,

$$FWHM_{CPT} \sim 2\left(\gamma_{eff} + \gamma_{BG}^{H}\right) \qquad \text{Eq. 6.5}$$

This equation is useful to define the experiments limits regarding buffer gas pressure, considering the samples described in chapter 5 and in the previous section on CPT in pure Cs-filled samples, and making use of the parameters experimentally defined in chapter 4, section 4.3.3 (diffusion coefficient of $0.09\ cm^2/s$ and collisional cross-section of $3 \times 10^{-22}\ cm^2$). For that experiment, a mixture of Ar and N_2 of 29% and 71%, respectively was used. Figure 6.8 shows the calculated FWHM for the four K-ARF and capillaries samples analysed in the previous section. In the absence of optical power broadening, it is expected a minimum line-width of $\sim 1.5\ kHz$, $\sim 3.2\ kHz$, $\sim 3.7\ kHz$ and $\sim 7\ kHz$, for C305, C140, K125 and K65, respectively. Note also that the line-width decreases

monotonically for every sample for buffer gas pressures around $100\ torr$, and every curve has its global minimum at buffer gas pressure values beyond atmospheric pressure ($760\ torr$).

The theoretical analysis of the expected CPT line-widths for different buffer gas pressures shed light on two main challenges to be overcome. The first is related to the UHV system operating at pressures higher than the atmospheric. Most of the equipment used is calibrated to operate at low pressure values. For instance, Pirani pressure gauges and vacuum pumps used in this experiment would operate out of specifications at higher pressure ranges. The second point to be addressed is related to the Cs vapour behaviour in the presence of a large concentration of buffer gas. If not carefully performed, the buffer gas addition can deplete the Cs vapour density from inside the HC-PCFs and capillaries.

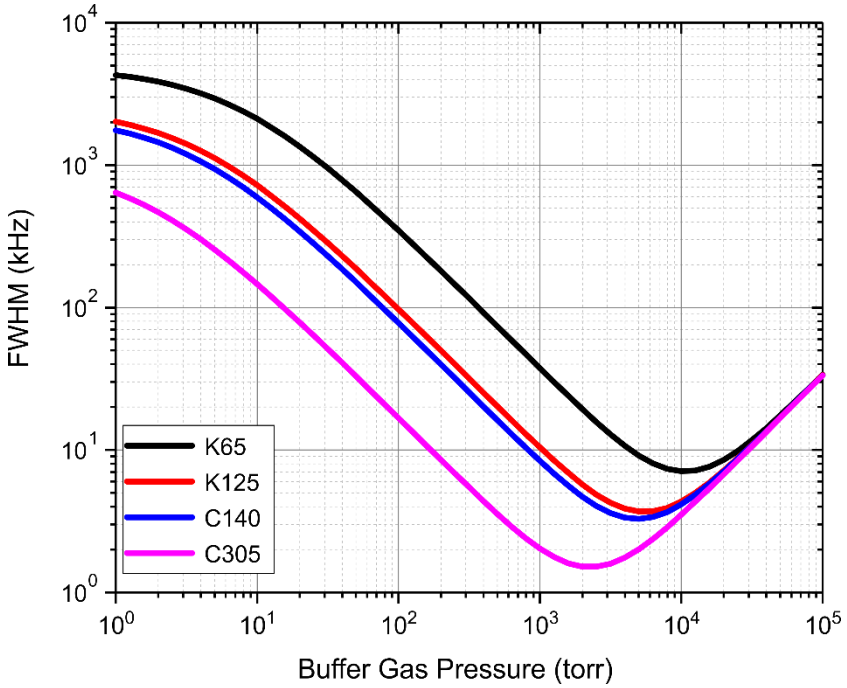

Figure 6.8: Calculated CPT line-width as a function of the buffer gas pressure for the four HC-PCFs and capillary samples characterised in the previous section. Optical power broadening was not considered in the analysis. Minimum line-widths of $\sim 1.5\ kHz$, $\sim 3.2\ kHz$, $\sim 3.7\ kHz$ and $\sim 7\ kHz$, for C305, C140, K125 and K65, respectively, are predicted. The parameters used in this calculation were experimentally defined in chapter 4, for CPT in millimetre size cells filled with Cs vapour and with a buffer gas mixture of Ar-N_2, with a ratio of 35%-65%, respectively.

In order to study the effects of the buffer gas in Cs-filled HC-PCFs and micrometre size capillaries, a mixture of Ar-N_2, with ratio $35\% - 65\%$ and with purity of 99.999% was injected into the UHV system using a precise needle valve. The samples used for this study are the same as those described in the previous sections, where I have measured the CPT in pure Cs-filled HC-PCFs and micrometre size capillaries. The samples geometrical parameters and Cs-filling status just before the measurement started are listed in Table 6.1. The buffer gas base pressure was indirectly

characterised by monitoring the Cs D1 lines shift. It is expected that such lines shifts linearly as a function of the Ar and N_2 partial pressures [31]. Four points of pressure were measured and the CPT spectroscopy of the 0-0 resonance was performed for each sample. The line-width, contrast and frequency shift were monitored during the experiment. In the following section, I discuss how the pressure values were estimated as a function of the Cs D1 line frequency shift.

6.2.2 Buffer Gas Pressure Characterisation

The HC-PCFs and capillary samples used in the experiments previously described were filled with a mixture of Ar-N_2, with partial ratios of $35\ \%$ and $65\ \%$. The filling was undertaken in a non-deterministic way, since the Pirani pressure gauge attached to the UHV system was not calibrated for this type of gas mixture. The buffer gas base pressure was thereby characterised by monitoring the shift of the Cs D1lines, $6^2S_{1/2}F = 4 \rightarrow 6^2P_{1/2}F = 3$ and $6^2S_{1/2}F = 4 \rightarrow 6^2P_{1/2}F = 4$. Both gas specimens will cause a shift of the Cs D lines towards lower frequencies [31]. Kozlova et al. have studied in detail the frequency shift caused by N_2 and Ar specimens for Cs D1 lines and also the CPT resonance shift caused by same gases [31], [32]. According to their report, the frequency shift rate for applied pressure of Ar and N_2 are -6.63 ± 0.05 MHz/torr and -8.21 ± 0.02 MHz/torr, respectively, at a temperature of $295.5\ K$. The pressure for a given buffer gas can be determined by the following expression [31],

$$p = \frac{\Delta\nu}{\delta_m}\left(\frac{T}{T_m}\right), \qquad \text{Eq. 6.6}$$

where $\Delta\nu$ is the frequency shift, δ_m is the pressure frequency shift rate, T_m is the temperature at which δ_m was measured and T is the temperature of the atomic vapour. Eq. 6.6 can be adapted to a mixture of gas by simply replacing δ_m by its mean $\langle\delta\rangle = \sum a_m\delta_m$, where a_m is the normalised concentration of each specimen of the gas mixture and δ_m is its associated pressure frequency shift rate. For this experiment, $\langle\delta\rangle = 0.35(-6.63 \pm 0.05) + 0.65(-8.21 \pm 0.02)\ MHz/torr = (7.66 \pm 0.03)\ MHz/torr$. The average value of the pressure as a function of the resonance shift for a buffer gas mixture of Ar-N_2, with ratio of $35\ \%$ and $65\ \%$, at a temperature of 46 C, can be estimated as follows,

$$\langle p\rangle = \frac{\langle\Delta\nu\rangle}{7.66}\left(\frac{319}{295.5}\right) \Longrightarrow \langle p\rangle \sim 0.14\ \langle\Delta\nu\rangle. \qquad \text{Eq. 6.7}$$

With Eq. 6.7, one is able to estimate the pressure required to shift the Cs D1 lines by $\Delta\nu$.

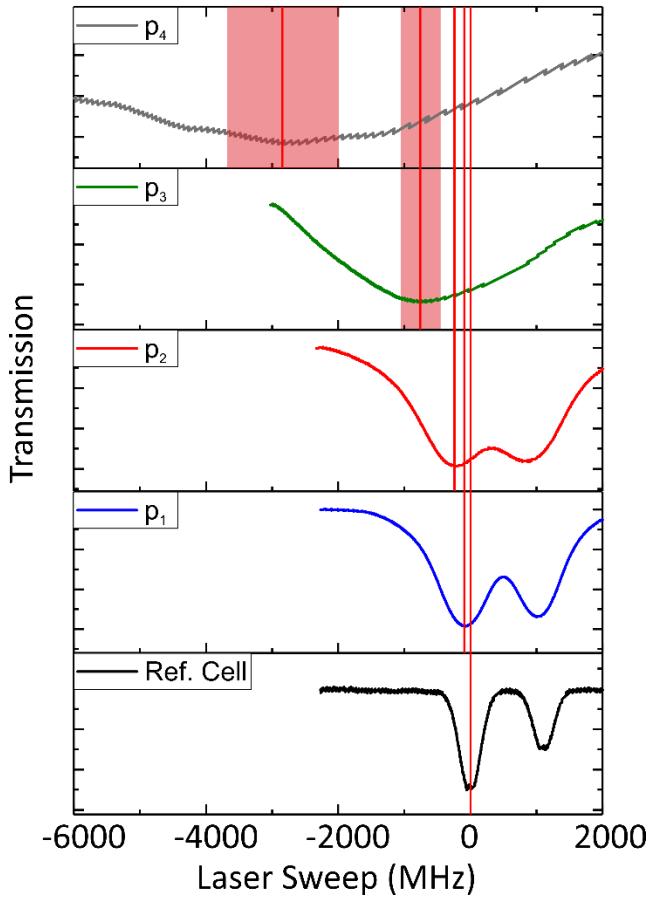

Figure 6.9: Cs D1 lines absorption lines obtained from sample K125 for four different buffer gas pressures. Note that at high pressure values, the two hyperfine transitions overlap due to the presence of buffer gas.

The characterisation of the buffer gas pressure injected in the UHV chamber was performed as follows. The cylinder containing the buffer gas was kept opened and a leak valve was used to control precisely the flow of gas into the chambers, while monitoring the optical transmission of the fibre sample filled with Cs. As the pressure increased in the chamber, the Cs transition lines started to broaden and shift towards lower frequencies. Figure 6.9 shows the Cs D1 lines ($6^2S_{1/2}F = 4 \rightarrow 6^2P_{1/2}F = 3$ and $6^2S_{1/2}F = 4 \rightarrow 6^2P_{1/2}F = 4$) absorption spectroscopy of the K125 sample for four different pressure points. Note that at each pressure point, the spectral position of the absorption lines was measured for the four HC-PCFs located in the chambers. The red vertical lines in the graph shown in Figure 6.9 indicates the resonance position. For pressure points p3 and p4, the broadening of the neighbour resonances was so great that they became undistinguishable. At these two pressure points, larger measurement errors were considered and they are depicted as transparent red stripes in each graph. Table 6.3 lists the frequency shift observed for samples K65, K125 and C305 and the estimated pressure, calculated using Eq. 6.7.

The characterisation performed in this section should be only seen as a best effort estimate of the pressure. The confidence in the values obtained for pressure points p3 and p4 is very low, as the variance of the mean value is over $50\ \%$ for p3 and around $35\ \%$, for p4.

Table 6.3: Hyperfine absorption line shift due to buffer gas presence in Cs-filled K65, K125 and C305.

Sample	Resonance shift (MHz)			
	P1	P2	P3	P4
K65	104 ± 6	206 ± 10	1250 ± 300	2815 ± 1000
K125	90 ± 6	206 ± 10	725 ± 250	2885 ± 1050
C305	103 ± 6	--	--	2814 ± 1000
Estimated pressure (torr)	13.8 ± 0.8	28 ± 1	138 ± 36	397 ± 140

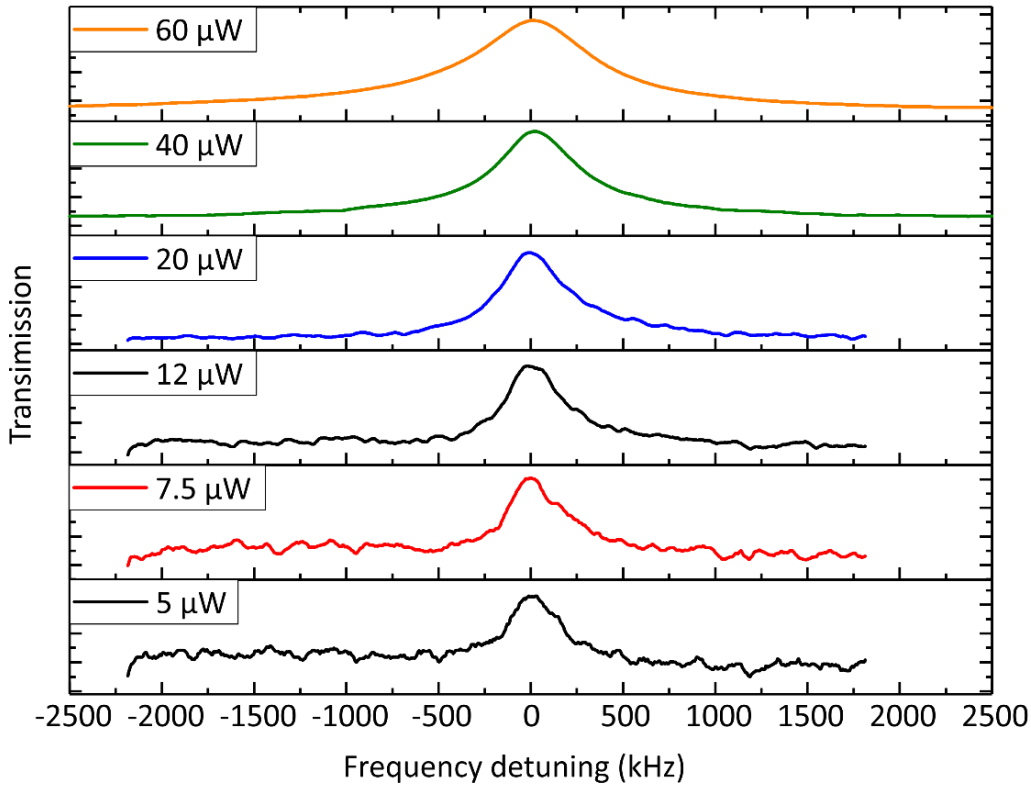

Figure 6.10: 0-0 CPT dark resonance spectroscopy from K65 filled with Cs and with 14 torr of a buffer gas mixture containing Ar:N_2, for different input optical power levels and longitudinal magnetic field of $\sim 0.39\ mT$.

In the next two section, I analyse the narrowing of the CPT dark resonances as a function of the applied buffer gas pressure, for the capillary samples C140 and C305 and for the HC-PCF samples K65 and K125. The contrast and linewidth were measured for different total pressures of the buffer gas mixture of Ar:N_2, as a function of the laser input power, ranging from $5\ \mu W$ to $80\ \mu W$, and for an applied longitudinal magnetic field of $\sim 0.39\ mT$.

6.2.3 CPT in HC-PCFs filled with Cs vapour and N_2:Ar buffer gas mixture

The 0-0 CPT dark resonance (in the presence of magnetic field) traces were collected using the same optical apparatus described in chapter 5 and previously in this chapter. The data collection was carried out for two K65 and two K125 samples and the data presented here shows the average values observed on both samples. The 0-0 resonance was monitored for six different values of optical input power and for circularly polarised light. Figure 6.10 shows the CPT resonance evolution as a function of the input optical power. The resonance was obtained from a K65 sample, filled with Cs atoms and with 14 torr of N_2:Ar, with partial ratio of 65%/35%, respectively. Note that in the low power regime (first panels from the bottom of the figure) the signals considerably noisier than of high input powers. Such a diminished amplitude is a direct result of the CPT contrast behaviour as a function of the laser power, and will be measured and discussed in the following section.

A. Dark resonance contrast

The contrast of the 0-0 dark resonance was measured for the K65 and K125 HC-PCFs samples for the four pressure values applied and estimated in the previous section. Figure 6.11(a) shows a stack of contrast versus input laser power graphs for K125 filled with Cs. Each panel is related to a given pressure point ($14\ torr$, $28\ torr$, $138\ torr$ and $397\ torr$). The maximum contrast values as well as the input power at which it occurred have changed as the pressure step has increased. From the bottom to the top, one can observe that the maximum contrast has moved towards weak optical input powers. The maximum contrast also decreased as the buffer gas pressure increased. It has dropped from about $4.5\ \%$, for $14\ torr$, to $\sim 0.3\ \%$, for $397\ torr$. The optical power at which the maximum was located shifted from $> 80\ \mu W$ to $\sim 12\ \mu W$.

The 0-0 dark resonance contrast for K65 behaved similarly to that for K125, as just described. Figure 6.11(b) depicts a stack of contrast versus optical input power graphs, for K65 photonic cells filled with Cs vapour and for different pressures of buffer gas. Similarly to K125, as the buffer gas pressure was increased, the maximum contrast decreased and the power at which the maximum was located moved towards weak optical input powers. The contrast decreased from $\sim 6\ \%$ to $\sim 0.5\ \%$ for a buffer gas pressure of $14\ torr$ and $397\ torr$, respectively. Its position shifted from $> 80\ \mu W$ to $\sim 5\ \mu W$, for the same pressure steps.

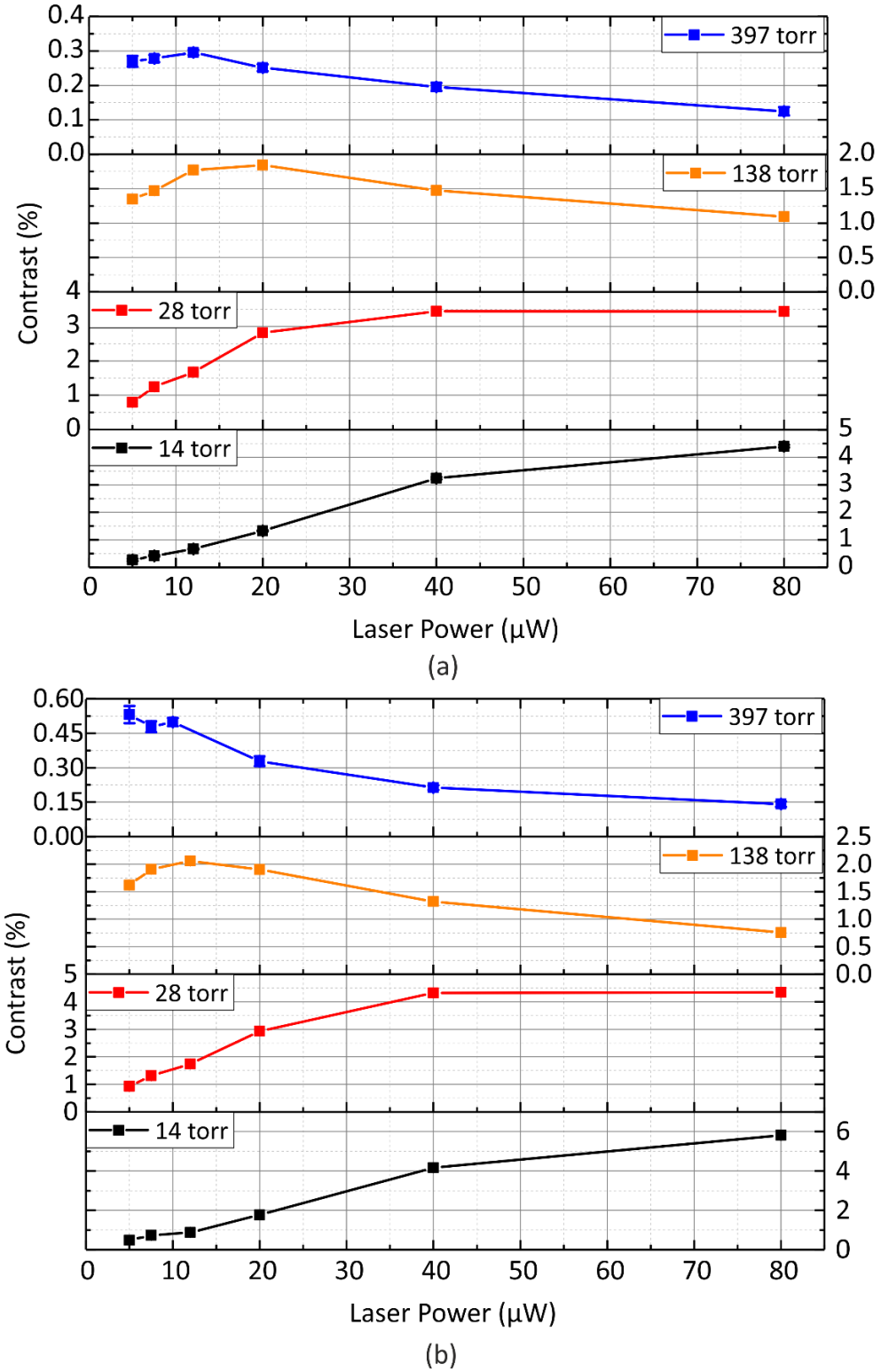

Figure 6.11: 0-0 dark resonance contrast for K125 (a) and K65 (b) samples filled with Cs vapour and different buffer gas pressures, varying from 14 $torr$ to 397 $torr$. The optical input power was varied from 5 μW to 80 μW and a longitudinal magnetic field of ~0.39 mT was applied over the samples. The data presented are the averaged data of two K65 and K125 samples measured simultaneously.

As observed in samples K65 and K125, the contrast curves as a function of the optical input power changed as the buffer gas pressure is increased. The general trend of CPT contrast was noted – monotonically increasing at *low* optical input power, followed by a global maximum and a decay in the *high* optical power regime. As the maximum point varies as a function of the buffer gas pressure, the low and high optical input power ranges also vary as a function of the optical input power. This result was observed and discussed in chapter 4, where the CPT 0-0 resonance was measured for a set of micrometre scale, stand-alone, vapour cells with different buffer gas pressure. Moreover, this result indicates indirectly that the resonance has narrowed in the presence of the buffer gas, confirming the empirical conclusions drawn in chapter 4.

The decreased maximum contrast is related to the number of buffer gas particles and the associated motion of the Cs atoms through buffer gas. As the atomic ensemble involving Cs atoms and buffer gas is an open system (fibre ends are open in the vacuum chamber), the number of atoms of Cs inside the hollow core decreases as the number of buffer gas molecules and atoms increases, as a result of the dynamics of the buffer gas flowing through the chambers. The decreased number of Cs atoms inside the hollow core of HC-PCFs (and I anticipate here, capillaries too) reduces the contrast, since the CPT resonance is a direct function of the Cs atomic density, as derived in chapter 4.

B. Dark resonance line-width

The contrast measurements just discussed indicated that resonance narrowing have taken place for K125 and K65 samples. It is a hypothesis raised from the fact that the global maxima for both samples varied with the buffer gas pressure. This can be a direct result of increased relaxation times – most likely the exchange between atom-wall collisions to atomic diffusion in a buffer gas rich environment broadening mechanism.

The line-width was obtained by measuring the FWHM of the resonance collected for four pressure values, same signal of which the contrast curves just presented were obtained. The line-width as a function of the optical input power for the four pressure points are shown in Figure 6.12(a) and (b), for K125 and K65 samples respectively. The line-width for all pressures and samples showed a linear dependency on the optical input power, in accordance to the theory and data analysed in chapter 4, for stand-alone Cs vapour cells. As the buffer gas pressure was increased, the minimum observable line-width reduced from $\sim 600\ kHz$ to $\sim 50\ kHz$, for K125 samples, and from $\sim 800\ kHz$ to $\sim 90\ kHz$, for the K65 sample. This is the first time line-widths below $\sim 100\ kHz$ have been observed in atomic features obtained from thermal vapours in HC-PCFs. It also defines $\sim 50\ kHz$ CPT line-width the new state-of-the-art for atomic features in alkali-vapour filled HC-PCFs. In comparison to previously reported line-widths, it figures about four times below the

recently achieved $\sim 200\ kHz$ EIT feature observed in HC-PCFs coated with antirelaxation polymer, filled with Rb-vapour [18]. I view this as the key result of my Ph.D.

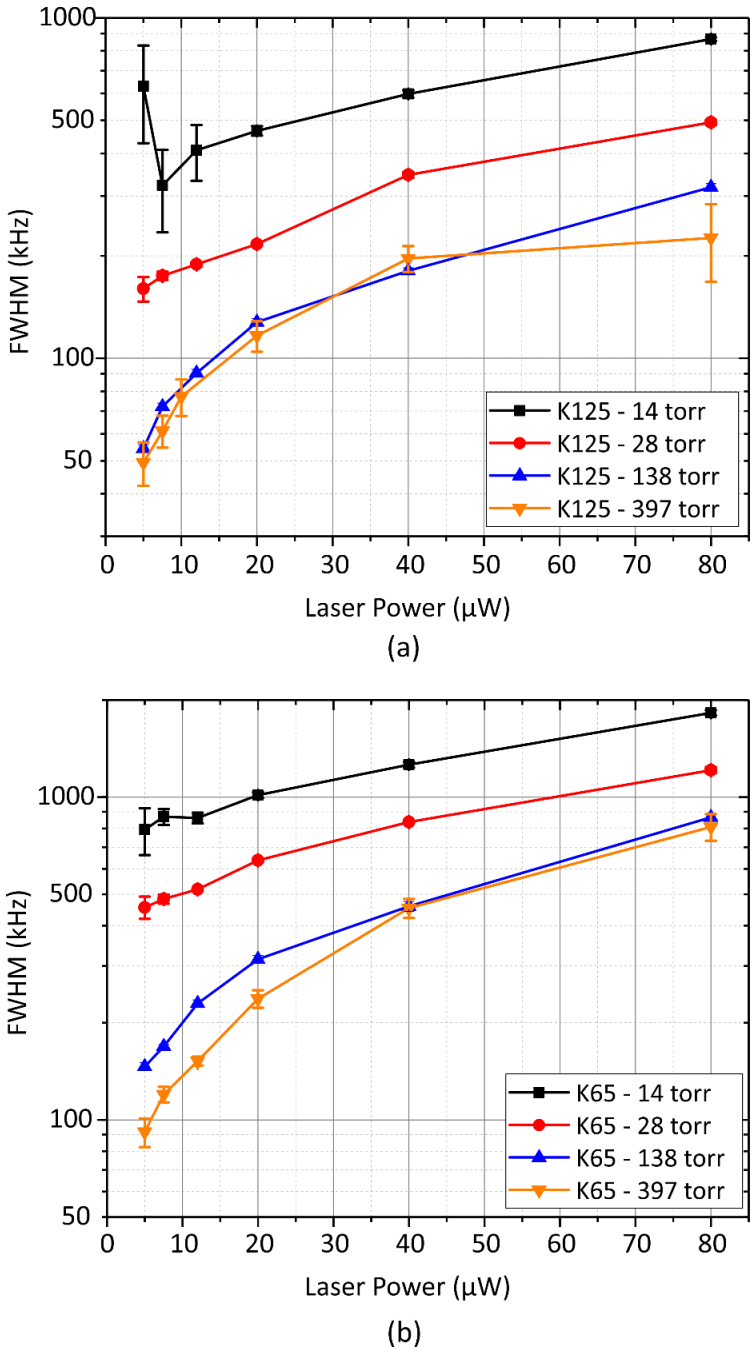

Figure 6.12: 0-0 dark resonance line-width for K125 (a) and K65 (b) samples filled with Cs vapour and different buffer gas pressures, varying from $14\ torr$ to $397\ torr$. The optical input power was varied from $5\ \mu W$ to $80\ \mu W$ and a longitudinal magnetic field of $\sim 0.39\ mT$ was applied over the samples. The data presented are the averaged data of two K65 and K125 samples measured simultaneously. More than two orders of magnitude of narrowing was observed in both samples, with minimum FWHM of $\sim 50\ kHz$ and $< 100\ kHz$ for K125 and K65, respectively.

The addition of buffer gas to the atomic ensemble and the associated reduction in the CPT line-width can be better understood by comparing the data from pure Cs-vapour filled HC-PCFs and from buffer gas added Cs-vapour HC-PCFs. Table 6.4 shows the line-width for K65 and K125 without and with buffer gas for an optical input power of $40\ \mu W$. By adding $14\ torr$ of N_2:Ar, the line-width has reduced 4.5 times, for K65, and over 7.5 times, for K125. The reduction was even greater for $138\ torr$ and $397\ torr$, reaching more than one order of magnitude in both samples. This analysis, however, only accounts for dynamic effects of the Cs vapour in the hollow core. When the optical input power was reduced by almost one order of magnitude (from $40\ \mu W$ to $5\ \mu W$), the line-widths of K65 and K125 were further reduced by an impressive 63 and 100 times, respectively.

The differences between the observed line-width for K65 and K125 Cs-loaded samples resides in the geometrical attributes of each sample. K125 has a larger hollow core with diameter of $\sim 125\ \mu m$ while K65 supports a hollow core of just $\sim 65\ \mu m$ in diameter. This subtle difference is enough to affect the diffusion and power broadening mechanisms. Firstly, the relaxation rate related to Cs atoms found in a buffer gas rich environment, Eq. 6.3, indicates that it should vary following the power law R^{-2}, where R is the hollow core radius. Therefore, larger hollow cores yield narrower CPT resonances, at the same pressure step. Secondly, the reduced hollow core size of K65 yield modes with higher intensity than K125, providing that the optical input power and coupling efficiency are kept at the same level for both samples. The higher mode intensity leads to a higher optical power broadening. Unfortunately, the experimental apparatus could only measure CPT resonances starting from $5\ \mu W$ of optical input power. Below this value, the signal was embedded in noise, requiring a more complex detection system involving phase sensitive detection, for example.

Table 6.4: Observed line-width for K65 and K125 filled with Cs vapour with and without buffer gas for P = $40\ \mu W$ and narrowest line-width observed (P = $5\ \mu W$).

Sample	Line-width (kHz)				
	No Buffer gas	14 torr of Buffer gas	138 torr of Buffer gas	397 torr of Buffer gas	Minimum line-width (P = $5\ \mu W$)
K65	5860 ± 80	1260 ± 25	460 ± 15	450 ± 30	92 ± 9
K125	4700 ± 195	600 ± 16	181 ± 3	190 ± 17	49 ± 7

6.2.4 CPT in capillaries filled with Cs vapour and N_2:Ar buffer gas mixture

For completeness and in order to understand if the waveguide properties of HC-PCFs play a role in the CPT resonance for straight samples, I have also conducted CPT spectroscopy in Cs-vapour capillary samples with the addition of buffer gas. Unlike in the past section where I analysed the CPT 0-0 dark resonance for four pressure steps, the capillary samples C140 and C305, loaded with Cs vapour and buffer gas, were only measured for $14\ torr$ and $397\ torr$. The characterisation of

the CPT resonance was identical to the one performed for HC-PCFs. In the following two section I discuss the contrast and line-width response of C140 and C305.

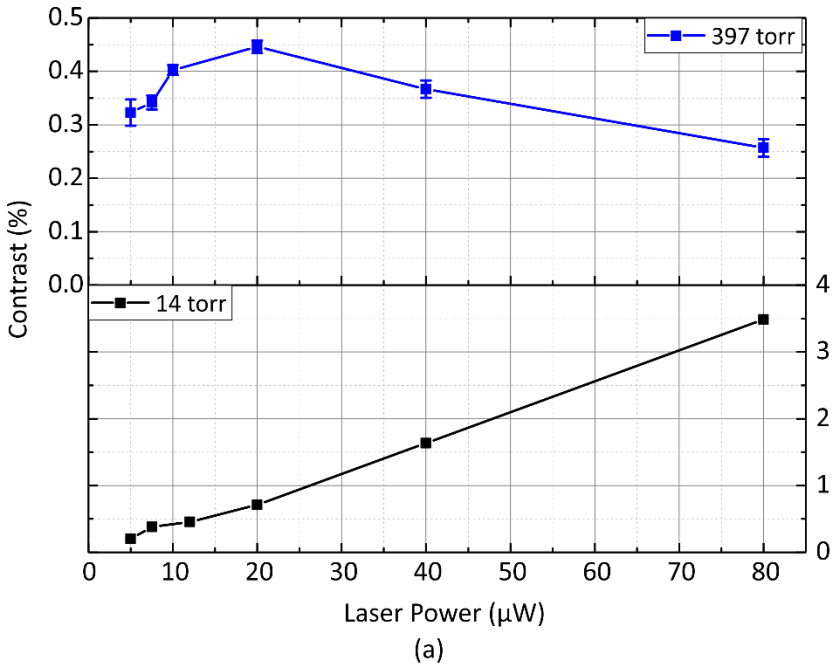

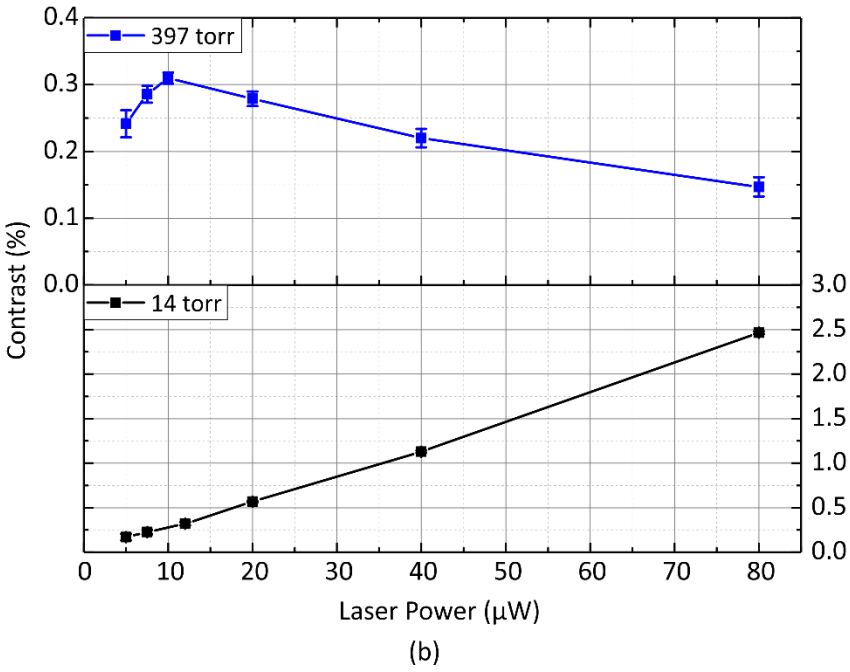

Figure 6.13: 0-0 dark resonance contrast for C140 (a) and C305 (b) samples filled with Cs vapour and for two different buffer gas pressures, $14\ torr$ and $397\ torr$. The optical input power was varied from $5\ \mu W$ to $80\ \mu W$ and a longitudinal magnetic field of $\sim 0.39\ mT$ was applied over the samples.

A. Dark resonance contrast

Figure 6.13(a) and (b) depict the CPT contrast as a function of the optical input power for C140 and C305, for $14\ torr$ and $397\ torr$. In summary, both samples showed similar trends at each pressure step. For $14\ torr$, both C140 and C305 the CPT contrast exhibited an almost linear trend,

proportional to the optical input power, with a maximum contrast value of ~3.5 % and ~2.5 %, respectively. For 397 $torr$, the contrast response changed as expected. The maximum contrast has shifted towards weak optical input power levels. The maximum contrast decreased to ~0.45 % and ~0.3 %, for C140 and C305 respectively.

The contrast response for different pressure settings followed the same trend observed in the stand-alone vapour cells, discussed in chapter 4, and also agrees with the data just presented in the previous section for HC-PCFs.

B. Dark resonance line-width

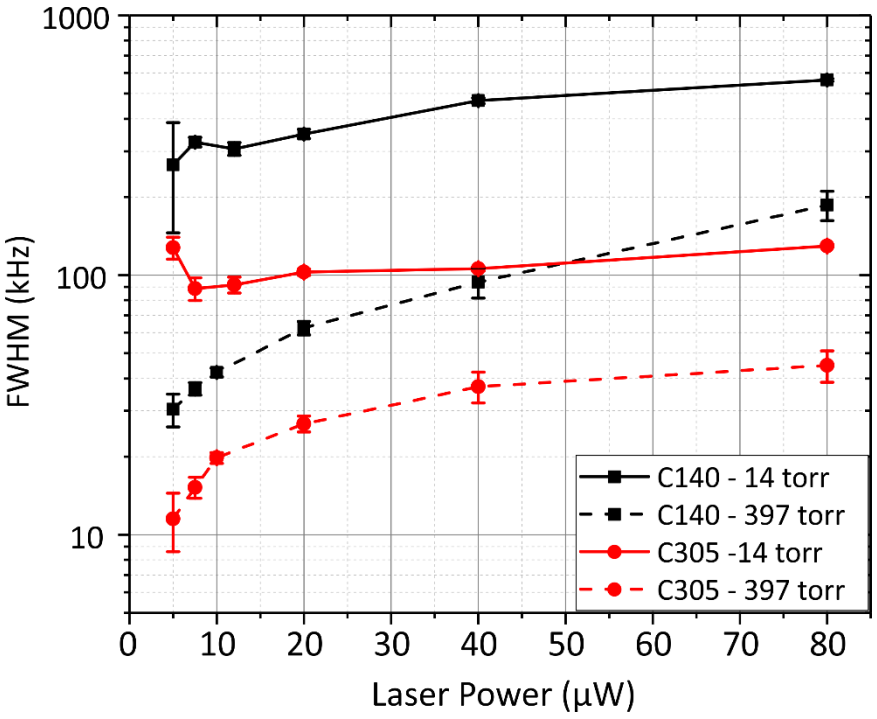

Figure 6.14: 0-0 dark resonance line-width for C140 (black curves) and C305 (red curves) samples filled with Cs vapour and for two different buffer gas pressures, 14 $torr$ (solid lines) and 397 $torr$ (dashed lines). The optical input power was varied from 5 μW to 80 μW and a longitudinal magnetic field of ~0.39 mT was applied over the samples. Minimum line-widths of ~30 kHz and ~11 kHz were observed for C140 and C305, respectively, for 397 $torr$ and optical input power of 5 μW.

The CPT line-widths measured from both C140 and C305 filled samples, as a function of the optical input power, are shown in Figure 6.14. The curves related to the pressure point of 14 $torr$ are depicted by solid lines and, for 397 $torr$, are depicted by dashed lines. The curves showed linear trends as a function of the optical input power level, similarly to HC-PCFs Cs-filled samples. The presence of the buffer gas reduced initially the CPT resonance line-width from C140 over 7 times, for 14 $torr$ applied, compared to the pure Cs-vapour filled sample. For 397 $torr$ of applied buffer gas, it has further reduced by over 45 times. This comparison was performed for different data sets,

however with same laser input power of $40\ \mu W$. Unfortunately, this comparison could not be performed for the C305 sample, since the filling level of the sample during the measurement of only pure Cs-vapour did not allow me to observe a resonance with low noise. Still, theC305 sample filled with Cs vapour and buffer gas had yielded the narrowest CPT lines observed in this experiment. For $14\ torr$, C305 yielded a CPT resonance with a FWHM of around $100\ kHz$. With $397\ torr$ applied, the FWHM decreased by about one order of magnitude, yielding a minimum line-width of $\sim 11\ kHz$, for an optical input power of $5\ \mu W$.

During the measurement of HC-PCF and capillary samples filled with Cs-vapour previously in this chapter, it was noted that K125 and C140 showed similar behaviour in terms of CPT resonance line-width response. This similarity resulted from the fact that the hollow core diameter and capillary inner diameter size, $125\ \mu m$ and $140\ \mu m$, respectively, were very similar. When the buffer gas is added, however, the dynamics of the Cs vapour change drastically and the relaxation rate dependency on the geometry also changes from R^{-1} to R^{-2}. This, summed up with the optical power broadening, explains the difference of almost $20\ kHz$ observed for FWHM at minimum power ($5\ \mu W$).

6.2.5 CPT Dark resonance Line-width as a function of the buffer gas pressure

After discussing the CPT characteristics for HC-PCF and capillary samples filled with Cs vapour and N_2:Ar buffer gas, I can finally demonstrate the direct effect of buffer gas in micrometre- scale HC-PCFs and capillaries. The line-width as a function of the buffer gas pressure graph is shown in Figure 6.15. From the estimated pressure values and from the theory developed in chapter 4, I can infer that the broadening mechanism governing the CPT resonance line-width at the pressure range is the atomic diffusion. At $\sim 400\ torr$, the line-width trend start to change, following K65 and K125 traces, indicating that power broadening is also present. Note also that the line-width of K65 is the broadest of all samples, followed by K125, C140 and finally C305.

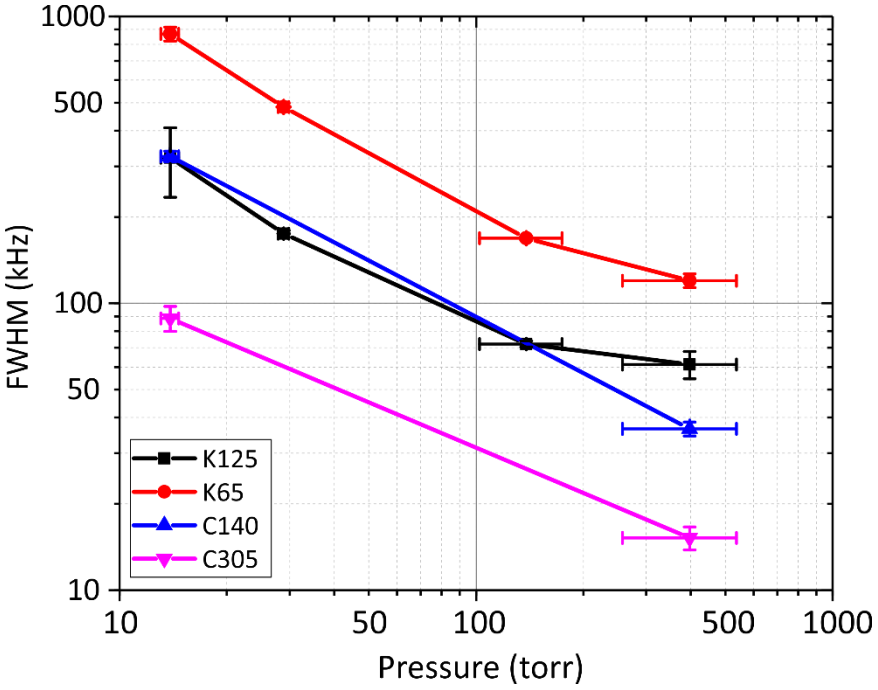

Figure 6.15: 0-0 dark resonance line-width as a function of the buffer gas pressure for K65, K125, C140 and C305 samples. The optical input power used was $7.5\ \mu W$. Note that the line-width decreases as the buffer gas pressure increases, indicating that the governing broadening effect at this pressure range is still the atomic diffusion broadening.

6.3 Conclusion

In this chapter I have demonstrated for the first time CPT dark resonance spectroscopy in HC-PCFs and capillaries with micrometre-scale inner diameters. Primarily, I have measured the contrast and line-width of HC-PCF and capillaries filled with pure Cs vapour as a function of optical input power, longitudinal magnetic field strength and polarisation of light. I have shown the atomic relaxation mechanisms related to optical power and magnetic field strength. By studying the performance of CPT dark resonance for linear and circular polarisation state of light, I showed that circular polarisation yield larger contrasts and narrower lines in most of the cases, especially at low optical power regime. In the high optical power range, linear polarisation of light shows better contrast values and line-widths. The difference of hollow core diameters of HC-PCFs and inner diameters of capillary samples showed to be an important parameter due to transit-time broadening. The smaller the core, the broader the resonance. Ultimate line-width values ranging from $4\ MHz$ to just below $20\ MHz$ were observed. Huge contrast of just below $50\ \%$ were observed for CPT in pure Cs filled samples in absence of a magnetic field. In the presence of a magnetic field, the contrast decreased to below $5\ \%$, for 0-0 dark resonance.

After the measrurement with only Cs vapour, the samples were filled with four different pressures of N_2:Ar, with partial ratio of $65\ \%$ - $35\ \%$. The four pressure points were estimated by following

the shift of the Cs hyperfine lines. The values of pressure estimated were: $14\ torr$, $28\ torr$, $138\ torr$ and $397\ torr$. Theoretical model indicated that from $1\ torr$ to $1000\ torr$ the CPT line-width is mainly governed by diffusion broadening. CPT spectroscopy of the HC-PCFs filled with Cs and buffer gas was performed at each pressure point. Reduction of the line-width of about 4 times to more than two orders of magnitude was observed. In absolute terms, line-widths of $\sim 90\ kHz$ and $\sim 50\ kHz$ were measured, for K65 and K125, respectively, for an optical input power of $5\ \mu W$ and longitudinal magnetic field strength of $\sim 0.39\ mT$. Contrasts at this level of optical power were below $0.5\ \%$. Capillary samples were also characterised, however only for buffer gas pressures of $14\ torr$ and $397\ torr$. The minimum line-width of $\sim 30\ kHz$ and $\sim 10\ kHz$ were observed at the same conditions as for HC-PCFs, respectively for C140 and C305, with a contrast below $0.5\ \%$.

Finally, the line-width as a function of the buffer gas pressure was analysed. The curves for K65 and K125 indicated that the diffusion broadening is one of the main governing effects at this pressure range, following the theoretical prediction. The line-width of $\sim 50\ kHz$ observed in this study for K125 is four times narrower than the most recent work on atomic narrow atomic features in HC-PCFs. This result sets a new record for narrowest line-width of an atomic feature measured for alkali-filled HC-PCFs and it is the key result reported in this thesis.

6.4 Chapter References

[1] P. S. J. Russell, P. Hölzer, W. Chang, a. Abdolvand, and J. C. Travers, "Hollow-core photonic crystal fibres for gas-based nonlinear optics," *Nat. Photonics*, vol. 8, no. 4, pp. 278–286, 2014.

[2] M. F. Saleh *et al.*, "Theory of Photoionization-Induced Blueshift of Ultrashort Solitons in Gas-Filled Hollow-Core Photonic Crystal Fibers," *Phys. Rev. Lett.*, vol. 107, no. 20, p. 203902, Nov. 2011.

[3] J. C. Travers, W. Chang, J. Nold, N. Y. Joly, and P. St. J. Russell, "Ultrafast nonlinear optics in gas-filled hollow-core photonic crystal fibers [Invited]," *J. Opt. Soc. Am. B*, vol. 28, no. 12, p. A11, Dec. 2011.

[4] F. Couny, F. Benabid, P. J. Roberts, P. S. Light, and M. G. Raymer, "Generation and photonic guidance of multi-octave optical-frequency combs," *Science*, vol. 318, no. 5853, pp. 1118–1121, Nov. 2007.

[5] P. Londero, V. Venkataraman, A. R. Bhagwat, A. D. Slepkov, and A. L. Gaeta, "Ultralow-Power Four-Wave Mixing with Rb in a Hollow-Core Photonic Band-Gap Fiber," *Phys. Rev. Lett.*, vol. 103, no. 4, p. 043602, Jul. 2009.

[6] C. Perrella, P. S. Light, T. J. Milburn, D. Kielpinski, T. M. Stace, and A. N. Luiten, “Anomalous two-photon spectral features in warm rubidium vapor,” *Phys. Rev. A*, vol. 94, no. 3, p. 033403, Sep. 2016.

[7] C. Perrella, P. S. Light, S. A. Vahid, F. Benabid, and A. N. Luiten, “Engineering Photon-Photon Interactions within Rubidium-Filled Waveguides,” *Phys. Rev. Appl.*, vol. 9, no. 4, p. 044001, Apr. 2018.

[8] G. Epple et al., “Rydberg atoms in hollow-core photonic crystal fibres.,” Nat. Commun., vol. 5, no. May, p. 4132, 2014.

[9] F. Benabid, P. Light, F. Couny, and P. Russell, “Electromagnetically-induced transparency grid in acetylene-filled hollow-core PCF.,” Opt. Express, vol. 13, no. 15, pp. 5694–5703, 2005.

[10] F. Couny, P. S. Light, F. Benabid, and P. S. J. Russell, “Electromagnetically induced transparency and saturable absorption in all-fiber devices based on 12C2H2-filled hollow-core photonic crystal fiber,” Opt. Commun., vol. 263, no. 1, pp. 28–31, Jul. 2006.

[11] P. S. Light, F. Benabid, F. Couny, M. Maric, and A. N. Luiten, “Electromagnetically induced transparency in Rb-filled coated hollow-core photonic crystal fiber,” *Opt. Lett.*, vol. 32, no. 10, p. 1323, May 2007.

[12] M. R. Sprague et al., “Broadband single-photon-level memory in a hollow-core photonic crystal fibre,” Nat. Photonics, vol. 8, no. 4, pp. 287–291, Apr. 2014.

[13] S. Okaba *et al.*, “Lamb-Dicke spectroscopy of atoms in a hollow-core photonic crystal fibre,” *Nat. Commun* 5, 4096, Jun. 2014.

[14] A. D. Slepkov, A. R. Bhagwat, V. Venkataraman, P. Londero, and A. L. Gaeta, “Generation of large alkali vapor densities inside bare hollow-core photonic band-gap fibers.,” Opt. Express, vol. 16, no. 23, pp. 18976–18983, 2008.

[15] A. D. Slepkov, A. R. Bhagwat, V. Venkataraman, P. Londero, and A. L. Gaeta, “Spectroscopy of Rb atoms in hollow-core fibers,” *Phys. Rev. A*, vol. 81, no. 5, p. 053825, May 2010.

[16] X. Zheng et al., “Ground-state population relaxation dynamics of polarized Rb atoms in Kagome HC-PCF,” in Conference on Lasers and Electro-Optics, 2016, p. SM2H.8.

[17] T. D. Bradley *et al.*, “Ground-state atomic polarization relaxation-time measurement of Rb filled hypocycloidal core-shaped Kagome HC-PCF,” *J. Phys. B At. Mol. Opt. Phys.*, vol. 49, no. 18, p. 185401, Sep. 2016.

[18] X. M. Zheng et al., “Narrow electromagnetically induced transparencies in Rb confined large-core core inner-wall coated Kagome HC-PCFs,” in Conference on Lasers and Electro-Optics, 2018, p. SM3L.3.

[19] X. M. Zheng et al., “In-situ dwell-time measurement of Rb at the inner-wall coated-surface of HC-PCF,” in Conference on Lasers and Electro-Optics, 2018, p. SM3L.4.

[20] C. Perrella, P. S. Light, J. D. Anstie, T. M. Stace, F. Benabid, and A. N. Luiten, “High-resolution two-photon spectroscopy of rubidium within a confined geometry,” Phys. Rev. A, vol. 87, p. 13818, 2013.

[21] C. Perrella, P. S. Light, J. D. Anstie, F. N. Baynes, F. Benabid, and A. N. Luiten, “Two-color rubidium fiber frequency standard,” Opt. Lett., vol. 38, no. 12, p. 2122, Jun. 2013.

[22] S. Knappe et al., “A chip-scale atomic clock based on 87Rb with improved frequency stability,” Opt. Express, vol. 13, no. 4, pp. 1249–1253, 2005.

[23] L. A. Liew, S. Knappe, J. Moreland, H. Robinson, L. Hollberg, and J. Kitching, “Microfabricated alkali atom vapor cells,” Appl. Phys. Lett., vol. 84, no. 14, pp. 2694–2696, 2004.

[24] S. Knappe, “MEMS Atomic Clocks,” *Compr. Microsystems*, pp. 571–612, Jan. 2008.

[25] C. T. Jacques Vanier, *The Quantum Physics of Atomic Frequency Standards: Recent Developments*. CRC Press, 2015.

[26] D. Steck, “Cesium D Line Data,” Notes, pp. 1–31, 2008. URL: https://steck.us/alkalidata/cesiumnumbers.1.6.pdf

[27] J. Vanier and C. Audoin, The Quantum Physics of Atomic Frequency Standards, v.1. IOP Publishing, 1989.

[28] M. Zhu, L. S. Cutler, J. E. Berberian, J. F. DeNatale, P. A. Stupar, and C. Tsai, “Narrow linewidth CPT signal in small vapor cells for chip scale atomic clocks,” in *Proceedings of the 2004 IEEE International Frequency Control Symposium and Exposition, 2004.*, pp. 100–103.

[29] J. Vanier, “Atomic clocks based on coherent population trapping: A review,” Appl. Phys. B Lasers Opt., vol. 81, no. 4, pp. 421–442, 2005.

[30] M. V. Balabas *et al.*, “High quality anti-relaxation coating material for alkali atom vapor cells,” *Opt. Express*, vol. 18, no. 6, p. 5825, Mar. 2010.

[31] O. Kozlova, S. Guérandel, and E. De Clercq, “Temperature and pressure shift of the Cs clock transition in the presence of buffer gases: Ne, N2, Ar,” Phys. Rev. A - At. Mol. Opt. Phys., vol. 83, no. 6, p. 062714, 2011.

[32] O. Kozlova, R. Boudot, S. Guerandel, and E. de Clercq, “Temperature Dependence Cancellation of the Cs Clock Frequency in the Presence of Ne Buffer Gas,” Instrumentation and Measurement, IEEE Transactions on, vol. 60, no. 7. pp. 2262–2266, 2011.

Chapter 7 Conclusions and Field Prospects

7.1 Conclusions

The study reported in this thesis contributes to the development of time and frequency reference cell technology based on HC-PCFs. The main advantages of photonic cells over commercially available reference cells are the small footprint, lack of need for any free-space optical alignment and compatibility with fibre-coupled systems. Conventional reference cells require free space optics in order to observe the atomic resonance, thereby increasing the complexity of the optical system used. In the following I summarise the activities covered:

- **Characterisation of ultra large core Kagome-lattice ARFs for Alkali vapour spectroscopy:** I had the opportunity to work with state-of-the-art K-ARFs fabricated at the ORC with optimised optical guidance at Cs D lines (at wavelengths around $\sim 880\ nm$). The fibres were characterised in terms of propagation and bend loss. The HC-PCFs were discussed in detail in chapter 2.
- **Theoretical and experimental study on optical fibres interconnections between optical fibres with dissimilar core sizes and guidance mechanism:** I have studied in detail the use of multimode interference and spatial mode beating to improve fibre interconnection between optical fibres with dissimilar cores. This associated device is referred to as mode field adapter (MFA). This is an alternative solution to the state-of-the-art of solid core to hollow core fibre interconnection that is currently based on tapering either the solid core fibre or the HC-PCF in order to achieve improved mode mismatching and insertion loss. In the study presented in chapter 3, I took advantage of the properties of graded-index fibre to obtain mode expansion and compression, improving the insertion loss between commercially available SMFs and solid core, large mode area, fibres and more sophisticated HC-PCFs. A proof-of-concept experiment was performed, followed by a very comprehensive theoretical study on the use of such MFAs. Considering the HC-PCF as a MMF, I have simulated the fully interconnected device (SMF to MMF back to SMF) at the wavelength of $1550\ nm$ and have calculated a minimum insertion loss figure of $0.91 \pm 0.2\ dB$. This figure considers the multimode interference caused when launching from a standard SMF to a MMF and then collecting the signal with another standard SMF. It also considers the Fresnel back reflections present when the optical signal change medium with different refractive indices. Experimental studies showed that the MFA can indeed be used for interconnections between standard SMF to HC-PCFs. HC-PBGFs were fully-connectorised to SMFs using suitable MFAs and showed an insertion loss figures around

$2.2\ dB$. K-ARFs were tested and showed average insertion loss from SMF to K-ARF of $0.43\ dB$ (single splice). The losses increased greatly to over $5\ dB$ when the second splice (K-ARF to SMF) was made. The GIFs used in this case did not have a parabolic refractive index profile and, thus, this can be one of the main source of losses.

- **Study of the CPT dark resonance line-width in commercial available cells with different buffer gas pressures:** anticipating that HC-PCFs filled with Cs-vapour would require a method to control the CPT dark resonance line-width (as a result of the micrometre size hollow cores and the time-of-flight of Cs atoms), I performed a series of experiments aiming to understand better the role of the buffer gas in the vapour dynamics, leading to a reduction in line-width of the CPT features. This was the first time to our knowledge that a group has methodically studied millimetre- size cells, filled with the same buffer gas mixture, but different pressures. In this study, I have concluded that for a set of reference cells ($1\ mm$ inner diameter and $50\ mm$ long), filled with Cs vapour and a buffer gas mixture of 71% of N_2 and 29% of Ar, the main broadening mechanism is still related to rate of the diffusion of Cs atoms in the buffer gas rich environment (for a buffer gas pressure range of $1\ torr$ to $120\ torr$). Other broadening mechanisms such as transit-time and power broadening are only observed at the low and high pressure range ends, respectively. This study is discussed in detail in chapter 4, where I present the CPT effect in alkali vapour and described a few mathematical expressions that are useful for modelling the line-width behaviour as a function of inhomogeneous and homogeneous broadening effects.
- **Ultra-high vacuum setup for HC-PCF alkali filling and in-situ CPT spectroscopy:** the success of filling HC-PCFs with alkali metal vapours is directly related to the quality of the UHV setup designed and built. For this project, I received advice from Prof Patrick Gill, Dr Mohsin Haji and Dr Thomas Bradley on the task of designing and building a new UHV setup capable of filling HC-PCF with Cs vapour and suitable to perform CPT spectroscopy in filled fibre samples in-situ. In addition to the UHV setup, an optical setup compatible with the UHV design was built, optimising light insertion and collection through UHV viewports. To achieve high resolution CPT spectroscopy, I had to study the quality of homogeneous and longitudinal magnetic field generators (solenoids and Helmholtz coils assemblies) in order to obtain magnetic fields longitudinal and homogeneous over the almost $100\ mm$ length of the optical path inside the UHV setup. The design of the UHV setup, optical implementations and mathematical modelling and demonstration of the magnetic field generators are found in chapter 5.
- **Characterisation of Cs-vapour density found within the HC-PCFs:** one of the requirements to perform CPT in HC-PCFs filled with Cs vapour is to understand the filling process and measurement of the atomic density found within the hollow core at a given time. In order

to perform this task, I had to develop a simple analytical model considering the atomic scattering rate of Cs D1 lines as a function of the input power. It was experimentally observed that the contrast of Cs D1 absorption lines decreased as a function of the laser input power when the laser intensity was set to be above the transition saturation intensity. This could be used to estimate the atomic density since the absorption lines behave as a linear function of the number of atoms [1]. It was observed that atomic density can rapidly build up to $10^8\ cm^{-3}$ in the first three days of filling and slowly stabilises to $10^9\ cm^{-3}$ throughout the following 6 days of filling, and then stayed stable over 20 days. These observations were consistent within all HC-PCFs and micrometre capillary samples chosen to perform CPT spectroscopy. The estimated atomic density of the HC-PCFs and capillaries as well as the theoretical modelling are found in chapter 5.

- **CPT dark resonance spectroscopy of HC-PCFs filled with pure Cs-vapour:** I performed and reported for the first time CPT dark resonance spectroscopy in HC-PCFs filled with pure Cs vapour. Using the UHV setup described in chapter 5, two pairs of K-ARFs with a hollow core diameter of $65\ \mu m$ and $125\ \mu m$ and micrometre scale capillaries with inner diameter of $140\ \mu m$ and $305\ \mu m$. Line-widths in the range of $10\ MHz$ for all samples, when filled with pure-Cs vapour were observed. The contrast values reported ranged from $3\ \%$ to $5\ \%$, when the magnetic field was applied, and below $50\ \%$, in the absence of magnetic fields. The trends of contrast and line-width of the CPT dark resonance were measured as a function of input laser power, applied magnetic field and the polarisation state of light. This study is found in chapter 6 and it one the key results reported in this thesis.
- **Line-width control of CPT dark resonances by adding a buffer gas mixture in HC-PCFs filled with Cs-vapour:** also in chapter 6, I reported the use of buffer gas for line-width control in CPT dark resonances observed in HC-PCFs filled with Cs-vapour. By varying the pressure of a mixture of $65\ \%$ N_2 and $45\ \%$ Ar, I demonstrated line-width narrowing by over two orders of magnitude in HC-PCFs. The minimum line-width reported here for HC-PCFs was $\sim 50\ kHz$ for a K-ARF with a hollow core diameter of $125\ \mu m$, in the presence of a magnetic field and for a buffer gas total pressure of $397\ torr$. The line-width reduction was monitored as a function of the applied buffer gas total pressure. The data trend for the K-ARFs showed that the line-width could have been further decreased. Theoretical models indicated that K-ARFs with $65\ \mu m$ and $125\ \mu m$ could yield a CPT dark resonance line-width as narrow as $7\ kHz$ and $3.5\ kHz$, respectively. This theoretical limit does not include additional broadening from different sources such as power broadening. The minimum line-width observed among the samples studied in this thesis was measured from C305, for a buffer gas pressure of $397\ torr$, with a line-width of $\sim 11\ kHz$. These two results are the state-of-the-art for narrowed atomic features in HC-PCFs filled with alkali-vapour. The line-width

reduction was followed by contrast reduction, as expected from the findings reported in chapter 4.

The results reported in chapter 6 for the minimum line-width in K-ARFs is about four times narrower than the current record of $\sim 200\ kHz$ in Rb filled K-ARFs, reported by Zheng et al [2]. Field Prospects

7.2 State of the Art and Field Prospects

The development of inner wall coatings for HC-PCFs, together with the use of buffer gas mixtures in order to control the coherence time of atoms has advanced the development of alkali based photonic cells towards practical applications. The decade-long studies led by Prof Benabid at the University of Limoges on HC-PCFs with inner hollow core walls coated with antirelaxation nano-films [2]–[4] together with the findings reported in chapter 6 of this thesis define the state-of-the-art in photonic cells for frequency and time references in terms of line-width control and narrowing. However, the field requires more investment and development in order to compete directly with commercially available reference cells. As discussed in chapter 6, the impact of the geometry on the narrowest line-width defines a theoretical limit for buffer gas use in alkali filled HC-PCFs. HC-PCFs with hollow core diameters of $125\ \mu m$ and $65\ \mu m$ support an ultimate minimum line-width of $\sim 3\ kHz$ and $\sim 7\ kHz$, respectively.

Photonic cell technology still requires development on a number of key points. Various groups have already proven the efficacy of photonic cells, using either HC-PBGFs or ARFs, for molecular gas lines [5]–[9], however improved low loss interconnection between conventional SMFs patch-cords to HC-PCFs is still needed. In chapter 3, I have described a potential method to minimise coupling losses in fibres with dissimilar mode fields by using a mode field adapter. The challenge becomes even greater when alkali vapour is used as the atom of choice. Conventional splice methods are not suitable for alkali vapour HC-PCFs, since they rely on an electric arc to melt the glass and create a robust bond between the fibres to be spliced. In order to splice alkali-filled HC-PCFs, a vacuum compatible technique is required.

I summarise in the following the key points where further investigations are still required.

1. **The use of ARFs with larger hollow cores:** The revolutionary design of NANFs [10] can be exploited in frequency and time reference applications as well. The simplified microstructure of NANFs can result in further narrowing of CPT dark resonances as a result of the rate of diffusion of Cs atoms in a buffer gas environment. As described in chapter 4, the diffusion rate is a function of the inverse of the square of the hollow core radius.
2. **Laboratory level demonstration of stability measurements of narrowed CPT dark resonances in HC-PCFs:** This is perhaps the next natural step towards implementation of a

reference frequency signal originated from an atomic feature measured from alkali filled HC-PCFs. In order to perform this experiment, one requires fine control of the temperature and laser power. It is also required to exactly match the operational temperature of the buffer gas used in order to minimise the shift of the central frequency of the CPT dark resonance as a function of the temperature.

3. **Stand-alone alkali-vapour photonic cells:** the demonstration of a fully-connectorised, stand-alone, HC-PCF filled with alkali vapour, with low insertion loss, is perhaps the most awaited event in the field. One of the key developments required is in vacuum compatible splice techniques. The challenge in this study is to define a method to hermetically seal the HC-PCFs with alkali vapour inside the hollow core, providing optimised optical coupling at both ends. High insertion loss can reflect in a loss penalty and low SNR, which are detrimental for laser frequency or radio frequency resonator locking setups.

7.3 References

[1] D. Steck, “Cesium D Line Data,” Notes, pp. 1–31, 2008. URL: https://steck.us/alkalidata/cesiumnumbers.1.6.pdf

[2] X. M. Zheng et al., “Narrow electromagnetically induced transparencies in Rb confined large-core core inner-wall coated Kagome HC-PCFs,” in Conference on Lasers and Electro-Optics, 2018, p. SM3L.3.

[3] X. M. Zheng et al., “In-situ dwell-time measurement of Rb at the inner-wall coated-surface of HC-PCF,” in Conference on Lasers and Electro-Optics, 2018, p. SM3L.4.

[4] T. D. Bradley *et al.*, “Ground-state atomic polarization relaxation-time measurement of Rb filled hypocycloidal core-shaped Kagome HC-PCF,” *J. Phys. B At. Mol. Opt. Phys.*, vol. 49, no. 18, p. 185401, Sep. 2016.

[5] F. Benabid, F. Couny, J. C. Knight, T. A. Birks, and P. S. J. Russell, “Compact, stable and efficient all-fibre gas cells using hollow-core photonic crystal fibres.,” Nature, vol. 434, no. 7032, pp. 488–491, 2005.

[6] K. Knabe et al., “10 kHz accuracy of an optical frequency reference based on ^12C_2H_2-filled large-core kagome photonic crystal fibers,” Opt. Express, vol. 17, no. 18, p. 16017, Aug. 2009.

[7] P. Meras, I. Y. Poberezhskiy, D. H. Chang, and G. D. Spiers, “Frequency stabilization of a 2.05 µm laser using hollow-core fiber CO 2 frequency reference cell,” Proc. SPIE 7677, Fiber Optic Sensors and Applications VII, 767713, p. 767713, April 2010.

[8] P. G. Westergaard et al., “Optical frequency standard using acetylene-filled hollow-core photonic crystal fibers,” Opt. Express, vol. 23, pp. 11227–11241, 2015.

[9] E. A. Curtis *et al.*, “Laser frequency stabilization and spectroscopy at 2051 nm using a compact CO2-filled Kagome hollow core fiber gas-cell system,” *Opt. Express*, vol. 26, no. 22, p. 28621, Oct. 2018.

[10] F. Poletti, “Nested antiresonant nodeless hollow core fiber,” Opt. Express, vol. 22, no. 20, pp. 23807–23828, 2014.